Supernovae and star formation in luminous infrared galaxies

By

Erik Kool

A thesis submitted to Macquarie University

for the degree of Doctor of Philosophy

Department of Physics & Astronomy

May 2019

Typeset in LaTeX 2_ε.

Statement of candidature

The content of this thesis is my own work, except where specifically described below.

The observing programs that form the basis of this thesis were the result of proposals from members of our collaboration. I contributed to all proposals as either the principal investigator (PI) or co-investigator (coI), except for the pilot program with GeMS/GSAOI in 2013. I prepared and conducted all classically scheduled adaptive optics (AO) observations at the Gemini South and Keck telescopes with the assistance of S. Ryder from the AAO in Sydney, Australia. I obtained the MUSE+GALACSI observations with the VLT. All observations with the Nordic Optical Telescope (NOT) were conducted by S. Mattila or T. Reynolds from Turku University in Turku, Finland. Radio observations with the VLA, EVN and VLBA were led and obtained by M. Pérez-Torres from the Instituto de Astrofísica de Andalucía in Granada, Spain. The observations with the Spitzer Space Telescope were obtained by S. Mattila. The observations with NACO on the VLT were obtained by S. Mattila. Optical data with the WHT was obtained by P. Jonker from Nijmegen University in Nijmegen, Netherlands.

I performed the data reduction of all near-infrared AO observations obtained with GeMS/GSAOI and NIRC2. The GeMS/GSAOI data processing in particular required the custom application of data processing package THELI to optimize image quality across the full field of view, where I was supported by THELI software designer M. Schirmer from Gemini South. Additionally, I performed the data reduction of all near-infrared data obtained with FLAMINGOS-2 on Gemini South, and archival data from VIRCAM on VISTA, and HAWK-I on the VLT. The GNIRS data from Gemini South was reduced by C. Baldwin and R. M. McDermid from Macquarie University in Sydney, Australia. All other data reduction was performed by the aforementioned collaborators who obtained the data.

I performed all analysis in this thesis, with a few exceptions. The light curve fitting in this thesis was performed by E. Kankare from Queen's University Belfast. The detection efficiency experiment in Chapter 2 was conducted by T. Reynolds. The SED fitting from Chapter 2 was performed by A. Efstathiou from the European University Cyprus in Cyprus.

S. Ryder and R. M. McDermid supervised this thesis and provided continuous and valuable feedback with regards to the methods, analysis and scientific interpretation of the work presented in this thesis.

Except where acknowledged in the customary manner, the material presented in this thesis is, to the best of my knowledge, original and has not been submitted in whole or part for a degree in any university.

Erik Kool

Acknowledgements

While we were on holiday four years ago, I received the invitation to start a PhD in Sydney. Our lazy morning abruptly turned quite hectic. The starting date was a mere three months away, which meant having to come to terms with moving across the world, but not at the same time. For me it was almost easy, I had a whole new world to explore and an exciting new project to focus on. Puck on the other hand had to deal with the Erik-shaped hole I had left. It took a year, and it didn't help her own PhD progress, but we made Sydney our home. Puck, this thesis is as much yours as it is mine. This time dinner is on me, but I'm sure it will be your treat very soon.

My supervisors, Stuart and Richard, this thesis would not have happened without you. I still find it unbelievable to have not one, but two supervisors as supportive as you have been. I flew to Australia without even knowing if the project had been granted any observing time, but since then I have been on so many trips across the world, and observed with so many incredible telescopes, I've lost count. Thanks for providing me with these opportunities. Given your very different fields of research, I am very content to have produced a thesis with such distinct contributions from you both.

I'd be remiss if I did not include my collaborators here, vital to this whole project. The SUNBIRD collaboration involves members across the world, and although it took some time and extensive travelling, I think I've shared a beer with almost everyone now. Seppo, Erkki, Tom, Miguel, Petri, Cristina, Mischa, Jari, Hanin, Rubén, Moses, thanks for your help and see you soon.

Finally, thanks to my friends, old and new, for keeping me sane along the way. Bas, Freek, Ido, Bart, Chris, Rob, Paul; Skype is a poor substitute so hopefully our next home will be closer to yours. Shane, Matt, Joao, Christina, Reece, Andrew, Glen, thanks for inviting or joining me in the regular escapes from the city, I'm looking forward to our last hurrah. The jacuzzi seems appropriate.

List of Publications

Peer-reviewed publications

- **E. C. Kool**, S. Ryder, E. Kankare, S. Mattila, T. Reynolds, R. M. McDermid, M. Á. Pérez-Torres, R. Herrero-Illana, M. Schirmer, A. Efstathiou, F. E. Bauer, J. Kotilainen, P. Väisänen, C. Baldwin, C. Romero-Cañizales, A. Alberdi, *First results from GeMS/GSAOI for project SUNBIRD: Supernovae UNmasked By Infra-Red Detection*, Monthly Notices of the Royal Astronomical Society, **473/4**, p.5641-5657 (2017)

- R. Herrero-Illana, M. Á. Pérez-Torres, Z. Randriamanakoto, A. Alberdi, A. Efstathiou, P. Väisänen, E. Kankare, **E. C. Kool**, S. Mattila, R. Ramphul, S. Ryder, *Star formation and AGN activity in a sample of local luminous infrared galaxies through multiwavelength characterization*, Monthly Notices of the Royal Astronomical Society, **470/2**, p.1634-1651 (2017)

- S. Ryder, R. Kotak, I. A. Smith, S. J. Tingay, **E. C. Kool**, J. Polshaw, *SN 1978K: An evolved supernova outside our Local Group detected at millimetre wavelengths*, Astronomy & Astrophysics, **595**, p.L9 (2016)

Non review publications

- S. Ryder, **E. C. Kool**, L. Chomiuk, *Radio Observations of Nova Muscae 2018 and Nova Carinae 2018 (ASASSN-18fv)*, The Astronomer's Telegram, **11504**, (2018)

- S. Ryder, **E. C. Kool**, L. Chomiuk, *Radio Detection of Nova Muscae 2018*, The Astronomer's Telegram, **11296**, (2018)

- S. Ryder, **E. C. Kool**, E. Kankare, S. Mattila, R. Kotak, J. Kotilainen, H. Kuncarayakti,

M. Pérez-Torres, Z. Randriamanakoto, T. Reynolds, C. Romero-Cañizales, S. Smartt, P. Väisänen, C. Stockdale, G. Anderson, *Radio Observations of SN 2018ec*, The Astronomer's Telegram, **11224**, (2018)

- S. Ryder, **E. C. Kool**, L. Chomiuk, *Radio Observations of Nova Muscae 2018)*, The Astronomer's Telegram, **11212**, (2018)

- S. Ryder, P. Lundqvist, M. Pérez-Torres, E. Kundu, **E. C. Kool**, C-I. Bjornsson, C. Fransson, *Radio constraints on the mass-loss rate of the Type Ia SN 2018gv*, The Astronomer's Telegram, **11211**, (2018)

- E. Kankare, S. Mattila, S. Ryder, **E. C. Kool**, R. Kotak, J. Kotilainen, H. Kuncarayakti, M. Pérez-Torres, Z. Randriamanakoto, T. Reynolds, C. Romero-Cañizales, S. Smartt, P. Väisänen, *Discovery of supernova candidate AT 2018ec in NGC 3256 with HAWK-I/GRAAL*, The Astronomer's Telegram, **11156**, (2018)

- M. Pérez-Torres, **E. C. Kool**, S. Ryder, S. Mattila, M. Fraser, E. Kankare, *VLBA observations of the nuclear transient AT 2017gbl in IRAS 23436+5257*, The Astronomer's Telegram, **10712**, (2017)

- **E. C. Kool**, S. Ryder, S. Mattila, T. Reynolds, G. Cannizzaro, E. Kankare, R. McDermid, M. Fraser, M. Pérez-Torres, T. Wevers, P. Jonker, P. Väisänen, S. Sweet, B. E. Tucker, *Discovery of luminous near-infrared transient AT 2017gbl in IRAS 23436+5257*, The Astronomer's Telegram, **10651**, (2017)

- **E. C. Kool**, S. Ryder, E. Kankare, S. Mattila, *First results from Project SUNBIRD: Supernovae UNmasked By Infra-Red Detection*, IAU Proceedings, **329**, (2017)

- S. Mattila, E. Kankare, **E. C. Kool**, S. Ryder, *High angular resolution radio and infrared view of optically dark supernovae in luminous infrared galaxies*, IAU Proceedings, **329**, (2017)

- S. D. Ryder, **E. C. Kool**, R. Kotak, *New radio observations of the Type IIn Supernova 1978K*, IAU Proceedings, **329**, (2017)

- S. Ryder, **E. C. Kool**, C. J. Stockdale, R. Kotak, C. Romero-Cañizales, G. Anderson, S. Amy, *Radio Non-Detection of SN 2017ahn*, The Astronomer's Telegram, **10147**, (2017)

- S. Ryder, **E. C. Kool**, L. Chomiuk, *ATCA Radio Monitoring of Nova Lup 2016 (ASAS-SN 16kt)*, The Astronomer's Telegram, **9644**, (2016)

- S. Ryder, **E. C. Kool**, C. J. Stockdale, R. Kotak, C. Romero-Cañizales, G. Anderson, *Radio Non-Detection of ASASSN-16cc = SN 2016aqf*, The Astronomer's Telegram, **9475**, (2016)

- **E. C. Kool**, S. D. Ryder, C. J. Stockdale, C. Romero-Cañizales, J. L. Prieto, R. Kotak, *Radio non-detection of ASASSN-15lh=SN2015L*, The Astronomer's Telegram, **8388**, (2016)

- S. Ryder, **E. C. Kool**, C. J. Stockdale, R. Kotak, *Radio Detection of SN 2016bas in ESO 163-G011*, The Astronomer's Telegram, **8836**, (2016)

- S. Ryder, **E. C. Kool**, C. J. Stockdale, C. Romero-Cañizales, R. Kotak, *Radio Non-Detection of ASASSN-16cc = SN 2016aqf*, The Astronomer's Telegram, **8815**, (2016)

- S. Ryder, **E. C. Kool**, C. J. Stockdale, R. Kotak, *Radio Detection of the Type IIn Supernova SMTJ07350518-6907531*, The Astronomer's Telegram, **7762**, (2015)

List of Acronyms

2MASS	Two Micron All Sky Survey
ADU	Analog to Digital Units
AGN	Active Galactic Nucleus
AIPS	Astronomical Image Processing System
ALFOSC	Andalucia Faint Object Spectrograph and Camera
AO	Adaptive Optics
AoN	Amplitude over Noise
ASAS-SN	All Sky Automated Survey for SuperNovae
BPT	Baldwin, Phillips and Terlevich diagram
CASA	Common Astronomy Software Applications package
CCSN	Core Collapse Supernova
CRTS	Catalina Real-Time Transient Survey
EVN	European VLBI Network
EW	Equivalent Width
F2	FLAMINGOS-2
FOV	Field Of View
FWHM	Full Width at Half Maximum
GeMS	Gemini Multi-Conjugate Adaptive Optics System
GLAO	Ground Layer Adaptive Optics
GNIRS	Gemini Near Infra-Red Spectrograph
GSAOI	Gemini South Adaptive Optics Imager
HAWK-I	High Acuity Wide field K-band Imager
HST	Hubble Space Telescope
IFU	Integral Field Unit
IRTF	NASA Infrared Telescope Facility
ISIS	Intermediate dispersion Spectrograph and Imaging System
kpc	kiloparsec
LGSAO	Laser Guide Star Adaptive Optics

LIRG	Luminous Infrared Galaxy
LOSS	Lick Observatory Supernova Search
MUSE	Multi Unit Spectroscopic Explorer
NACO	Nasmyth Adaptive Optics System + CONICA High Resolution IR Camera and Spectrometer
NED	NASA/IPAC Extragalactic Database
NGS	Natural Guide Star
NIRC2	Near Infrared Camera 2
NOT	Nordic Optical Telescope
NOTCam	Nordic Optical Telescope near-infrared Camera and spectrograph
NTT	New Technology Telescope
pPXF	Penalized Pixel-Fitting method
PSF	Point Spread Function
RBGS	Revised Bright Galaxy Sample
rms	root mean square
SDSS	Sloan Digital Sky Survey
SF	Star Formation
SFH	Star Formation History
SFR	Star Formation Rate
SMBH	Supermassive Black Hole
SN	Supernova
SNR	Signal to Noise Ratio
SSP	Simple Stellar Population
SUNBIRD	Supernovae UNmasked By Infra-Red Detection
SV	Science Verification
TNS	Transient Name Server
VIRCAM	VISTA InfraRed CAMera
VISTA	Visible and Infrared Survey Telescope for Astronomy
VLBA	Very Long Baseline Array
VLBI	Very Long Baseline Interferometry
VLT	Very Large Telescope
WCS	World Coordinate System
WHT	William Herschel Telescope

Abstract

The rate at which massive ($\gtrsim 8$ M$_\odot$) stars explode as core collapse supernovae (CCSN) can act as a tracer of the cosmic star formation history, independent from the conventional galaxy luminosity methods. However, estimates of the CCSNe rate suffer from significant statistical and systematic uncertainties. While upcoming next-generation optical survey telescopes will dramatically improve the statistics for determining the CCSN rate, they will still be prone to poorly understood systematic effects due to dust extinction and the restricted spatial resolution of seeing-limited observations.

In this thesis I present the methodology and results of project SUNBIRD (Supernovae UNmasked By Infra-Red Detection), in which we aim to characterize the population of CCSNe that remain hidden in the nuclear regions of galaxies due to bright background emission and significant dust extinction. Improved limits of this missed fraction will be crucial in reducing the systematic uncertainties of current and future CCSN surveys. We have observed a sample of luminous infrared galaxies (LIRGs), which have high star formation rates and host bright and complex nuclear regions, but so far have shown a prominent shortfall of CCSN discoveries. To uncover CCSNe in this regime, we observed in the near-infrared (near-IR), which is less affected by dust extinction compared to the optical, using state-of-the-art laser guide stars adaptive optics (LGS-AO) imagers GeMS/GSAOI on the Gemini South telescope and NIRC2 on the Keck II telescope. These combined capabilities provide diffraction-limited image quality on 8-10m class telescopes, and at wavelengths with an order of magnitude less dust extinction than in the optical, allowing us to sensitively probe the complex star-forming and nuclear regions of these dusty galaxies in a completely new way.

Over the course of project SUNBIRD we discovered four photometrically confirmed CCSNe and an additional five CCSN candidates. This has doubled the sample of AO-assisted CCSN discoveries in LIRGs, and includes one of the most nuclear CCSNe ever discovered in a LIRG (SN 2013if at 0.5″ or 0.2 kpc projected radial offset) and one of the most dust-extincted CCSN discovered in any galaxy (AT 2017chi with ∼12 magnitudes of extinction in V-band). Additionally, I discovered an extremely near-IR bright transient (AT 2017gbl) superimposed on its host's nucleus, believed to be a tidal disruption event.

By comparing the total sample of AO CCSNe discovered in LIRGs with all documented seeing-limited optical and near-IR discoveries, I show that our method is singularly effective in uncovering CCSNe in the nuclear regions. Whereas seeing-limited optical and near-IR discoveries drop off in the central kpc of LIRGs, AO-assisted CCSN discoveries increase dramatically, as expected from their centrally peaked star formation.

Finally, we have observed one of the SN factories in our sample, IRAS 18293-3413 with three CCSNe discoveries, with the cutting-edge AO-assisted MUSE integral field spectrograph at the ESO VLT. I show that, contrary to expectations, the CCSNe in this LIRG do not trace star formation well, but instead align with 'raw' Hα. This is likely due to the effects of dust extinction, implying that even when using near-IR observations, detailed knowledge about the distribution of star formation and dust will be a crucial factor when converting observed CCSNe to a supernova rate.

Contents

List of Figures

List of Tables

1 Introduction

The study of transients occupies a unique space in astronomy because transients, as opposed to the evolution of the most common building blocks in the Universe such as galaxies and stars, in general evolve over periods much shorter than human life times. As such it is only natural they intrigue astronomers and the public alike, in particular those transients that can be observed at extragalactic distances and are typically related to violent physical processes of stellar explosions or black holes. By now many different types of extragalactic transients have been identified and categorized, including supernovae (SNe), gamma-ray bursts (GRB), fast radio bursts (FRB) and tidal disruption events (TDE). Our understanding of the origin and mechanism of these extragalactic transients has not progressed as quickly as their rate of discovery, however, in large part due to the observing limits imposed by the large distances at which they occur. These types of transients are not exclusive to galaxies other than our own, but have only been observed at extragalactic distances because for a single galaxy such as the Milky Way the occurrence rate is very low. For example the expected core-collapse SN (CCSN) rate for the Milky Way is one every hundred years (Adams et al., 2013). The last SN observed in the Milky Way dates back to 1604, thought to have been a Type Ia SN instead (Vink, 2017), a SN type not brought about by core collapse. The best studied CCSN in history is SN 1987A in the Large Magellanic Cloud, not coincidentally also the most nearby SN in recent history.

However, these limitations in our understanding concerning their nature and mechanism has not kept astronomers from utilizing transients as a means to understand the Universe through their observed properties. A prime example for this contrast in extragalactic transient research is thermonuclear Type Ia SNe. Type Ia SNe are believed to be the result of a thermonuclear explosion of a degenerate carbon-oxygen white dwarf (WD) accreting mass in a binary system until the Chandrasekhar limiting mass ($\sim$1.4 $M_{\odot}$) is reached (Whelan and Iben, 1973). Despite hundreds of SN discoveries, progenitors to Type Ia SNe have never been observed and to this day there is no consensus whether the binary companion of the WD is a main sequence star/red giant star losing mass to the WD through Roche Lobe overflow, or if the explosion is the result of a double degenerate system with two merging WDs. But despite this lack of understanding, by using their well defined standard luminosity with empirical corrections to the light curve shape and colour, Type Ia SNe prove to be accurate distance indicators, or "standard candles" (Cadonau et al., 1985). This led to the ground-breaking discovery that the expansion of the Universe is not slowing but accelerating (Perlmutter et al., 1999, Riess et al., 1998)

Similarly to Type Ia SNe, the explosion mechanism of CCSNe (Type Ib/c and Type II) is a long-standing problem in astronomy, with various models attempting to predict the systematics of the SN explosion and remnant properties (Müller, 2017). While the progenitors of Type Ia SNe are long-lived low-mass stars, a CCSN is believed to be the result of the collapse of a short-lived massive ($\gtrsim$8 $M_{\odot}$) star at the end of its lifetime (Smartt, 2009). When the star develops an iron core larger than the Chandrasekhar limiting mass, the core is unable to support itself through electron degeneracy pressure and undergoes gravitational collapse at relativistic velocities. This contraction is halted once the density reaches the point where the strong nuclear force becomes repulsive, the inner core "bounces", and the subsequent outgoing shock waves accelerate material outwards, aided by a fraction of the vast number of neutrinos created under the extreme conditions in the core. The different observational subclasses of CCSNe are based on spectral and light curve features, and are believed to be related to the composition of the progenitors' envelope, mass loss history, presence of a binary companion, and initial mass. The progenitors of Type II SNe retained their hydrogen envelope resulting in a SN spectrum dominated by Balmer features, further subdivided into SNe showing a long plateau phase in their light curve (IIP) or linear decliners (IIL). Type Ib SNe have no Balmer lines, but still show helium features indicating the progenitor retained its helium envelope, while Type Ic SNe do not show hydrogen or helium spectral features (Gal-Yam, 2017). Figure 1.1 shows on the left typical spectra for different types of SNe with identifying features highlighted, and on the right the structure of their corresponding progenitors (Modjaz, 2011).

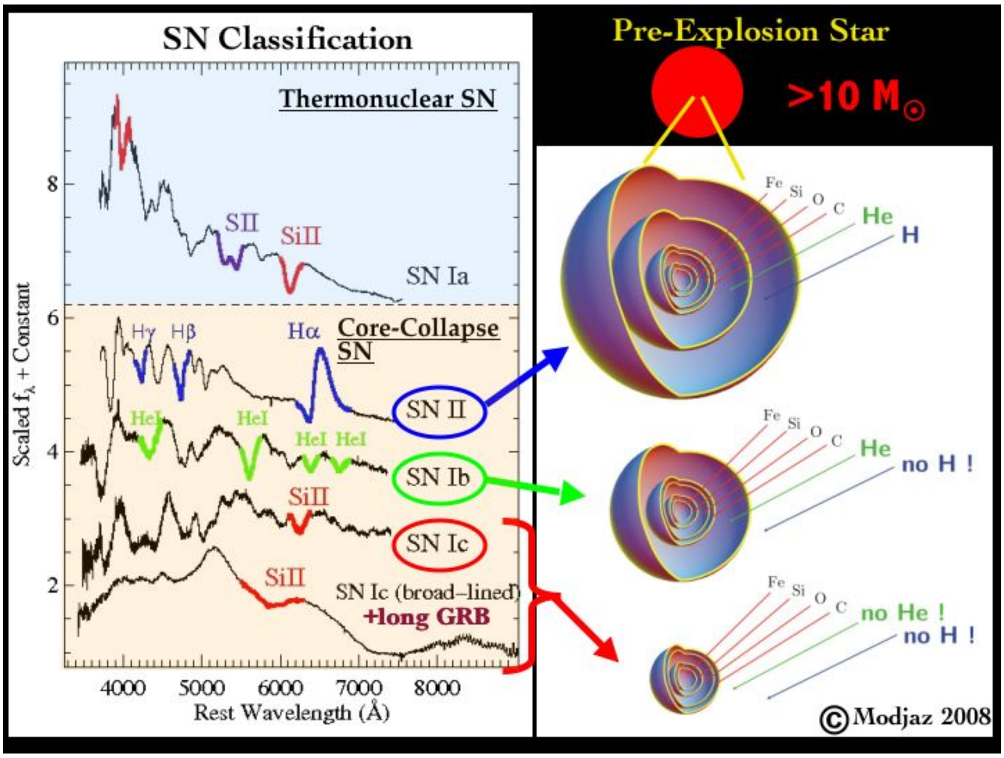

Figure 1.1: Typical spectra for different types of SNe with spectral features highlighted, and their corresponding progenitor shell structures, from Modjaz (2011).

The study of CCSNe, as well as their progenitors and remnants, can provide clues in many different areas. CCSNe and their progenitors play a significant role in the enrichment of the interstellar medium with heavier chemical elements, and using explosion mechanism models the nucleosynthesis of CCSNe can be determined (Umeda and Yoshida, 2017). The study of SN remnants allows for the study of the circumstellar and interstellar medium, as well as the mass loss history of the CCSN progenitor (Long, 2017). Based on theoretical calculations CCSNe are thought to be a significant source of dust formation, and observations in the IR help constrain this expectation (Williams and Temim, 2017). Finally, CCSNe and the rate at which they explode can also be used as cosmological tracers, for example of star formation.

1.1 CCSNe as a cosmological tracer of star formation

Just like Type Ia SNe, cosmological applications of CCSNe have been investigated that are independent from their explosion mechanism. Because CCSNe are typically not as bright as Type Ia SNe, and display a wide variety of luminosities and light curve evolution, there are limits to their usefulness as standard candles. Still, there have been attempts made to complement the current measurements of the Hubble constant by using Type IIP SNe as distance indicators. This involved relating the photospheric angular size of the SN with its expansion velocity (the expanding photosphere method, e.g., Eastman et al., 1996), or using an empirical correlation between plateau luminosity and expansion velocity (Hamuy and Pinto, 2002). So far these methods have not been as accurate in determining distances (~20%; Gall et al., 2018, Kasen and Woosley, 2009) as Type Ia SNe ($\lesssim$6%; Howell, 2011).

A different cosmological application of CCSNe relates to their progenitors. Because CCSNe are the result of the collapse of massive stars that have cosmologically short lives (7-45 Myr, e.g., Xiao et al., 2018), the rate of CCSNe should reflect the ongoing massive star formation (SF) at the explosion site. As such the rate of CCSNe can act as a probe of the SF rate of their hosts and, given the high peak luminosities of CCSNe, provide a determination of the cosmic star formation history (SFH) up to high redshift (Dahlen et al., 2004, Madau and Dickinson, 2014). The advantage of this method is that, while there are uncertainties in converting CCSNe rates into star formation rates (SFR), these uncertainties are observationally independent from conventional methods using galaxy luminosities, such as Hα, infrared (IR) and ultraviolet (UV). Additionally, an accurate determination of the evolution of the CCSN rate with redshift would constrain the chemical enrichment of galaxies, as CCSNe are the source of all metals heavier than iron in the universe.

For this method to be viable, it has to be accurately calibrated against other known SF tracers, which so far has been done by comparing observed CCSN rates with the rates predicted from the cosmic SFH as determined through galaxy luminosities.

1.1.1 Predicted CCSN rate

The predicted CCSN rate as a function of redshift is determined by multiplying the SFR as a function of redshift by the fraction of stars that form CCSNe. Madau and Dickinson (2014) determined the cosmic SFH from ultraviolet (UV) and infrared (IR) data to be:

$$\varphi(z) = 0.015\frac{(1+z)^{2.7}}{1+[(1+z)/2.9]^{5.6}}\,\mathrm{M_\odot\,year^{-1}\,Mpc^{-3}} \tag{1.1}$$

Given an assumed initial mass function (IMF) $\phi(m)$, the number of CCSN progenitors per unit formed stellar mass k is:

$$k = \frac{\int_{m_l}^{m_u} \phi(m)\,\mathrm{d}m}{\int_{m_{min}}^{m_{max}} m\,\phi(m)\,\mathrm{d}m} \tag{1.2}$$

with m_l and m_u the lower and upper mass limits for a CCSN progenitor, and m_{min} and m_{max} the lower and upper mass cut-off of the IMF $\phi(m)$. Note that while k depends on the adopted IMF, so does the derived SFR $\varphi(z)$ through the SF indicators used, including Hα, UV and IR. These indicators directly (UV) or indirectly (optical/UV light reprocessed by dust and emitted in the IR) probe the young massive end of the stellar mass range, which is similar to the mass range of stars exploding as CCSNe. This means variations in the adopted IMF should only have a minor effect on the expected CCSN rate derived this way. Assuming a Salpeter IMF with cut-offs of 0.1 and 125 $M_{\odot}$, and SN progenitor mass limits of 8 and 40 $M_{\odot}$ (Smartt, 2009), the number of stars that explode as CCSNe per unit mass is $k = 0.0068$ (Madau and Dickinson, 2014). The comoving volumetric CCSN rate is then defined as $R_{CC}(z) = \varphi(z) \times k$.

1.1.2 Observed CCSN rates

There has been a lot of work done on determining the CCSN rate at different redshifts. The study of Cappellaro et al. (1999) was one of the first measurements of CCSN rates based on a relatively large number of SNe, by combining the logs of several SN searches at the time and a long-term amateur visual search by Evans (1997). The sample consisted of ~67 local (z~0) unobscured CCSNe discovered in normal galaxies and was expressed in terms of optical galaxy luminosity. Dahlen et al. (2004) extended the observed CCSN rates with redshift using 17 CCSNe across two redshift bins discovered with the Advanced Camera for Surveys (ACS) on the Hubble Space Telescope (HST). They showed an overall increase by a factor of ~7 compared to the local rate, in reasonable agreement with a compilation of SFR data derived from UV-luminosity densities and IR data sets (Giavalisco et al., 2004).

Based on a refined normalization of the cosmic SFH, Hopkins and Beacom (2006) concluded the CCSN rate measurements derived in Cappellaro et al. (1999) and Dahlen et al. (2004) were lower than the CCSN rates inferred from the cosmic SFH. Botticella et al. (2008) observed a similar difference between the SFH from Hopkins and Beacom (2006) and their CCSN rate at $\langle z \rangle$ = 0.21 derived as part of the Southern inTermediate Redshift ESO Supernova Search (STRESS), concluding that in order to probe the link between SN and SF rates it was necessary to reduce the uncertainties in the cosmic SFH. The Lick Observatory Supernova Search (LOSS Leaman et al., 2011a,b), conducted with the Katzman Automatic Imaging Telescope (KAIT; Filippenko et al., 2001), significantly improved the local CCSN rate measurement based on 440 CCSNe discoveries (Li et al., 2011b) from a volume limited sample of 14882 galaxies monitored for 10 years. The Supernova Legacy Survey increased the sample at higher redshift, using 117 CCSNe with a median redshift of z = 0.29, see Table 1.1.

Horiuchi et al. (2011) proceeded to collect the cosmic CCSN rate measurements determined in the aforementioned studies and compared them with the CCSN rate prediction using the cosmic SFH from Hopkins and Beacom (2006). Their results suggested that the measured CCSN rate was a factor of ~2 smaller than the prediction from the cosmic SFH, up to a redshift of ~1; the so-called 'Supernova rate problem', shown in Fig. 1.2. However, locally this discrepancy was not seen. Using 14 CCSNe within 11 Mpc, Botticella et al. (2012) compared the local CCSN rate with standard SFR measurements based on Hα, far UV and total IR galaxy luminosities. Good agreement of the CCSN rate was found with the SFR as derived through the FUV and IR luminosities, although the SFR based on Hα was lower by a factor of almost 2.

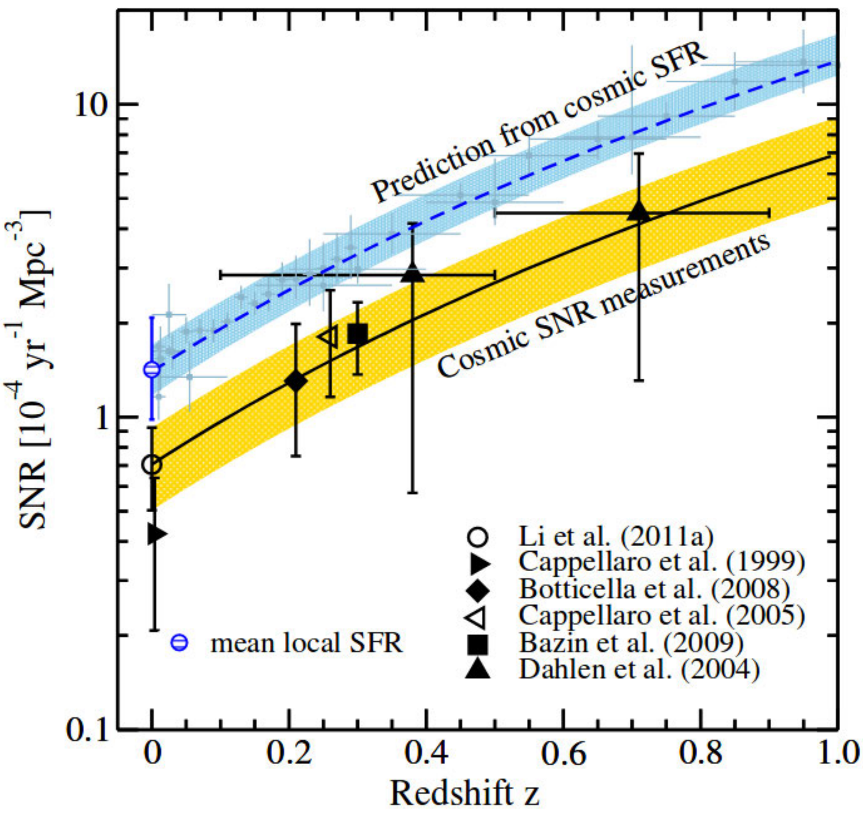

Figure 1.2: The 'Supernova Rate problem', from Horiuchi et al. (2011). The comoving CCSN rate as predicted by the cosmic SFH from Hopkins and Beacom (2006) is a factor of 2 larger than the cosmic CCSN rate measured by SN surveys.

At higher redshift Dahlen et al. (2012) and Melinder et al. (2012) bridged the gap between observed and predicted CCSN rates by applying the empirically derived missed-fraction correction from Mattila et al. (2012) (further discussed in Section 1.3). Dahlen et al. (2012) completed the HST/ACS study of Dahlen et al. (2004) with an increased sample of 45 CCSNe at redshift $\langle z \rangle$ = 0.39, 0.73 and 1.11. Melinder et al. (2012), based on a sample of 9 CCSNe as part of the Stockholm

VIMOS Supernova Survey (SVISS), determined a CCSN rates at redshift $\langle z \rangle = 0.39$ and 0.73, respectively, see Table 1.1. Based on their results Melinder et al. (2012) stressed the importance of systematic effects and dust extinction in particular, when trying to estimate the CCSN rate at moderate to high redshift.

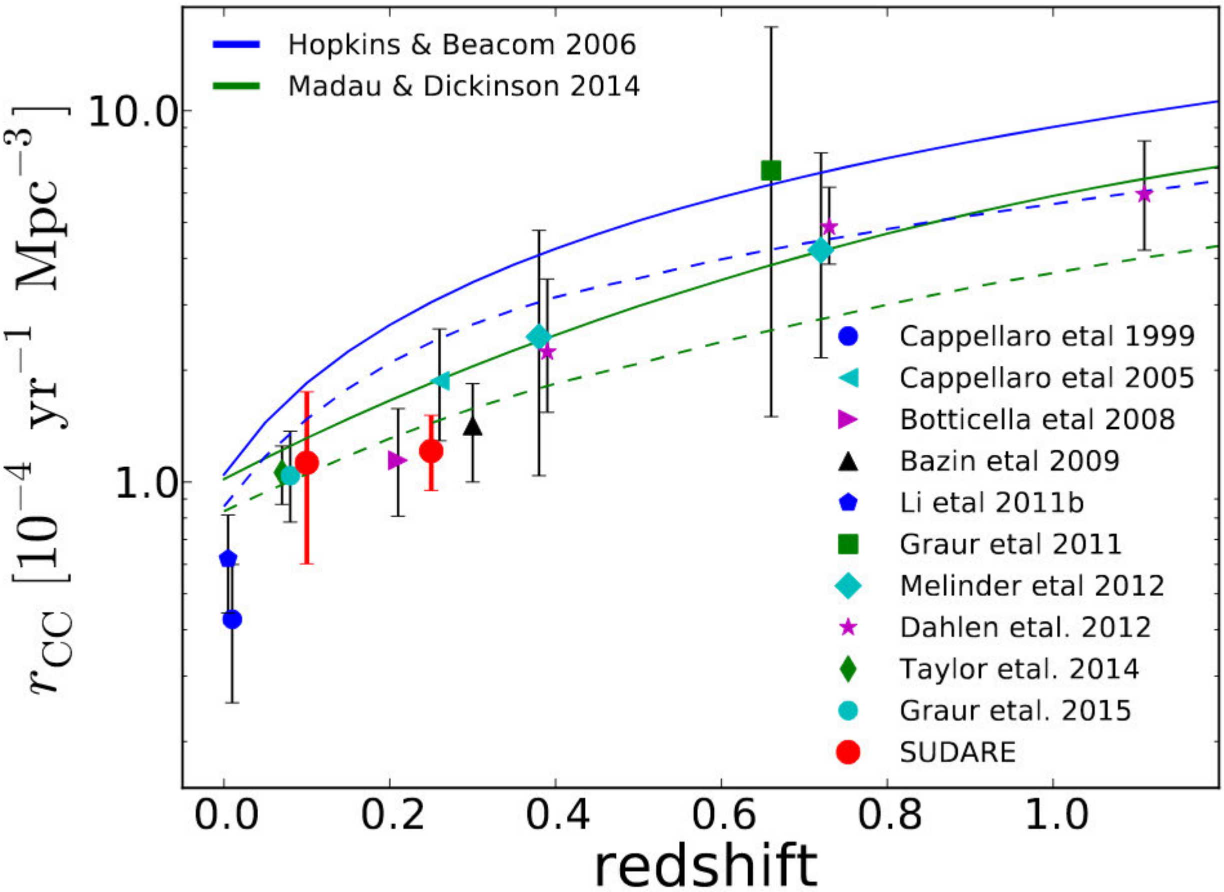

Figure 1.3: CCSN rates per unit volume, from Cappellaro et al. (2015). Solid lines show the predicted CCSN rates based on the cosmic SFH from Hopkins and Beacom (2006) in blue and Madau and Dickinson (2014) in green. The dashed lines show the predicted rates, corrected for the missed SN fraction from Mattila et al. (2012).

Finally, Cappellaro et al. (2015) (SUDARE VST-OmegaCAM SN search) and Strolger et al. (2015) (CANDELS/CLASH SN surveys) compared CCSN rates with the updated cosmic SFH from Madau and Dickinson (2014), based on samples of 50 and 44 CCSNe at redshift $0.2 < z < 0.8$ and $0.1 < z < 2.5$, respectively (see Table 1.1). Both studies found their rates in good agreement with the prediction from the cosmic SFH. Fig. 1.3 shows the CCSN rate as fitted by Cappellaro et al. (2015) including the cosmic SF histories by Hopkins and Beacom (2006) and Madau and Dickinson (2014) and CCSN rate measurements obtained previously. This figure also includes the results from Graur et al. (2011), Taylor et al. (2014) and Graur et al. (2015), see Table 1.1 for the reported rates. Note that not only the SN rate measurements have considerable uncertainties, but also the cosmic SF histories are affected by uncertainty as is clearly shown by the two cosmic SF histories displayed in Fig. 1.3. Some sources of uncertainty in the cosmic SFH are the interpretation of light as mass, the measurements of star formation that is obscured by dust, and a possible evolution of the stellar IMF (Madau and Dickinson, 2014, Wilkins et al., 2008).

Study	Redshift (z)	CCSN rate (10^{-4} yr^{-1} Mpc^{-3})
Li et al. (2011a)	0	$0.62^{+0.07}_{-0.07}{}^{+0.17}_{-0.15}$
Taylor et al. (2014)	0.072	1.06 ± 0.19
Graur et al. (2015)	0.075	$1.04^{+0.33}_{-0.26}{}^{+0.04}_{-0.11}$
Strolger et al. (2015)	0.08	0.72 ± 0.06
Cappellaro et al. (2015)	0.1	$1.13^{+0.62}_{-0.53}{}^{+0.49}_{-0.49}$
Cappellaro et al. (2015)	0.25	$1.21^{+0.27}_{-0.27}{}^{+0.47}_{-0.47}$
Bazin et al. (2009)	0.29	$1.42 \pm 0.3 \pm 0.3$
Melinder et al. (2012)	0.39	$3.29^{+3.08}_{-1.78}{}^{+1.98}_{-1.45}$
Dahlen et al. (2012)	0.39	$3.00^{+1.28}_{-0.94}{}^{+1.04}_{-0.57}$
Graur et al. (2011)	0.66	$6.9^{+9.9}_{-5.4}$
Melinder et al. (2012)	0.73	$6.40^{+5.30}_{-3.12}{}^{+3.65}_{-2.11}$
Dahlen et al. (2012)	0.73	$7.39^{+1.86}_{-1.52}{}^{+3.20}_{-1.60}$
Dahlen et al. (2012)	1.11	$9.57^{+3.76}_{-2.80}{}^{+4.96}_{-2.80}$
Strolger et al. (2015)	2.0	$3.7^{+3.1}_{-1.6}$

Table 1.1: A selection of recent measurements of CCSN rates at different redshifts. Reported statistical errors are shown first, followed by systematic errors. All studies apply a Hubble constant of $H_0 = 70$ km s^{-1} Mpc^{-1}.

1.2 CCSN rate uncertainties

Cappellaro et al. (2015) argued that the systematic errors in the SN and SF rates remain too large to invoke a supernova rate problem in the first place, something that is well reflected in Fig. 1.3. The supernova rate problem resulted from comparing CCSN rates to the cosmic SFH prediction from Hopkins and Beacom (2006) marked with the blue line, which clearly lies above almost all CCSN rate measurements before or since. The predicted rates based on the cosmic SFH from Madau and Dickinson (2014) marked with the green line shows a better alignment at higher redshift, but it shows a surplus of predicted CCSNe in the local Universe. The CCSN rates in the local Universe appear better fitted by the dashed lines, which indicate the two cosmic SFH predictions taking into account the fraction of hidden SNe from Mattila et al. (2012). An essential step to resolving this mismatch is to improve the errors associated with CCSN rate measurements, especially at high redshift. Fig. 1.3 also shows how an accurate cosmic CCSN rate evolution in turn can provide an independent consistency check of the cosmic SFH, given the significant difference between the two presented cosmic SFHs. Two main sources of uncertainty in the measurement of CCSN rates are SN statistics, and the missed-fraction correction. Here we describe each of these in more detail.

1.2.1 Poor supernova statistics

An important source of uncertainty contributing to the large error bars of the CCSN rates shown in Fig 1.3 is the statistical error, in particular at high redshift. For example, the CCSN rate derived in Dahlen et al. (2012) is based on one of the largest samples of CCSNe past z~0.1 for a total of 45 CCSNe, of which only 11 fall in the highest redshift bin centred on z = 1.1. This is an issue that cannot be easily resolved, but history has shown that it is likely just a matter of time. Fig. 1.4 shows the detections of SNe per year dating back to the 1880s, from Stritzinger and Moriya (2018) and courtesy of M. Sullivan, for a total of 20,000 SN discoveries so far. The numbers in this figure also include Type Ia SNe, but the trend is very clear.

There is no reason to believe this trend will not continue. Currently ~5 SNe are discovered and confirmed each day through wide-field all sky surveys such as CRTS, Drake et al. (2009); ASAS-SN, Shappee et al. (2014); Pan-STARRS1, Chambers et al. (2016); (i)PTF, Rau et al. (2009); and SkyMapper, Scalzo et al. (2017). However, this pales in comparison with the expected rates produced by the large next-generation survey telescopes currently being designed or built. The Zwicky Transient Facility (ZTF; Smith et al., 2014) has just started observations and observes the entire Northern sky ~300 times a year for transients. The Large Synoptic Survey Telescope (LSST) is nearing first light, and is forecast to produce 100,000 transient alerts per night and three to four million photometric SN discoveries during its ten-year survey[1]. The 4MOST survey[2] on the VISTA telescope is expected to produce a sample of 30,000 spectroscopically confirmed SNe (Stritzinger and Moriya, 2018) during its lifetime. And finally the James Webb Space Telescope (JWST) has surveys designed to detect SNe up to redshift z = 7.5 (Hartwig et al., 2017, Wang et al., 2017).

However, one of the most important systematic uncertainties in measurements of CCSN rates

[1]https://www.lsst.org/science/transient-optical-sky/supernovae
[2]https://www.4most.eu/cms/

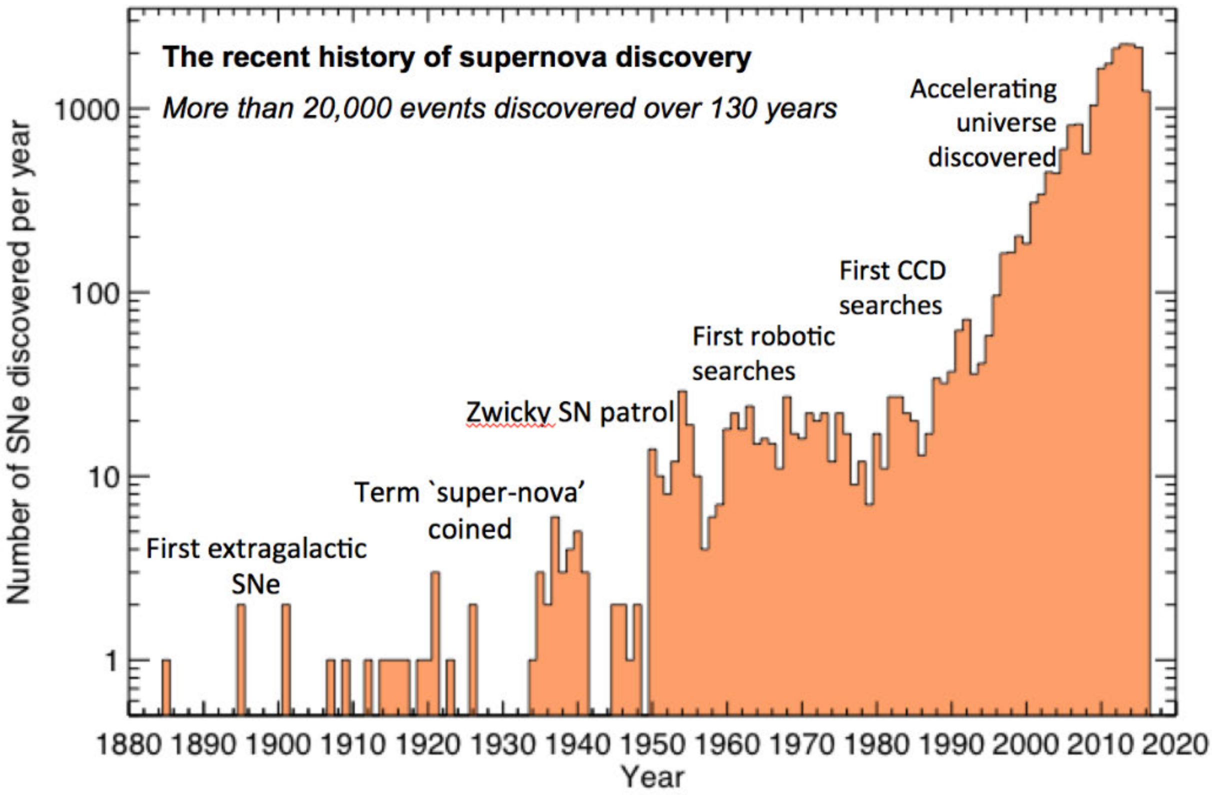

Figure 1.4: Histogram of supernovae discoveries since the 1880s. From Stritzinger and Moriya (2018), figure courtesy of M. Sullivan.

will not easily be resolved by an increased number of SN detections. All the aforementioned ground-based surveys will monitor for SNe at optical wavelengths in natural seeing conditions. It will be necessary to correct for the fraction of SNe that are not being observed in regimes of high dust extinction and in spatially complex crowded fields. This is critical for CCSN rates, since these conditions are most prominent in starburst galaxies, which are host to exceedingly high CCSN rates.

1.2.2 Missed SN fraction correction

In order to determine the intrinsic SN rate based on a limited sample of discoveries, it is critical for any SN rate measurement to account for the fraction of SNe that are systematically not being observed. Typically the dominant factors for missing SNe are dust extinction and reduced detection efficiency in regions of bright background such as the nuclear regions of galaxies. The degree of dust extinction a SN will be subject to depends on the dust content of the galaxy, and the relative position of the SN in the galaxy. Hatano et al. (1998) presented a semi-analytical model to account for dust extinction and inclination effects in normal spiral galaxies, by simulating SN positions within a spiral galaxy with a given dust content. They predicted a strong deficit of bright CCSNe inside a projected radius of a few kiloparsec (kpc). Bazin et al. (2009) adopted this model to find it increased their CCSN rate at z = 0.29 by 15%, while Dahlen et al. (2004) combined it with a starburst extinction law to reflect the increase of starburst galaxies with redshift, resulting in a 60% rate increase at z ~ 0.3 and a 100% increase at z ~ 0.7.

The impact of starburst galaxies on the observed CCSN rate as a function of redshift was further explored by Mannucci et al. (2007). They argued that a missed-fraction correction to CCSN rates based on a sample of local galaxies is not appropriate to use at all redshifts, because at higher redshift the SF activity does not predominantly occur in relatively clean environments as it does locally, but in dusty starburst galaxies. This is supported by Magnelli et al. (2009, 2011) who showed that by a redshift of z ~ 1 SF in starburst galaxies like luminous and ultraluminous infrared galaxies (LIRGs and ULIRGs) dominates over that in normal galaxies, see Fig. 1.5.

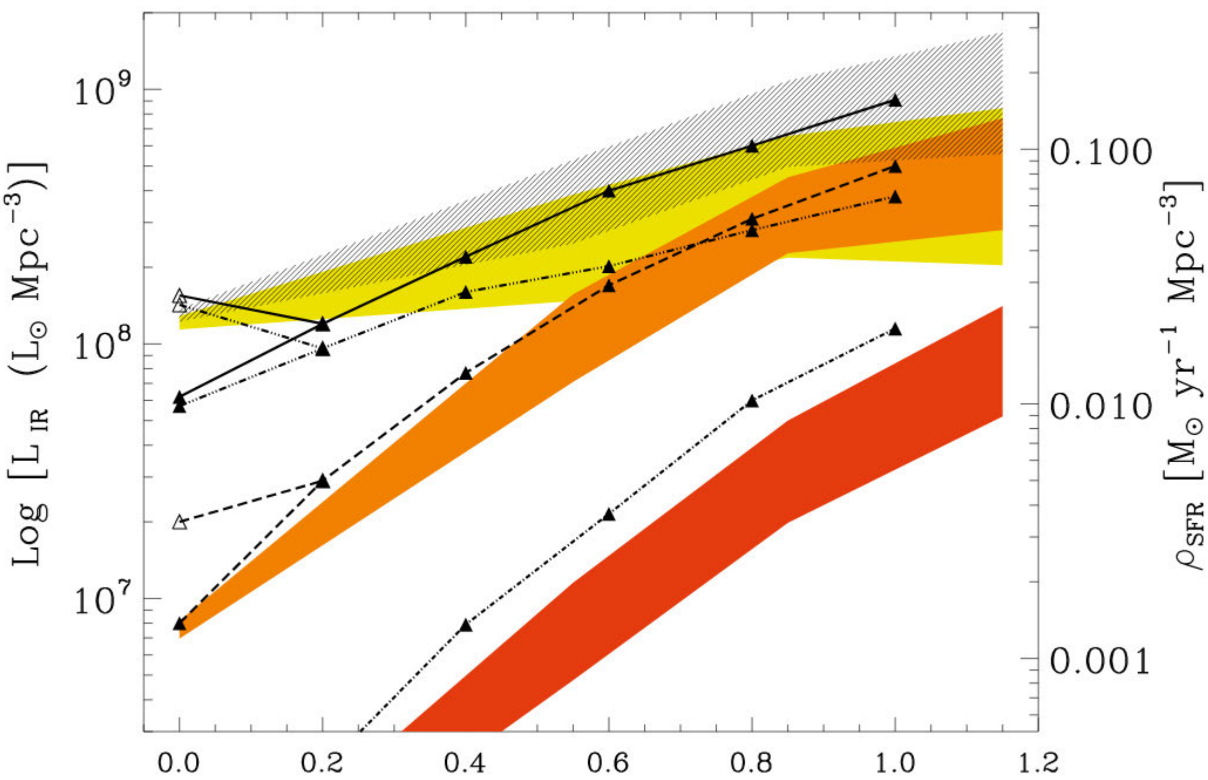

Figure 1.5: From Magnelli et al. (2009), showing the total comoving IR energy/SFR density as a function of redshift in grey. In yellow, orange and red are shown the relative contribution of normal galaxies, LIRGs and ULIRGs, respectively. The triangles represent the earlier results from Le Floc'h et al. (2005) of the same properties.

1.3 SN rates in luminous infrared galaxies

LIRGs and ULIRGs are defined as galaxies with IR luminosities of $L_{\rm IR} > 10^{11}$ $L_\odot$ and $L_{\rm IR} > 10^{12}$ $L_\odot$, respectively (Sanders et al., 2003). They exhibit high SF rates and are host to large amounts of dust. SF in starburst galaxies such as LIRGs and ULIRGs is believed to be well traced by their IR luminosity (e.g., Le Floc'h et al., 2005), with the high luminosity a result of dust absorption of UV light from hot young stars getting re-emitted in the IR. (U)LIRGs constitute only a small fraction of galaxies in the local Universe, but at higher redshift (U)LIRGs are the main contributor to SF, as shown in Fig. 1.5. (U)LIRGs display a wide variety in morphology, including both normal spiral galaxies as well as galaxies disturbed due to mergers or interactions with one or more companion galaxies, enhancing SF in the nuclear regions in particular (Väisänen et al., 2012). As a result of their high SF rates, starburst-dominated (U)LIRGs have an elevated expected CCSN rate of the order of one per year (Mattila and Meikle, 2001), which is ~100 times larger than the Milky Way CCSN rate.

In addition to CCSNe, (U)LIRGs also appear to have an over-abundance of tidal disruption events (TDE), where a star in close approach to a supermassive black hole is ripped apart by the large tidal forces, resulting in a bright flare (Rees, 1988). Recently, Tadhunter et al. (2017) presented the discovery of a TDE candidate in LIRG IRAS F01004-2237, a result from monitoring a sample of 15 (U)LIRGs over 10 years. Based on this detection in such a limited sample they suggested that the rate of TDEs is intrinsically higher in (U)LIRGs than in the general galaxy population, especially considering the view of the nucleus of IRAS F01004-2237 is unusually clear of dust. With most (U)LIRG central starburst regions enshrouded in dust, the true rate could be even higher. This was further supported by the discovery of an extremely luminous dust-obscured TDE in LIRG Arp 299 (Mattila et al., 2018).

With dust extinction and SF strongly correlated (Choi et al., 2006), the fraction of missed SNe will be severe in (U)LIRGs. This was well shown by Richmond et al. (1998), who conducted a search for SNe in LIRGs and starburst galaxies at optical wavelengths. Despite intrinsically high SF rates in LIRGs, they failed to observe an elevated CCSN rate with respect to 'normal' galaxies, and none of the CCSN discoveries occurred in the host galaxy's nucleus.

This led to multiple studies to determine the CCSN rate in LIRGs and other starburst galaxies in the near-IR, since in the near-IR extinction is vastly reduced compared to optical wavelengths ($A_{\rm K} \sim 0.1 \times A_{\rm V}$). Grossan et al. (1999) obtained a large sample of observations of starburst galaxies in K'-band, but failed to discover any SNe, which they attributed to a lack of spatial resolution (typical point spread function (PSF) of 2.2″ Full Width at Half Max (FWHM)). Mannucci et al.

(2003) observed 46 local LIRGs in natural seeing conditions in *K'*-band and detected three CCSNe, including two that had not been observed in the optical. Still, this was an order of magnitude smaller than the rate estimated from the galaxies' $L_{\rm FIR}$, which they claimed demonstrated that even at near-IR wavelengths 80% of CCSNe in LIRGs are still undetected. Cresci et al. (2007) observed 17 LIRGs with HST/NICMOS in the *F160W* filter and did not find any confirmed SNe. Miluzio et al. (2013) observed 30 LIRGs across three semesters in service time with HAWK-I on the VLT in natural seeing conditions in *K*-band and detected five CCSNe. They claimed good agreement with the expected rate, but assumed a large fraction (~60-75%) remained hidden in the nuclear regions (<2 kpc) due to reduced search efficiency and extinction. Currently the SPIRITS (SPitzer InfraRed Intensive Transients Survey; Kasliwal et al., 2017) survey employs the use of the Spitzer space telescope to discover transients in the mid-IR in starburst galaxies and LIRGs, resulting in several dust-obscured CCSNe discoveries (Jencson et al., 2018, 2017) and a determination of a missed fraction of CCSNe missed in nearby galaxies of $38.5^{+26.0}_{-21.9}$% (Jencson et al., 2019).

Mattila et al. (2012) presented new empirical limits on the fraction of CCSNe missed by optical surveys as a function of redshift, based on monitoring of LIRG Arp 299. Arp 299 is one of the most IR luminous LIRGs within 50 Mpc and a prolific SN factory with 7 CCSN discoveries since 1992. Mattila et al. (2012) used an approach somewhat similar to the previous modelled estimate from Mannucci et al. (2007), but used a larger sample of CCSNe and an improved understanding of the evolution of LIRGs and ULIRGs with redshift (Elbaz et al., 2011). For rest-frame optical surveys they found a missed SN fraction of ∼19% locally, rising to ∼38% at a redshift of z = 1.2, see Fig. 1.6.

These corrections were successfully applied to bridge the gap between observed and predicted CCSN rates in several studies (e.g., Dahlen et al., 2012, Melinder et al., 2012), or used as a high extinction scenario for CCSN rates at high redshift (z=2; Strolger et al., 2015). However, as is shown in Fig. 1.6 with the dashed lines indicating the systematic uncertainties, and the results from the targeted near-IR LIRG SN surveys, there remains considerable uncertainty in the CCSN rate from LIRGs. With a dozen CCSN discoveries in total, the number of discoveries from near-IR studies in natural seeing conditions have also lagged behind the expected CCSN rate. This was typically attributed to limitations in temporal coverage, lack of contrast against the extremely luminous background and/or inadequate spatial resolution in order to resolve the crowded and complex nuclear regions in LIRGs.

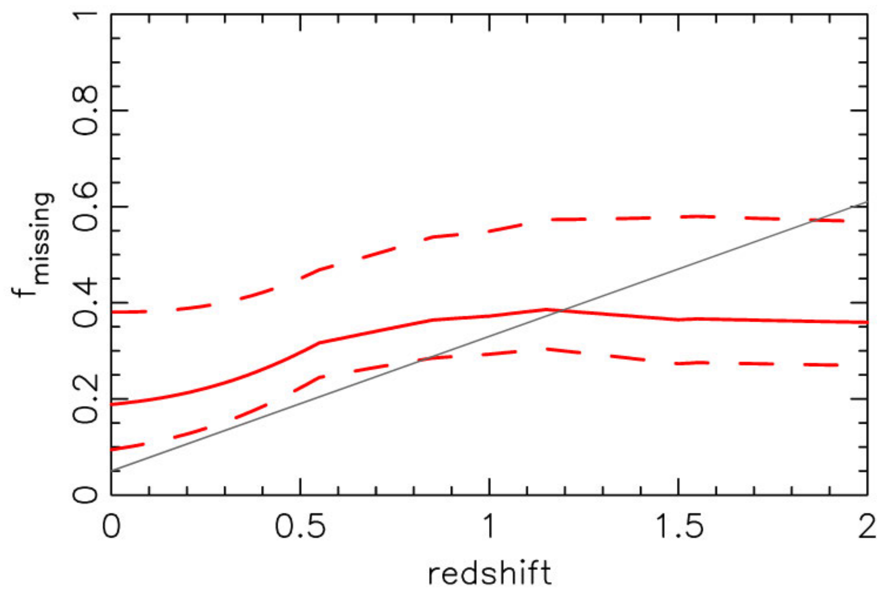

Figure 1.6: The fraction of CCSNe that will be missed by rest-frame optical surveys as a function of redshift, from Mattila et al. (2012). The solid red line shows the nominal estimate, and the dashed lines the low and high estimates as described in the paper. The grey line indicates the modelled estimate from Mannucci et al. (2007).

1.4 Adaptive optics

It is clear that in order to improve the constraints on the missed fraction of CCSNe, a larger statistical sample of CCSNe in obscured and clumpy galaxies is required. Recent studies have used near-IR ground-based laser guide star (LGS) adaptive optics (AO) imaging to overcome the limitations in spatial resolution and contrast issues affecting the earlier near-IR surveys (Kankare et al., 2008, 2012, Mattila et al., 2007). Although the studies employing AO were limited in scope, they have had considerable success uncovering SNe in LIRGs with an additional five near-IR CCSN discoveries. Promisingly, several of these CCSNe have been within a few hundred pc from the hosts' nuclei, with extinctions up to 17 magnitudes in V-band (Kankare et al., 2008).

Adaptive optics is a technique where distortions caused by atmospheric turbulence are corrected for in real-time by deformable mirrors, providing a spatial resolution close to the telescopes diffraction limit (~0.06″ in K-band on an 8 metre-class telescope). The shape of the wavefront, distorted by the turbulent atmosphere, is determined by a wave front sensor using a point source as a reference beacon. The wavefront is then restored by applying a correction opposite to the distortion through the use of a deformable mirror, whose surface shape is changed by actuators several hundred times a second. Classical AO uses a guide star of sufficient brightness very close to the target as a reference beacon. As a sufficiently bright star will not always be available, this severely limits sky coverage, and the correction degrades quickly with distance from the guide star. By using a laser to create artificial guide stars instead, a much larger fraction of the sky can be accessed with AO (e.g., d'Orgeville et al., 2012, Wizinowich et al., 2006). Additionally, through the application of multiple deformable mirrors correcting for aberrations produced by different layers of atmosphere, the corrected FOV can be significantly increased. This technique is called multi-conjugate adaptive optics (MCAO) and is used by the Gemini South Adaptive Optics Imager (GSAOI; Carrasco et al., 2012, McGregor et al., 2004) with the Gemini Multi-Conjugate Adaptive Optics System (GeMS; Neichel et al., 2014b, Rigaut et al., 2014) on the Gemini South telescope. Fig. 1.7 shows the improvement of MCAO over classical AO and seeing-limited observations in an image of NGC 288 observed with GeMS/GSAOI[3].

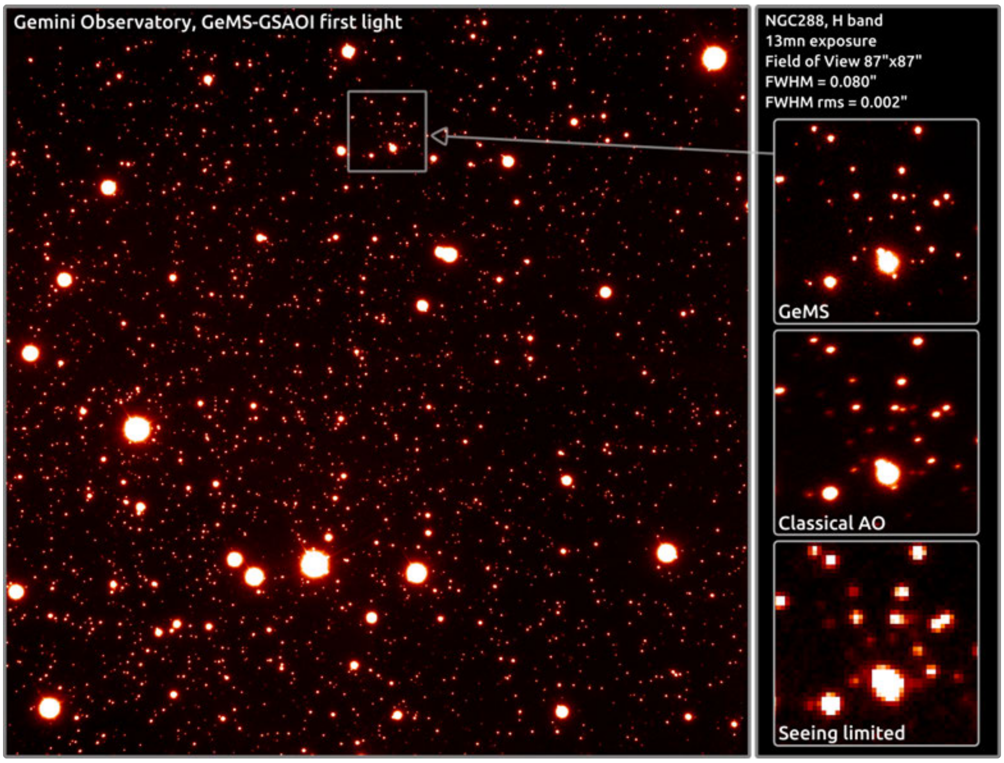

Figure 1.7: First light image of GeMS/GSAOI, showing the globular star cluster NGC 288. The right panels show a comparison of the GeMS/GSAOI image with classical AO and seeing-limited observations of the same field.

Another application of AO uses multiple wavefront sensors to measure wavefront aberrations towards multiple guide star directions, which can be natural or laser guide stars. A single deformable mirror is then used to correct for the average wavefront signal at ground level, which is typically the most turbulent layer in the atmosphere. This technique is known as ground layer adaptive optics (GLAO) and is used to achieve moderate seeing enhancement over a large FOV.

[3]https://www.gemini.edu/node/11715

1.5 This thesis

Building on the results of the programs employing AO, we commenced in 2015 project SUNBIRD (Supernovae UNmasked By Infra-Red Detection): a systematic search for CCSNe in a sample of LIRGs within 150 Mpc using laser guide star AO imaging. We use state-of-the-art laser guide star AO imagers on two of the largest optical/IR telescopes in the world: GeMS/GSAOI on the Gemini South telescope, and NIRC2 on the Keck II telescope (Wizinowich et al., 2006). This allows us to achieve a spatial resolution that lets us probe close in to the nuclear regions. We observe in the near-infrared 2.15 μm K_s-band, which is less affected by dust extinction compared to the optical. The SUNBIRD project aims to characterise the population of CCSNe in the dusty and crowded star forming regions of LIRGs and in this way improve the constraints on the fraction of CCSNe missed due to dust obscuration and/or nuclear vicinity.

In this thesis project SUNBIRD is described and the current results presented. The first two chapters focus on the methodology of the project, and the CCSNe discovered with GeMS/GSAOI on the Gemini South telescope (Chapter 2) and with NIRC2 on the Keck telescope (Chapter 3). The chapters include a new method to obtain a uniform data quality across the full field of view (FOV) of widefield AO data to optimize SN recovery, and a description of the fitting procedure used to identify dust-obscured CCSNe based on sparse photometric data. Across the Gemini and Keck programs four photometrically-confirmed CCSNe and three CCSN candidates were discovered, as well as an extremely luminous transient superimposed on its LIRG host's nucleus, the luminosity and light curve of which did not conform with any CCSN scenario, but instead is thought to be a TDE.

The results are put into context in Chapter 4, where the impact of the CCSN discoveries and methodology of project SUNBIRD is investigated by comparing them with all reported near-IR and optical CCSN discoveries in LIRGs in the literature. The discoveries made in project SUNBIRD represent a significant increase of the sample of CCSNe discovered in the near-IR with AO, and as such preliminary conclusions can be drawn about the effectiveness of the method employed in project SUNBIRD, and the implications of the projects discoveries on the fraction of CCSNe that are missed by optical surveys.

Finally, in Chapter 5 a case study is presented of the environment of three CCSNe discovered in SN factory IRAS 18293-3413, a well monitored LIRG from project SUNBIRD. The study is based on optical integral field unit (IFU) spectroscopic data obtained during science verification of the MUSE facility, the combination of the MUSE IFU instrument and its cutting-edge AO system GALACSI on the Very Large Telescope (VLT) in Chile. The local conditions at the SN sites in terms of SF rate, metallicity, stellar population age and dust extinction are compared against the rest of the galaxy and discussed.

In Chapter 6 the findings are summarized. Throughout this thesis we assume $H_0 = 70$ km s^{-1} Mpc^{-1}, $\Omega_\Lambda = 0.7$, and $\Omega_M = 0.3$. Unless stated otherwise, a Salpeter IMF with $\alpha = 2.35$ is assumed.

2

Project SUNBIRD: Gemini South

2.1 Introduction

At the start of 2015 we commenced project SUNBIRD (Supernovae UNmasked By Infra-Red Detection): a systematic search for CCSNe in a sample of LIRGs within 150 Mpc using laser guide star adaptive optics (LGS-AO) imaging with the Gemini South Adaptive Optics Imager (GSAOI, Carrasco et al. 2012, McGregor et al. 2004) with the Gemini Multi-Conjugate Adaptive Optics System (GeMS, Neichel et al. 2014b, Rigaut et al. 2014) on the Gemini South telescope. Project SUNBIRD aims to characterise the population of CCSNe in the dusty and crowded star forming regions of LIRGs and in this way improve the constraints on the fraction of CCSNe missed due to dust obscuration and/or nuclear vicinity.

In this chapter project SUNBIRD is introduced. The sample selection and observing strategy are laid out, and the methodology of the project explained, which includes image processing of GeMS/GSAOI data, image subtraction, photometry and light curve fitting. Finally we present the first CCSN discoveries made in project SUNBIRD with GeMS/GSAOI, and present a detection efficiency case study. This chapter is in large part based on Kool et al. (2018), published in *Monthly*

Notices of the Royal Astronomical Society (MNRAS). An analysis of the recovery efficiency of the full sample of project SUNBIRD, and the conversion into an observed CCSN rate and subsequent comparison with the rate expected from SF rate tracers will be conducted when the project has finished, and does not fall within the scope of this thesis.

LIRG	RA (J2000)	Dec. (J2000)	Distance (Mpc)	log $L_{\rm IR}$ ($L_\odot$)	r_{CCSN} (yr^{-1})	Epochs #
Arp 256	00 18 50.9	-10 22 36	114	11.48	0.81	1
NGC 1204	03 04 40.5	-12 20 26	64	10.96	0.25	1
ESO 491-G020	07 09 47.0	-27 34 10	43	10.97	0.25	1
MCG +02-20-003	07 35 42.5	+11 42 36	72	11.13	0.37	1
IRAS 08355-4944	08 37 02.3	-49 54 32	115	11.62	1.12	2
NGC 3110	10 04 02.7	-06 28 35	79	11.36	$0.14^{\dagger}$	4
ESO 264-G036	10 43 07.0	-46 12 43	99	11.34	0.59	4
ESO 264-G057	10 59 02.4	-43 26 33	82	11.15	0.38	1
NGC 3508	11 03 00.1	-16 17 23	61	10.97	0.25	2
ESO 440-IG058	12 06 53.0	-31 57 08	111	11.45	0.51^{*}	4
ESO 267-G030	12 14 12.6	-47 13 37	96	11.26	0.49	5
NGC 4575	12 37 52.1	-40 32 20	63	11.03	0.29	2
IRAS 17138-1017	17 16 36.3	-10 20 40	83	11.49	0.75^{*}	5
IRAS 18293-3413	18 32 40.2	-34 11 26	85	11.74	1.97^{*}	4
NGC 7674	23 27 57.0	+08 46 44	122	11.56	0.98	1

Table 2.1: SUNBIRD GeMS/GSAOI LIRG sample. Distances are from the NASA/IPAC Extragalactic Database (NED[1]), Virgo/GA corrected. CCSN rates are based on the empirical relation with $L_{\rm IR}$ from Mattila and Meikle (2001), unless otherwise indicated: CCSN rate based on SED fits from Herrero-Illana et al. (2017), denoted by $*$, or this work, denoted by $\dagger$. Values of log $L_{\rm IR}$ are from Sanders et al. (2003), adjusted for updated distances. Final column shows number of epochs obtained with GeMS/GSAOI.

2.2 Galaxy Sample

The sample of LIRGs observed with GeMS/GSAOI for project SUNBIRD was selected from the IRAS Revised Bright Galaxy Sample (RBGS; Sanders et al., 2003). The main constraints to the sample selection originated from the instrument we used, GeMS/GSAOI on the Gemini South telescope, which requires guide stars of sufficient brightness and vicinity for the AO correction (see section 2.3). Additionally we limited the sample to galaxies that are closer than 150 Mpc (z=0.027) in order to be able to resolve the central regions as close to the nucleus as possible. At this distance a typical AO corrected FWHM of 0.1″ corresponds to ~75 pc. We omit LIRGs where a significant contamination due to an active galactic nucleus (AGN) to the IR luminosity could be expected, and thus exclude targets with 'warm' IRAS colours, requiring f25/f60 < 0.2 (e.g. Farrah et al., 2005). The only exception is IRAS 08355-4944 with f25/f60 = 0.24, which is included in the sample based on SED fitting results, where it was shown to have a high SF rate of ~85 $M_\odot$ yr^{-1} (Dopita et al., 2011), typical for a SF dominated LIRG. We included targets with IR luminosities L(8-1000μm) in RBGS of $\log(L_{\rm IR}) > 10.9$, see Table 2.1. LIRGs are defined as having $\log(L_{\rm IR}) > 11.0$, but we decided to include some slightly less IR-luminous galaxies to fill out the coverage in R.A. of the sample.

2.3 Observing Strategy

The near-IR observations were obtained with GeMS/GSAOI on the Gemini South telescope. GSAOI is a near-IR AO imaging camera fed by GeMS and records images in a 85″× 85″ field-of-view (FOV) with a pixel scale of 0.0197″ pixel^{-1}, delivering close to diffraction limited images between 0.9 - 2.4 µm. Adaptive optics is a technology where atmospheric distortion of an incoming wave-front is corrected through the use of tip-tilt and deformable mirrors. A first order correction of the tilt of the wave-front is done with the use of a tip-tilt mirror. Higher order aberrations are then corrected with deformable mirrors. Natural guide star (NGS) AO requires a sufficiently bright guide star nearby to the science target, severely limiting the sky area accessible by AO. Using a laser tuned to the sodium D line at 589.0 nm to create an artificial star by stimulating sodium atoms at ~ 90 km altitude enables access to a much larger sky area. LGSAO does require a natural guide star for tip-tilt correction, since tip-tilt derived from the laser guide star includes tip-tilt up- and downwards, but this guide star may be much fainter than for NGS AO and further from the science target. An optimal uniform AO correction across the FOV of GeMS requires three NGS for tip-tilt correction in addition to the 5-point sodium laser guide star (LGS) pattern. The minimum requirement for AO correction at the time of the observations was at least one NGS of sufficient brightness ($m_{\rm R}$ < 15.5 mag) available within the 1′ radius patrol field of the wave front sensor probes and one on-detector guide window star ($m_{\rm H}$ < 13.5 mag) within the 40″ FOV of any of the four GSAOI detectors at all dither positions. This proved to be the main restriction in target selection, as a relatively bright star was required within a limited patrol field.

The SN search was conducted in K_s-band, as this is where, compared to J- and H-band, AO performs best and extinction due to dust is lowest. Each target was imaged with a 9 step dither pattern for 120s at each position with a step size large enough (>5″) to cover the gaps between the detectors. The targets were typically centred on one of GSAOI's four arrays, with orientation depending on the galaxy and the locations of the NGS. Employing the efficient cadence strategy from Mattila and Meikle (2001) for near-IR CCSN searches, we aimed to observe each galaxy twice each semester. In practice we achieved this cadence for half of the sample while the remainder of the sample galaxies was observed less frequently, due to seasonal weather variations, sodium layer return, and interruptions due to aircraft and satellite avoidance (see Table 2.1). If a night did not allow for coverage of all observable targets, priority was given to galaxies with a high expected SN rate and those for which at least one GeMS/GSAOI epoch was already available for the purpose of optimal image subtraction. Expected SN rates were based on the empirical relation from Mattila and Meikle (2001):

$$r_{SN} = 2.7 \times 10^{-12} \times L_{\mathrm{IR}}/\mathrm{L}_{\odot}\ \mathrm{yr}^{-1} \tag{2.1}$$

The targets in our sample with just one epoch were checked for SNe against archival high-resolution VLT/NACO (Nasmyth Adaptive Optics System Near-Infrared Imager and Spectrograph, 0.055″ pixel^{-1}; Lenzen et al. 2003, Rousset et al. 2003) AO images, obtained by members of the SUNBIRD collaboration as part of a predecessor program (Randriamanakoto et al., 2013) and available for the whole sample.

Our total sample of LIRGs covered with GeMS/GSAOI, from the pilot program in 2013 until 2017, consists of 15 galaxies up to a distance of 122 Mpc. Our 2013 pilot program and the first semester of 2015 were observed in queue mode, where observations are executed by telescope staff when the required observing conditions are met. In total we were awarded ~27 hours of queue mode time, which resulted in 18 epochs of LIRGs. In contrast in 2016 and 2017 we were awarded a total of six classically scheduled nights for ~60 hours of observing time, but due to poor observing conditions and technical issues we only obtained 10 epochs during these nights. The other 10 epochs from Table 2.1 were obtained from the archive or through other programs. Even though for some LIRGs there were only one or two NGS available and AO correction was not optimal, across our full data set a typical point-spread function (PSF) of ~0.07″ - 0.12″ FWHM was achieved.

[1]The NASA/IPAC Extragalactic Database (NED) is operated by the Jet Propulsion Laboratory, California Institute of Technology, under contract with the National Aeronautics and Space Administration.

2.4 Multi-wavelength follow up

Following a potential SN detection in K_s, the source was first checked for proper motion between exposures, to exclude a passing minor planet[2]. Follow up with GeMS/GSAOI in H and J was done as soon as possible, which due to observing constraints typically occurred in the next GeMS/GSAOI observing window. As these observing windows were two to three months apart, rapid follow up of the SN candidate in the near-IR/optical was done with other instruments: in *JHK* with NACO on the VLT (PI: S. Mattila), or contemporaneously with the Nordic Optical Telescope (NOT, Djupvik and Andersen 2010, PI: S. Mattila) in *r'*- and *i'*-band with ALFOSC[3] (Andalucia Faint Object Spectrograph and Camera, 0.19″ pixel^{-1}) and in *JHK* with NOTCam (Nordic Optical Telescope near-infrared Camera and spectrograph, 0.234″ pixel^{-1}).

In addition to near-IR and optical imaging, two SN candidates were observed at radio wavelengths with the Karl G. Jansky Very Large Array (JVLA, PI: M. Pérez-Torres). A detection would provide important information about the nature of the SN and rule out a Type Ia SN, as even the most nearby Type Ia have yet to be detected at radio wavelengths (e.g. Chomiuk et al., 2016, Hancock et al., 2011, Perez-Torres et al., 2015). The intrinsic rate of Type Ia SNe in LIRGS is estimated to be ~5% of that of CCSNe (Mattila et al., 2007). As a final step, when possible near-IR spectroscopic coverage was obtained, under natural seeing conditions using the cross-dispersed mode of the Gemini Near Infra-Red Spectrograph (GNIRS, PI: S. Ryder) on Gemini North (Elias et al., 2006a,b). The follow up observations are described in more detail in Section 2.7.

2.5 Data reduction

2.5.1 GeMS/GSAOI data reduction with THELI

The GeMS/GSAOI data were reduced using data reduction package THELI[4] (Erben et al., 2005, Schirmer, 2013), generally following the procedures described in Schirmer (2013) and Schirmer et al. (2015). GeMS/GSAOI exposures suffer from a distortion pattern with a static component introduced by the AO system GeMS, and variable distortion components depending on NGS configurations, position angle and elevation (Neichel et al., 2014a, Schirmer et al., 2015). THELI uses *Scamp* (Bertin, 2006) for astrometric calibration and distortion correction of individual exposures

[2]http://www.minorplanetcenter.net/cgi-bin/checkmp.cgi

[3]The data presented here were obtained in part with ALFOSC, which is provided by the Instituto de Astrofisica de Andalucia (IAA-CSIC) under a joint agreement with the University of Copenhagen and NOTSA.

[4]https://www.astro.uni-bonn.de/theli/

prior to final co-addition, based on reference catalogues of point sources measured in distortion-free images of the same field, such as from HAWK-I on the VLT or VIRCAM on the VISTA telescope. In this way an optimal data quality across the FOV is obtained. As the GeMS/GSAOI data set required non-standard data processing, we will describe the optimisations and adaptations we applied of the procedures as described in Schirmer (2013) and Schirmer et al. (2015) in detail in the following paragraphs. The focus is on astrometric calibration of images with low number source density, required for correcting the distortion pattern present in GeMS/GSAOI data.

Calibration and background modelling

The science exposures were divided by a master flat combined from typically 10 dome flats, and the background removed by running a two-pass background model. In short, the first pass is a simple background model subtraction of a median combination of all exposures without masking to remove the bulk of the signal, whereas in the second pass objects are masked by applying SExtractor (Bertin and Arnouts, 1996) for source identification. A static background model was used if the exposure sequence did not last longer than 1 hour. In a few cases a dynamic model was warranted using a running median of 6 images. In contrast to Schirmer et al. (2015) no *mask expansion factor* or *collapse correction* was deemed necessary for this work.

Astrometric calibration

The astrometric calibration of individual dithered images prior to coaddition in THELI enables the distortion correction of GeMS/GSAOI data, but also requires the most attention to properly process the data. Because of the low number source density, no single combination of parameter settings for the packages that THELI employs (*Scamp*, *Swarp*: Bertin et al. (2002) and SExtractor) proved to be sufficient for all GeMS/GSAOI data sets, some informed adjustments were always required. Most settings are well covered in the THELI documentation and aforementioned procedures, but the following adjustments were not obvious and were vital for the astrometric calibration of our GeMS/GSAOI data.

In all of the datasets the comparatively small FOV of GSAOI in combination with sparsely populated fields meant all-sky astrometric reference catalogues were insufficient for astrometric calibration of the individual frames. Instead secondary reference catalogues were first created with THELI based on K_s-band archival data of ground-based widefield instruments: HAWK-I on the VLT or VIRCAM on the VISTA telescope. These were calibrated against typically 100-1000 sources in the FOV from the Two Micron All Sky Survey (2MASS), which have individual uncertainties of ~100 milliarcseconds (mas), resulting in astrometric uncertainties of the reference images of $\lesssim$ 10 mas. After successfully constructing a distortion corrected coadded GeMS/GSAOI image, subsequent GeMS/GSAOI epochs were calibrated against a reference catalogue extracted from this image. Depending on field crowding of the astrometric reference image and its spatial resolution, the parameter DEBLEND_MINCONT in *postcoadd.conf.sex* in the THELI reduction folder needed to be adjusted (decreased when working with a GeMS/GSAOI reference image).

The WCS header information in our raw GeMS/GSAOI data was generally accurate within ~5″ but this proved to be not precise enough in fields with few matching reference sources. In almost all cases it was necessary to update the CRPIX1/2 keywords in the headers to match with the coordinates of the reference catalogue. Then, as described in section 3.5.1 in Schirmer et al. (2015), a refined median estimate of the relative array positions and orientations from all exposures in a night is used (MOSAIC_TYPE = FIX_FOCALPLANE), and as we have adjusted the reference pixel manually no WCS matching is required: MATCH = N.

THELI uses SExtractor to create a source catalogue from the science images, which are then fitted to the corresponding sources (within CROSSID_RADIUS) in the reference catalogue to obtain a distortion correction. This process is done for each array separately and the SExtractor settings might not be appropriate for both the array containing the galaxy (high source number density) and an array covering a sparse field. In some cases in order to recover all four arrays it was necessary to run the source extraction individually with appropriate settings (most importantly detection thresholds DETECT_THRESH and DETECT_MINAREA and de-blending parameter DEBLEND_MINCONT). This can be achieved by suspending the parallel manager script and the details are described in the THELI documentation[5].

Astrometric errors were calculated by taking the square root of the quadratic sum of the astrometric uncertainty of the constructed reference catalogue and the astrometric errors produced by THELI.

2.5.2 NOT and NACO data reduction

The near-IR NOTCam instrument data were reduced with a slightly modified version of the external NOTCAM package[6] (v. 2.5) within IRAF[7]. The reduction steps included flat field correction, distortion

[5]https://astro.uni-bonn.de/$\sim$theli/gui/advancedusage.html

[6]http://www.not.iac.es/instruments/notcam/guide/observe.html

[7]IRAF is distributed by the National Optical Astronomy Observatory, which is operated by the Association of Universities for Research in Astronomy (AURA) under cooperative agreement with the National Science Foundation (Tody, 1993)

correction, sky subtraction, and stacking of the individual exposures for increased signal-to-noise ratio. The optical *r'*- and *i'*-band ALFOSC images were reduced using the QUBA pipeline (Valenti et al., 2011), including bias subtraction and flat field correction.

The near-IR data taken with VLT/NACO were reduced using the NACO pipeline, which is based on the ESO Common Pipeline Library (CPL)[8]. The jittered on-source images were flat field corrected, then median-combined to create a sky frame. Bad pixels were removed and the sky was subtracted from the individual images. The images were then stacked using a 2-D cross-correlation routine.

2.5.3 GNIRS near-IR spectroscopy data reduction

We used the cross-dispersed spectroscopy mode, providing a complete spectrum within 0.8-2.5 μm at an instrumental resolution of $R \sim 1700$. The data were reduced using version 2.6 of the XDGNIRS pipeline[9]. Briefly, the spectra were cleaned of pattern noise caused by the detector controller, using the python code from the Gemini website[10]. Radiation events from the radioactive lens coatings on the GNIRS short camera were identified and interpolated over using IRAF's *fixpix* task. Files were divided by a combined master flat field, created from a combination of quartz-halogen and IR flats taken after each science observation. Subtraction of a sky frame removed night sky emission lines as well as other static artefacts in the detector, such as stable hot pixels. The orders were rectified using daytime pinhole flats, wavelength calibrated using an argon arc frame and 1D spectra were extracted from each order using IRAF task *apall*. Telluric correction and flux calibration were done using an A-type star, which was observed immediately before or after each science object. Each order of the science target was multiplied by a black body spectrum of the telluric star's effective temperature, scaled to the K-band flux of the standard star for an approximate 2MASS flux calibration, and the orders were joined together using the IRAF task *odcombine*.

2.6 Methods

2.6.1 Image subtraction

Supernova candidates were identified by image subtraction, where a newly obtained galaxy observation is subtracted from an observation of the same galaxy obtained at an earlier epoch. Subtraction

[8]http://www.eso.org/sci/software/cpl/

[9]http://drforum.gemini.edu/topic/gnirs-xd-reduction-script/

[10]http://www.gemini.edu/sciops/instruments/gnirs/data-format-and-reduction/cleanir-removing-electronic-pattern-0

of different epochs was done using a slightly modified (to accept manual stamp selection) version of image subtraction package ISIS 2.2 (Alard, 2000, Alard and Lupton, 1998), where the software matches the PSF as well as flux and background levels of a previously aligned pair of images by deriving an optimal convolution kernel based on a selection of small windows (or “stamps”) around objects with high signal-to-noise. See Figs. 2.1-2.3 for the subtractions of the galaxies where SN candidates were identified. In the case of IRAS 18293-3413 the subtraction process resulted in considerable residuals at locations of high signal-to-noise, such as the nucleus and other bright compact sources. This was a result of having to prioritise an optimal subtraction for the central regions, as the SN is located very close to the nucleus. AO is optimized for point sources, but for a bright nuclear region with some intrinsic morphology the PSF is likely to vary between epochs. As such, the extraction of a SN signal in a location with such a steep background gradient is non-trivial, because any deviations from a perfect PSF match will produce large residuals. Despite our best efforts it was not possible to obtain a uniform subtraction across the full image. The smoothest subtraction of the nucleus was obtained by selecting a large number (>10) of small stamps near and in the galaxy to map the PSF around the SN location as well as possible, but this resulted in the residual patterns visible in the subtraction at the locations of bright compact objects in the field.

2.6.2 Photometry

The photometry of the objects was measured using the SNOOPY[11] package in IRAF, where a PSF is fitted to the SN residual in the subtracted image. The PSF was derived from 10 isolated field stars in the FOV of the one image that was not convolved during subtraction (i.e. the image with poorest image quality). SNOOPY removes a simple background estimate from the region surrounding the SNe (excluding the innermost region around the object) during PSF fitting, but as the SN detections are generally located in nuclear regions with large and variable background signal, the PSF fitting is performed on the SN residual in the subtracted image, where the complex background has already been removed. The photometry was calibrated against 5 2MASS stars in the FOV, when available, resulting in a typical uncertainty in the zero point of ~0.04 mags. Systematic errors in the local background subtraction were estimated by simulating and PSF fitting nine artificial stars in a three by three grid pattern around the SN position in the subtracted image. The photometric uncertainty determined this way is a function of local crowding and source magnitude, increasing with subtraction noise and poor signal-to-noise, and typically dominated the photometric errors.

[11] SNOOPY, originally presented in Patat (1996), has been implemented in IRAF by E. Cappellaro. The package is based on *daophot*, but optimised for SN magnitude measurements

The FOV of NGC 3110 did not offer any suitable catalogue reference stars and only one clear isolated field star for PSF fitting purposes. This field star acted as the PSF model and photometric reference for SN 2015ca after the field star's JHK_s magnitudes were determined from NOT images calibrated against 5 2MASS sources.

In case of a non-detection, a 5-σ upper limit was determined by simulating stars of decreasing apparent magnitude in steps of 0.5 mags at the SN location using the task *mkobjects* in IRAF package *artdata*, prior to subtraction. The signal-to-noise was based on the aperture flux of the residual of the simulated star compared to 80 empty positions in the field around the SN location using IRAF task *phot*.

Photometric error analysis

Photometric errors were propagated from the 2MASS photometric reference stars. From each of the five 2MASS reference stars a zero point was derived, with an error calculated as the square root of the quadratic sum of the 2MASS error and aperture fit error produced by SNOOPY, where the 2MASS error was typically dominant. Based on these five values a single weighted mean zero point was derived, with an error equal to the standard error of the mean. The final photometric error of the SN magnitude was calculated as the square root of the quadratic sum of the zero point error and the PSF fitting error as produced by SNOOPY.

2.6.3 Light curve template fitting

To determine the type of the discovered SNe, the observed light curve data points during the rise and fall of the SN were fitted using (reduced) χ^2 minimization to three prototypical template light curves, representing Type IIP, IIn and stripped envelope Type IIb and Ib/c SNe, similarly to Kankare et al. (2014, 2008). The three prototypical CCSNe templates were chosen on the basis of being well characterized and having a well sampled light curve in the near-IR covering the different stages of SN evolution during at least the first 150 days since explosion. It should be noted that there is non-negligible diversity in SNe even within a given type, and thus the sources detected here could differ from the templates. We opted to use light curves of single SNe as templates due to the lack of near-IR light curves of CCSNe in the literature covering all relevant stages of evolution, including the rise and long term decline of the CCSNe. Future work will include light curve templates based on samples of subtypes. The templates we used (see Fig. 2.6, 2.7 and 2.8) are as follows:

- **Type IIP:** A type IIP template fit was carried out based on the photometric evolution of SN 1999em. *UBVRI* light curves of SN 1999em (Leonard et al., 2002) were transferred into *ugri* using the conversions of Jester et al. (2005). *JHK* light curves were obtained from Krisciunas et al. (2009). The distance modulus μ, total V-band line-of-sight extinction A_V, and explosion date t_e of the used template SNe were adopted for the analysis from the literature. For SN 1999em, μ = 30.34 mag, t_e = 2451475.0 in JD, and A_V = 0.34 mag were reported by Krisciunas et al. (2009).

- **Type IIn:** A type IIn template fit was carried out using the published light curves of SN 1998S (Fassia et al., 2000, Liu et al., 2000, Mattila and Meikle, 2001). Similar to SN 1999em, the Johnson-Cousins light curves were converted into the SDSS system using the transformations of Jester et al. (2005). For SN 1998S, μ = 31.15 mag, t_e = 2450872.5 in JD, and A_V = 0.68 mag were adopted from Fassia et al. (2000).

- **Type IIb/Ib/Ic:** Well-sampled multiband light curves of Type IIb SN 2011dh (Ergon et al., 2015, 2014) were used as a general template for stripped-envelope SNe, since the photometric evolution of Type IIb SNe appears to be fairly similar to that of Type Ib/c SNe (e.g. Arcavi et al., 2012). Ergon et al. (2014) finds for SN 2011dh values of μ = 29.46 mag, t_e = 2455713.0 in JD, and A_V = 0.22 mag.

All the bands are fitted simultaneously with three free parameters: the line-of-sight extinction A_V, time t_0 between explosion date and discovery, and a fixed constant C applied to all bands, representing the intrinsic magnitude difference between SNe. Upper limits are used to constrain the template fits where necessary. Galactic line-of-sight extinction values are adopted from NED based on the dust maps of Schlafly and Finkbeiner (2011) and are fixed in the fit. For host galaxy and Galactic extinction, the Cardelli et al. (1989) extinction law was used. Kankare et al. (2014) showed that based on limited light curve information as in the case for our SNe it is not trivial to disentangle between different extinction laws, and we opted to use only Cardelli et al. (1989) for consistency and because it is a genuine line-of-sight extinction law.

2.7 Observations and Discoveries

2.7.1 SN 2013if in IRAS 18293-3413

SN 2013if (Kankare et al., 2017a) in IRAS 18293-3413 was discovered with GeMS/GSAOI (PI: S. Ryder) on 2013 April 21, see Fig. 2.1. Subtraction of a K_s-band image taken with NACO on

UT Date	Instrument	Filter	Magnitude
SN 2013if (IRAS 18293-3413)			
2012 September 14.1	NACO	K_s	>19.2
2013 April 21.3	GeMS/GSAOI	K_s	18.53±0.09
2013 May 8.4	NACO	K_s	18.61±0.12
2013 May 8.4	NACO	H	18.93±0.21
2013 May 24.3	GeMS/GSAOI	K_s	19.22±0.11
2013 June 11.1	GeMS/GSAOI	K_s	19.12±0.11
2013 June 11.1	GeMS/GSAOI	H	19.03±0.16
2013 June 11.1	GeMS/GSAOI	J	>18.7
SN 2015ca (NGC 3110)			
2015 March 11.1	GeMS/GSAOI	K_s	18.73±0.11
2015 March 27.8	NOT	r'	>20.0
2015 March 27.9	NOT	i'	>21.0
2015 April 5.9	NOT	K_s	17.91±0.22
2015 April 6.0	NOT	H	18.63±0.19
2015 April 6.0	NOT	J	19.39±0.21
2015 May 29.9	GeMS/GSAOI	K_s	20.22±0.12
2015 May 31.9	GeMS/GSAOI	H	20.67±0.09
2015 May 31.9	GeMS/GSAOI	J	21.25±0.08
2016 Feb. 19.2	GeMS/GSAOI	K_s	>21.5
2016 Feb. 19.3	GeMS/GSAOI	H	>22.0
2016 Feb. 19.4	GeMS/GSAOI	J	>22.8
SN 2015cb (IRAS 17138-1017)			
2015 March 6.3	GeMS/GSAOI	K_s	16.56±0.09
2015 March 17.2	NOT	r'	>22.5
2015 March 17.3	NOT	i'	21.10±0.12
2015 April 6.2	NOT	K_s	17.12±0.22
2015 April 6.3	NOT	H	17.06±0.10
2015 April 6.3	NOT	J	18.34±0.18
2015 May 2.3	NOT	J	18.71±0.57
2015 June 1.2	GeMS/GSAOI	K_s	18.97±0.10
AT 2015cf (NGC 3110)			
2015 March 11.1	GeMS/GSAOI	K_s	20.97±0.13
2015 May 29.9	GeMS/GSAOI	K_s	21.4±0.2
2015 May 31.9	GeMS/GSAOI	H	>22.7
2015 May 31.9	GeMS/GSAOI	J	>22.8

Table 2.2: GeMS/GSAOI-discovered supernova near-IR and optical photometry

the VLT on 2004 September 13 (Mattila et al., 2007) showed a positive residual 0.2″ North and 0.4″ West (200 pc projected distance) from the nucleus. WCS matching in THELI with a catalogue of 180 sources extracted from a VISTA image (VISTA Hemisphere Survey or VHS[12]) yielded R.A. = $18^{h}32^{m}41.10^{s}$ and Decl. = $-34°11'27.24''$, with 0.03″ and 0.03″ uncertainty in R.A. and Decl., respectively. SN positions were determined using centroiding in IRAF in the subtracted images to avoid the effects of strong background. Follow-up observations were made with NACO on 2013 May 8 in K_s and H, and with GeMS/GSAOI in K_s on 2013 May 24 and in K_s, H and J on 2013 June 11. SN 2013if was detected in all the follow up images with the exception of the final J-band image, see Table 2.2. Supernova-free comparison GeMS/GSAOI images required for optimal image subtraction were obtained in K_s, H and J on 2015 June 2 (PI: S. Ryder).

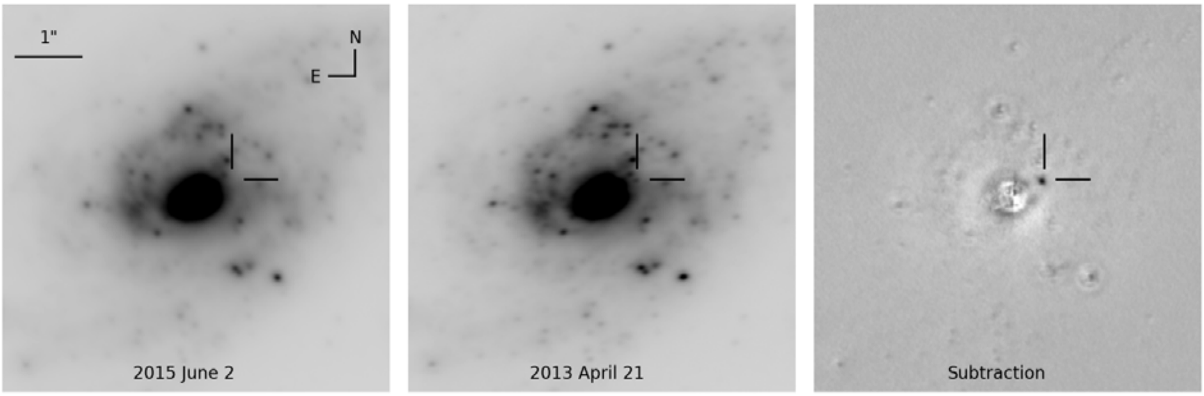

Figure 2.1: SN 2013if in IRAS 18293-3413, discovered with GeMS/GSAOI in K_s-band, see Section 2.7.1. From left to right with linear scaling: Reference image (June 2015), discovery image (April 2013) and the image subtraction.

2.7.2 SN 2015ca in NGC 3110

The discovery image of SN 2015ca (Kool et al., 2016) in NGC 3110 was observed on 2015 March 11 (PI: S. Ryder), see Fig. 2.2. As a reference image a NACO K_s-band image from 2010 December 28 was used (Randriamanakoto et al., 2013). The subtracted image revealed a point source along the northern spiral arm of the galaxy 4.3″ North and 8.0″ West from the nucleus, corresponding to a projected distance of ~3.5 kpc. WCS matching in THELI with a catalogue of >300 sources extracted from a HAWK-I image (Miluzio et al., 2013) yielded R.A. = $10^{h}04^{m}01.57^{s}$ and Decl. = $-06°28'25.48''$, with 0.03″ and 0.04″ uncertainty in R.A. and Decl., respectively. Follow up observations with the NOT were carried out on 2015 March 27 in r' and i' and on April 5 in K_s, H and J, and with GeMS/GSAOI in K_s, H and J on 2015 May 29 and 31 and in K_s, H and J on 2016

[12]http://www.vista-vhs.org/

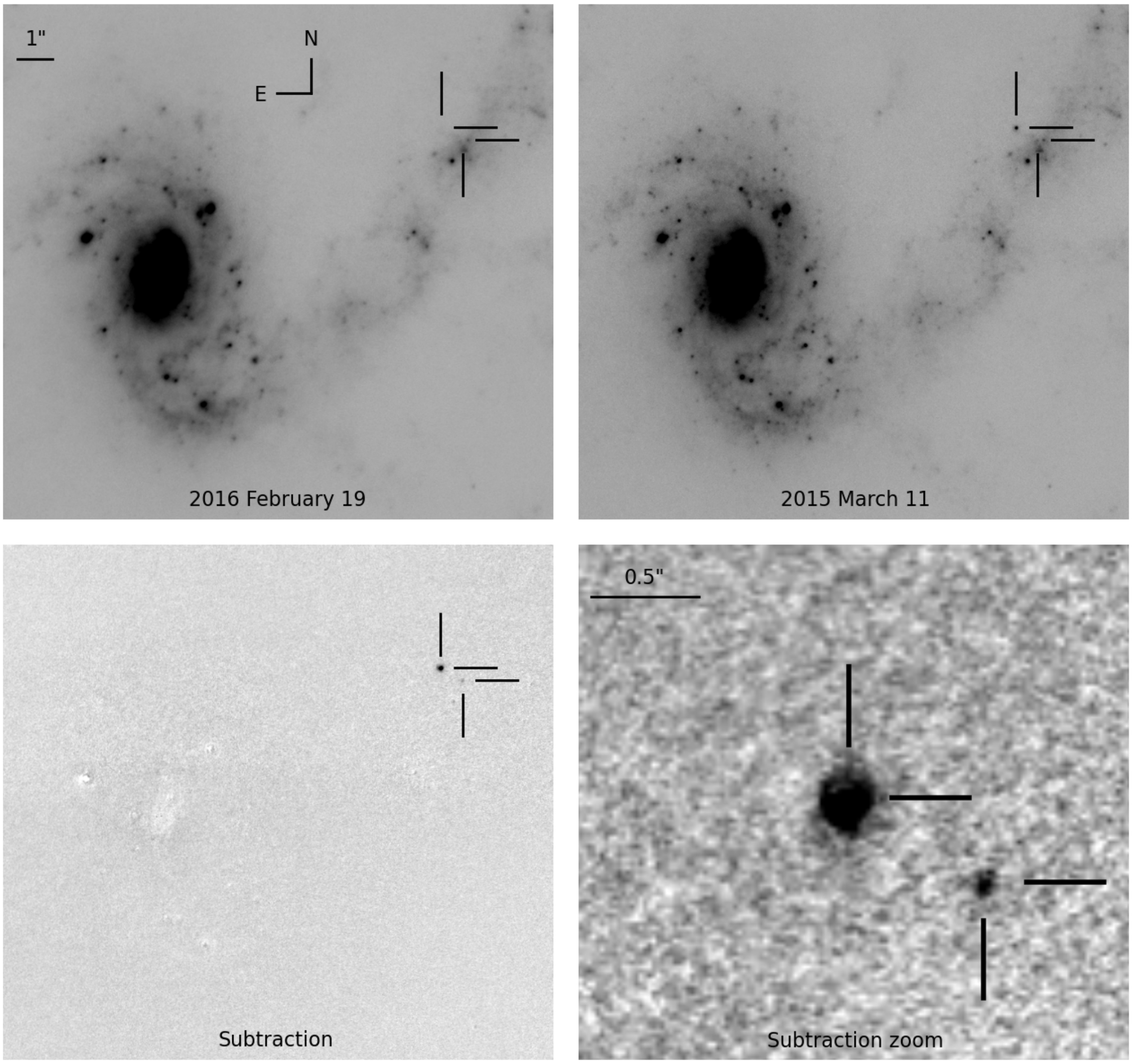

Figure 2.2: SN 2015ca and AT 2015cf, discovered in NGC 3110 with GeMS/GSAOI, see Section 2.7.2. Top row, with linear scaling, shows the reference image (February 2016) and discovery image (March 2015). Bottom row shows the full image subtraction and zoomed in around SN 2015ca, which shows AT 2015cf visible to the South-West.

February 19. SN 2015ca was detected in all near-IR bands in April and May 2015, but was not detected in any optical bands; see Table 2.2. It had faded below our detection limits in February 2016.

2.7.3 SN 2015cb in IRAS 17138-1017

SN 2015cb (Kool et al., 2017a) in IRAS 17138-1017 was discovered with GeMS/GSAOI on 2015 March 6; see Fig. 2.3. Subtraction of a GeMS/GSAOI image from 2013 March 22 revealed a residual point source 1.4″ North and 0.6″ East (600 pc projected distance) from the nucleus. WCS

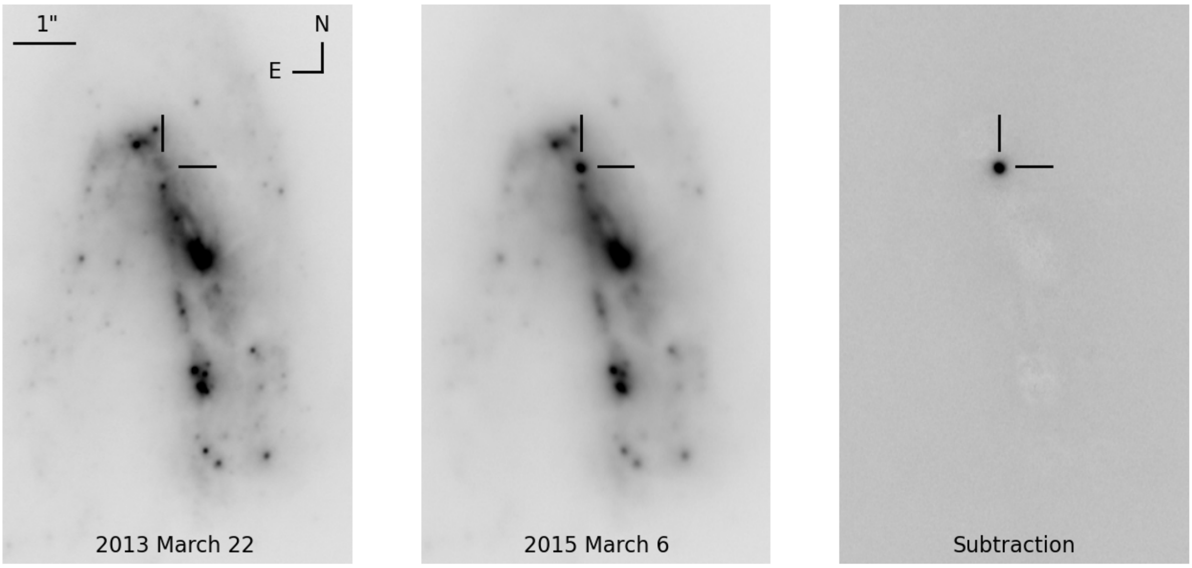

Figure 2.3: SN 2015cb in IRAS 17138-1017, discovered with GeMS/GSAOI, see Section 2.7.3. From left to right, with linear scaling: Reference image (March 2013), discovery image (March 2015) and image subtraction.

matching in THELI with a catalogue of 76 sources extracted from a VISTA image yielded R.A. = $17^{h}16^{m}35.84^{s}$ and Decl. = $-10°20'37.48''$, with $0.04''$ and $0.04''$ uncertainty in R.A. and Decl., respectively. Follow up observations with the NOT were carried out on 2015 March 17 in optical (in i'- and r'-band, FWHM $\sim 1.1''$), on April 6 in K_s, H and J (FWHM $\sim 1.0''$), and with GeMS/GSAOI in K_s on 2015 June 1. SN 2015cb was detected in all follow up observations except in r'; see Table 2.2.

2.7.4 AT 2015cf in NGC 3110

The discovery image of SN 2015ca in NGC 3110 from 2015 March 11 showed a second transient source at R.A. = $10^{h}04^{m}01.53^{s}$ and Decl. = $-06°28'25.84''$; see Fig. 2.2. AT 2015cf (Kool et al., 2017b) is just $0.6''$ S and $0.4''$ W of SN 2015ca, as shown in the zoomed panel in Fig. 2.2. The PSF of this source matches well with that of SN 2015ca and field stars in the image. The magnitude for this source at this epoch, bootstrapped off of SN 2015ca, is 20.97±0.13. It is not visible in any of the NOT epochs, which is not surprising as with a mere $0.7''$ separation from SN 2015ca it was likely blended with it in the subtraction. The GeMS/GSAOI K_s image from 2015 May 29 does show a residual at the same position with a magnitude of 21.4±0.2, confirming that it is in fact a real transient. The H and J observations from the same epoch did not show the source, likely as a result of poorer image quality and/or due to significant extinction. In February 2016 it was not visible in any band.

2.7.5 Radio observations

VLA observations

We observed IRAS 17138-1017 and NGC 3110 with the VLA on 2015 April 8-9 under program 15A-471 (PI: Pérez-Torres), while the VLA was in B-configuration. We observed IRAS 17138-1017 at K-band (centred at 22 GHz) with a total bandwidth of 8 GHz, and NGC 3110 at X-band (10 GHz), with 4 GHz of bandwidth, in both cases using full polarization.

We used the bright quasar 3C286 for flux and bandpass calibration, and J0943-0819 and J1733-1304 to calibrate the phases of IRAS 17138-1017 and NGC 3110, respectively. We performed a standard data reduction using the Common Astronomy Software Applications package (CASA; McMullin et al., 2007). We imaged our datasets using multi-frequency synthesis (MFS) with natural weighting, yielding a synthesized beam size and a root mean square (rms) of $0.56'' \times 0.30''$ and 9 μJy beam^{-1} for IRAS 17138-1017 and $0.96'' \times 0.66''$ and 15 μJy beam^{-1} for NGC 3110, respectively.

Neither observation showed a local maximum coincident with the SN position. In the case of SN 2015cb in IRAS 17138-1017, any point source was most likely blended with the significant background signal in the central regions of the LIRG; see Fig. 2.5. SN 2015ca and AT 2015cf in NGC 3110 also coincide with local radio emission potentially masking possible source detections; see Fig. 2.4. For further details on the radio limits, see Section 2.8.

eEVN observation

We also observed the region around SN 2015ca and AT 2015cf in NGC 3110 with the electronic European VLBI Network (eEVN, PI: M. Pérez-Torres) on 10 May 2016. We used the eEVN at an observing frequency of 5.0 GHz, using an array of nine telescopes for about 2-hr, including overheads for calibration purposes and slew time. We observed the transients phase-referenced to the nearby source J0959-0828, using a typical duty cycle of four minutes. We used the strong source 3C273B as fringe finder and bandpass calibrator. All the data were correlated at the EVN MkIV data processor of the Joint Institute for VLBI in Europe (JIVE, the Netherlands), using an averaging time of 2 s.

We used AIPS for calibration, data inspection, and flagging of our eEVN data, using standard procedures. We then imaged a FOV of $1'' \times 1''$ centred at R.A. = $10^{\mathrm{h}}04^{\mathrm{m}}01.572^{\mathrm{s}}$ and Decl. = $-06^{\circ}28'25.480''$, and applied standard imaging procedures using AIPS, without averaging the data either in time, or frequency, to prevent time- and band- width smearing of the images. We did not detect any signal above 101 μJy/b (=5σ) in the field surrounding SN 2015ca. Several sources at the

3-σ level were detected, but repeated imaging with different cleaning schemes showed that these were spurious detections, implying that there was no evidence of radio emission from SN 2015ca. AT 2015cf was not covered in the 1″×1″ FOV.

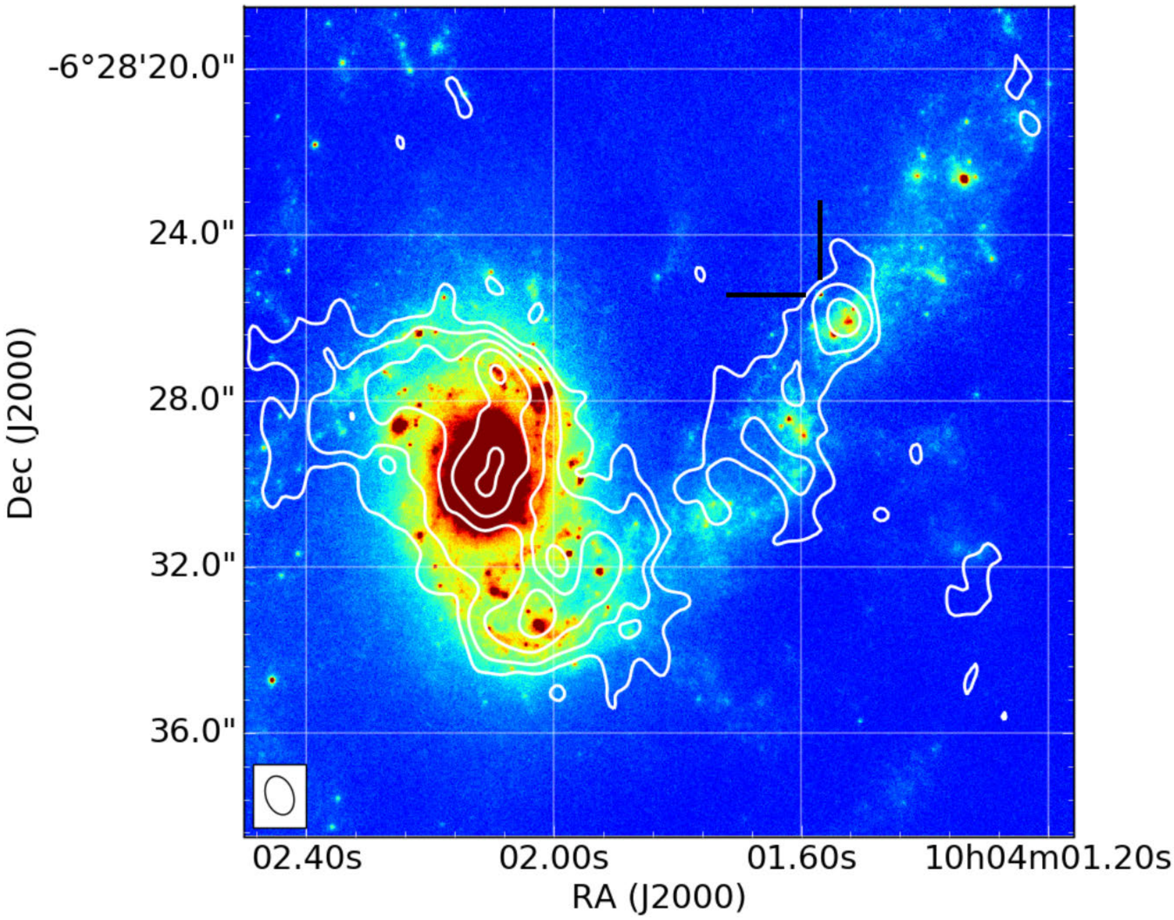

Figure 2.4: X-band (10 GHz) VLA contours overlaid on GeMS/GSAOI detection image of SN 2015ca and AT 2015cf. SN 2015ca is indicated by tick marks, AT 2015cf is separated by just 0.7″.

2.7.6 Near-IR spectroscopic observations

We obtained near-IR spectroscopy of SN 2015ca and SN 2015cb through Director's Discretionary Time with GNIRS on the Gemini North telescope on 2015 May 23 (PI: S. Ryder). These observations were obtained in natural seeing conditions ~70 days after discovery. We opted for near-IR spectroscopy as the SNe were located in crowded regions and expected to be significantly dust extincted. Image quality in the near-IR is typically better and less affected by dust extinction than the optical. The SNe were too faint to acquire directly, so a blind offset from a bright star was required. There was no clear indication of a point source in the slit, and the spectra did not show

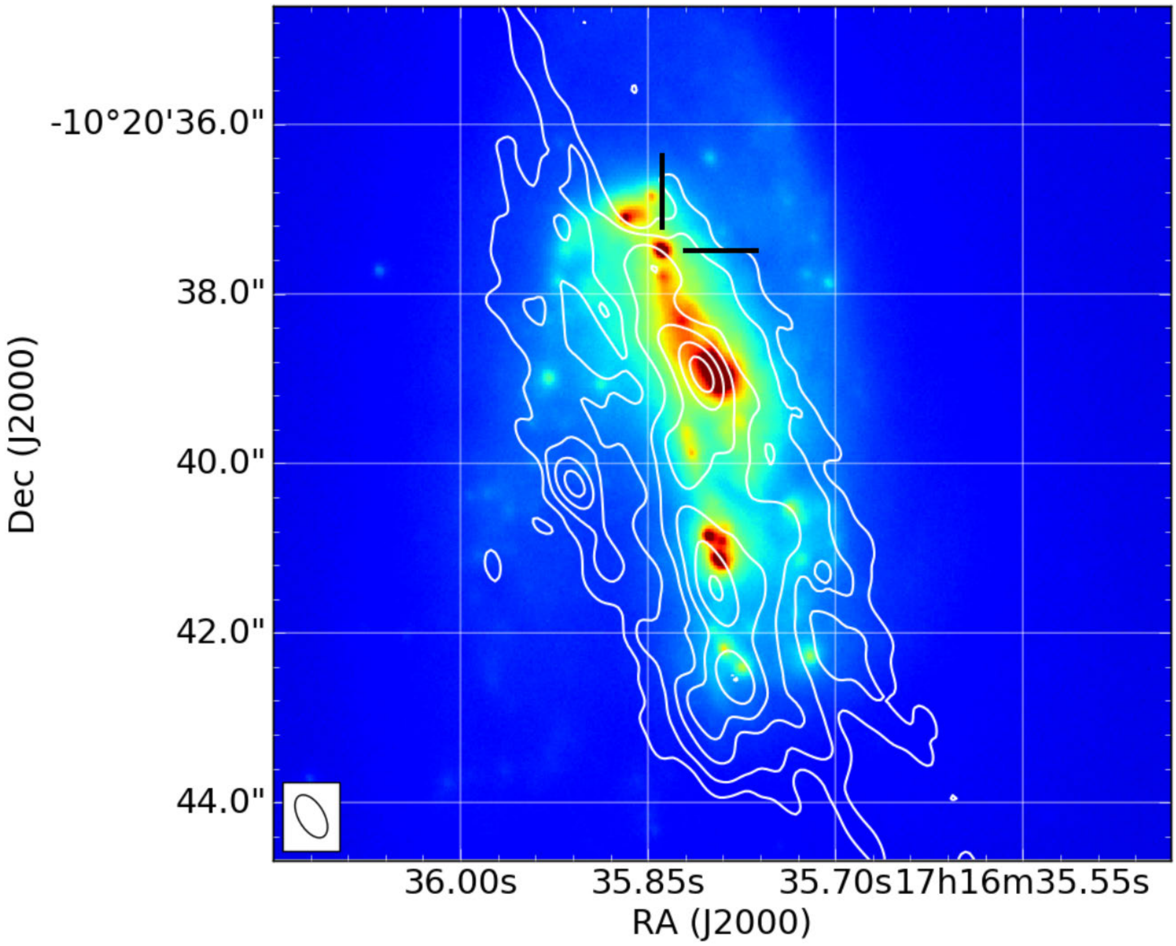

Figure 2.5: K-band (22 GHz) VLA contours overlaid on GeMS/GSAOI detection image of SN 2015cb, with the SN indicated by tick marks.

any emission lines associated with CCSNe. As such the obtained spectra could not be used to constrain the SN types of SN 2015ca or SN 2015cb.

2.8 Analysis

2.8.1 SN 2013if

The best template fit for SN 2013if with a $\tilde{\chi}^2$ of 4.7 is a Type IIP caught in the tail phase (see Fig. 2.6 and Table 2.3), although the other templates fit the data with comparable values of $\tilde{\chi}^2$. A Type IIP caught in the tail phase is deemed most likely as, in addition to the fitting results, it is the only fit where no magnitude shift C is required and the SN discovery is not before or at the maximum of the light curve. This means it does not require a sub-luminous supernova as opposed to the Type IIn fit with similar $\tilde{\chi}^2$, and it does not require discovery during the very short-lived

Template	A_V	t_0	C	$\tilde{\chi}^2$
SN 2013if (IRAS 18293-3413)				
IIP, plateau	$0.0^{+2.8}_{-0.0}$	67^{+1}_{-14}	$1.8^{+0.1}_{-0.4}$	7.1
IIP, tail	$0.0^{+2.5}_{-0.0}$	136^{+83}_{-13}	$0.0^{+0.5}_{-1.7}$	4.7
IIn	$0.0^{+2.7}_{-0.0}$	19^{+12}_{-3}	$3.1^{+0.1}_{-0.5}$	5.0
IIb/Ib/Ic	$0.0^{+2.9}_{-0.0}$	18^{+3}_{-2}	$1.5^{+0.1}_{-0.5}$	7.4
SN 2015ca (NGC 3110)				
IIP	$3.4^{+1.0}_{-1.7}$	58^{+14}_{-5}	$1.5^{+0.4}_{-0.3}$	3.8
IIn	$2.7^{+0.2}_{-0.7}$	25^{+17}_{-9}	$3.0^{+0.2}_{-0.2}$	10.3
IIb/Ib/Ic	$2.8^{+0.3}_{-0.4}$	16^{+5}_{-2}	$1.3^{+0.2}_{-0.2}$	5.0
Ia	$6.9^{+0.1}_{-0.7}$	5^{+1}_{-1}	$0.4^{+0.3}_{-0.2}$	17.9
SN 2015cb (IRAS 17138-1017)				
IIP, plateau	$4.6^{+0.3}_{-0.1}$	64^{+11}_{-7}	$-0.7^{+0.1}_{-0.3}$	11.7
IIP, tail	$3.6^{+0.4}_{-0.1}$	134^{+15}_{-4}	$-2.2^{+0.2}_{-0.3}$	29.0
IIn	$5.2^{+0.3}_{-0.1}$	24^{+5}_{-4}	$0.5^{+0.2}_{-0.2}$	32.4
IIb/Ib/Ic	$4.7^{+0.1}_{-0.6}$	19^{+10}_{-1}	$-1.1^{+0.1}_{-0.2}$	11.2
AT 2015cf (NGC 3110)				
IIP	> 7.0	> 139	< 1.6	-
IIb/Ib/Ic	> 0.0	> 105	< 2.0	-

Table 2.3: Results from fitting light curve templates to the three SNe, with line-of-sight extinction A_V, time t_0 between explosion date and discovery, and a fixed constant C representing the intrinsic magnitude difference between SNe. The final column shows the resulting $\tilde{\chi}^2$ for each fit.

phase around maximum light.

The fit of the tail phase Type IIP is along a linearly extrapolated tail with a very slow colour evolution, so the fitting parameter time t_0 between explosion and detection is poorly constrained by the data. However a NACO image from 2012 September 14, 219 days prior to discovery, does not show a detection with an upper limit of 19.2 in K_s, allowing for the constraints on t_0. Regardless of SN type, it is noteworthy that all four template fits are best fitted with an extinction A_V of ~0. This is surprising as the SN is very close to the nucleus where significant extinction would be expected. Negligible extinction suggests we are observing the SN in the foreground of the host's nuclear regions. The projected distance to the nucleus of its host galaxy of 200pc makes SN 2013if the second most nuclear SN discovered in a LIRG after SN 2010cu (Kankare et al., 2012).

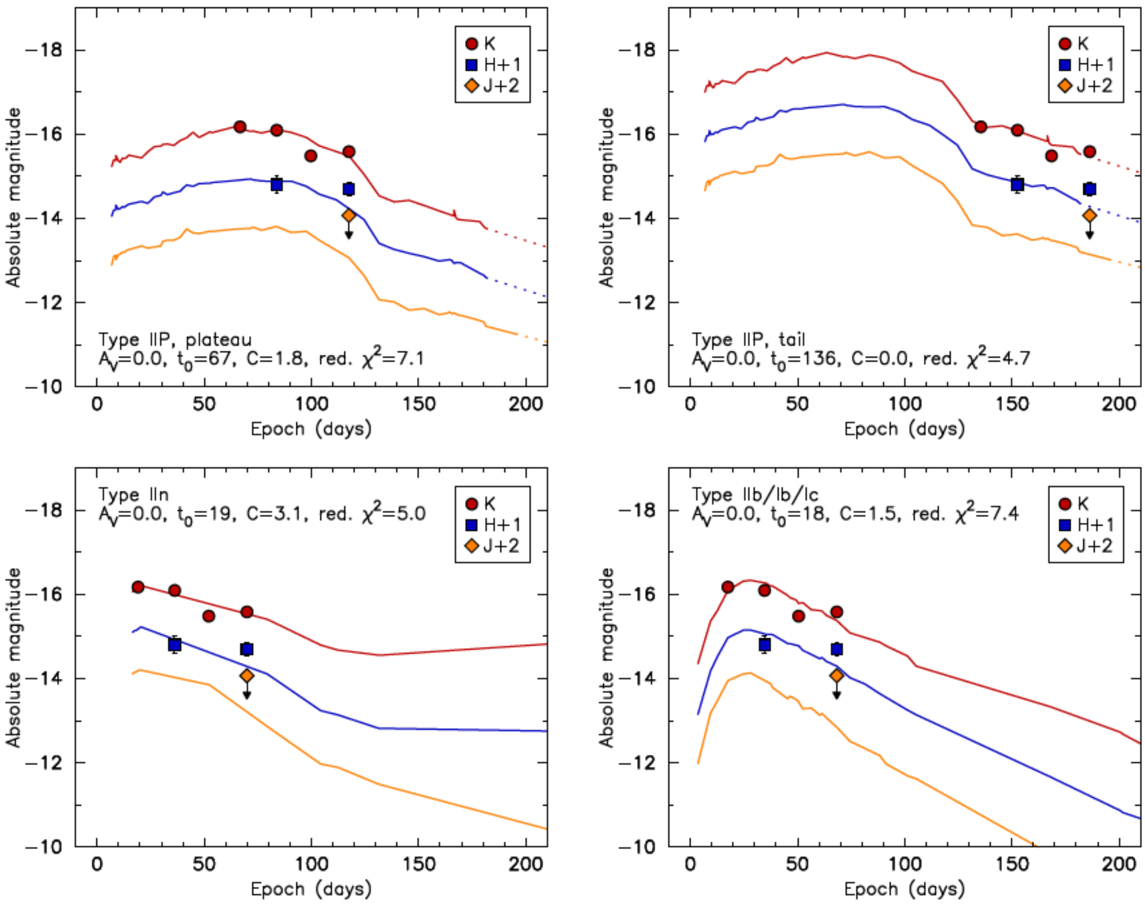

Figure 2.6: Template light curve fits for SN 2013if in IRAS 18293-3413 are shown: Type IIP fitted in the plateau and tail phase, Type IIn, and Type IIb/Ib/Ic. The most likely scenario for SN 2013if is a Type IIP caught in the tail phase, as the light curve fits the data well without requiring a magnitude shift, see Section 2.8.1.

2.8.2 SN 2015ca

SN 2015ca is best fitted by the Type IIP template, with $\tilde{\chi}^2 = 3.8$, but the stripped envelope template fits the data too, with $\tilde{\chi}^2 = 5.0$; see Fig. 2.7 and Table 2.3. In both cases the fit requires moderate extinction ($A_V = 3.4^{+1.0}_{-1.7}$ and $A_V = 2.8^{+0.3}_{-0.4}$, respectively) and a magnitude shift of ~1.5. However neither template fits well the brightest epoch from 2015 April 6 with the NOT. The Type IIn template is poorly fitted by the data, and seems inconsistent with the *JHK* upper limits of the final epoch. We also fitted a Type Ia light curve to the data based on the light curve of SN 2011fe (Matheson et al., 2012, Zhang et al., 2016), because SN 2015ca exploded in an isolated location seemingly far from recent SF. With a $\tilde{\chi}^2 = 17.9$ the Type Ia fit was clearly inferior to the core collapse scenarios. The Type IIn, stripped envelope, and Type Ia fits have been forced to take into account the *i*'-band limit from the NOT, i.e. the *i*'-band curve is basically matching with the i-band limit. The Type IIP fit was consistent with the limit based on the detections.

The follow up at radio wavelengths with the VLA and eEVN did not show any detections of SN 2015ca. For the two likely scenarios the radio luminosity for Type IIP SNe typically peaks between ∼20-70 days post explosion and are much fainter than stripped envelope SNe, which peak between 10-150 days post explosion (Romero-Cañizales et al., 2014). In the case of the IIP fit, the VLA non-detection would have been 86^{+14}_{-5} days post explosion, meaning the relatively faint radio signature of the SN would already have been on the decline. For the stripped envelope fit, the observation occurred 44^{+6}_{-2} days post explosion, which coincides more closely with radio peak luminosities for the type. For instance for SN 2011dh, the prototypical SN used for the stripped envelope template, the observation would have been at peak (∼40 days) with a luminosity forty times brighter than SN 1999em, the SN used for the Type IIP template ($\sim 8 \times 10^{26}$ erg s^{-1} Hz^{-1} versus $\sim 2 \times 10^{25}$ erg s^{-1} Hz^{-1}, respectively). However, as the SN is coincident with strong host galaxy signal, it is not possible to exclude certain SN types definitively based on the VLA observation.

The eEVN non-detection of SN 2015ca at 5 GHz with a 3σ upper limit of 60 μJy beam^{-1} ($<4 \times 10^{26}$ erg s^{-1} Hz^{-1}) occurred 60 days post discovery. This would have been 118^{+14}_{-5} days for the Type IIP fit and 76^{+6}_{-2} days post explosion for the stripped envelope fit. This means a Type IIP SN would have been well past peak luminosity and at any point along the light curve below the detection limit. On the other hand a stripped envelope SN would have been much closer in time to peak with a luminosity well above the upper limit, This is shown in Fig. 4 of Romero-Cañizales et al. (2014) for the majority of stripped envelope SNe with the exception of more extensively stripped Type Ic SNe, like 2002ap or 2007gr. As such the eEVN upper limit rules out a large fraction of stripped envelope SNe, implying a Type IIP scenario is more likely for SN 2015ca.

2.8.3 SN 2015cb

The SN 2015cb data is best fitted by the templates of a Type IIP caught in the plateau phase or a stripped envelope SN, with $\tilde{\chi}^2 = 11.7$ and $\tilde{\chi}^2 = 11.2$, respectively; see Fig. 2.8 and Table 2.3. In both cases a slightly more luminous than average SN has been observed (magnitude shifts $C = -0.7^{+0.1}_{-0.3}$ and $C = -1.1^{+0.1}_{-0.2}$, respectively) with a moderate extinction of ∼4.5 magnitudes in V. To take into account the r'-band limit, all template fits were required for the limit to at least match the r'-band template curve. Similar to SN 2015ca, the lack of a radio detection with the VLA a month after discovery favours a Type IIP scenario, but the presence of significant contamination around the SN location prevents obtaining a strong upper limit to conclusively exclude a stripped envelope SN. No eEVN observations were available for SN 2015cb.

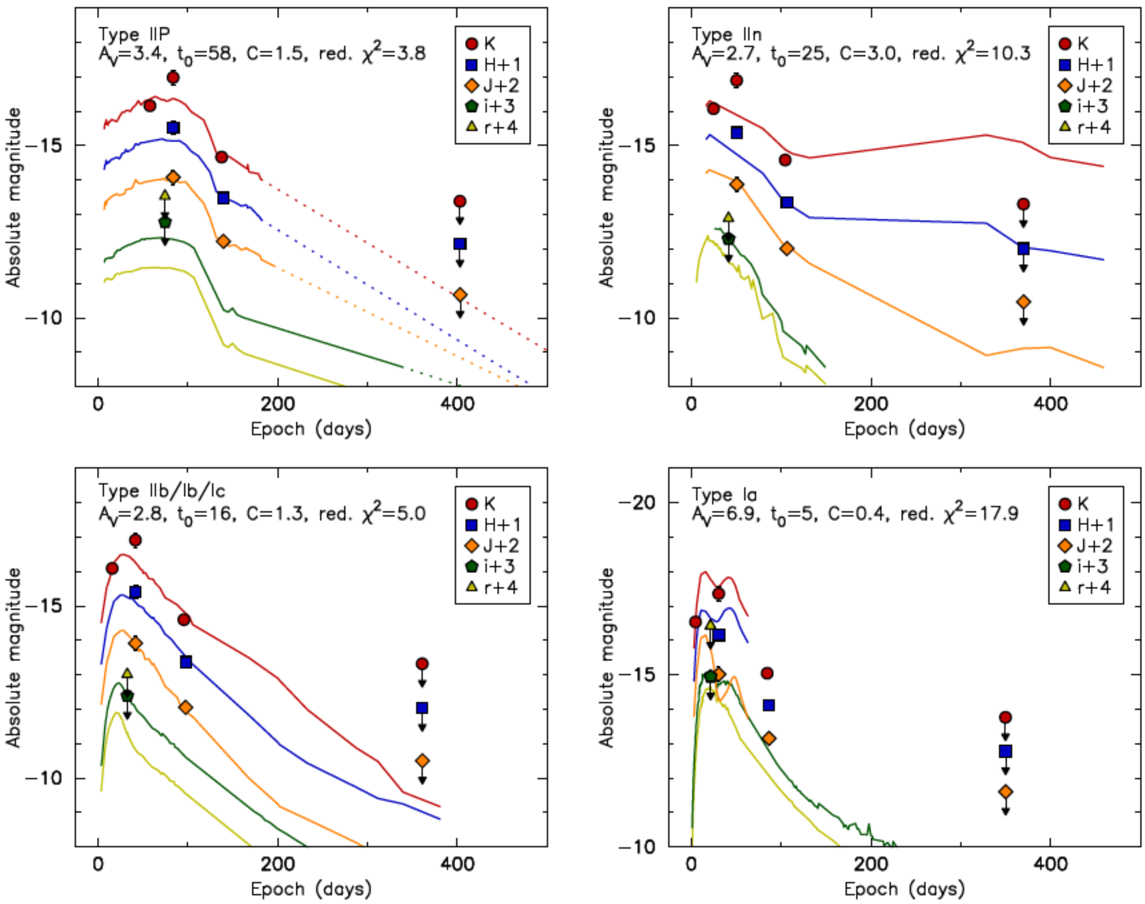

Figure 2.7: Template light curve fits for SN 2015ca in NGC 3110 are shown: Type IIP fitted in the plateau phase, Type IIn, Type IIb/Ib/Ic and Type Ia. The near-IR data points at epoch 400 and all optical data points are upper limits. The data is well fitted by both the Type IIP and the stripped envelope template. Due to the non-detections in radio, the Type IIP scenario is deemed most likely, see Section 2.8.2.

2.8.4 AT 2015cf

If AT 2015cf were a young SN, this would yield an unlikely combination of extremely high line-of-sight extinction and/or intrinsically very sub-luminous SN. Furthermore, the K_s-band decline rate of AT 2015cf from 2015 March 11 until 2015 May 29 (0.5 ± 0.4 mag / 100 days) is within errors roughly consistent with the theoretical ^{56}Co decay rate with complete γ-ray trapping (Dessart et al., 2013). However, typically H-poor SNe decline more rapidly in the tail phase. Nonetheless, to estimate parameter limits, we consider both the Type IIP and IIb/Ib/Ic template options, with the former providing a somewhat better fit due to the aforementioned decline rate, see Table 2.3 and Fig. 2.9. The NOT observations in *JHKs* from 2015 April 6 cover the site of AT 2015cf, but due to the poorer data quality (FWHM ~1.0″) and the small separation from SN 2015ca of 0.7″, the presence of the residual of SN 2015ca in the subtracted image prevents us from obtaining any

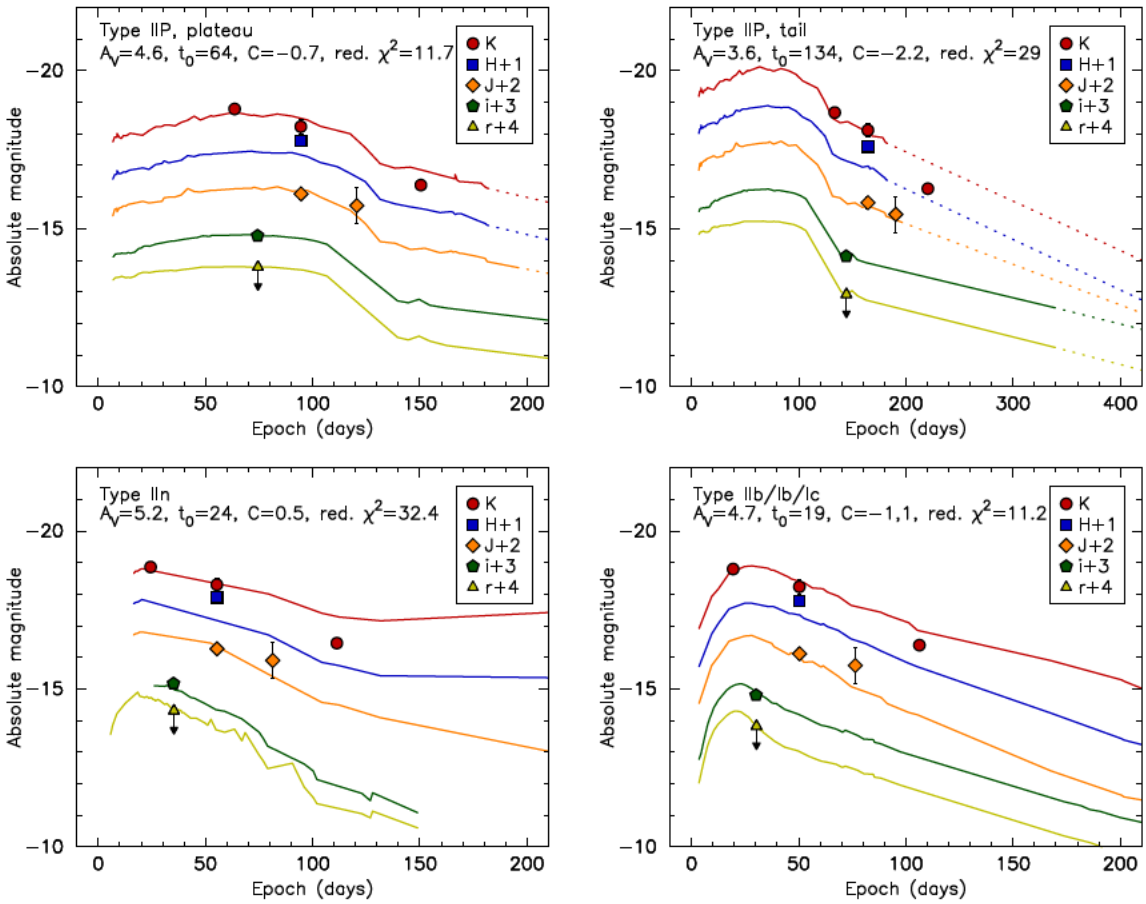

Figure 2.8: Template light curve fits for SN 2015cb in IRAS 17138-1017 are shown: Type IIP fitted in the plateau and tail phase, Type IIn, and Type IIb/Ib/Ic. Both the Type IIP and stripped envelope templates fit equally well. Due to strong background contamination the radio non-detection of SN 2015cb does not provide additional constraints in this case, see Section 2.8.3.

meaningful upper limits for AT 2015cf. The NOT optical upper limits from 2015 March 27 are the same as obtained for SN 2015ca, but the AT 2015cf data are fitted to a much fainter stage in the templates, which means the optical upper limits do not provide useful constraints to the template fits. As such we have opted not to include the NOT upper limits in Table 2.3 and Fig. 2.9. The eEVN non-detection of SN 2015ca does not cover the position of AT 2015cf and cannot be used to constrain the SN type. We conclude that the observations of AT 2015cf are most consistent with an old, possibly H-rich, CCSN.

2.8.5 CCSN rate of NGC 3110

Table 2.4 shows for NGC 3110 the SF rate, starburst age, CCSN rate and the origin of its bolometric luminosity. This is based on modelling the multi-wavelength SED of NGC 3110, using data points available from the literature ranging from optical to submillimetre photometry (U et al., 2012),

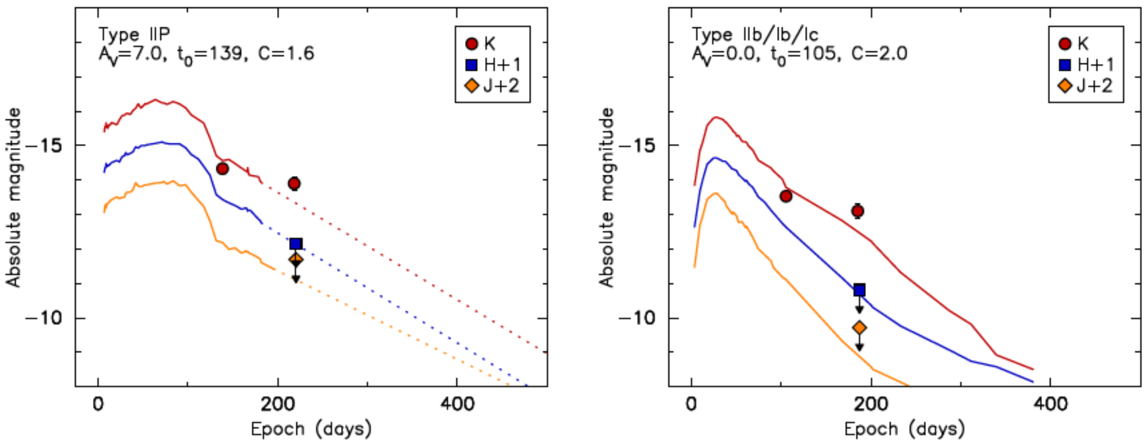

Figure 2.9: Template light curve fits for AT 2015cf in NGC 3110 are shown: Type IIP and Type IIb/Ib/Ic. The decline rate is consistent with a CCSN scenario, but the lack of data prevents confirmation of AT 2015cf as a bona fide SN, see Section 2.8.4.

Total luminosity ($10^{11} L_\odot$)	$2.59^{+0.03}_{-0.08}$
Starburst luminosity ($10^{11} L_\odot$)	$0.42^{+0.08}_{-0.02}$
Disk luminosity ($10^{11} L_\odot$)	$2.17^{+0.03}_{-0.13}$
AGN luminosity ($10^{11} L_\odot$)	<0.01
SF rate, averaged	
over the past 50 Myr ($M_\odot$ yr^{-1})	$12.7^{+0.7}_{-1.1}$
Starburst age (Myr)	$13.8^{+0.9}_{-2.4}$
Core-collapse supernova rate (SN yr^{-1})	$0.14^{+0.01}_{-0.01}$

Table 2.4: NGC 3110 SED model fitting parameters and derived physical quantities

by combining libraries of starburst, AGN torus and disk component models. For more details see Herrero-Illana et al. (2017) and references therein, with the difference that a spheroidal/cirrus component was fitted instead of a disk (Efstathiou et al, *in preparation*).

We found that the SED of the host galaxy NGC 3110 was best fitted by a disk model with a minor starburst component. Table 2.4 shows the best fit parameters and Fig. 2.10 the best fitting model. This means the dominant contributor to the galaxy's total luminosity is not the starburst luminosity, but rather the luminosity of the disk component, which is in strong contrast with the other two SN hosts IRAS 18293-3413 and IRAS 17138-1017 (Herrero-Illana et al., 2017). The SF rate of NGC 3110 based on the SED fit amounts to $12.7^{+0.7}_{-1.1}$ $M_\odot$ yr^{-1}. This is significantly lower than the SF rate based on the total IR luminosity as reported by Sanders et al. (2003), which amounts to ~ 35 $M_\odot$ yr^{-1} applying the relation between SF rate and total IR luminosity from Mattila and Meikle

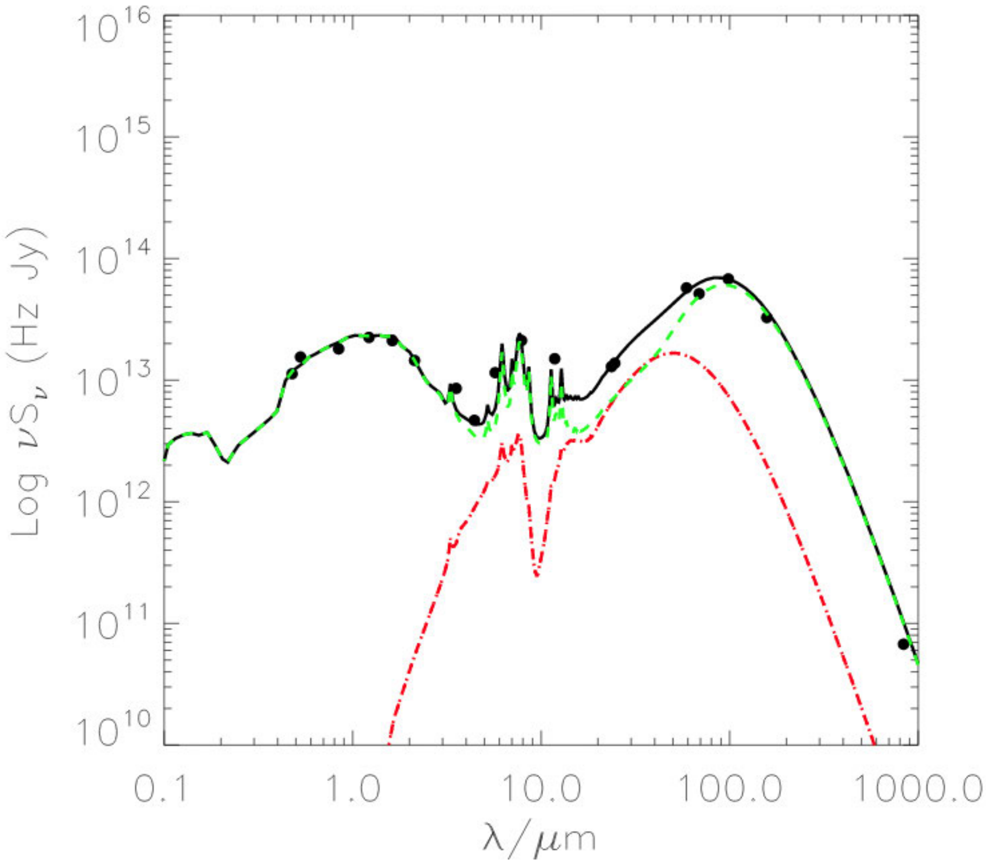

Figure 2.10: Best SED fitting model of NGC 3110, the host of SN 2015ca. The data points are indicated by the dots, starburst contribution by the red line and disk component by the green line. No AGN contribution was required to fit the data. The total fit is shown by the black line. The results from the SED fit suggests a lower SF rate for NGC 3110 than expected based on IR luminosity, see Section 2.8.5.

(2001). This results in a CCSN rate for NGC 3110 that is significantly lower ($0.14^{+0.01}_{-0.01}$ SN yr^{-1}) than the expectation from the LIRG's IR luminosity, which would be ~ 0.6 SN yr^{-1} when applying Eq. 2.1. The source of this discrepancy lies with the origin of the IR luminosity, which according to the multi-wavelength SED fit in this galaxy is dominated by the the disk component, as opposed to a starburst. The IR luminosity related to the disk component would then originate from reprocessed radiation from old stars not massive enough to explode as SNe.

Finding two concurrent CCSNe in a galaxy with a CCSN rate of 0.14 yr^{-1} is peculiar, but not impossible. If we assume a Poisson distribution and that SNe are detectable for 3 months in near-IR, as has been the case for the discoveries in this chapter, the probability of discovering two CCSNe in any of the four epochs of NGC 3110 is 4% and 0.2% for an expected yearly SN rate of 0.6 and 0.14, respectively. If we assume the same rates for our whole sample (36 epochs in total), this increases to 30.8% and 1.8%, respectively.

The CCSN nature of SN 2015ca is well established, see Section 2.8.2. The CCSN nature of AT 2015cf remains poorly constrained, but other plausible scenarios with sufficiently high rates are not known to the author. One possible explanation for this discrepancy is that the starburst age is significantly underestimated. A higher starburst age would give a higher CCSN rate. One important difference between the model fit for NGC 3110 and the other LIRGs studied by Herrero-Illana et al. (2017) is that in the case of NGC 3110 we lack Spitzer IRS data for the whole galaxy (because of its large angular size), which would constrain our model further.

2.8.6 Detection efficiency

To evaluate how effective our detection method was at recovering SNe, we calculated the detection efficiency in the data by simulating artificial sources in an epoch typical for our sample. We chose to simulate SNe in the GeMS/GSAOI epoch from 2013 April 21 of IRAS 18293-3413, as it is a fairly typical LIRG at a typical distance within our sample and host to SUNBIRD discovery SN 2013if. SNe were simulated in the central region of the galaxy, defined as containing 80% of the galaxy light. We constructed a model PSF from three bright field stars, placed it in a random position in this region and then performed a subtraction as described in Section 2.6.1. To recover the source, aperture photometry was taken at the simulation location and a 3x3 grid of apertures around it, separated by twice the FWHM. The source was considered recovered when the source flux exceeded three times the standard deviation of the counts recorded in the surrounding aperture grid. The results were split into three regions: the central 100 pc (<0.25″), where the residuals from subtraction are very large; a wider nuclear region of 300 pc omitting the central 100 pc (0.25″ - 0.75″); and the remaining area, which extended to 600-800 pc (0.5″ - 2″).

This was repeated for a range of magnitudes and an S-curve (e.g. Dahlen et al., 2008, Kankare et al., 2012) was fitted to the data. We derive a preliminary 50% detection efficiency at magnitudes of 16.7, 19.3 and 20.7 for the three regions referred to above, respectively. As expected, our detection efficiency is significantly reduced in the central 100 pc of the galaxy. SN 2013if was detected in this galaxy at magnitude 18.53 at 200 pc from the nucleus, halfway across the second region, which agrees well with the derived 50% detection efficiency for the region. For LIRGs such as this, there is significant variation in the chances of detection, heavily dependent on the local galaxy structure and proximity to the nucleus. Additionally, differences in the data quality between epochs affects detection efficiency. This is reflected by the non-detection of SN 2013if in J-band (where AO-performance in near-IR typically is worst) from 2013 June 11, with an upper limit magnitude of 18.7. An expanded approach to the evaluation of detection efficiency across multiple near-IR AO surveys, including project SUNBIRD, will be presented in a future publication (Reynolds et al, *in prep*).

2.9 Summary

In this chapter the methodology and the first results of project SUNBIRD are introduced. We discuss in detail our method of processing GeMS/GSAOI data to achieve a uniform image quality across the full field of view, which to date is one of just a couple of methods to do so. We have presented the first three CCSN discoveries from this project, as well as one candidate. With a radial offset from the nucleus of 0.5″ (200 pc projected distance) SN 2013if is the second most nuclear SN discovered in a LIRG after SN 2010cu (Kankare et al., 2012). Based on light curve fitting and radio limits we deem SN 2013if and SN 2015ca most likely to have been Type IIP SNe, but we do not have sufficient data to confirm the subtype of SN 2015cb.

3

Project SUNBIRD: Keck

3.1 Introduction

Project SUNBIRD was extended to the Northern Hemisphere at the start of 2016 through observations with the LGSAO supported near-IR imager NIRC2 on the Keck II telescope on Maunakea in Hawai'i. While NIRC2 has a smaller FOV than GSAOI, as a single conjugate AO imager there is less overhead involved and guide star requirements are not as strict as for GeMS/GSAOI. As a result more LIRGs could be accessed and more epochs could be obtained on a given observing night. In this chapter a description of the Keck program is provided and we report on the discoveries made with NIRC2 in 2016 and 2017.

3.2 Galaxy Sample

The sample of LIRGs observed with NIRC2 on the Keck telescope was selected from the IRAS Revised Bright Galaxy Sample (RGBS; Sanders et al., 2003), similarly to the Gemini South sample. Keck has a single conjugate AO system where one deformable mirror corrects for one turbulent layer in the atmosphere, as opposed to two with GeMS. LSGAO observing with NIRC2 requires one NGS of m_R < 17.0 mag within 60″ from the target, which allows access to a much larger sample of LIRGs. As a result all targets in the Keck sample had IR luminosities L(8-1000μm) in the RBGS of $\log(L_{IR}) > 11.0$. The sample was limited to LIRGs with distances up to 160 Mpc (z=0.037), where a typical achieved image quality of 0.08″ corresponds to ~60 pc.

3.3 Observing Strategy

The instrument NIRC2 on the Keck II telescope is a near-IR imager designed for the Keck AO system. NIRC2 operates from 1 to 5 µm with a FOV of 40″× 40″ when observing in wide-field mode at a pixel scale of 0.04″ pixel^{-1}. We observed in wide-field mode to allow for enough sky in the frame to dither on target without having to offset for sky frames. At a typical image quality of 0.07″ - 0.1″ this meant in most cases we were slightly under sampled.

Seven and a half classical nights with NIRC2 were awarded to project SUNBIRD between April 2016 and December 2017. Out of those nights, three full nights were lost due to clouds and/or humidity. During the remaining 4.5 nights a total of 55 epochs were observed across 25 targets, see Table 3.1. Under ideal circumstances a new target could be observed every 30 minutes. Priority was given to LIRGs with prior AO or HST observations available, followed by LIRGs with high CCSN rates. Due to loss of observing time and limits in year-round visibility the maximum number of epochs we could obtain of any LIRG was 4, with many targets observed less frequently. The targets with just one epoch were checked for SNe against archival AO images observed with ALTAIR/NIRI (ALTtitude conjugate Adaptive optics for the InfraRed/Near InfraRed Imager; Hodapp et al., 2003) on Gemini North in a preceding program (Kankare et al., 2008). If not available, the observations were checked against archival *F160W* HST/NICMOS images from the Hubble Legacy Archive[1].

Each target was observed for 120s at 9 dither positions in K_s-band, with a typical 10″ step size to properly model the background while keeping the target within the FOV. The 120s observations consisted of consecutive shorter exposures immediately coadded upon completion. The number of exposures depended on the ADU count in a test exposure taken prior to the full observation, with the default setting 6 coadds of 20s. Given the relatively large pixels in wide-field mode and the brightness of LIRG nuclei, in some cases exposure times were reduced to as short as 3s (40 coadds) to stay linear on the detector ($\lesssim$8000 ADU).

[1]https://hla.stsci.edu/

3.4 Multi wavelength follow up

During an observing night the data were reduced with THELI immediately after observing and IRAF was used to perform a basic coadd without distortion correction for the sake of efficiency. This allowed us to check for transient sources against earlier epochs by blinking image pairs in DS9[2] within an hour after obtaining the data. In case of a SN candidate discovery we could then immediately follow up with NIRC2 in H- and J-band. This enabled us to obtain images in all three near-IR bands at the night of discovery for three of the four transients discovered in the Keck program.

On a longer timescale, we would observe the transient with NIRC2 in JHK_s during the next observing night if still visible, typically 3 months later. Additional follow up imaging of the discovered transients was obtained in the near-IR with NOTCam on the NOT and in the optical with ALFOSC on the NOT (PI: S. Mattila) and ACAM (Benn et al., 2008) on the William Herschel Telescope (WHT, PI: P. Jonker). Spectroscopy follow up was obtained in the near-IR with GNIRS on the Gemini North telescope (PI: E. Kool) and SpeX (Rayner et al., 2003) on the NASA Infrared Telescope Facility (IRTF, PI: E. Hsiao), and in the optical with the Intermediate dispersion Spectrograph and Imaging System (ISIS) on the WHT (PI: P. Jonker). At radio wavelengths we followed up with the Very Long Baseline Array (VLBA, PI: M. Pérez-Torres) interferometer. Other follow up included mid-IR observations with the IRAC (Infrared Array Camera; Fazio et al., 2004) on the NASA Spitzer Space Telescope (PI: S. Mattila).

3.5 Data reduction

3.5.1 NIRC2 data reduction with THELI and IRAF

Data were reduced with THELI using the procedures described in Chapter 2. Successful coaddition with THELI depends on having access to archival imaging such as VIRCAM/VISTA or VLT/HAWK-I data to construct an astrometric reference catalogue. For our NIRC2 data these were not always available. A further complication was the relatively small FOV ($40'' \times 40''$) of NIRC2 compared to GeMS/GSAOI, limiting the access to field stars to act as astrometric references. Some of the observed LIRGs were bright and compact and lacked a sufficient number of compact objects spread across the galaxy. As a consequence not all LIRGs in our sample could be fully reduced and coadded using THELI. In those cases the data were processed in two steps. First the data were

[2]http://ds9.si.edu/

LIRG	RA (J2000)	Dec. (J2000)	Distance (Mpc)	log L_{IR} ($L_{\odot}$)	r_{CCSN} (yr^{-1})	Epochs #
IRAS 01173+1405	01 20 02.7	+14 21 42	131	11.69	1.33	3
NGC 695	01 51 14.0	+22 34 55	136	11.62	1.33	1
NGC 1275	03 19 46.7	+41 30 37	74	11.26	0.49	2
IRAS F03217+4022	03 25 05.2	+40 33 32	99	11.35	0.60	2
MCG+08-11-002	05 40 43.3	+49 41 41	82	11.46	1.07∗	3
UGC 3351	05 45 48.6	+58 42 02	65	11.28	0.51	1
IRAS F06076-2139	06 09 45.1	-21 40 22	160	11.65	1.21	2
NGC 2388	07 28 54.2	+33 49 07	61	11.28	0.51	1
NGC 3110	10 04 02.7	-06 28 35	79	11.36	0.17†	1
IC 2810	11 25 47.3	+14 40 23	152	11.64	1.19	1
Arp 299	11 28 31.3	+58 33 42	50	11.45	1.45∗	2
ESO 507-G070	13 02 51.3	-23 55 10	105	11.49	1.00	1
VV 250a	13 15 34.9	+62 07 26	138	11.81	1.72	1
UGC 8387	13 20 34.9	+34 08 24	107	11.73	1.78∗	3
NGC 5331	13 52 16.6	+02 06 08	150	11.66	1.22	2
VV 340a	14 57 00.3	+24 37 01	152	11.75	1.50	3
NGC 6240	16 52 58.6	+02 24 03	113	11.92	1.80∗	3
IRAS F16516-0948	16 54 24.2	-09 53 22	106	11.32	0.42∗	2
IRAS F17138-1017	17 16 36.3	-10 20 40	83	11.49	0.75∗	3
IRAS 17578-0400	18 00 32.0	-04 00 55	67	11.47	0.79∗	4
IRAS 18090+0130	18 11 37.3	+01 31 40	131	11.65	1.22	4
IRAS 20351+2521	20 37 18.6	+25 31 42	147	11.61	1.11	2
NGC 7469	23 03 15.5	+08 52 25	70	11.65	1.21	3
IC 5298	23 16 01.7	+25 33 33	117	11.61	1.09	3
IRAS 23436+5257	23 46 05.8	+53 14 00	146	11.58	1.03	2

Table 3.1: Keck NIRC2 LIRG sample. Distances are from NED, Virgo/GA corrected. CCSN rates are based on the empirical relation with L_{IR} from Mattila and Meikle (2001), unless otherwise indicated: CCSN rate based on SED fits from Herrero-Illana et al. (2017), denoted by ∗, or from Chapter 2, denoted by †. Values of log L_{IR} are from Sanders et al. (2003), adjusted for updated distances. Final column shows number of epochs obtained with NIRC2.

flatfielded and background subtracted using THELI, but coadded in IRAF with *idedither_comb*, a task written by Seppo Mattila. In this task a compact object or star that is visible in all frames is selected. The exposures are then stacked with shifts corresponding to the offset of the centroid of the reference star compared to the centroid of the star in the first exposure. The resulting coadd does not account for image distortion, which means it is optimized around the reference star but image quality decreases with radius. If the reference star is near or in the compact galaxy, the loss of image quality in the relevant regions is small. In the second step, the newly coadded image was used to act as a reference image for coaddition of the original data set with THELI. The advantage of this method is that because a reference image with comparable image quality and FOV is available (it is based on the same data set after all), it is trivial to extract a usable reference catalogue. Given this reference catalogue, with THELI the exposures can be coadded while accounting for image distortion. Using this iterative approach, the resulting coadded images had an improved and uniform image quality, when compared to the result from the intermediate simple image stack using *idedither_comb*.

The downside of this approach is that the absolute astrometry of the image is not accurate, because no external reference image with accurate astrometry was used. While absolute astrometry is not required for image subtraction, it is vital when a SN candidate is discovered to allow for accurate reporting and follow up. In this case an astrometric solution was found by manually matching field stars in the image with coordinates from the Pan-STARRS1 data archive[3] using IRAF task *ccmap*.

3.5.2 Other data reduction

The NOTCam and ALFOSC observations obtained with the NOT were reduced as described in Section 2.5.2. GNIRS observations were reduced using the method described in Section 2.5.3. SpeX observations were obtained through the NUTS survey[4] and reduced by M. Shahbandeh at Florida State University. VLBA data were reduced by members of our collaboration following the procedures described in Section 2.7.5. Spitzer data was pipeline-reduced from the Spitzer Legacy archive.

[3]https://panstarrs.stsci.edu/
[4]http://csp2.lco.cl/not/

3.5.3 Image subtraction, photometry and light curve fitting

Image pairs were aligned and subtracted using image subtraction package ISIS 2.2, as described in Chapter 2. Photometry of the discovered transients was measured using the SNOOPY package in IRAF in the same way as for GeMS/GSAOI data. However, given the smaller FOV of NIRC2 compared to GSAOI, more often than not the discovery images lacked 2MASS photometric reference stars. In some cases 2MASS stars were available, but were catalogued with magnitudes inconsistent with the magnitudes of isolated 2MASS field stars located in a wide-field NOTCam image, likely due to the impact of the nearby galaxy. These stars usually lacked an assigned error in the 2MASS catalogue. Using these inconsistent 2MASS stars produced large errors in the derived zero point. This was solved by (re)calibrating any photometric reference star used in the Keck FOV, whether they were available in the 2MASS catalogue or not. Five isolated 2MASS stars, that included photometry with errors in JHK_s, were selected in a wide-field NOTCam image. After checking if the individual photometric stars produced consistent zero points, new magnitudes were obtained for the 2MASS and/or reference stars nearby to the galaxy within the NIRC2 FOV, using PSF fitting with SNOOPY.

See Fig. 3.1 for an example of the recalibration of NIRC2 photometric reference stars (in red) through field stars (in blue) in a wide-field NOTCam image. Obtaining magnitudes through PSF fitting was deemed appropriate given the level of background emission from the galaxy at the positions of the photometric reference stars in the NIRC2 image. The new photometric errors were determined following the steps described in Section 2.6.2. This approach also had the advantage of producing a consistent photometric reference frame between observations of the same transient with instruments of vastly different image quality and FOV, as is the case with NIRC2 and NOTCam. In some cases the transient was superimposed on a bright nucleus, the subtraction of which could have introduced systematic errors, as suboptimal modelling of the background would have affected all epochs of a transient in the same way. Finally the light curves were fitted to the prototypical CCSNe templates described in Chapter 2.

3.6 Observations and Discoveries

3.6.1 AT 2016jhy in IRAS F06076-2139

A transient in IRAS F06076-2139 was discovered on 2016 October 19 with NIRC2 (PI: S. Ryder), designated AT 2016jhy (Kool, 2018b). An archival VLT/NACO image from 2010 was used as a subtraction reference, resulting in a point-like residual superimposed on the Southern nucleus of

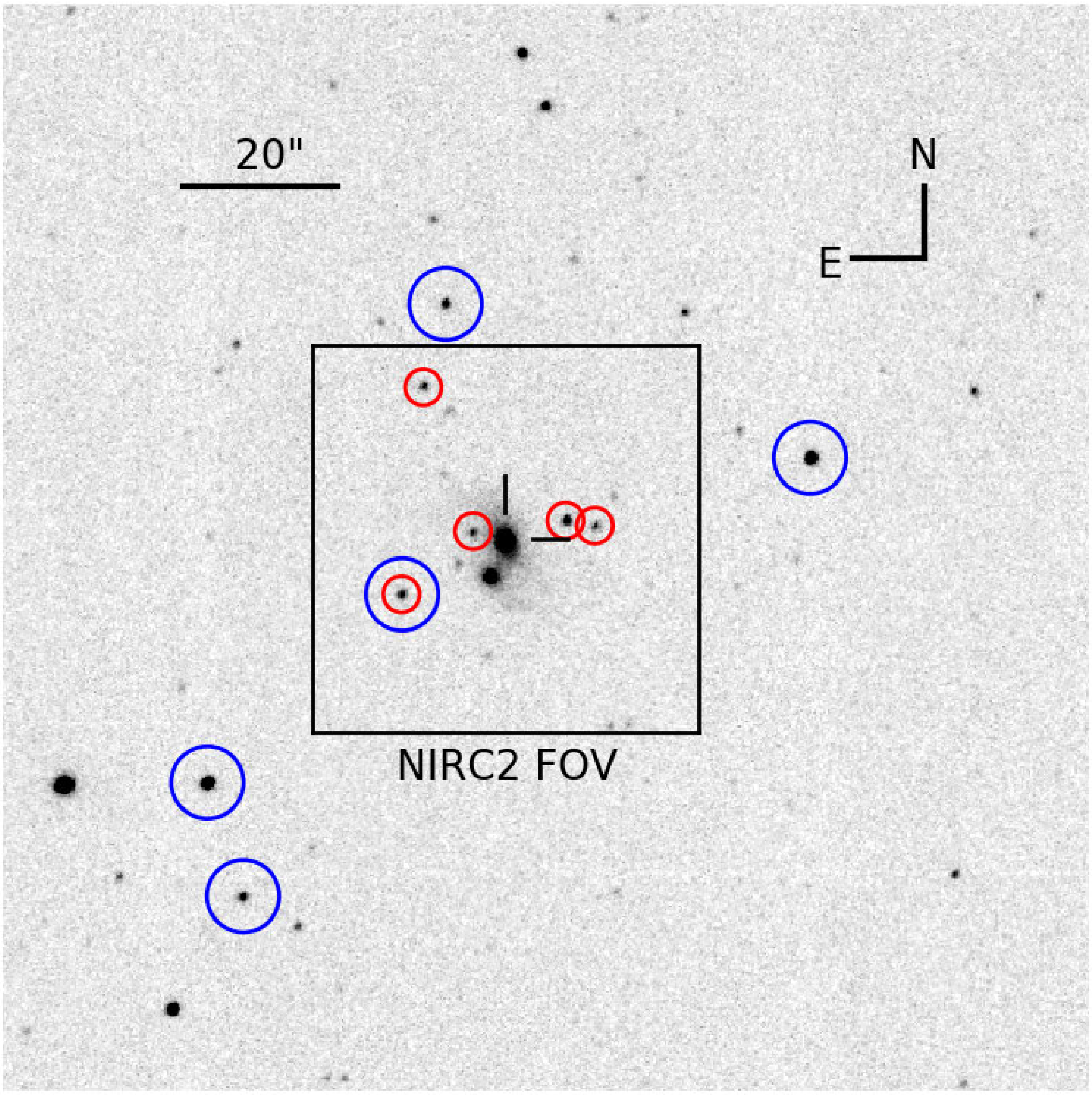

Figure 3.1: IRAS 23436+5257 as observed with NOTCam on the NOT. Blue circles indicate 2MASS photometric reference stars used to calibrate the field stars in the NIRC2 FOV, indicated by red circles, as described in Section 3.5.3. The position of AT 2017gbl superimposed on the Northern nucleus of its host galaxy is indicated by tick marks.

this interacting galaxy located at R.A. = $6^{h}09^{m}46.01^{s}$ and Decl. = $-21°40'31.26''$, see Fig. 3.2. Follow up in K_s-band with F2 on Gemini South (PI: E. Kool) on 2017 March 12 and with NIRC2 on 2017 December 12 similarly revealed a residual at the same position after subtracting the NACO reference image, with PSF's matching well with those of isolated field stars in the images. Between the discovery epoch and the most recent epoch the source did not appear to have changed much in magnitude, see Table 3.5.

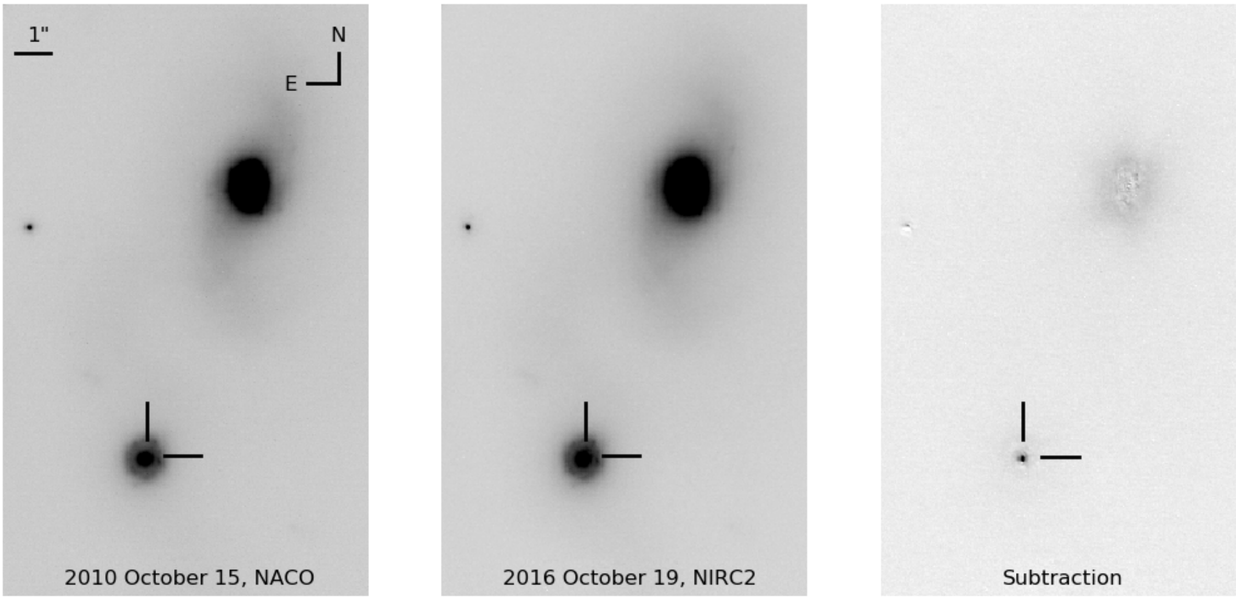

Figure 3.2: AT 2016jhy superimposed on the Southern nucleus of IRAS F06076-2139, in K_s-band, see Section 3.6.1. From left to right with linear scaling: Reference VLT/NACO image (October 2010), discovery NIRC2 image (October 2016) and the image subtraction.

3.6.2 AT 2017chi in NGC 5331

The host galaxy of AT 2017chi (Kool, 2017), NGC 5331, was part of the SUNBIRD Keck sample of LIRGs. However, AT 2017chi was discovered with the near-IR imaging spectrograph FLAMINGOS-2 (F2 Eikenberry et al., 2012) on Gemini South on 2017 March 13 during an observing night allocated to the GeMS/GSAOI SUNBIRD program (PI: E. Kool). There were technical issues with GeMS, but the seeing conditions were excellent (FWHM ~0.35″) so we opted to continue our program with F2. F2 is a non-AO wide-field imager, so target selection was not restricted by guide star requirements or limited to our GSAOI sample, but image quality was limited to the seeing conditions. As a result priority was given to extended LIRGs with high expected CCSN rates from the combined NIRC2 and GSAOI sample, such as the interacting LIRG NGC 5331.

Subtraction of the F2 discovery image with an archival K_s-band VLT/HAWK-I image from 2011 May 26 showed a positive residual 1.1″ South and 2.1″ West (1.7 kpc projected distance) from the nucleus of the Southern component of this interacting galaxy, see Fig. 3.3. WCS matching in THELI with a catalogue of 21 2MASS sources in the FOV yielded R.A. = $13^h52^m16.09^s$ and Decl. = +02°06′03.96″, with 0.04″ and 0.04″ uncertainty in R.A. and Decl., respectively. Follow up observations were obtained with F2 on 2017 March 27 in H and J, and with NIRC2 on 2017 April 6 and 2017 July 8 in K_s, H and J (PI: S. Ryder). Transient-free imaging in H and J was obtained on 2018 May 12 with F2 through the Fast Turnaround program at Gemini South (PI: K. Maeda). AT 2017chi was detected in JHK_s in 2017 March and April, but only in K_s in the final NIRC2 epoch in 2017 July, see Table 3.5.

An optical spectrum was obtained through the extended-Public ESO Spectroscopic Survey for Transient Objects[5] (ePESSTO) on 2017 March 24 with EFOSC2 (ESO Faint Object Spectrograph and Camera; Buzzoni et al., 1984) on the ESO New Technology Telescope (NTT). The spectrum did not show any SN signatures, likely due to the effects of dust extinction and a bright local background.

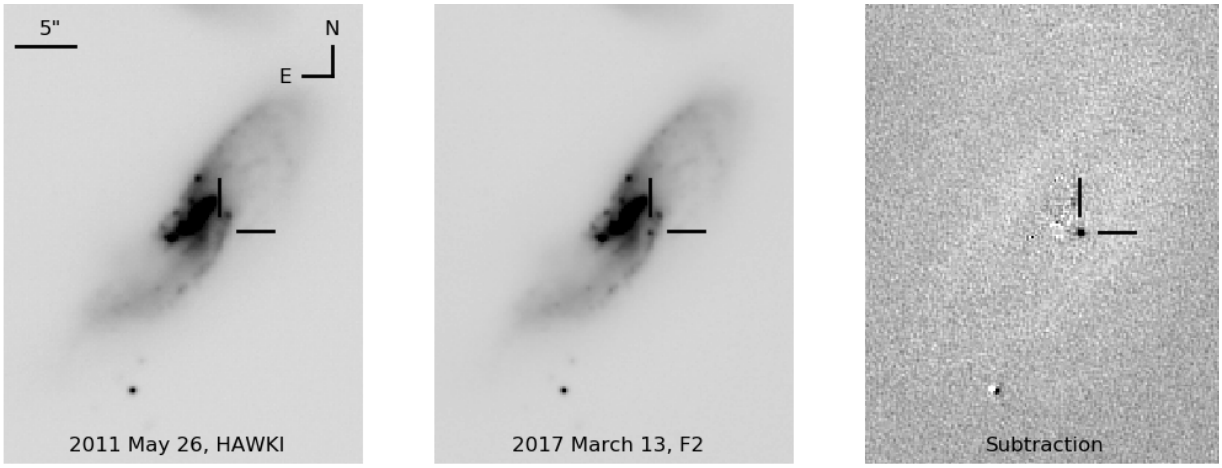

Figure 3.3: AT 2017chi in NGC 5331 discovered with F2, in K_s-band, see Section 3.6.2. From left to right with linear scaling: Reference HAWK-I image (May 2011), discovery image (March 2017) and the image subtraction.

3.6.3 AT 2017gbl in IRAS 23436+5257

AT 2017gbl was discovered in IRAS 23436+5257 in K_s-band with NIRC2 (PI: S. Ryder) on 2017 July 8 (Kool et al., 2017c); see Fig. 3.1 and Fig. 3.4. Initially the host galaxy was observed with 6 coadds of 20s per 120s exposure, as was deemed appropriate during the first NIRC2 epoch from 2016 October 21. However at these settings the Northern nucleus now saturated the detector, so exposure time was reduced to 3s to keep counts linear on the detector and the galaxy was re-observed in K_s-band, directly followed by H- and J-band. Subtraction with K_s, H and J observations from 2016 showed an extremely bright residual coincident with the Northern nucleus of its host galaxy. Registering the image with 20 sources from the PanSTARRS-1 archive yielded R.A. = $23^h46^m05.52^s$ and Decl. = $+53°14'01.29''$, with $0.03''$ and $0.05''$ uncertainty in R.A. and

[5] http://www.pessto.org/

Decl., respectively.

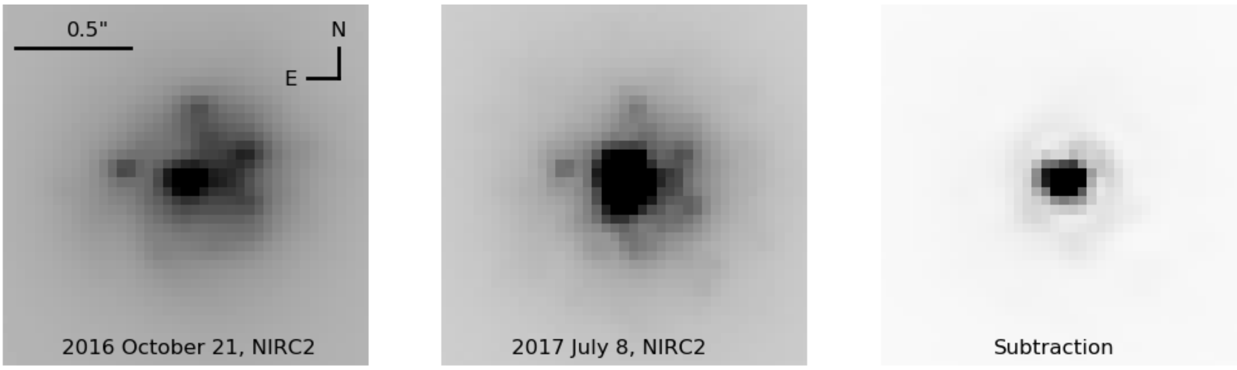

Figure 3.4: AT 2017gbl superimposed on the Northern nucleus of IRAS 23436+5257, discovered with NIRC2 in K_s-band, see Section 3.6.3. From left to right with linear scaling: Reference NIRC2 image (October 2016), discovery image (July 2017) and the image subtraction.

Follow up imaging was obtained at an almost monthly cadence in the near-IR with NOTCam on the NOT, from discovery of the transient until the latest epoch in January 2018 by the NOT Unbiased Transient Survey (NUTS) collaboration[6]. The transient was revisited with NIRC2 in K_s-band on 2017 December 5. In the optical AT 2017gbl was observed with ALFOSC on the NOT in i' and z' on 2017 November 28, and with ACAM on the WHT (PI: P. Jonker) in g', r', i' and z' on 2017 July 10 and in i' and z' on 2017 August 27.

In the near-IR transient-free reference imaging was available from 2016 October 21, obtained with NIRC2 on Keck as part of project SUNBIRD. As this was obtained with the same instrument as the discovery data, image subtraction for the discovery NIRC2 epoch was robust. However, due to the large difference in image quality between the AO reference epoch and further seeing-limited follow-up imaging with NOTCam, it was necessary to smooth and rebin the NIRC2 reference epoch using IRAF tasks *gauss* and *blkavg* to better match the image quality of the NOTCam data before image subtraction. In the optical transient-free reference imaging from WHT/ACAM and NOT/NOTCam was used from 2018, after verifying the transient had fully faded from view at this point by comparing with archival pre-outburst Pan-STARRS1 data.

AT 2017gbl has steadily declined in magnitude in the near-IR since discovery but has remained visible in all bands for all epochs obtained so far, see Table 3.2. In the optical the transient was recovered in all four filters in the first epoch, and has remained visible in the subsequent follow up in i' and z', see Table 3.3.

[6]http://csp2.lco.cl/not/

UT Date	Telescope/Instrument	Magnitude		
AT 2017gbl (IRAS 23436+5257)				
		J	H	K_s
2016 October 21.5	Keck/NIRC2	-	-	-
2017 July 8.5	Keck/NIRC2	16.03 ±0.03	14.45 ±0.04	13.22 ±0.07
2017 July 27	NOT/NOTCam	16.13 ±0.04	14.60 ±0.03	13.29 ±0.04
2017 August 18	NOT/NOTCam	16.50 ±0.02	14.84 ±0.03	13.47 ±0.05
2017 September 3	NOT/NOTCam	16.68 ±0.05	14.93 ±0.04	13.60 ±0.05
2017 September 29	NOT/NOTCam	16.80 ±0.05	15.17 ±0.04	13.74 ±0.04
2017 October 16	NOT/NOTCam	16.99 ±0.08	15.27 ±0.05	13.76 ±0.06
2017 December 5.2	Keck/NIRC2			14.26 ±0.04
2018 January 3	NOT/NOTCam	17.96 ±0.13	16.14 ±0.10	14.74 ±0.08

Table 3.2: AT 2017gbl near-IR photometry

UT Date	Telescope/Instrument	Magnitude			
		g'	r'	i'	z'
2017 July 10	WHT/ACAM	21.22±0.09	19.93±0.02	19.08±0.02	18.36±0.03
2017 August 27	WHT/ACAM	-	-	19.66±0.05	18.96±0.05
2017 November 28	NOT/ALFOSC	-	-	20.79±0.04	20.45±0.03

Table 3.3: AT 2017gbl optical photometry

Multi-wavelength and spectroscopy follow up

In addition to imaging we obtained spectroscopy in the optical and the near-IR. Optical spectra were obtained with ISIS on the WHT on 2017 August 30 (PI: P. Jonker) and in the near-IR we obtained spectra with GNIRS on Gemini North on 2017 September 1 through Director's Discretionary Time (DDT, PI: E. Kool) and with SpeX on the IRTF on 2017 October 28 through the NUTS collaboration. In radio members of our collaboration observed AT 2017gbl with the VLBA on 2017 August 15 (Perez-Torres et al., 2017) and on 2017 October 20 at 4.4 and 7.6 GHz (PI: M. Pérez-Torres). Bright et al. (2017) observed AT 2017gbl three times between 2017 July 12 and Aug 10 with AMI (Arcminute Microkelvin Imager Large Array; Zwart et al., 2008) at 15.5 GHz, and again on 2018 February 27. An unresolved source was detected at all radio frequencies.

Finally in mid-IR follow up imaging was obtained at 3.6 and 4.5 μm with IRAC on the Spitzer

UT Date	Telescope/Instrument	Magnitude	
		3.6 μm	4.5 μm
2017 November 13	*Spitzer*	11.56 ± 0.11	10.84 ± 0.09
2017 December 19	*Spitzer*	11.75 ± 0.11	10.98 ± 0.10
2018 March 23	*Spitzer*	11.97 ± 0.13	11.18 ± 0.11

Table 3.4: AT 2017gbl mid-IR photometry after subtraction of the pre-outburst magnitude of the host nucleus, see Section 3.6.3.

space telescope on 2017 November 11, 2017 December 19 and 2018 March 23 (PI: S. Mattila). Table 3.4 shows the magnitude of AT 2017gbl at 3.6 μm and 4.5 μm after subtracting the pre-outburst magnitude of the nucleus of 11.24 ± 0.05 and 10.84 ± 0.06 at 3.6 μm and 4.5 μm respectively, based on an archival image from 2011.

3.6.4 AT 2017jzy in NGC 695

AT 2017jzy (Kool, 2018a) was discovered with NIRC2 on 2017 December 5 in NGC 695; see Fig. 3.5. There was no previous (archival) AO imaging of the host available, so an archival HST/NICMOS *F160W* image (Haan et al., 2011) was used to act as a subtraction reference for the H-band discovery image. *F160W* is a broadband filter with a cut-on of 1.4μm and a cut-off of 1.8 μm, which is similar to H-band (1.49 to 1.78 μm). The subtraction revealed a transient at R.A. = $1^{h}51^{m}13.90^{s}$ and Decl. = $+22°34'54.97''$, 4.4″ South and 6.3″ West (5.1 kpc projected distance) from the nucleus. In the same night the galaxy was also observed in K_s- and J-band, with the transient visible in all three bands. We followed up with NOTCam in K_s, H and J on 2018 January 3 in natural seeing conditions, but the transient was not discernible, likely due to the faint source having blended with the background.

3.6.5 Archival NICMOS SN candidates

Many LIRGs in the SUNBIRD Keck sample were observed for the first time using AO, and as such adequate reference imaging was not readily available. In that case, until a second epoch could be obtained, newly obtained images were compared with archival HST/NICMOS images when available. NICMOS filters do not extend to K_s, so in case of a clear image difference in K_s we would also observe the target in H-band. This resulted in the discovery of AT 2017jzy, but transients were also discovered in the archival NICMOS data. These data were not obtained with

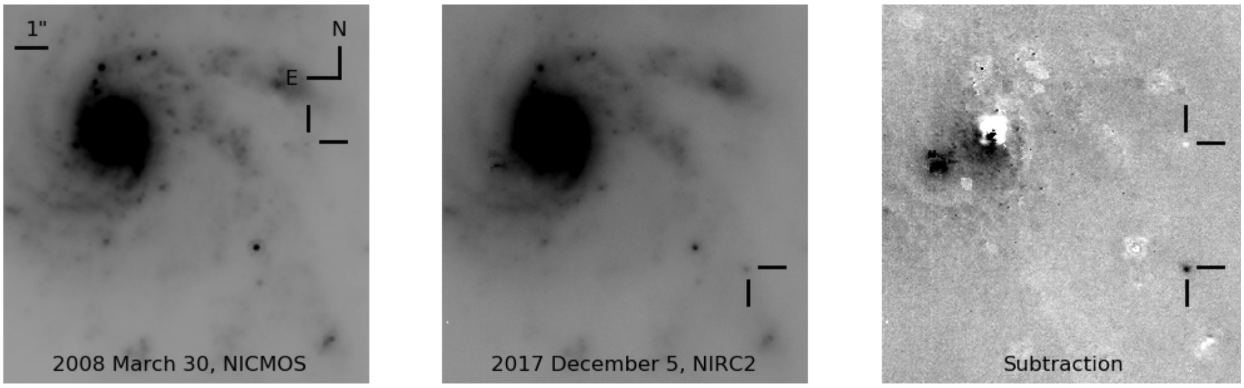

Figure 3.5: AT 2017jzy in NGC 695, discovered in H-band, see Section 3.6.4. Also indicated 4″ North of AT 2017jzy is a transient visible in the archival NICMOS reference image. From left to right with linear scaling: reference HST/NICMOS image (March 2008), discovery NIRC2 image (December 2017) and the image subtraction.

the purpose of transient detection, so typically no follow up imaging was available.

The subtraction of the H-band discovery image of AT 2017jzy in NGC 695 with an archival $F160W$ NICMOS image from 2008 August 29 showed a second residual located in the NICMOS image at R.A. = $1^{\mathrm{h}}51^{\mathrm{m}}13.90^{\mathrm{s}}$ and Decl. = $+22°34'54.97''$, 4″ North of AT 2017jzy and 4.2 kpc projected distance from the nucleus, see Fig 3.5. Just as with AT 2017jzy it has a PSF well matched with isolated field stars in the discovery image, a good indication it is a real source. No further HST/NICMOS epochs or other imaging of sufficient image quality could be found in the archives.

The subtraction of a K_s-band observation of NGC 1275 from 2016 October 21 with an archival $F160W$ NICMOS image from 1998 March 16 showed a clear point-like residual at R.A. = $3^{\mathrm{h}}19^{\mathrm{m}}48.87^{\mathrm{s}}$ and Decl. = $+41°30'46.89''$ in the NICMOS image, 5.0″ North and 7.8″ East of the nucleus (3.3 kpc projected distance). We did not obtain an epoch in H-band to verify this discovery, because an archival $F160W$ image from the HST/WFC3 IR imager observed on 2015 February 22 was available to act as a reference image. While the $F160W$ filters from NICMOS and WFC3 are not identical, they are sufficiently similar to verify the source as a transient, see Fig. 3.6.

The two NICMOS transients will be unofficially designated as AT 1998xx and AT 2008xx throughout this thesis.

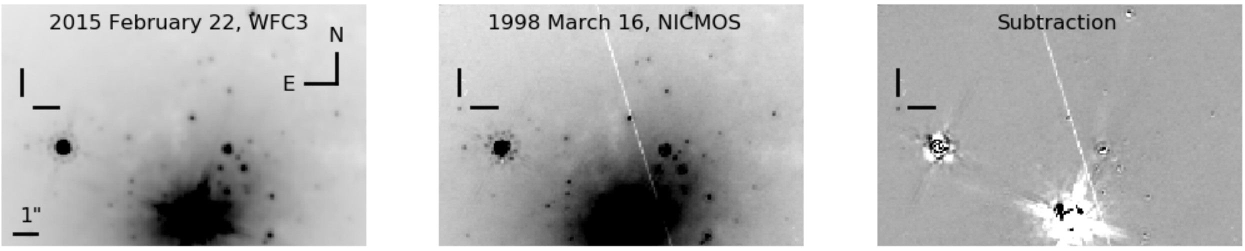

Figure 3.6: A transient in NGC 1275 observed with NICMOS on 1998 March 16, see Section 3.6.5. From left to right with linear scaling: HST/WFC3 subtraction reference image (February 2015), discovery NICMOS image (March 1998), and the subtraction. The residuals visible in the subtracted image are due to a bright nucleus in NGC 1275 and artefacts (stripe and hot pixels) in the NICMOS image. Image is cropped to exclude un-subtracted regions not covered by NICMOS.

3.7 Analysis

3.7.1 AT 2016jhy

At a distance of 160 Mpc the apparent discovery magnitude of AT 2016jhy corresponds to an absolute magnitude M_{K_s} = -17.94 ± 0.06, adopting a Galactic line-of-sight extinction of A_{K} = 0.021 (Schlafly and Finkbeiner, 2011). This is is well within the range of all the SN templates we use to fit light curves with, see for example the light curve fits of SN 2015cb in Section 2.8.3. However, the follow up observations showed no decline in brightness of AT 2016jhy, in fact after 419 days the transient appears to have gotten incrementally brighter (M_{K_s} = -18.16 ± 0.05), see Table 3.5. The only SN template that fits such an evolution is the Type IIn template. Because AT 2016jhy was only observed in K_s-band and has a flat evolution, its light curve has not been fitted to the IIn template because it would not constrain any of the fitting parameters. The comparison with the SN on which the IIn template is based is easily made however: SN 1998S was discovered in NGC 3877 with an absolute magnitude M_K = -19.3 ± 0.2 and after 88 days declined to M_K = -18.0 ± 0.2. Afterwards the SN did not change significantly in magnitude until the end of the documented monitoring, with M_K = -17.5±0.3 354 days later (Mattila and Meikle, 2001). In terms of K_s-band light curve evolution and absolute magnitude AT 2016jhy behaves in a very similar way. Long term monitoring of the near-IR light curve would be required to confirm or refute a SN Type IIn scenario for AT 2016jhy. As Type IIn SNe are among the most luminous SNe at radio wavelengths after ~1000 days (Romero-Cañizales et al., 2014), radio follow up could provide additional constraints on the nature of AT 2016jhy.

The location of AT 2016jhy superimposed on the Southern nucleus of its host galaxy suggests an alternative scenario, where the additional flux is related to a supermassive black hole (SMBH)

UT Date	Telescope/Instrument	Filter	Magnitude
AT 2016jhy (IRAS F06076-2139)			
2010 October 15.3	VLT/NACO	K_s	-
2016 October 19.6	Keck/NIRC2	K_s	18.10±0.06
2017 March 12	Gemini South/F2	K_s	18.07±0.09
2017 December 12.5	Keck/NIRC2	K_s	17.88±0.05
AT 2017chi (NGC 5331)			
2017 March 13.3	Gemini South/F2	K_s	18.00±0.11
2017 March 27.2	Gemini South/F2	H	19.27±0.08
2017 March 27.3	Gemini South/F2	J	21.10±0.15
2017 April 6.4	Keck/NIRC2	K_s	18.58±0.06
2017 April 6.5	Keck/NIRC2	H	19.30±0.15
2017 April 6.5	Keck/NIRC2	J	21.55±0.23
2017 July 8.3	Keck/NIRC2	K_s	19.14±0.13
2017 July 8.3	Keck/NIRC2	H	>20.5
2018 May 12	Gemini South/F2	H	>21.0
AT 2017jzy (NGC 695)			
2017 December 5.3	Keck/NIRC2	K_s	-
2017 December 5.3	Keck/NIRC2	H	18.4±0.2
2017 December 5.4	Keck/NIRC2	J	-
AT 2008xx (NGC 695)			
2008 August 29.3	HST/NICMOS	H	19.5±0.2
AT 1998xx (NGC 1275)			
1998 March 16.8	HST/NICMOS	H	19.9±0.2

Table 3.5: NIRC2 supernova candidates near-IR photometry

or active galactic nucleus (AGN) such as an event thought to be the explanation for AT 2017gbl. According to an optical IFU study with VIMOS (Arribas et al., 2008) the Southern nucleus has [NII]/Hα line ratios characteristic for HII-like excitation, in contrast with the AGN-like [NII]/Hα line ratios of the Northern nucleus. Lacking any clear spectroscopic evidence for an AGN and the long time scale of the transient means AGN related activity is a less plausible explanation.

3.7.2 AT 2017chi

AT 2017chi was best fitted with the IIn template, see Fig. 3.7 and Table 3.6. The main constraint on the fitted subtypes is provided by the 2017 July K_s epoch. In order to accommodate this detection,

AT 2017chi (NGC 5331)				
Template	A_V	t_0	C	$\tilde{\chi}^2$
IIP, plateau	$11.2^{+1.1}_{-1.4}$	6^{+1}_{-3}	$-1.2^{+0.3}_{-0.2}$	15.7
IIP, tail	$14.6^{+0.9}_{-1.7}$	157^{+47}_{-12}	$-3.6^{+0.3}_{-0.8}$	17.0
IIn	$11.8^{+1.8}_{-1.2}$	64^{+3}_{-11}	$-0.42^{+0.23}_{-0.18}$	9.4
IIb/Ib/Ic	$12.9^{+0.9}_{-1.6}$	81^{+7}_{-1}	$-3.2^{+0.3}_{-0.2}$	18.5

Table 3.6: Results from fitting light curve templates to AT 2017chi, with line-of-sight extinction A_V, time t_0 between explosion date and discovery, and a fixed constant C representing the intrinsic magnitude difference between SNe. The final column shows the resulting $\tilde{\chi}^2$ for each fit.

the Type IIb/Ib/Ic and IIP tail templates are fitted with large constant shifts C implying unusually luminous SNe for the types. This is less so the case for the Type IIP plateau template fit, but here the early epochs are poorly fitted, and it does not fit with the H-band limit from the 2017 July 8 epoch. All three template fits also have large $\tilde{\chi}^2$ of 16-18. The Type IIn template fits the photometry much better with a $\tilde{\chi}^2$ = 9.4, and only has a minor constant shift C, meaning it is similar in absolute magnitude to the prototypical IIn SN used for this template, SN 1998S.

As discussed in Section 3.7.1 SN 1998S had a long extended flat tail in K-band and a slightly declining long tail in H-band. AT 2017chi had faded from view in H and J at the time the transient-free reference imaging was obtained with F2, on 2018 May 12. This is 425 days after discovery, and assuming a time since explosion of 64 days as fitted for Type IIn, the F2 observations occurred 489 days since explosion. In H-band SN 1998S had declined ~3.5 magnitudes after 450 days (Mattila and Meikle, 2001). A similar decline would put AT 2017chi well below the detection limit in H-band at the time of the F2 observations, so this does not provide constraints on AT 2017chi as a Type IIn.

Finally, the Type IIn fit of AT 2017chi includes a large extinction A_V of 11.8 magnitudes, which makes it the most extincted SN in a LIRG except for SN 2008cs (Kankare et al., 2008). This explains well why the optical spectrum obtained with the NTT did not show any SN features. It is worth noting that although AT 2017chi is clearly fitted best as a Type IIn, the other three template fits include similar extinction values. Similarly to Type IIn (candidate) AT 2016jhy, follow up observations in radio could further confirm AT 2017chi as a Type IIn.

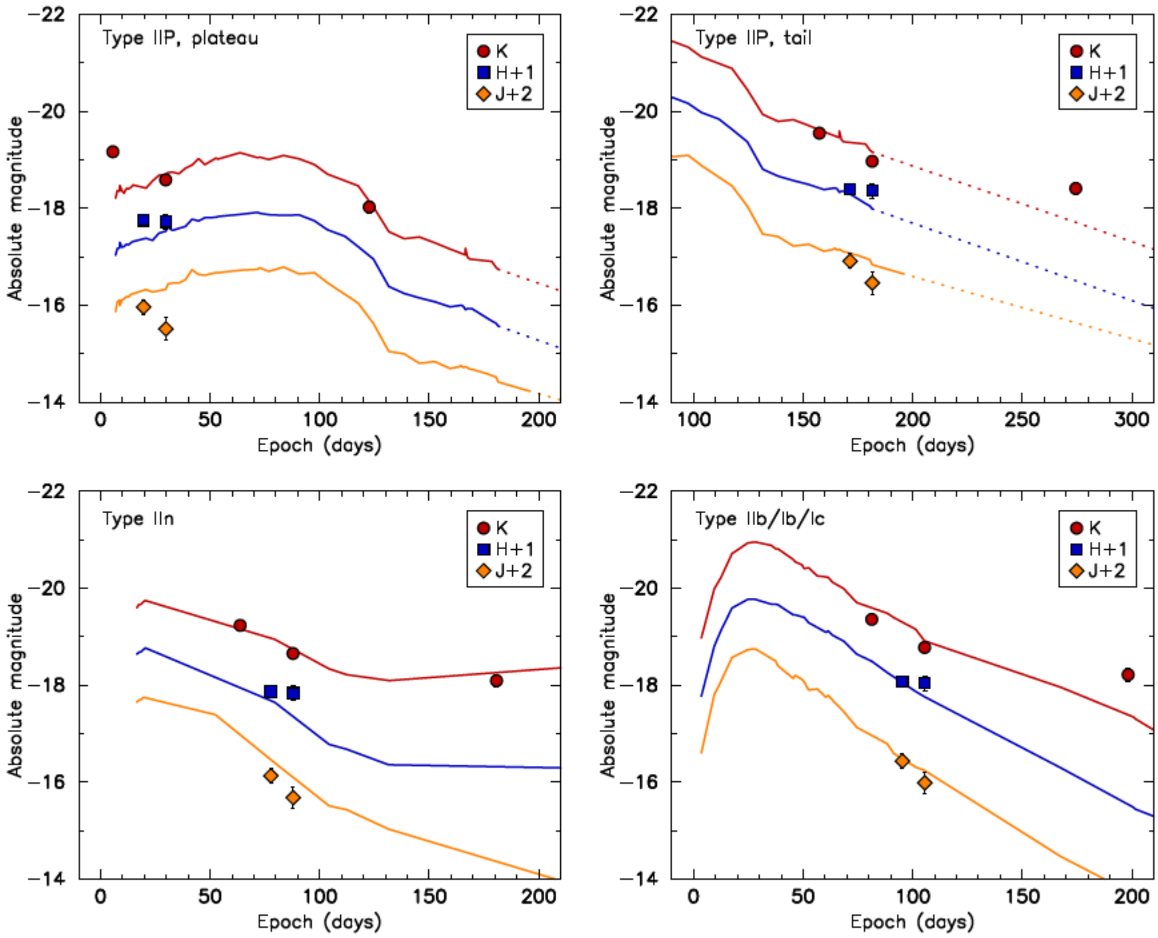

Figure 3.7: Template light curve fits for AT 2017chi in NGC 5331 are shown: Type IIP fitted in the plateau ($\tilde{\chi}^2$ = 15.7) and tail phase ($\tilde{\chi}^2$ = 17.0), Type IIn ($\tilde{\chi}^2$ = 9.4), and Type IIb/Ib/Ic ($\tilde{\chi}^2$ = 18.5). The Type IIn template provided the best fit, and required only a minor constant shift C, as opposed to the other templates, see Section 3.7.2.

3.7.3 AT 2017gbl

Photometry

Fig. 3.8 shows the light curve evolution of AT 2017gbl in the near-IR, mid-IR and the optical in apparent magnitudes, corrected for Galactic line-of-sight extinction (Schlafly and Finkbeiner, 2011). Assuming a host galaxy luminosity distance of 146 Mpc the discovery K-band magnitude corresponds to an absolute magnitude of M_{K} = -22.7. The peak absolute magnitude of the transient decreases towards shorter wavelengths, with M_{H} = -21.5, M_{J} = -20.0 in the near-IR and $M_{\mathrm{z'}}$ = -17.8, $M_{\mathrm{i'}}$ = -17.2 and $M_{\mathrm{r'}}$ = -16.5 in the optical.

The observed peak magnitudes are much brighter than any of the CCSNe subtypes we so far have fitted light curves for, which hints at a potentially different origin for AT 2017gbl. The detection of AT 2017gbl across nine bands allows us to constrain the energetics of the event, and thus its

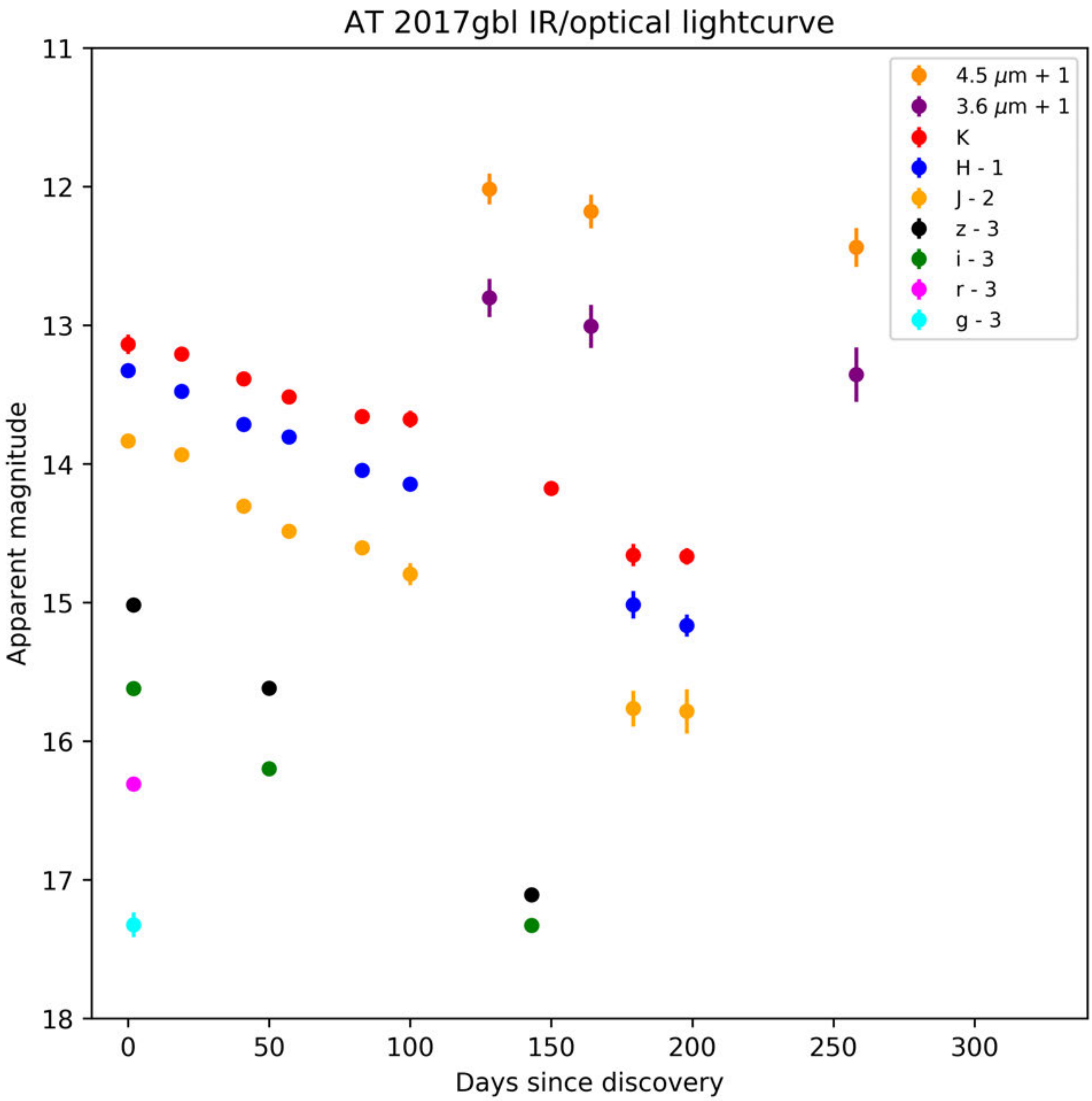

Figure 3.8: IR and optical evolution of AT 2017gbl in apparent magnitudes. For clarity mid-IR observations at 4.5 and 3.6μm are offset downwards with 1 magnitude, and H, J and i' are offset upwards with 1, 2 and 3 magnitudes, respectively. Discovery epoch and K_s-band epoch at Julian Day 24571092 were obtained with NIRC2 on Keck, the mid-IR epochs with Spitzer, and the other epochs with NOTCam or ALFOSC on the NOT.

nature, by fitting its SED, assuming it emits as a blackbody. When we plot the SED of AT 2017gbl using the near-IR and mid-IR fluxes at the epochs of the Spitzer observations, we note that they can be well described by a blackbody, see Fig. 3.9. The JHK_s measurements from NOTCam and NIRC2 were fitted with a linear function to obtain the interpolated values at the time of the Spitzer epochs. The third Spitzer measurement occurred after the final NOTCam epoch, so it was assumed

Table 3.7: SED blackbody parameters

UT Date	Component	Radius	Temperature	Luminosity
		(10^{-2} pc)	(K)	(10^{43}erg/s)
20171113	Infrared	4.6 ± 0.4	1030 ± 30	1.7 ± 0.4
20171219	Infrared	5.0 ± 0.6	950 ± 40	1.4 ± 0.4
20180323	Infrared	5.0 ± 0.7	890 ± 50	1.1 ± 0.4

the linear trend continued in JHK_s and an extrapolated value was used for the third blackbody fit. The EMCEE python implementation (using a script kindly provided by M. Fraser from University College Dublin, Ireland) of the Markov chain Monte Carlo method (Foreman-Mackey et al., 2013) was used to estimate the best blackbody fit parameters, with a 1σ confidence interval, see Fig. 3.10 for an example and Table 3.7 for the resulting blackbody temperatures in Kelvin and radii in pc. The optical flux of AT 2017gbl was so small at time of the first mid-IR epoch it did not provide any meaningful constraints to the blackbody fit and was not included.

With the SED well fitted by a blackbody, and given the relative fluxes in the near-IR and the optical, we assume most of the UV and optical light originating from the transient event was absorbed by surrounding dust, and what is observed in IR is the thermal re-emission from the dust. The radius associated with the blackbody fit then represents the size of the emitting region at the fitted temperature. This means over the epochs the radius has increased from 0.042 pc to 0.049 pc and the temperature has decreased from 1026 K to 845 K. Using these parameters we can calculate the luminosity in erg/s at the Spitzer epochs with the Stefan-Boltzmann law:

$$L = 4\pi R^2 \sigma T^4 \tag{3.1}$$

where R is the radius of the blackbody in cm, T its temperature in Kelvin and σ the Stefan-Boltzmann constant (5.670×10^{-5} erg cm^{-2} s^{-1} K^{-4}). The total radiated energy of AT 2017gbl in the IR was then estimated by integrating the luminosity over the time between the discovery epoch in near-IR and the final Spitzer epoch, assuming a linear decline between epochs. Over the course of 258 days the energy radiated in IR from AT 2017gbl totalled $1.9\pm0.4 \times 10^{50}$ erg. This is a lower limit, since the transient was discovered after (or at) peak and the prior evolution and rise time is not included. Additionally, because we lack any observations at longer wavelengths, it is not possible to exclude a second cooler component, the luminosity of which will not be included in this single blackbody component fit.

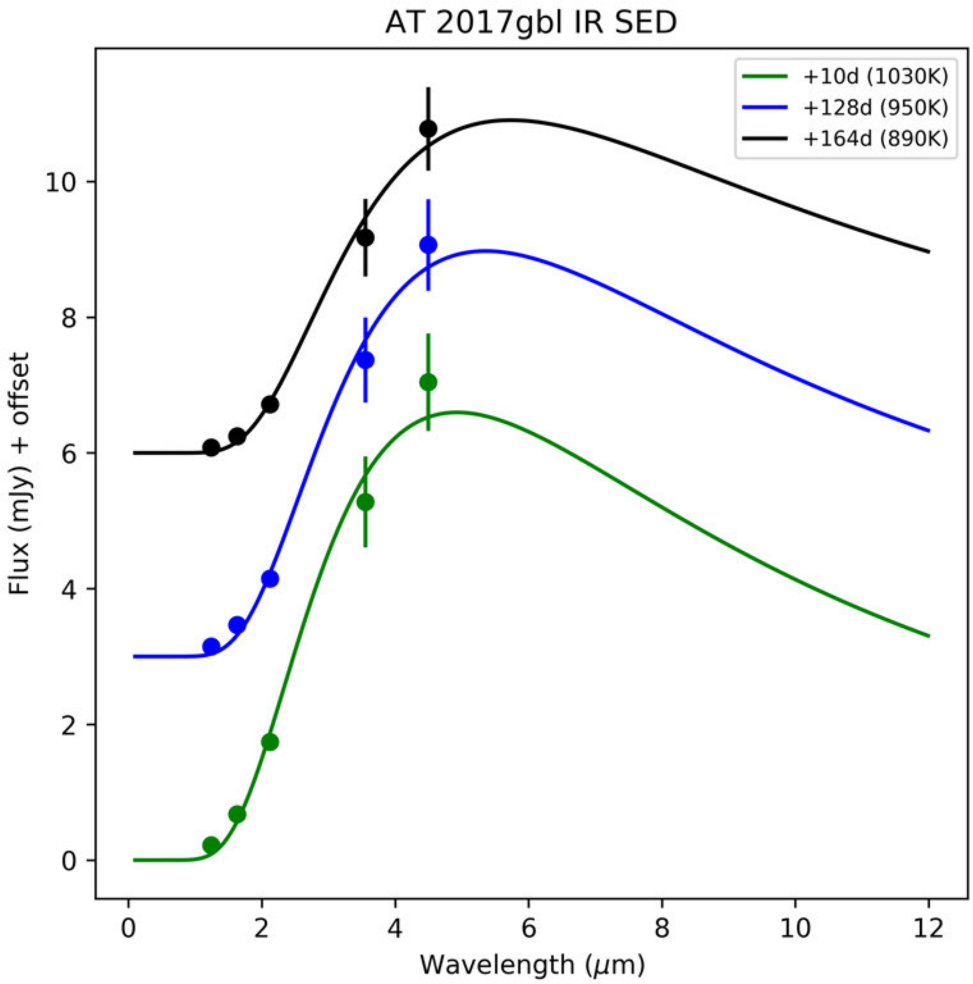

Figure 3.9: Blackbody fits of the mid-IR and interpolated near-IR fluxes at three Spitzer epochs, see Section 3.7.3. Epoch 2017 November 13 in green, 2017 December 19 in blue and offset by +3 mJy, and 2018 March 23 in black and offset by +6 mJy.

Spectroscopy

The optical ISIS spectrum obtained 53 days after discovery was dominated by narrow emission lines commonly associated with LIRGs, such as Hα, [NII] and [SII]. The near-IR GNIRS spectrum observed two days later, on 2017 September 1, showed a similar picture with strong emission lines consistent with LIRGs such as Paschen and Brackett recombination lines, He I, H_2 and [Fe II] (Burston et al., 2001, Valdés et al., 2005), see Fig. 3.11. From the two spectra obtained so far, the near-IR spectrum is most likely to contain features associated with the transient, as at the time of the observations the transient was already faint in the optical ($m_{i'} \sim 19.6$) but still very bright in the near-IR ($m_K \sim 13.6$). However, there is no apparent origin of the transient's extreme near-IR brightness in terms of emission lines. In order to pinpoint any continuum increase or spectral features related to AT 2017gbl, a second epoch is required as a reference in both the optical and

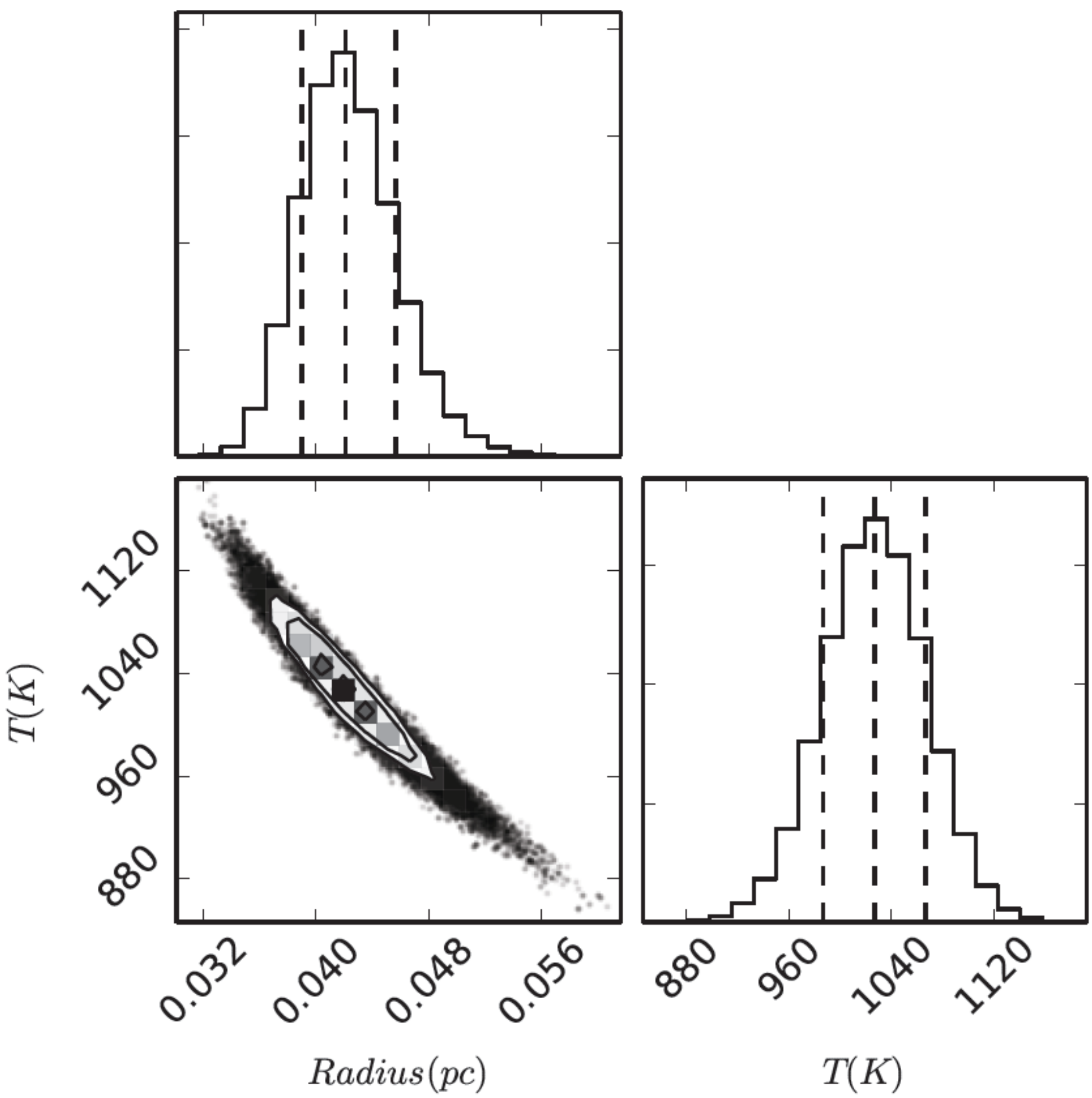

Figure 3.10: Fitted temperature and radius parameters for epoch 2017 November 13, by the MCMC method using the EMCEE python package. The top and bottom right panels show the fitted parameters, radius and temperature respectively, with the fitted values indicated by the centre lines, and the 1σ confidence interval indicated on either side. The bottom left panel shows the fitting results in radius-temperature parameter space.

the near-IR after the transient has faded from view.

Radio

At 15.5 GHz the AMI observations did not show an evolution significant within 3σ, with measurements of 6.0 ± 0.3 mJy, 6.7 ± 0.3 mJy and 6.7 ± 0.3 mJy for the three epochs in 2017 July

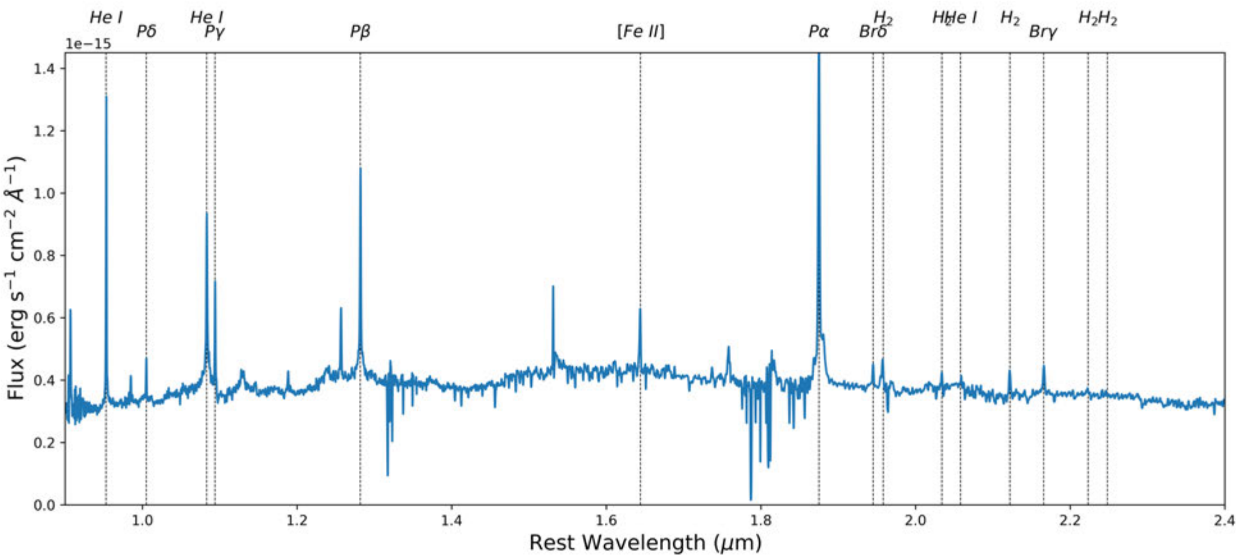

Figure 3.11: Near-IR spectrum of the Northern nucleus of IRAS 23436+5257 from 2017 September 1 in rest wavelength. Some emission and absorption features commonly associated with LIRGs are indicated. The spectrum does not show a clear origin for the extreme IR brightness of AT 2017gbl. A follow-up spectrum obtained after the transient has faded significantly will be required to identify this origin, and to relate any spectral features to the transient. If AT 2017gbl is the result of a dust echo of an energetic nuclear transient, which is well represented by a blackbody, we would only expect the continuum to decrease.

and August, and 5.4 ± 0.3 mJy on 2018 February 27. The VLBA observations from 2017 August 15 at 4.4 GHz and 7.6 GHz showed one unresolved source within the 1″ by 1″ FOV at R.A. = $23^{h}46^{m}05.517275^{s}$ and Decl. = +53°14′01.26050″. This is 0.04″ from the near-IR position, well within the astrometric error margin. The source had peak flux densities of 0.93 ± 0.05 mJy and 1.81 ± 0.05 mJy at 4.4 and 7.6 GHz, respectively. This implies an inverted spectral index (α = 1.22) and a luminosity at 7.6 GHz of 4.2×10^{28} erg s^{-1} Hz^{-1}. Given the co-location with the near-IR transient and the compactness, radio emission level and inverted spectrum we assume we are observing either a low-luminosity AGN and/or the transient itself. The second VLBA epoch showed a significant increase in flux at 4.4 GHz and 7.6 GHz to 2.03 ± 0.04 and 2.70 ± 0.04 mJy, respectively. Not only had the flux density increased, the spectral index also changed significantly (α = 0.52). This implies the transient is responsible or contributing significantly to the flux of the radio source, and the changing spectral index indicates an evolution of the source from optically thick (positive α) to optically thin synchrotron emission (negative α) (Mattila et al., 2018). Further observations are required to monitor the evolution of the source.

Interpretation

As a LIRG the expected CCSN rate of IRAS 23436+5257 based on its IR luminosity is high at 1.0 yr^{-1}, but it is quite clear AT 2017gbl is not a normal CCSN. The observed peak magnitude excludes any of the CCSNe subtypes we so far have fitted light curves for. The radiated energy output of $>1.9\times10^{50}$ erg in the near-IR is further confirmation, as the total bolometric radiated energy output of a normal Type II CCSN is typically less then 10^{49} erg (Utrobin, 2007). However, there have been observations of extremely bright SNe, so-called superluminous SNe (SLSN). SNe are defined as SLSNe if they reach M_V < -21, and range up to M_V = -22.5 (Gal-Yam, 2012). The brightest SLSNe have been measured to emit 1-2×10^{51} erg of energy (Drake et al., 2010, Smith et al., 2007), which means a SLSN scenario is a possibility based on the measured total radiated energy of AT 2017gbl.

Given the position coincident with the nucleus of its host galaxy, another plausible scenario is where the transient event is related to the accretion of a central SMBH. The transient could be linked to the intrinsic variability of an AGN, or be the result of a tidal disruption event (TDE), where a star passes within the tidal radius of a SMBH and gets torn apart (Rees, 1988). Typical AGN variability is stochastic in nature and varies by only a few tenths of a magnitude (MacLeod et al., 2012), which does not fit with the observed smooth light curve evolution and intense brightening of AT 2017gbl, but there have been observations of major flares in AGN that could match the observed energy output (Graham et al., 2017). TDE's can also be sufficiently bright (Leloudas et al., 2016) and interestingly, there is evidence of an increased TDE rate in LIRGs compared to the general galaxy population (Tadhunter et al., 2017). An AGN flare or a TDE require the presence of a central SMBH, but so far there has not been any evidence of an AGN in IRAS 23436+5257, based on its PAH 3.3 μm emission feature (Yamada et al., 2013) or in hard X-ray (Koss et al., 2013). However, the log([NII]/Hα) line flux ratio was estimated from the ISIS spectrum to be -0.07 ± 0.01, which places the nucleus of IRAS 23436+5257 for any value of the [OIII]/Hβ line ratio in a region on the BPT diagram where ionization due to a combination of SF and AGN is expected (Kewley et al., 2001). We have so far been unable to estimate the [OIII]/Hβ line ratio because with redshift these lines fall >5100Å where the sensitivity in the blue arm of ISIS drops off sharply and subsequently the spectrum is poorly flux calibrated.

Almost all of these scenarios are based on transients discovered and monitored at optical wavelengths, which makes a direct photometric comparison difficult because AT 2017gbl appears significantly dust-obscured and as a result is relatively faint in the optical. There are some exceptions, most notably Arp299B-AT1 (henceforth referred to as AT1), an extremely bright transient discovered in 2005 in the B-nucleus of interacting LIRG Arp 299 (Mattila et al., 2018). AT1 was discovered in the near-IR as part of a search for dust-obscured CCSNe in starburst galaxies, a precursor to project SUNBIRD. Similarly to AT 2017gbl it was extremely bright in the near-IR, but hardly visible at optical wavelengths. Over the next decade an expanding resolved radio jet was observed coincident with the position of AT1, and the transient was interpreted to have arisen from a TDE. Another nuclear near-IR bright transient was PS1-10adi, discovered in the centre of SDSS J204244.74+153032.1 (Kankare et al., 2017b). PS1-10adi evolved over ~1000 days and was bright in both optical and near-IR, reaching a peak in H-band of M_{H} of -25. The brightness is thought to have resulted from shock interaction between expanding material and surrounding dense matter, and the energy budget was explained by either a SLSN or TDE variant.

The photometric properties and energetics in the IR of AT 2017gbl are strikingly similar to those of AT1. The maximum magnitudes in the near-IR of AT 2017gbl in JHK_s of 16.03, 14.45 and 13.22 correspond to a flux in mJy of 0.62, 1.70 and 3.44, respectively. At a distance of 45 Mpc for AT1, this would correspond to fluxes of 6.53, 17.89 and 36.21 mJy in JHK_s, although these cannot be considered peak magnitudes, as AT 2017gbl was discovered after peak. By comparison, the flux in near-IR of AT1 peaked at 4.20, 13.70 and 46.04 in JHK_s, respectively. Both peak fluxes and the near-IR relative colours are similar, although AT1 has been redder than AT 2017gbl throughout its evolution, implying it was affected by heavier dust extinction. Although not as extreme as for AT1, the colours of AT 2017gbl have been growing redder over time. The IR photometry fluxes of AT 2017gbl are fitted well with a linear decline, and the transient has been declining more rapidly at shorter wavelengths, with decline rates of 1.0, 0.9, 0.8, 0.4 and 0.3 mags/100 days in J, H, K_s, 3.6μm and 4.5μm, respectively. The optical photometry also agrees well with a significant difference in dust extinction between the two transients; whereas AT 2017gbl has a faint but clear detection in the i'-band, AT1 was not observed in the optical. In terms of blackbody fit parameters the two transients are again very similar. So far AT 2017gbl has declined in temperature from 1026 K to 845 K, with a blackbody radius increasing from 0.042 pc to 0.049 pc. At its first mid-IR epoch AT1 had a fitted temperature of 1045 K with a 0.0423 pc radius, which over the following 200 days evolved to a temperature of 983 K with a 0.0596 pc radius.

The main difference between the two transients is the time-scale, and as a result the energetics in the IR. AT 2017gbl was discovered after peak in both near-IR and mid-IR, and a non-detection on 2016 October 21, 260 days earlier, constrains the start of the event. AT1 evolved much slower, taking ~1700 days to reach peak in near-IR, and ~2200 days in mid-IR. A decline in flux in IR as steep as for AT 2017gbl was never observed for AT1. As a result the energy radiated in IR during the evolution of AT1 was much higher, > 1.5×10^{52} erg. Due to the lack of any counterpart in the optical, it was assumed 100% of the light from the TDE was absorbed by a dusty torus and polar dust clouds and re-emitted in the IR. This appears not to be the case for AT 2017gbl given the detections in optical, suggesting a less dense medium of polar dust, which would also explain the relatively fast evolution of AT 2017gbl. If we assume the density and geometry of the dust is the main cause of the difference in IR between these two transients, the underlying object could very well be the same, a TDE. The difference in energetics could be due to energy radiated in shorter wavelengths for AT 2017gbl, which is supported by the optical detections. Unfortunately we do not have a reliable i'-band detection past 2017 August 27, so it is not possible to check for optical excess in the blackbody SEDs with a first epoch on 2017 November 13. Also AT 2017gbl appears to have been discovered after peak, and the energy radiated prior to discovery is difficult to constrain.

Given the similarities with AT1 a TDE scenario looks promising for AT 207gbl, but based on the current data it is not possible yet to distinguish the different scenarios. The interpretation of AT1 as a TDE was to a large extent based on its morphological evolution at radio wavelengths. With two VLBA epochs with detections of an unresolved source, it is not possible yet to deduce a similar behaviour in radio for AT 2017gbl. However the observed increase in flux density looks promising, and continued monitoring of the transient with the VLBA and possibly at higher angular resolution with EVN should shed more light on the nature of AT 2017gbl.

3.7.4 AT 2017jzy

AT 2017jzy was discovered by subtracting an archival HST/NICMOS $F160W$ image from the H-band NIRC2 discovery image. Colour transformations from $F160W$ to H-band have been determined in literature, but they also require $F110W$ observations (Brandner et al., 2001), which are not available for NGC 695. Because the transformation is minimal ($m_{160} - H = (0.072 \pm 0.041)(m_{110} - m_{160}) + (0.032 \pm 0.045)$) it is assumed here the two images share the same photometric system, and the potential error introduced this way will be reflected in the final magnitude error. Additionally, because of the limited FOV of NICMOS and NIRC2, no 2MASS catalogue stars were available for photometric calibration. The zero point of the image was determined based on three isolated compact objects in the NICMOS FOV, whose magnitudes were calculated using the conversion from the NICMOS Data Handbook[7]:

$$m = \mathrm{ZP(Vega)} - 2.5\log(\mathrm{PHOTFNU} \times \mathrm{CR} \times \langle \mathrm{F}_{\nu(\mathrm{Vega})} \rangle^{-1}) \tag{3.2}$$

[7]http://documents.stsci.edu/hst/nicmos/documents/handbooks/DataHandbookv6/nic_ch54.html

where ZP(Vega) = 0.0 is the zero point of Vega, CR the calibrated count rate in the image from a 6.5 pixel aperture multiplied by a 1.1877 aperture correction in units of DN sec^{-1}, PHOTFNU = 1.4923012×10^{-6} Jy sec DN^{-1} the bandpass-averaged flux density per the fits header, and $\langle F_{\nu(\mathrm{Vega})} \rangle$ = 1040.7 Jy the flux of Vega in the $F160W$ filter. PSF fitting to the SN residual in the subtracted image using the zero point obtained in this way resulted in a magnitude in H of 18.4 ± 0.2, which at a distance of 136 Mpc corresponds to an absolute magnitude $M_H = -17.3 \pm 0.2$. The same method was applied to determine the magnitude of the transient in the NICMOS reference image mentioned in Section 3.6.5, see Table 3.5. The SN magnitudes in J and K_s were poorly constrained due to a lack of adequate reference imaging. The poorly constrained photometry and the lack of additional epochs prevented us from fitting SN light curve templates, and confirming AT 2017jzy as a bona fide SN.

3.8 Summary

In this chapter we have presented the results from the Keck program of project SUNBIRD, which includes one photometrically confirmed CCSN and four CCSN candidates, as well as a TDE candidate. Based on its photometry AT 2017chi in NGC 5331 was determined to be a Type IIn SN, with a fitted extinction of 11.8 magnitudes in V-band. This makes AT 2017chi the second or third most extincted SN ever discovered, after SN 2008cs (17-19 mag Kankare et al., 2008) and SN 2004ip (5-40 mag Mattila et al., 2007). Given the extended and luminous evolution in radio of Type IIn SNe, follow up at radio wavelengths can assist confirming both AT 2017chi and Type IIn SN candidate AT 2016jhy in IRAS F06076-2139.

AT 2017gbl superimposed on the nucleus of IRAS 23436+5257 is the first transient discovery in project SUNBIRD that does not fit with a CCSN scenario. We show that the radiated energy output at IR wavelengths of this extremely near-IR bright transient already exceeds that of Type II SNe, and can only be explained by either a superluminous SN, an uncommonly bright AGN flare, or a tidal disruption event. The characteristics of the transient are very similar to those of a TDE discovered in the near-IR in LIRG Arp 299, and the differences in evolution time-scale could be explained by differences in dust morphology. As the transient appears to be increasing in flux at radio wavelengths, further radio monitoring could confirm this as the third TDE ever to have been discovered in a LIRG (Mattila et al., 2018, Tadhunter et al., 2017).

4

Core-collapse supernovae in Luminous Infrared Galaxies

4.1 Introduction

In this chapter we analyse the sample of CCSNe (and CCSN candidates) discovered in project SUNBIRD using AO-imagers GeMS/GSAOI on Gemini South and NIRC2 on Keck. The sample is compared against all other documented optical and IR CCSN discoveries in LIRGs to evaluate the efficiency of detecting SNe by observing in the near-IR using AO - the method used in project SUNBIRD. Such a comparison was presented in Kool et al. (2018), which we update here to include the new discoveries from Keck presented in Chapter 3. Additionally the subtypes of the total sample of LIRG CCSNe are compared against known CCSN subtype distributions from the literature.

4.2 The CCSN sample

4.2.1 Optical discoveries

The sample of CCSNe in LIRGs that is treated in this chapter is composed of all documented (up to May 2018) discoveries in the optical and the IR, including the discoveries from project SUNBIRD. The optical sample is a result from cross referencing all galaxies in the IRAS RBGS with $L_{IR} > 10^{11} L_{\odot}$ (corrected to H_0 = 70 km s^{-1}) with the most up to date SN catalogues available: Open Supernova Catalog[1] (Guillochon et al., 2017); Asiago Supernova Catalog[2] (Barbon et al., 1999); Transient Name Server[3] and ASAS-SN[4] (Shappee et al., 2014). Type Ia SNe were excluded, as well as SNe without a documented subtype. Table 4.1 shows the resulting sample of 40 optical CCSN discoveries, including LIRG host, R.A. and Dec., subtype, projected distance to the nucleus in kpc and the documented discoverer. If the discovery circular and/or publication of the SN did not include an offset from the nucleus, the projected distance was determined using the provided coordinates and those of the nucleus as seen in SDSS, in which case the error in determining the offset was assumed to be 1″ to reflect the uncertainty of the absolute astrometric positions of the SN and host nucleus. In all other cases nuclear offsets in this chapter are given with 0.1″ precision, even for AO discoveries, for the same reasons.

4.2.2 Infrared discoveries

The IR sample consists of spectroscopically or photometrically confirmed CCSNe, as well as CCSN candidates. The sample is subdivided between discoveries made in natural seeing conditions (non-AO) and discoveries assisted by AO. The non-AO SNe are listed in Table 4.2, and the AO SNe in Table 4.3. All CCSN discoveries in the near-IR in LIRGs have been the result of SN searches targeting starburst galaxies and/or LIRGs, including project SUNBIRD. As the division between AO and non-AO is primarily one of spatial resolution, the space-based SPIRITS CCSN discoveries with Spitzer/IRAC (1.5″ diffraction limit) have been included in the non-AO sample, and those discovered with HST/NICMOS (~0.17″ diffraction limit in $F160W$ filter) are included in the AO sample. The table also includes dust extinction in A_V, determined through light curve fitting for the AO discoveries, or as reported in the literature for the non-AO discoveries. The transients in the table typed as candidates lack both spectroscopic confirmation and sufficient photometric epochs

[1] https://sne.space/
[2] https://heasarc.gsfc.nasa.gov/W3Browse/all/asiagosn.html
[3] https://wis-tns.weizmann.ac.il/
[4] http://www.astronomy.ohio-state.edu/~assassin/index.shtml

for CCSN template light curve fitting. Based on their absolute magnitudes, point-source PSF and discovery in a LIRG, they are considered most likely to be CCSNe as discussed for example in the case of AT 2015cf (Section 2.8.4). However as other scenarios cannot be ruled out they are treated as candidates throughout the analysis in this chapter. Note that AT 2017gbl from the Keck program has not been included here, as its characteristics do not fit any CCSN scenario.

4.2.3 Additional unpublished IR discoveries from VLT/NACO

In addition to the SUNBIRD CCSN discoveries and the LIRG CCSNe reported in the literature, three CCSN candidates discovered with VLT/NACO have been included in the IR sample. These discoveries were the result of an extended observing program on the VLT with NACO (PI: S. Mattila) to uncover CCSNe in LIRGs, but have not been published before. This is the program that also led to the discovery of SN 2004ip (Mattila et al., 2007). The data were reduced by Tom Reynolds and Seppo Mattila of Tuorla Observatory, and kindly shared with the author. Similarly to the NICMOS transients from Chapter 3, in this thesis the NACO SN candidates will have the unofficial designations of AT 2012xx (in IRAS 18293-3413), AT 2012xy (in ESO 440-IG058) and AT 2012xz (in IRAS 17578-0400). In this section the NACO discoveries have had their photometry updated and are briefly described and analysed so that they can be included in the IR sample, whereas a more thorough analysis will be presented in Reynolds et al. (in prep).

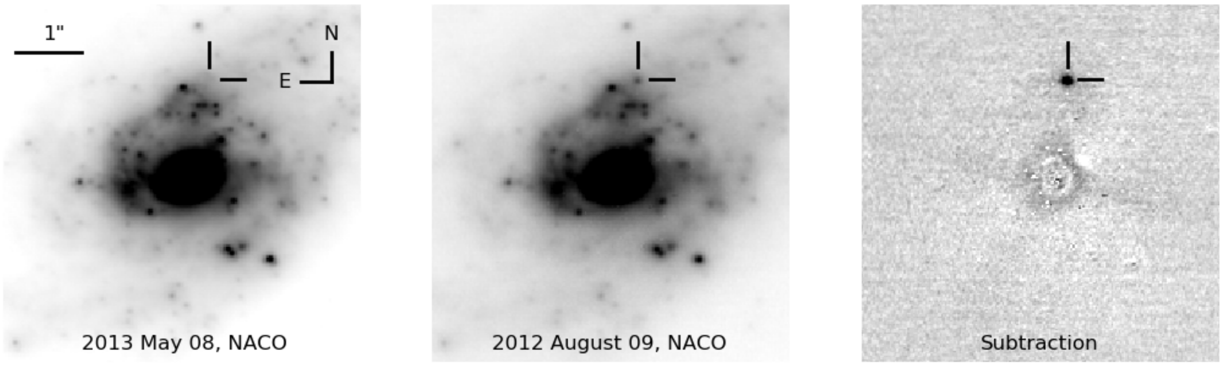

Figure 4.1: AT 2012xx in IRAS 18293-3413 in K_s-band, see Section 4.2.3. From left to right with linear scaling: Reference VLT/NACO image (May 2013), discovery VLT/NACO image (August 2012) and the image subtraction.

Name	LIRG host	R.A. (J2000)	Dec. (J2000)	Type	D_{proj} (kpc)	Discovered by
SN1983V	NGC 1365	03:33:31.63	-36:08:55.0	Ic	7	Evans et al.
SN1993G	NGC 3690	11:28:33.43	+58:33:31.0	IIL	3.7	Treffers et al.
SN1996D	NGC 1614	04:34:00.30	-08:34:44.0	Ic	2.1	Drissen et al.
SN1998T	NGC 3690	11:28:33.14	+58:33:44.0	Ib	1.5	BAOSS
SN1999bx	NGC 6745	19:01:41.44	+40:44:52.3	II	5	LOSS
SN1999D	NGC 3690	11:28:28.38	+58:33:39.0	II	6	BAOSS
SN1999ec	IC 2163/NGC 2207	06:16:16.16	-21:22:09.8	Ib	14	LOSS
SN1999ex	IC 5179	22:16:07.27	-36:50:53.7	Ib	6	Martin et al.
SN1999gl	NGC 317B	00:57:40.07	+43:47:35.6	II	2	Boles
SN2000bg	NGC 6240	16:52:58.18	+02:23:51.5	IIn	9	LOSS
SN2000cr	NGC 5395	13:58:38.37	+37:26:12.4	Ic	10	Migliardi/Dimai
SN2001du	NGC 1365	03:33:29.11	-36:08:32.5	II	7	Evans
SN2001eq	PGC 70417	23:04:56.78	+19:33:04.8	Ic	6	LOTOSS
SN2001is	NGC 1961	05:42:09.07	+69:21:54.8	Ib	14	BAOSS
SN2003H	IC 2163/NGC 2207	06:16:25.68	-21:22:23.8	Ib Pec	6	LOTOSS
SN2003hg	NGC 7771	23:51:24.13	+20:06:38.3	IIP	3.2	LOTOSS
SN2004bf	UGC 8739	13:49:15.45	+35:15:12.5	Ic	8	LOSS
SN2004ed	NGC 6786	19:10:53.62	+73:24:27.6	II	5	Armstrong
SN2004gh	MCG-04-25-06	10:24:31.60	-23:33:18.4	II	2.0	LOSS
SN2005H	NGC 838	02:09:38.52	-10:08:43.6	II	0.4	LOSS
SN2007ch	NGC 6000	15:49:47.82	-29:23:13.7	II	3.6	Monard
SN2008fq	NGC 6907	20:25:06.19	-24:48:27.6	II	1.4	LOSS
SN2009ap	ESO 138-G27	17:26:43.23	-59:55:57.9	Ic	1.2	Pignata et al.
SN2010as	NGC 6000	15:49:49.23	-29:23:09.7	Ib/c	0.6	Maza et al.
SN2010bt	NGC 7130	21:48:20.22	-34:57:16.5	II	6	Monard
SN2010gg	ESO 602-G25	22:31:25.47	-19:01:54.8	II	6	Pignata et al.
SN2010gk	NGC 5433	14:02:35.94	+32:30:30.7	Ic	2.0	LOSS
SN2010jp	IC 2163/NGC 2207	06:16:30.63	-21:24:36.3	II	130	Maza et al.
SN2010O	NGC 3690	11:28:33.86	+58:33:51.6	Ib	1.6	Newton/Puckett
SN2012by	UGC 8335	13:15:28.90	+62:07:47.8	II	10	Rich
SN2013ai	IC 2163/NGC 2207	06:16:18.35	-21:22:32.9	II	9	Conseil
SN2013cc	NGC 1961	05:41:58.76	+69:21:40.9	II	19	Itagaki
SN2013dc	NGC 6240	16:52:58.97	+02:24:25.2	IIP	11	Block
SN2014dj	NGC 317B	00:57:40.18	+43:47:35.1	Ic	1.5	Rich
SN2014eh	NGC 6907	20:25:03.86	-24:49:13.3	Ic	14	LOSS
SN2015ae	NGC 7753	23:47:06.15	+29:29:07.4	II	6	Itagaki
SN2015U	NGC 2388	07:28:53.87	+33:49:10.6	Ibn	1.8	LOSS
PS15aaa	IC 564	09:46:20.73	+03:04:22.1	II	3	Pan-STARRS
SN2017ffm	NGC 7592	23:18:23.02	-04:24:58.27	II	6	Pan-STARRS
SN2018zd	NGC 2146	06:18:03.18	+78:22:00.90	IIn	10	Itagaki

Table 4.1: CCSNe hosted by LIRGs discovered in the optical, from cross referencing the IRAS Revised Bright Galaxy Sample with the Open Supernova Catalog, Asiago Supernova Catalog, the Transient Name Server and the ASAS-SN supernova sample.

Seeing limited near-IR CCSN discoveries in LIRGs							
Name	LIRG host	RA (J2000)	Dec. (J2000)	Type	Reference	Extinction A_V (mag)	D_{proj} (kpc)
SN1992bu	NGC 3690	11:28:31.5	+58:33:38	Ib/c?	van Buren et al. (1994)		1.0
SN1999gw	UGC 4881	09:15:54.7	+44:19:55	II	Maiolino et al. (2002)		2.9
SN2001db	NGC 3256	10:27:50.4	-43:54:21	II	Maiolino et al. (2002)	5.5	1.5
SN2005U	NGC 3690	11:28:33.22	+58:33:42.5	IIb	Mattila et al. (2005b)	0	1.4
SN2005V	NGC 2146	06:18:38.28	+78:21:28.8	Ib/c	Mattila et al. (2005a)		0.5
SN2010hp	MCG-02-01-52	00:18:50.01	-10:21:40.6	IIP	Miluzio et al. (2013)	0.5	2.1
SN2010P	NGC 3690	11:28:31.38	+58:33:49.3	Ib/IIb	Kankare et al. (2014)	7	1.2
PSN2010	IC 4687	18:13:40.213	-57:43:28.00	Candidate	Miluzio et al. (2013)	0-8	6.5
PSN2011	IC 1623A	01:07:46.229	-17:30:29.48	Candidate	Miluzio et al. (2013)	0.5	3.2
SN2011ee	NGC 7674	23:27:57.34	+08:46:38.1	Ic	Miluzio et al. (2013)	0	8.9
SPIRITS 14buu	IC 2163/NGC 2207	06:16:27.2	-21:22:29.2	Candidate	Jencson et al. (2017)	1.5	2.0
SPIRITS 15c	IC 2163/NGC 2207	06:16:28.49	-21:22:42.2	IIb	Jencson et al. (2017)	2.2	2.1

Table 4.2: CCSN discoveries in IR in LIRGs in natural seeing conditions, as reported in the literature. The space-based SPIRITS discoveries are included in this sample based on the Spitzer/IRAC diffraction limit of 1.5″. Transients not confirmed spectroscopically or photometrically are typed as candidate CCSNe.

Adaptive optics near-IR CCSN discoveries in LIRGs							
Name	LIRG host	RA (J2000)	Dec. (J2000)	Type	Reference	Extinction A_V (mag)	D_{proj} (kpc)
AT1998xx	NGC 1275	03:19:48.87	+41:30:46.89	Candidate	Section 3.6.5		3.3
SN2004ip	IRAS 18293-3413	18:32:41.15	-34:11:27.5	II	Mattila et al. (2007)	5-40	0.5
SN2004iq	IRAS 17138-1017	17:16:35.90	-10:20:37.9	II	Kankare et al. (2008)	0-4	0.7
SN2008cs	IRAS 17138-1017	17:16:35.86	-10:20:43.0	II	Kankare et al. (2008)	17-19	1.5
AT2008xx	NGC 695	01:51:13.90	+22:4:54.97	Candidate	Section 3.6.5		4.2
SN2010cu	IC 883	13:20:35.35	+34:08:21.86	II	Kankare et al. (2012)	0-1	0.2
SN2011hi	IC 883	13:20:35.39	+34:08:21.69	II	Kankare et al. (2012)	5-7	0.4
AT2012xx	IRAS 18293-3413	18:32:41.12	-34:11:26.00	IIP	Section 4.2.3	1.8	0.6
AT2012xy	ESO 440-IG058	12:06:51.88	-31:56:59.21	Candidate	Section 4.2.3		1.5
AT2012xz	IRAS 17578-0400	18:00:31.86	-04:00:52.94	Candidate	Section 4.2.3		0.3
SN2013if	IRAS 18293-3413	18:32:41.10	-34:11:27.24	IIP	Section 2.7.1	0-3	0.2
SN2015ca	NGC 3110	10:04:01.57	-06:28:25.48	IIP	Section 2.7.2	3	3.5
SN2015cb	IRAS 17138-1017	17:16:35.84	-10:20:37.48	IIP?	Section 2.7.3	4.5	0.6
AT2015cf	NGC 3110	10:04:01.53	-06:28:25.84	Candidate	Section 2.7.4	2-5	3.5
AT2016jhy	IRAS F06076-2139	06:09:46.01	-21:40:31.26	Candidate	Section 3.6.1		0.0
AT2017chi	NGC 5331	13:52:16.09	+02:06:03.96	IIn	Section 3.6.2	11.8	1.7
AT2017jzy	NGC 695	01:51:13.90	+22:34:54.97	Candidate	Section 3.6.4		5.1
SN2018ec	NGC 3256	10:27:50.77	-43:54:06.3	Ic	Kankare et al. (2018)	3-4	1.7

Table 4.3: CCSN discoveries in IR in LIRGs assisted by AO, from project SUNBIRD and as reported in the literature. The space-based HST/NICMOS discoveries are included in this sample based on the diffraction limit of 0.17″. Transients not confirmed spectroscopically or photometrically are typed as candidate CCSNe.

AT 2012xx in IRAS 18293-3413

AT 2012xx was discovered in IRAS 18293-3413 on 2012 August 9 in K_s-band, at R.A. = $18^h32^m41.12^s$ and Decl. = $-34°11'26.01''$, $0.2''$ West and $1.5''$ North (0.6 kpc projected distance) from its host's nucleus, see Fig. 4.1. Follow up observations were obtained on 2012 August 26 in K_s and on 2012 September 14 in H and K_s, with the transient visible in both bands. The host galaxy was again observed with AO on 2013 April 21 with GeMS/GSAOI, by which time the transient had faded from view. A non-detection with VLT/NACO on 2011 August 9 provided a pre-outburst constraint. The photometry was fitted to light curve templates of Type IIP in plateau phase, Type IIn and Type IIb/Ib/Ic, see Fig. 4.2. Table 4.5 shows the resulting fitting parameters. As is clear from the figure and table, the photometry AT 2012xx is exceptionally well fitted by the Type IIP template, with an extinction of $A_V = 1.8$, the discovery epoch 57 days since explosion, and the SN 0.7 magnitude fainter than SN 1999em, the basis for the Type IIP template. This puts the GeMS/GSAOI non-detection at ~312 days since explosion, which does not constrain the Type IIP fit as it would have faded from view by then.

AT 2012xy in ESO 440-IG058

AT 2012xy was discovered in ESO 440-IG058 on 2012 July 17 in K_s-band, at R.A. = $12^h06^m51.88^s$ and Decl. = $-31°56'59.21''$, $2.7''$ West and $1.2''$ South (1.5 kpc projected distance) from its host's nucleus, see Fig. 4.3. ESO 440-IG058 was again observed on 2013 February 2 with GeMS/GSAOI in K_s, but the transient was no longer visible. With only one, although unambiguous, data point it was not possible to fit any light curves to the photometry of AT 2012xy. It will be treated as a CCSN candidate for the rest of this chapter.

AT 2012xz in IRAS 17578-0400

AT 2012xz was discovered in IRAS 17578-0400 on 2012 July 18 in K_s-band, at R.A. = $18^h00^m31.86^s$ and Decl. = $-04°00'52.94''$, $0.2''$ West and $0.8''$ North (0.3 kpc projected distance) from its host's nucleus. A second epoch was obtained on 2012 August 8 and 9 in K_s and H, respectively. The transient was faint but visible in K_s after subtraction of a NACO reference image from 2011 May 17, but had fallen below the detection limit in H-band. Similarly to AT 2012xy, the photometry was insufficient for light curve fitting, so AT 2012xz will be treated as a CCSN candidate for the rest of this chapter.

UT Date	Filter	Magnitude
AT 2012xx (IRAS 18293-3413)		
2011 August 9	K_s	>19.5
2012 August 9	K_s	17.68±0.11
2012 August 26	K_s	17.75±0.11
2012 September 14	K_s	17.73±0.11
2012 September 14	H	18.09±0.05
2013 April 21	K_s	>21.0
AT 2012xy (ESO 440-IG058)		
2012 July 17	K_s	18.0±0.1
2013 February 2	K_s	>21.5
AT 2012xz (IRAS 17578-0400)		
2012 July 18	K_s	19.26±0.07
2012 August 8	K_s	19.63±0.09
2012 August 9	H	>20.5

Table 4.4: NACO SN candidates near-IR photometry

4.3 SN recovery efficiency in LIRGs

In order to evaluate how effective project SUNBIRD's detection method is at recovering SNe, a detection efficiency experiment would be required for all epochs of all LIRGs observed in the program, as discussed in Section 2.8.6. A comprehensive analysis covering all our facilities is being carried out by Tom Reynolds from Tuorla Observatory, the results of which were not available at the time of submission of this thesis. However, it is possible to consider the usefulness of a LIRG CCSN survey in the near-IR with the use of LGSAO as compared to the alternatives, by comparing the three different LIRG CCSNe samples: the discoveries in IR with (LGS)AO, the discoveries in IR in natural seeing conditions, and the optical discoveries in natural seeing conditions. Across the optical and the IR so far there have been 61 spectroscopically and/or photometrically confirmed CCSNe documented in the literature or this thesis, as well as 10 CCSN candidate discoveries in the IR. Project SUNBIRD so far has contributed four photometrically confirmed CCSNe and five CCSN candidates.

First we compare the number of observed CCSN LIRG discoveries to the expected total number of CCSNe. To estimate the total expected CCSN rate in LIRGs, we sum the total IR luminosity of

AT 2012xx (IRAS 18293-3413)				
Template	A_V	t_0	C	$\tilde{\chi}^2$
IIP	$1.8^{+1.3}_{-0.9}$	57^{+2}_{-12}	$0.7^{+0.1}_{-0.2}$	0.3
IIn	$0.0^{+0.3}_{-0.0}$	115^{+11}_{-2}	$0.5^{+0.1}_{-0.1}$	33.7
IIb/Ib/Ic	$0.0^{+1.7}_{-0.0}$	17^{+1}_{-2}	$0.5^{+0.1}_{-0.3}$	11.0

Table 4.5: Results from fitting light curve templates to AT 2012xx, with line-of-sight extinction A_V, time t_0 between explosion date and discovery, and a fixed constant C representing the intrinsic magnitude difference between SNe. The final column shows the resulting $\tilde{\chi}^2$ for each fit.

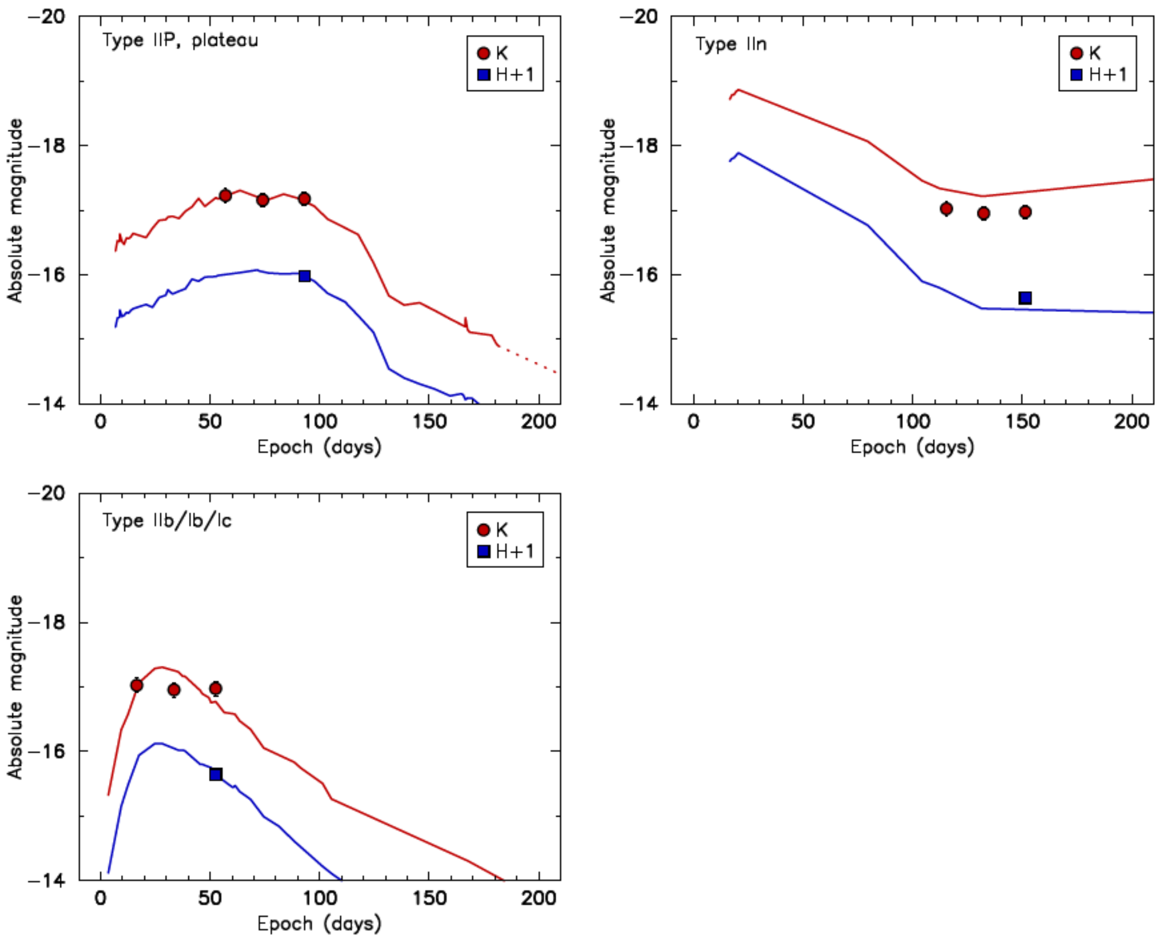

Figure 4.2: Template light curve fits for AT 2012xx in IRAS 18293-3413 are shown: Type IIP, Type IIn, and Type IIb/Ib/Ic. The Type IIP template fits the data extremely well, implying an extinction of A_V = 1.8, the discovery epoch 57 days since explosion, and the SN 0.7 magnitude fainter than SN 1999em, see Section 4.2.3.

all galaxies in the IRAS Revised Bright Galaxy Sample (RBGS, median redshift z = 0.082) defined as LIRGs ($\log(L_{IR}) > 11.0$). A total of 218 galaxies in the RGBS match that criteria, assuming H_0

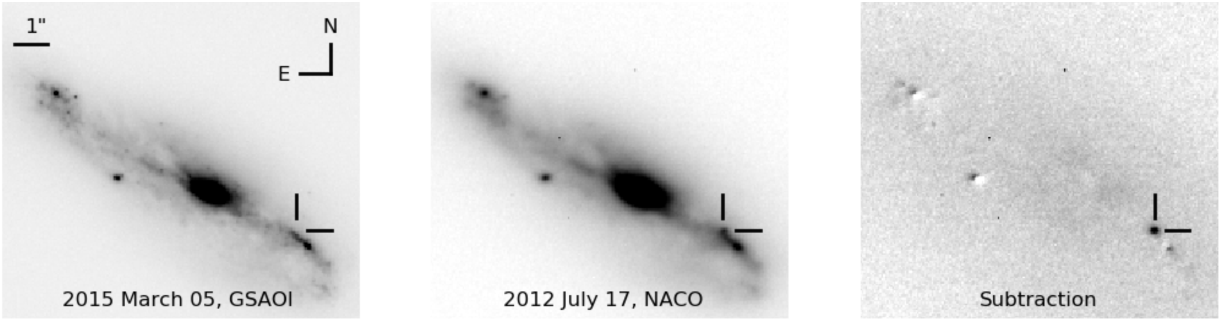

Figure 4.3: AT 2012xy in ESO 440-IG058 in K_s-band, see Section 4.2.3. From left to right with linear scaling: Reference GeMS/GSAOI image (March 2015), discovery VLT/NACO image (July 2012) and the image subtraction.

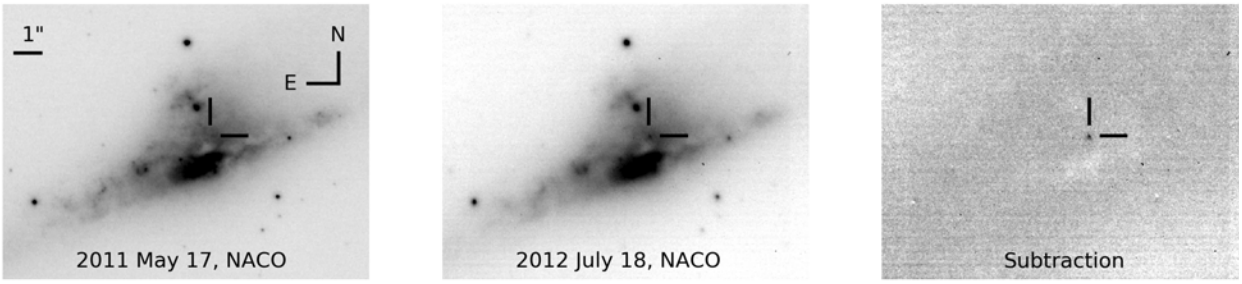

Figure 4.4: AT 2012xz in IRAS 17578-0400 in K_s-band, see Section 4.2.3. From left to right with linear scaling: Reference VLT/NACO image (May 2011), discovery VLT/NACO image (July 2012) and the image subtraction.

= 70 instead of 75 km s^{-1} Mpc^{-1}. The total IR luminosity of these 218 galaxies is $L_{IR} = \sim 10^{14}$ $L_{\odot}$. Following Hayward et al. (2014) and references therein, assuming a Salpeter IMF, this results in a SF rate of $\sim 1.1\times10^3$ $M_{\odot}$ yr^{-1}. If the number of stars that explode as CCSNe per unit mass is k = 0.0068 (Madau and Dickinson, 2014), the expected CCSN rate of all LIRGs is $\sim$ 75 CCSNe yr^{-1}. Note that this is slightly lower than the rate based on the empirical relation from Mattila and Meikle (2001), see Eq. 2.1 in Chapter 2, which amounts to ~250 CCSNe yr^{-1}.

From these expected CCSN rates follow that in total around 1200-4000 CCSNe have exploded in LIRGs since the start of this century. This is two orders of magnitude larger than the actual observed number of CCSNe (60) in LIRGs, implying $\gtrsim$95% of CCSNe in LIRGS are not being observed. Of course the sky has not been monitored continuously throughout this period, but especially in the past decade in the optical there have been many wide-field optical SN searches monitoring large swaths of the sky for SNe on a regular basis, such as LOSS (Leaman et al., 2011a), CSP (Hamuy et al., 2006), CRTS (Drake et al., 2009), ASAS-SN (Shappee et al., 2014), Pan-STARRS1 (Chambers et al., 2016) and SkyMapper (Scalzo et al., 2017). In the past decade 19 CCSNe were discovered in the optical in LIRGs, versus an expected ~2500. For example ASAS-SN, an all sky optical supernova search running since June 2013, has discovered ~500 SNe so far, including 140 CCSNe up to a redshift of 0.08, none of which were located in LIRGs (Holoien et al., 2017a,b,c).

Using some broad assumptions, we can compare the discoveries in LIRGs from project SUNBIRD with the optical discoveries reported in the literature in the years 2015-2017 when SUNBIRD ran on the Gemini and Keck telescopes. We obtained 78 epochs across 37 LIRGs during these three years. Assuming we would not miss a SN exploding in the three months preceding an AO observation, our total time covered was 234 months. This is $\sim 3\%$ of the full coverage of all 218 LIRGs over 3 years. During our coverage from 2015 until 2017 we discovered 3 CCSNe and 3 CCSN candidates. Based on the expected CCSN rate in all LIRGs of 75 CCSNe yr^{-1}, a total of 225 CCSNe exploded during that time. This means under these assumptions and a coverage factor of all LIRGs by our program of 3%, our discovery rate of 6 CCSNe (candidates) was well matched with the expected number of 0.03 * 225 = 6.7 CCSNe. In contrast, in the optical only four CCSN discoveries were reported in the literature during the years 2015-2017. Assuming the number of wide-field optical surveys active at the time would not have missed any CCSNe in a LIRG during those years, this means in the optical only $\sim 2\%$ of all LIRG CCSNe were detected, and 98% missed.

4.3.1 Optical versus IR

A first order analysis of the relative distribution of CCSN discoveries across the optical and the IR offers an explanation. The total number of optically discovered CCSNe (40) is of a similar order of magnitude as the total number of CCSNe discovered in the IR (20, or 30 including candidates). However, in terms of the temporal coverage of LIRGs the optical and the IR are very dissimilar. For simplicity's sake we will express coverage in terms of number of observing epochs. In the IR the monitoring for SNe in LIRGs has been dominated by programs targeting starburst galaxies, such as Grossan et al. (1999) (~500 epochs), Mannucci et al. (2003) (234 epochs), Mattila et al. (2004) (120 epochs), Kankare et al. (2008, 2012) (60 epochs), Miluzio et al. (2013) (210 epochs), the ongoing SPIRITS survey (Jencson et al., 2017) and project SUNBIRD (90 epochs). This amounts to a conservative upper limit of a total of 2000 epochs of LIRGs in the IR.

By virtue of optical surveys having a larger FOV and greater availability, the coverage of LIRGs in the optical extends over a longer time baseline with higher cadence than in the IR. For example the Lick Observatory Supernova Survey (LOSS, Leaman et al. 2011a) observed 14882 galaxies over the course of 11 years, with an average of 150 observations per galaxy. This sample included

~100 LIRGs, which amounts to 15000 epochs of LIRGs in the optical for LOSS alone. If we also account for optical wide-field surveys such as ASAS-SN, PanSTARRS1 and CRTS that monitor the whole sky for SNe on a regular basis, it is safe to say the coverage of LIRG observations in the optical is *at least* an order of magnitude higher than in the IR.

Given the similar number of CCSN discoveries in the optical and the IR, this implies SN discovery in LIRGs is substantially more efficient in the IR. As the IR is less affected by dust extinction compared to the optical, and LIRGs are host to large amounts of dust, this is likely in large part a result of reduced sensitivity in the optical due to dust extinction.

4.3.2 Spatial resolution

When we separate the IR sample between CCSNe discovered in natural seeing conditions and CCSNe discoveries assisted by AO, we can evaluate the effects of spatial resolution on recovery efficiency independent of dust extinction differences. There have been a similar number of CCSNe discovered in natural seeing conditions (9) as there have been from AO-assisted programs (11), see Tables 4.2 and 4.3. If we include CCSN candidates, there are more AO discoveries (18) than non-AO discoveries (12). However, the temporal coverage of LIRGs is again very dissimilar between the two regimes. AO-assisted observations of LIRGs in the IR have been the result of a few targeted SN searches. Across Mattila et al. (2007) with VLT/NACO, Kankare et al. (2008, 2012) with ALTAIR/NIRI, and project SUNBIRD with GeMS/GSAOI and NIRC2 there have been ~240 epochs in the near-IR with AO. If we add the 17 HST/NICMOS epochs from Cresci et al. (2007), this amounts to a total of ~260 epochs of high spatial resolution (AO) imaging of LIRGs. The IR non-AO SN programs listed before exceed the AO sum total by a factor of four, implying that SN discovery is much more efficient with AO than in natural seeing.

Fig. 4.5 clearly shows the cause of this difference. Plotted are the nuclear offsets of the IR CCSN discoveries with and without AO-assistance in bins of 1 kpc. The dotted line at 4 kpc indicates a cutoff applied to account for selection effects due to differences in FOV. The FOV of AO-imagers are limited and 4 kpc corresponds to 11″ at a typical distance of 75 Mpc of a LIRG hosting a discovered SN. This is the limit of the CCSN search radius of ALTAIR/NIRI on Gemini North, the smallest FOV (22″) of the IR instruments with which CCSNe have been discovered in LIRGs. As such, this should be treated as a lower limit, since for example the FOV of GeMS/GSAOI is much larger at 85″.

Despite the small samples, the distributions of CCSN discoveries with and without AO with offsets > 1 kpc are very similar, but AO-assisted discoveries dominate the smallest offset bin. Half

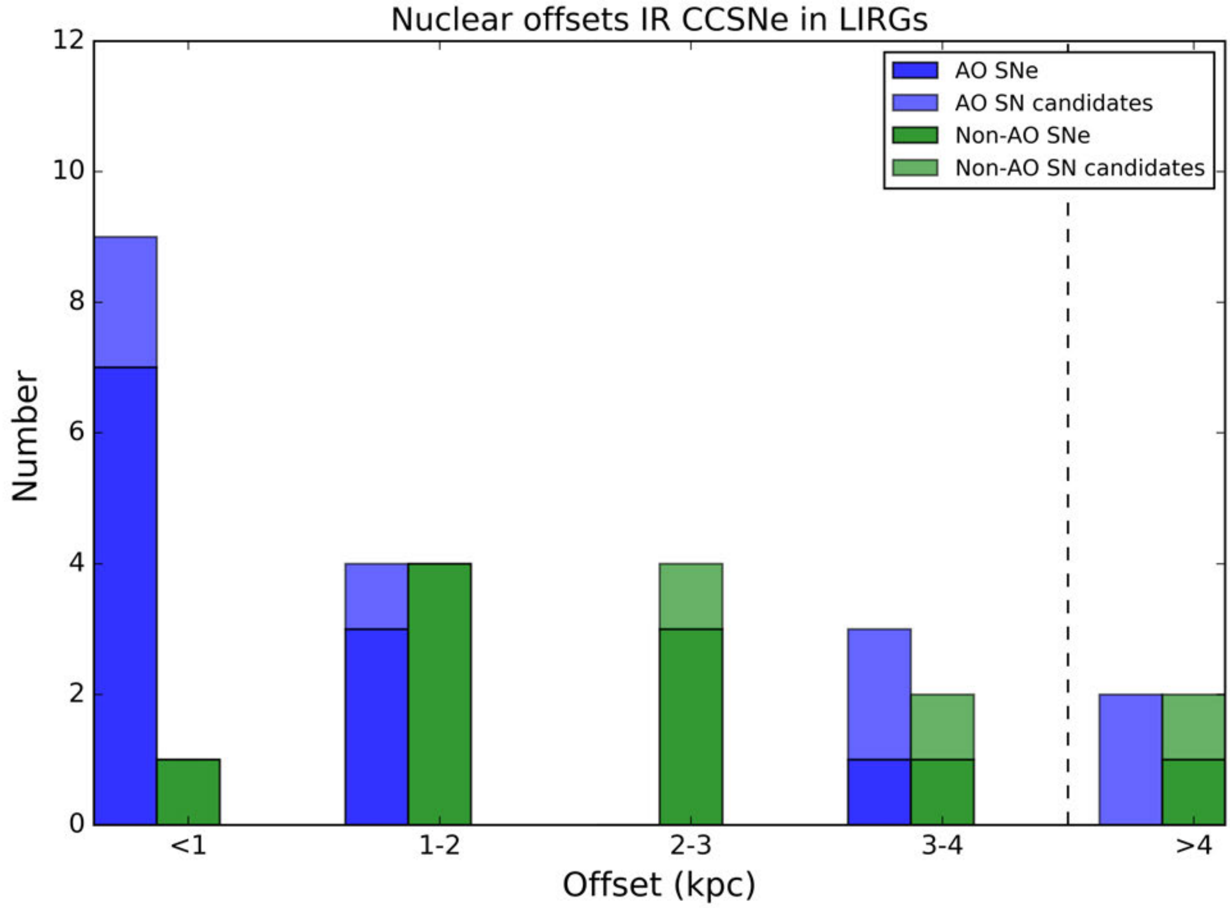

Figure 4.5: Nuclear offset distribution for all CCSNe discovered in LIRGs in IR, see Section 4.3.2. In blue are shown the discoveries in the IR with AO instruments and in green the IR CCSN discoveries in natural seeing conditions, with stacked on top CCSN candidates. The dotted line at 4 kpc marks the limit of the smallest FOV of the instrument used for the AO CCSN discoveries, ALTAIR/NIRI on Gemini North, at a typical distance for LIRGs with SN discoveries of 75 Mpc.

of the AO SNe (candidates) were discovered in their hosts' inner kpc, while in natural seeing only one of the thirteen seeing-limited IR discoveries has a projected offset smaller than 1 kpc. The simplest explanation for these conclusions is that the improved spatial resolution for AO-assisted imaging at these wavelengths provides enhanced sensitivity to CCSNe detection in these dusty and compact star forming objects.

We combine the three different samples in Fig. 4.6, which shows the distribution of nuclear offsets of the IR AO, IR non-AO, and optical samples, where the numbers have been corrected for binsize to an arbitrary value that can be thought of as a CCSN surface density. For the >4 kpc bin an outer limit of 10 kpc was adopted. We expect CCSN density to follow star formation density, which to first order peaks in the nucleus in LIRGs (Alonso-Herrero et al., 2009). This means in an area corrected distribution plot, we would expect CCSN discoveries to peak in the nuclear regions

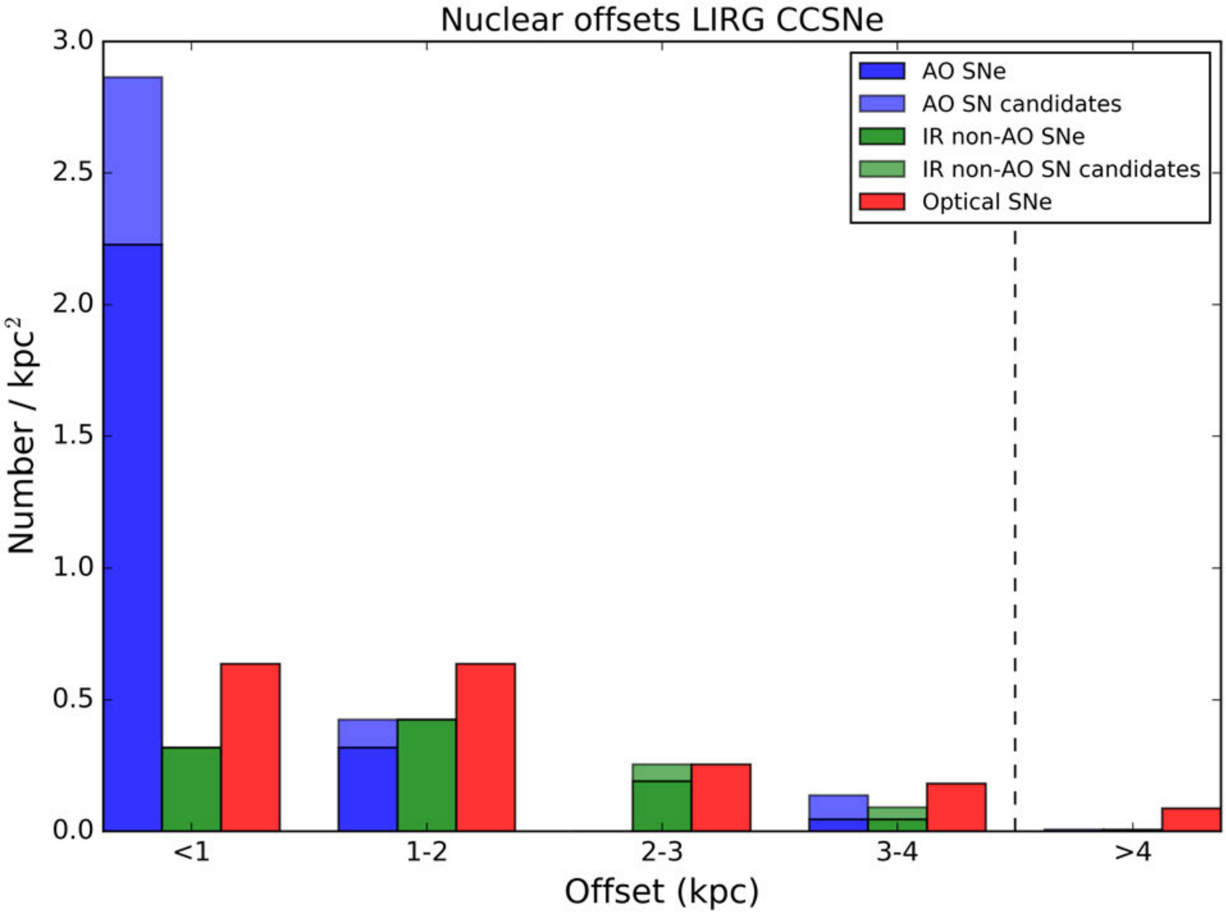

Figure 4.6: Distribution of LIRG CCSNe (candidates) with the number of CCSNe (candidates) normalized by binsize, see Section 4.3.2.

as well, while dropping off towards the outer regions. In Fig. 4.6 we see this behaviour for all three samples down to a nuclear offset of 1 kpc. However, in the smallest offset bin both non-AO IR and optical discoveries *decrease*, while the number of AO IR discoveries increases dramatically. This shows very clearly that our approach is singularly effective in uncovering CCSNe in nuclear regions (where the majority of star formation in LIRGS occurs), and crucial in characterizing this population of CSSNe that will remain invisible through other means.

The CCSN radial distribution as seen in IR AO studies agrees well with work on the spatial distribution of CCSNe and CCSN remnants in the nuclear regions of three starburst galaxies and a sample of spiral galaxies using high-angular resolution ($\lesssim 0.1''$) radio VLBI observations studied by Herrero-Illana et al. (2012). Here it was found that the SN radial distribution in the LIRGs Arp 220 and Arp 299 was centrally peaked with a very steep SN surface number density profile when compared to the SN radial distribution in regular spiral galaxies from Hakobyan et al. (2009). The SNe and SN remnants in Herrero-Illana et al. (2012) have radial distances almost exclusively smaller than the most centrally located SN in Table 4.2, which is not surprising given the superior spatial resolution, but limited FOV, of VLBI. As such the VLBI observations can be seen as an extension of the trend observed between IR AO and optical, again due to a combination of longer wavelengths and increased spatial resolution.

Finally, most of the IR CCSNe in Table 4.2 also include reported or light curve fitted extinctions in A_V. We expect to first order the distribution of dust to trace SF (Choi et al., 2006) and peak in the nucleus, and as a consequence CCSNe observed in the nucleus typically to be more affected by dust extinction. If we do not observe a clear trend, this would imply most of the high extinction events are still being missed. We check if there is a relation between nuclear offset and extinction, and whether there is a difference between the AO and non-AO samples. Fig. 4.7 shows the SN extinctions plotted versus nuclear offset. Across the full IR sample there does not appear to be a trend with offset, with low-extincted SNe spread across all offsets. However, the three most extincted CCSNe have in fact occurred within the inner 2 kpc of their host galaxy, so the lack of a clear trend could also be a result of the limited sample size. Furthermore, the offsets plotted here are projected offsets and should be considered lower limits. A SN close to the nucleus could have exploded in the foreground with an associated low extinction, as appears to have been the case with SN 2013if. In terms of differences between the AO and non-AO samples, there is no significant difference in median extinction (3.5 ± 2.1 for AO SNe and 1.5 ± 0.8 for non-AO SNe), but again in terms of nuclear offset the figure shows a clear difference between the two samples.

4.4 Summary

To investigate the impact of the new CCSN discoveries from project SUNBIRD and the effectiveness of our method, we gathered from the literature all CCSN discoveries in LIRGs in the optical and the IR. This sample consists of 60 confirmed and 10 candidate CCSNe, out of which 18 were discovered using IR AO, including this project. We show a clear distinction in nuclear offset distribution between these AO events and the other optical and IR discoveries. Half of the CCSN (candidate) discoveries from AO programs occurred in the inner kpc of their hosts, but only a small fraction of the non-AO IR and optical CCSNe had offsets smaller than 1 kpc. This tells us that the majority of CCSNe explode in the nuclear regions, and the method adopted in project SUNBIRD is singularly effective in uncovering them. We conclude that the $<$100 pc scale resolution offered by AO is critical to explore the full range of local SN environments and obtain a statistically representative volume of dust-obscured nuclear CCSNe, required to characterize the population of CCSNe that remain invisible to any future seeing-limited optical wide-field SN survey.

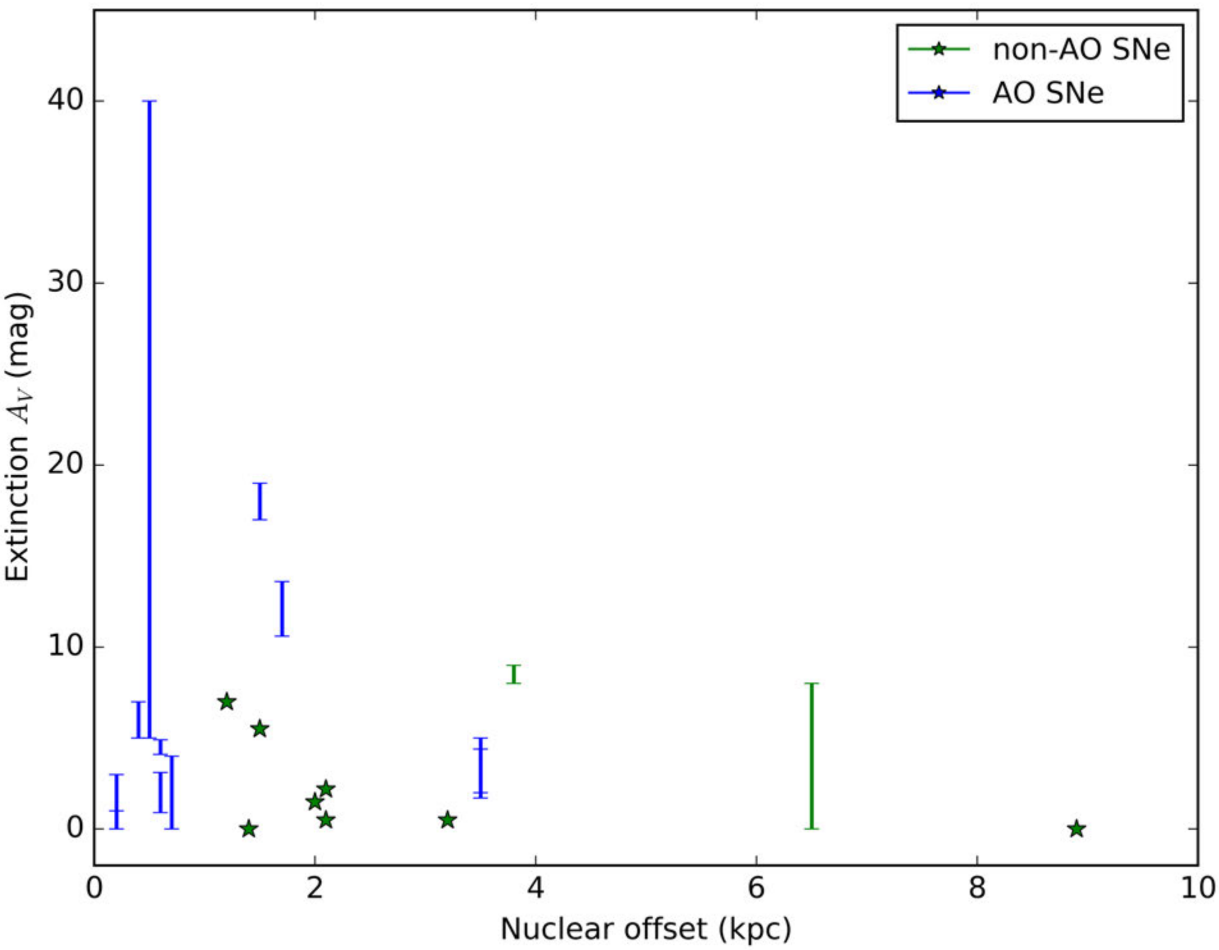

Figure 4.7: Extinction in A_{V} versus nuclear offset of the CCSN discoveries in IR with known extinction, see Section 4.3.2. AO discoveries are plotted in blue, natural seeing discoveries in green. CCSNe with a ranged extinction or an extinction with known errors are plotted as bars.

5

Investigating supernova environments with MUSE

5.1 Introduction

In this chapter the SN sites in IRAS 18293-3413 are investigated using a data set obtained with the MUSE facility. The MUSE facility consists of the state-of-the-art integral field spectrograph MUSE on the VLT, supported by its new Ground Layer Adaptive Optics (GLAO) system GALACSI. IRAS 18293-3413 is a LIRG from the SUNBIRD sample that has been observed extensively with AO imagers in the near-IR with 10 epochs over the past 7 years, resulting in three CCSNe. High spatial resolution integral field unit (IFU) spectroscopy allows us to compare in detail the local conditions at these SN sites, such as star formation rate (SFR) and dust extinction, with the rest of the galaxy. In addition, the local metallicity and stellar population age can provide limits to the SN progenitors' age and mass, and potentially constrain the subtypes of these SNe.

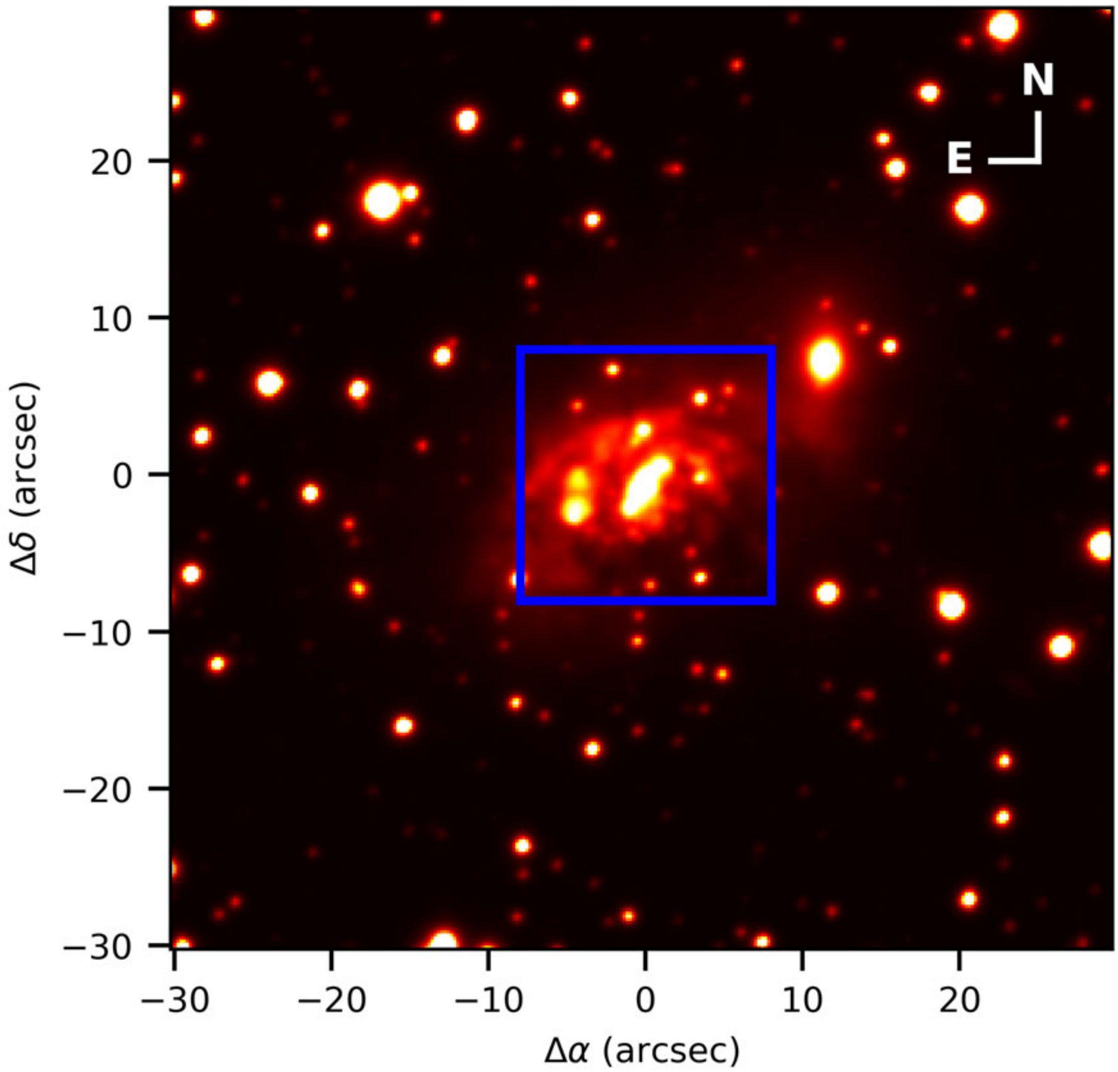

Figure 5.1: The full 60″ by 60″ MUSE image of IRAS 18293-3413 collapsed along the spectral axis, with the 16″ by 16″ stamp used in this chapter for spectral fitting indicated by the blue box, see Section 5.2. The companion of IRAS 18293-3413 is visible ∼12″ West and ∼7″ North.

5.2 Observations and data reduction

The panoramic integral-field spectroscopic observations of IRAS 18293-3413 were carried out on the 18th of September, 2017, with the Multi-Unit Spectroscopic Explorer (MUSE; Bacon et al., 2010) instrument mounted on UT 4 of the VLT. MUSE is a state-of-the-art IFU spectrograph that splits the light into 24 sub-fields each feeding an IFU, allowing for an unprecedented $1' \times 1'$ field of view (FOV) at a $0.2'' \times 0.2''$ spatial sampling, and a wavelength coverage of 4650 - 9300 Å with a 1.25 Å pixel^{-1} spectral sampling and a mean resolution of $R \sim 3000$. The observations in this chapter were the result of time granted to observe two SN factories from our sample during the Science Verification phase of GALACSI (PI: E. Kool[1]). GALACSI is a GLAO system developed

[1]ESO Programme ID 60.A-9194(A)

to increase the image quality of MUSE and was commissioned at the end of the summer of 2017. Competitively awarded SV observations were obtained in August and September 2017, with data immediately made public. GALACSI uses four LGS and one deformable secondary mirror to correct for atmospheric turbulence occurring within the first few hundred meters above the telescope. GLAO is a seeing enhancement technique, with guide sources distributed in a relatively large FOV where the single deformable mirror corrects for the average wave front signal. This is an efficient technique if turbulence is concentrated in the ground layer, and typically results in a factor 2 gain in the energy concentration of a star.

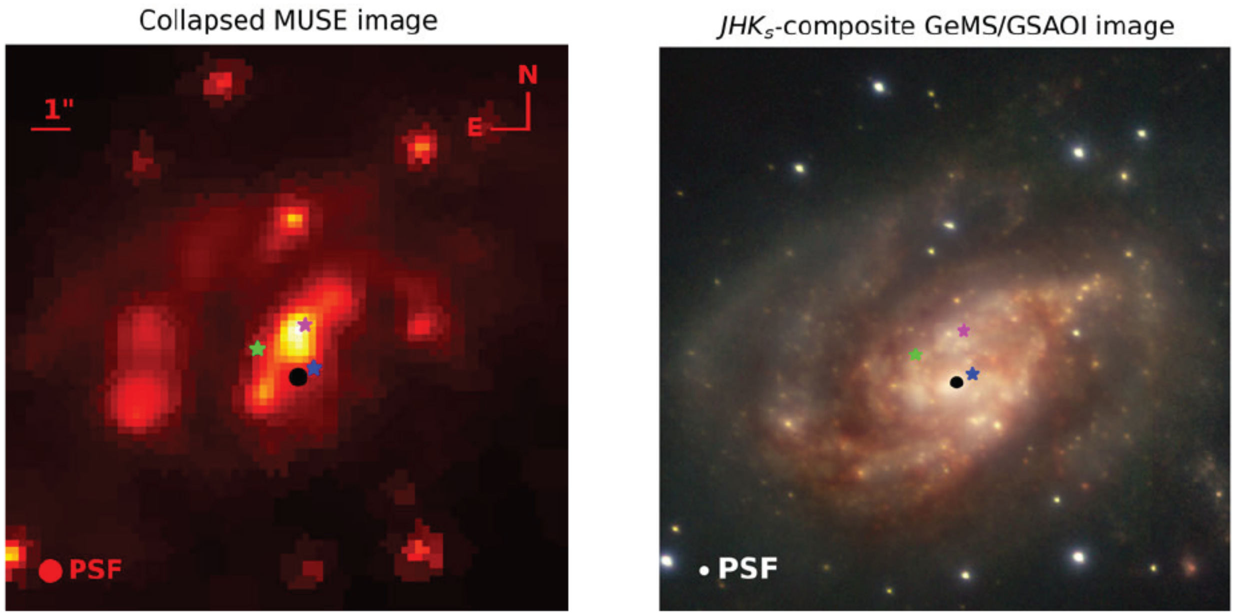

Figure 5.2: The left panel shows the 16″ by 16″ cropped and collapsed MUSE image of IRAS 18293-3413. The right panel shows an aligned 3-colour composite near-IR image, obtained with AO-imager GeMS/GSAOI on 2013 April 21. The position of the nucleus in near-IR is indicated by the circle, and the SN positions of SN 2004ip, AT 2012xx and SN 2013if by a lime, magenta and blue star, respectively.

The observations consisted of four on-source exposures of 630s, each rotated by 90 degrees in order to account for detector artefacts and mitigate systematic variations in the spectral line spread function, giving a total of 2520s on source. The data were reduced and combined using the ESO MUSE data reduction pipeline version 2.2 (Weilbacher et al., 2014), which included bias subtraction, flat fielding, and wavelength and flux calibration. As the galaxy did not fill the FOV, no off-source blank sky observations were required, but instead peripheral blank sky spaxels were used to create the sky spectrum to subtract. The spectral region affected by the NaD laser (5800 - 5970 Å) was blocked with a narrow spectral 'notch' filter, and the corresponding spectral range is masked during the various reduction steps. The atmospheric seeing during the observing night for the four exposures ranged from 0.8″ to 1.1″ at 6500Å. After ground layer AO correction and cube reconstruction the FWHM of the PSF measured using stars in the combined MUSE cube was between 0.6″ at 9000 Å and 0.7″ at 5000 Å. Fig. 5.1 shows the full MUSE image of IRAS 18293-3413, collapsed along the spectral axis, where the blue square indicates the borders of the cropped image analysed in this study. Fig. 5.2 shows a side by side comparison of the cropped MUSE image and a composite near-IR JHK_s AO image observed with GeMS/GSAOI, with the nucleus as seen in the near-IR and the three SN sites indicated. The coordinate system in all figures of this chapter is centred on the position of the near-IR nucleus in the GeMS/GSAOI data, at R.A. = $18^h32^m41.14^s$ and Decl. = $-34°11'27.47''$, with 0.03″ and 0.03″ uncertainty in R.A. and Decl., respectively.

5.3 Methods and Analysis

5.3.1 Spectral fitting with pPXF

As the focus of this chapter lies on the local conditions of the SN sites which all lie in the central 2″ of the galaxy, the data was cropped to a 16″ by 16″ stamp centred on the galaxy, see Fig. 5.1 and 5.2. This encompassed almost all of the galaxy light, while it greatly reduced computing time of the spectral fitting. It does not include the elliptical galaxy to the Northwest of IRAS 18293-3413, believed to be a companion galaxy with a radial velocity offset of 500 km s^{-1} (Väisänen et al., 2008). Analysis of this interaction, and the large scale dynamics of the galaxy, will be included in future work. The data were spatially binned to achieve a signal-to-noise ratio (SNR) in the continuum of at least 30 per spectral pixel in each bin. In and around the nucleus, the SNR requirement was typically met by single spectral pixels (spaxels) without the need for binning, while in the outer regions, flux of adjoining spaxels was added to obtain the minimum SNR. This was done using the Voronoi binning scheme (Cappellari and Copin, 2003), where the data are partitioned in such a way as to preserve the maximum spatial resolution given a minimum SNR constraint. The spectrum in each bin was then fitted using the Penalised Pixel-Fitting code (pPXF; Cappellari and Emsellem (2004), Cappellari (2017)), which uses a weighted combination of stellar population model template spectra to infer the stellar kinematics and populations at that location. We use the models of Vazdekis et al. (2010), spanning a range of 0.08 to 15.85 Gyr in age, and -1.71 to 0.22 in metallicity (Z). Emission lines from ionized gas were fitted simultaneously with the stellar continuum by including individual Gaussian templates, each centred on the wavelength of an expected emission line, namely: Hβ (λ4861), Hα (λ6563), [SII] (λ6716,6731), [OI] (λ6300,6364), [OIII] (λ4959,5007) and [NII] (λ6548,6583). In this chapter we are primarily interested in the emission line fluxes, but by simultaneously fitting the continuum, absorption is also accounted for. This is critical for emission lines such as Hβ, where the strength of absorption can be comparable to or stronger than the strength of emission. Additionally we opted to include a reddening curve as part of the template fit, instead of using e.g. a generic polynomial to account for continuum variations due to dust or instrumental effects. Fitting for reddening offers less freedom in fitting the continuum than a polynomial, but in this way it is possible to quantify the extinction affecting the continuum (see Section 5.3.4 for more details). Fig. 5.3 presents an example of a spectral fit with pPXF of a bin in the outer regions, with the 'notch' region shaded red. Fig. 5.4 shows the corresponding emission line fits of Hβ, [OIII], Hα and [NII], showcasing the need to fit continuum absorption especially in Hβ. The Balmer line templates are set to use the same kinematics as the forbidden lines. The [NII] and [OIII] are fitted as doublets, and a theoretical doublet ratio of three to one was assumed to obtain the primary line strengths of [NII]λ6583 and [OIII]λ5007, required to determine metallicity. An amplitude over noise (AoN) ratio was determined for all emission lines, with the peak flux of the emission line fit defined as the amplitude, and the noise calculated as the standard deviation of the fit residuals of 50 spectral pixels to either side of the emission line (e.g. Sarzi et al., 2006), or in case of Hα past the neighbouring [NII] emission lines. An emission line was considered detected with an AoN of 10 for Hα, and an AoN of 5 for the other emission lines.

5.3.2 Velocity field

Fig. 5.5 shows the gas kinematics resulting from combined fitting of the Balmer lines Hβ and Hα, as well as the stellar kinematics from fitting absorption lines. The gas kinematics display a reasonably smooth velocity field, which is surprising because from the AO near-IR imaging IRAS 18293-3413 appears to have a disturbed and complicated morphology. The position of the dynamical centre appears to be very close to the near-IR nucleus, indicated by the red circle. The stellar kinematics overall appear to follow the gas, but the velocity field is more noisy and the kinematic centre not as well defined.

Based on the prominent dust lanes on the Southwest side of the system, which are also visible in the AO image (Fig. 5.2), Väisänen et al. (2008) interpreted the South side to be the near side and concluded IRAS 18293-3413 to be a strong candidate for a rare leading arm galaxy. Their line-of-sight velocity curve from long-slit spectroscopy along the major axis agrees well with our

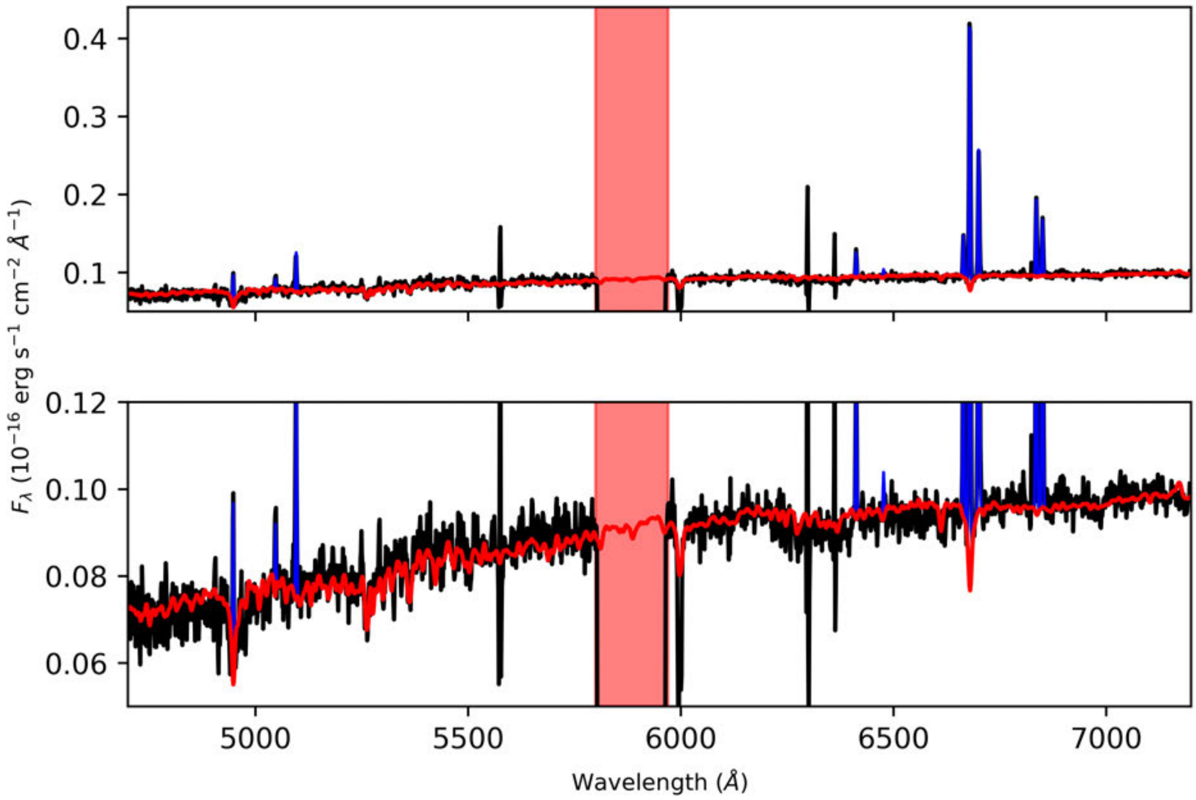

Figure 5.3: Spectral fitting results of the spectrum (in observed wavelengths) of a bin in the outer regions, composed of 26 spaxels, showcasing both absorption and emission features, see Section 5.3.1. See Fig. 5.4 for its fitted emission lines. Spectrum in observed wavelengths is shown in black, the continuum fit in red and the superimposed emission line fits in blue. Note the masked region between 5800 - 5970 Å due to the NaD laser.

own observed range in velocities, but as Väisänen et al. (2008) discussed the key issue is the determination of the orientation of the galaxy. This chapter focuses on the local environment of the three SNe in this galaxy, and as such the analysis of the global kinematics, required to solve this issue, does not fall within the scope of this chapter. Still, we will keep this in mind in the rest of this chapter.

5.3.3 Emission line flux

The line flux of emission lines was calculated in pPXF by summing the components of the emission line fit. This was done separately for each spatial bin, see Fig. 5.6 for the 'raw' flux maps of the emission lines most important to this study. Because the binned spectra are the sum of the constituent spaxels, the integrated flux is divided by the bin area in arcsec^2 to infer the emission line flux surface density. Also indicated are the SN positions and the nucleus as seen in the near-IR.

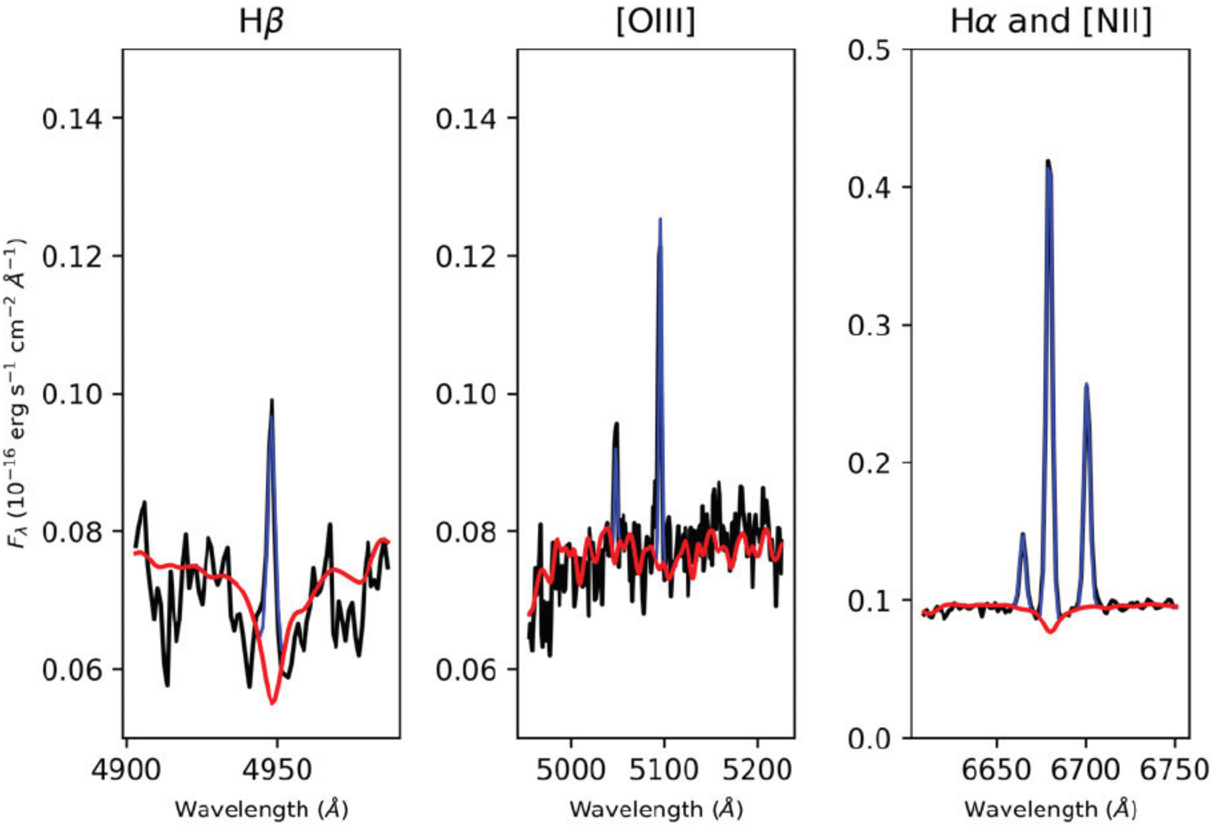

Figure 5.4: Spectral fitting results of a bin in the outer regions (see Fig. 5.3) around emission lines Hβ (left panel), [OIII] doublet (center panel) and Hα and [NII] (right panel), in observed wavelengths. Spectrum is shown in black, the continuum fit in red and the superimposed emission line fits in blue.

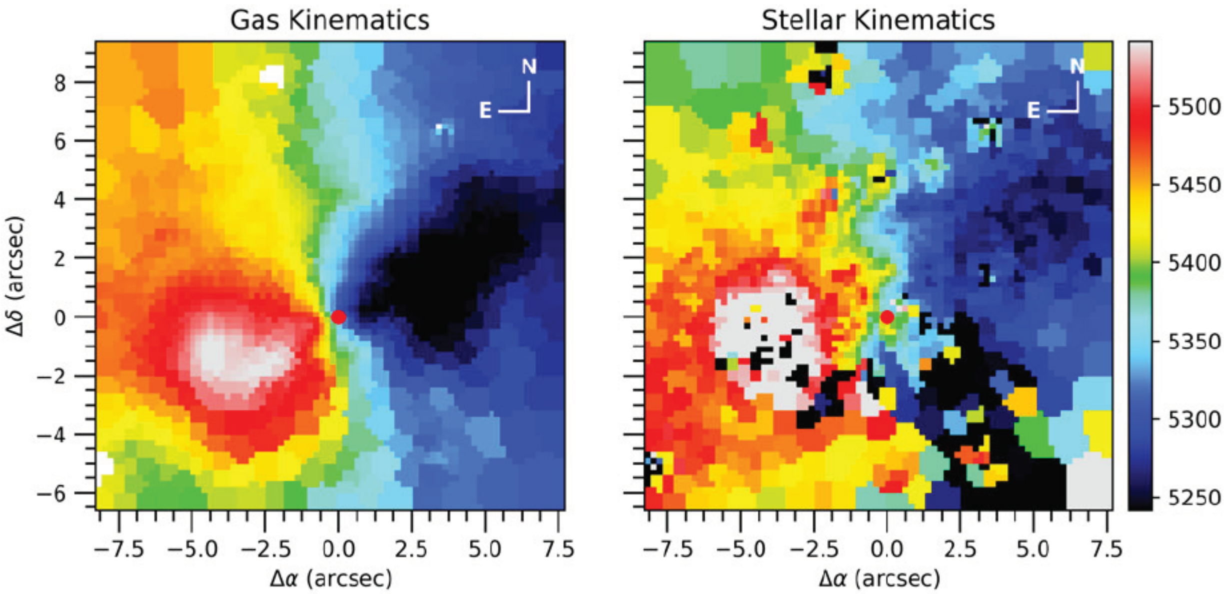

Figure 5.5: The gas kinematics of IRAS 18293-3413 from fitting emission lines (left panel) and the stellar kinematics from fitting the absorption lines (right panel), see Section 5.3.2.

The maps are flagged based on AoN as discussed in Section 5.3.1. The emission line fluxes have been de-reddened for foreground Galactic extinction, using the standard expression:

$$F_{\rm i} = F_{\rm o}\ 10^{0.4A_\lambda} \tag{5.1}$$

where $F_{\rm i}$ and $F_{\rm o}$ are the intrinsic and observed flux respectively, and A_λ the extinction affecting the observed flux. The NASA/IPAC Extragalactic Database (NED) offers a range of A_λ for IRAS 18293-3413 based on the dust maps of Schlafly and Finkbeiner (2011). The SDSS *ugriz* values were fitted with a second order polynomial to derive for each emission line the extinction A_λ appropriate for the wavelength.

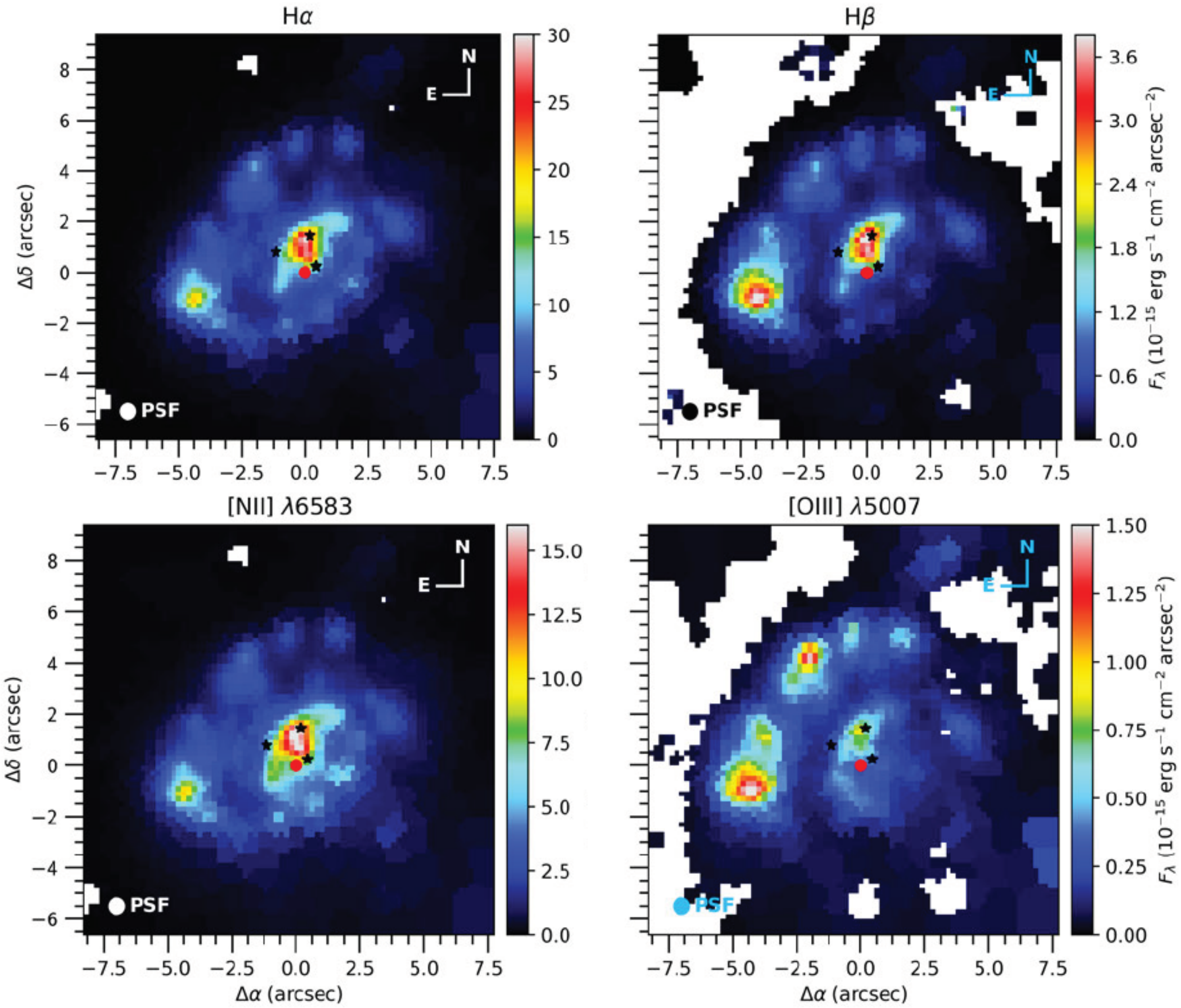

Figure 5.6: Observed emission line fluxes of Hα (top left), Hβ (top right), [NII] (bottom left) and [OIII] (bottom right), corrected for Galactic foreground extinction, see Section 5.3.3. Some spaxels have been masked based on AoN. The AO corrected PSF is shown, as are the SN sites indicated by black stars and the near-IR nucleus indicated by the red circle.

An initial inspection of the raw ionized gas emission line fluxes in Fig. 5.6 shows a number of recognizable features in common with the IR imaging, in particular the bright nucleus, and the star-forming regions along the spiral arms. Differences between the red (Hα and [NII]) and blue (Hβ and [OIII]) lines are likely due to the significant amounts of dust present in the galaxy. The nucleus as seen in the collapsed image (Fig. 5.2, left panel) coincides with the nuclear peak in Hα, Hβ and [NII], but is offset by $\sim 1''$ North with respect to the nucleus as seen in near-IR.

5.3.4 Dust extinction

In addition to the Galactic foreground extinction, we correct for dust in two complementary ways. First, the spectral fit with pPXF includes a free parameter allowing for continuum reddening expressed in $E(B-V)$, assuming a Calzetti extinction curve (Calzetti et al., 2000). A map of the reddening obtained this way is shown in the right panel of Fig. 5.7 expressed in A_V, adopting $A_\mathrm{V} = R_\mathrm{V} \times E(B-V)$ where R_V = 4.05 (Calzetti et al., 2000). In this chapter this is considered to be the attenuation affecting the continuum.

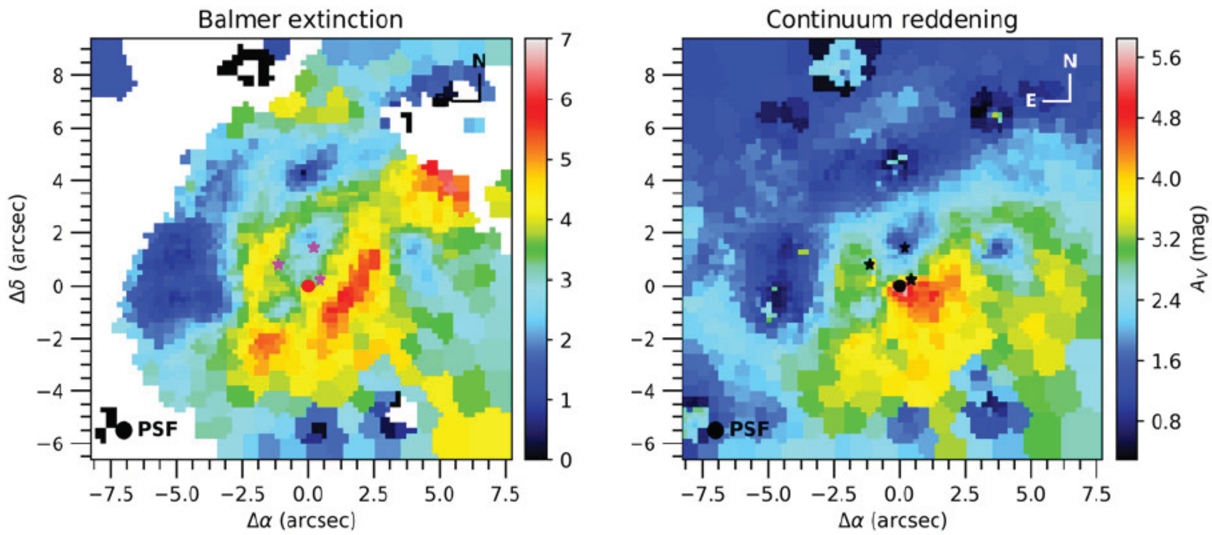

Figure 5.7: Dust extinction in A_V, from the Balmer decrement, on the left. Continuum reddening from spectral fitting with pPXF on the right. See Section 5.3.4 for more information.

Second, the effect of dust along the lines of sight to the regions of Balmer emission is estimated using the Balmer decrement. The Balmer decrement is defined as the ratio of the fluxes in the Balmer emission lines Hα and Hβ. The expected value of this ratio is set by quantum physics as 2.86, assuming Case B recombination, an electron temperature $T_e \sim 10^4$ K and electron density $N_e \sim 10^4$ cm^3 (Osterbrock, 1989), and any deviation may be attributed to dust extinction. The attenuation correction factor F_ac based on the Balmer decrement, following the Cardelli extinction law (Cardelli et al., 1989) with a reddening slope of 2.36, is calculated as:

$$F_{\mathrm{ac}} = \left(\frac{f_{\mathrm{H}\alpha}/f_{\mathrm{H}\beta}}{2.86}\right)^{2.36} \tag{5.2}$$

The extinction in each bin based on the Balmer decrement is shown in the left panel of Fig. 5.7 in terms of A_{V}. In addition to AoN masking, bins with a non-physical Balmer decrement of <2.86 were also masked. As this extinction is measured using the Balmer line emission fluxes, it is considered as a more reliable estimate of the extinction along sight lines towards regions of star formation.

As can be seen in Fig. 5.7 the continuum reddening is centrally peaked, whereas the Balmer extinction appears to peak along a band South of the nucleus in SE-NW direction. The continuum reddening peaks at ~5 magnitudes in A_{V}, while the Balmer extinction ranges to ~7 magnitudes. This implies a heavier dust content associated with sight lines to regions of ongoing star formation.

The dust extinction at the position of the nucleus as seen in near-IR is high in both plots. This explains well why the nucleus as seen in optical is offset 1″ to the North, where extinction is significantly lower. Also, both plots share a region of low extinction ~5″ East and ~1″ South to the East of the near-IR nucleus, while all nebular emission lines show a (secondary) peak at that position, see Fig. 5.6. The absence of dust extinction explains the prominence relative to the nucleus of the blue emission lines Hβ and [OIII]. Finally, the Balmer extinction map corresponds very well with the galaxy as seen in the optical from Väisänen et al. (2008), with prominent features in B-band coinciding with low local extinction. It confirms their observation that most of the dust is situated in the region SW of the nucleus.

5.3.5 Hα star formation rate

Hα luminosity is a well-established tracer of current star formation, once the underlying stellar absorption and attenuation due to dust has been taken into account (e.g., Catalán-Torrecilla et al., 2015, Davies et al., 2016). Spatially resolved star formation rates (SFR) were calculated based on the line flux of Hα after correcting for dust using the Balmer decrement. Bins with a AoN of < 5 in Hβ were masked out to prevent extreme F_{ac} values based on poor fits. The conversion from Hα line flux to SFR (Kennicutt, 1998) in solar masses per year is defined as:

$$\mathrm{SFR}\ (\mathrm{M}_{\odot}\mathrm{yr}^{-1}) = 7.9 \times 10^{-42} L(\mathrm{H}\alpha) \tag{5.3}$$

Here $L(\mathrm{H}\alpha)$ is the dust corrected luminosity in Hα:

$$L(\mathrm{H}\alpha) = 4\pi \times D_L^2 \times \mathrm{H}\alpha \times F_{\mathrm{ac}} \times 1.25 \tag{5.4}$$

with Hα the integrated line flux in erg/s/cm^2/Å as fitted by pPXF; D_L the luminosity distance in cm; and a factor 1.25 to account for the spectral pixel size of MUSE in Angstroms. The resulting SFR map of IRAS 18293-3413 is shown in Fig. 5.8. Star formation is concentrated along what appears to be a spiral arm in clockwise direction originating NW of the nucleus, similar to the structure visible in the Balmer extinction map, while the Hα peak North of the nucleus has become less prominent. This suggests a correlation between extinction in the line emitting region and the rate of star formation, which has been shown to be the case in starburst galaxies (Dopita et al., 2002), as well as in less intensely star forming spirals (Sarzi et al., 2018). This is further confirmed by the disappearance in the SFR map of the feature $\sim 5''$ East and $\sim 1''$ South of the nucleus, so prominently visible in the blue emission line maps, see Fig. 5.6. While this feature clearly exhibits nebular emission, it coincides with a region of little to no dust extinction, and as a result in the SFR map it decreases significantly relative to other dust-obscured regions. This displays the importance of dust correction when calculating the SFR of a galaxy.

The SFR from Hα integrated across all bins in the $16''$ by $16''$ stamp amounts to 55 $M_\odot$ yr^{-1}, compared to 2.9 $M_\odot$ yr^{-1} when not corrected for dust. This compares well with the SFR estimated from archival Spitzer 24μm flux (less affected by dust extinction) which, using the conversion relation from Alonso-Herrero et al. (2006), gives 51 $M_\odot$ yr^{-1}. The SFR inferred from a far-IR luminosity of $\log(L_{\rm FIR}) = 11.74\ L_\odot$ (see Chapter 2) amounts to 94.7 $M_\odot$ yr^{-1}, using the conversion from Kennicutt (1998):

$$\mathrm{SFR}\ (M_\odot\ \mathrm{yr}^{-1}) = \frac{L_{\rm FIR}}{5.8 \times 10^9\ L_\odot} \tag{5.5}$$

There is a significant discrepancy between the star formation based on Hα and the far-IR. This is not surprising: Rodríguez-Zaurín et al. (2011) found a median ratio of 0.06 for $\mathrm{SFR_{H\alpha}/SFR_{IR}}$ for sample of LIRGs using Hα without a reddening correction. For IRAS 18293-3413 this ratio is $2.9/94.7 = 0.03$, placing the galaxy well within the range of the values of their sample of LIRGs. They also reported a median value of 0.27 for $\mathrm{SFR_{H\alpha}/SFR_{IR}}$ using dereddened Hα. In our case this ratio is 0.58, and although on the higher end, this still falls well within the scatter shown by their sample. Note that in Rodríguez-Zaurín et al. (2011) the correction for reddening is only applied to the nuclear regions, and not across the whole galaxy as we have for IRAS 18293-3413. This could account for the relative large increase in the $\mathrm{SFR_{H\alpha}/SFR_{IR}}$ ratios between using reddened and dereddened Hα. It could also be that IRAS 18293-3413 is particularly dust affected for a LIRG. Finally, the remainder of the mismatch between $\mathrm{SFR_{H\alpha}}$ and $\mathrm{SFR_{IR}}$ is likely due to contributions to the IR flux that is completely obscured at optical wavelengths, or at least cannot be detected in

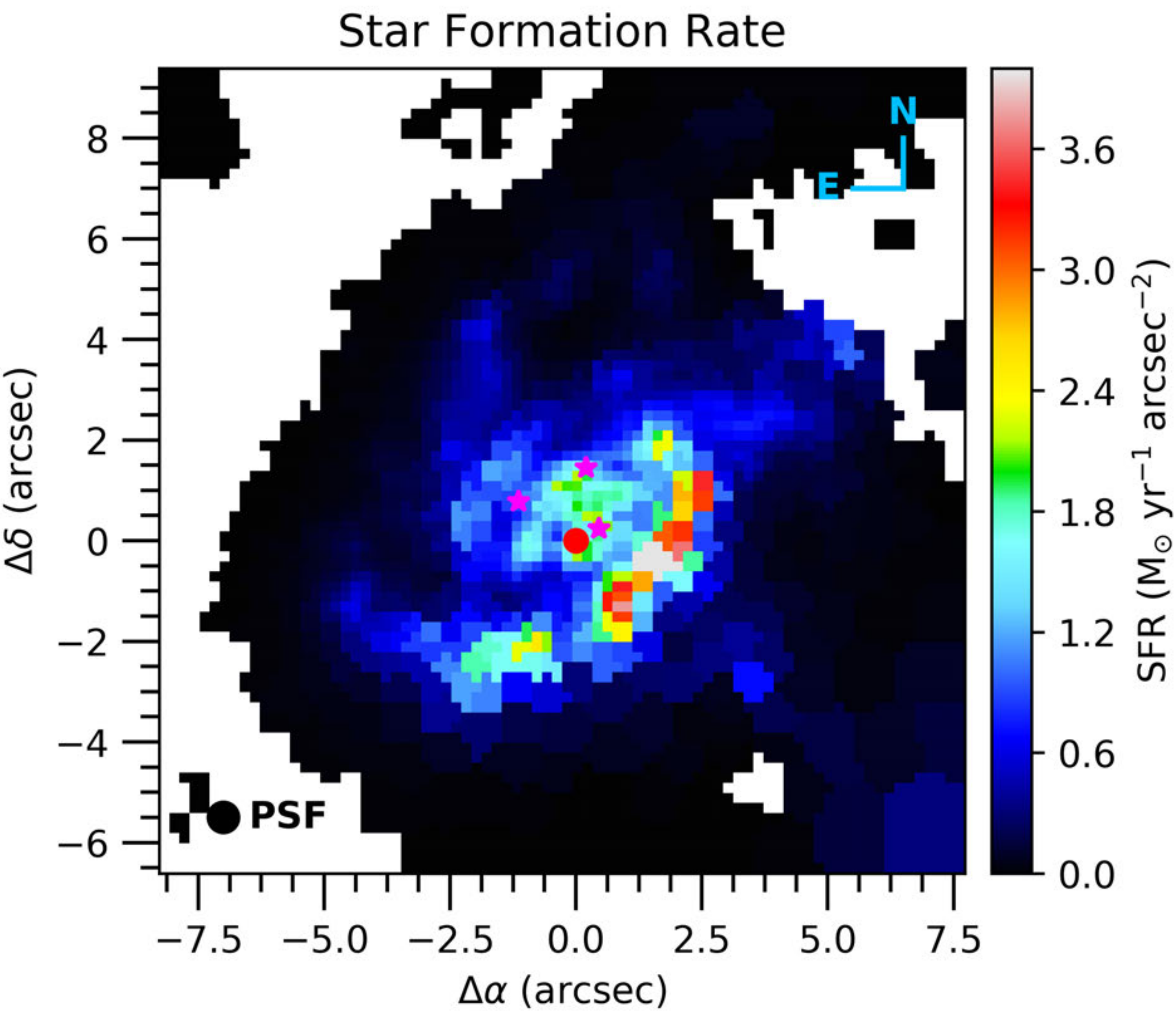

Figure 5.8: Star formation rate based on dust corrected Hα, with masking based on Hβ AoN requirement, see Section 5.3.5.

both Hα and Hβ, preventing dust correction. The Balmer dust correction will not account for this, while at longer wavelengths in the IR this is star formation that can be traced.

5.3.6 Hα equivalent width

Hα equivalent width (EW) is a measurement of how strong the emission line is compared with the continuum. Where Hα line flux is an indicator of ongoing star formation, Hα EW can be used to constrain the stellar population age. As stellar populations grow older the number of ionizing stars responsible for the Hα emission line, such as massive short-lived OB stars, will decline in numbers, while the number of lower-mass stars that contribute to the continuum remain constant. As a result Hα EW will decrease over time, assuming star formation has occurred in a single instantaneous starburst (Kuncarayakti et al., 2013, Levesque and Leitherer, 2013).

Hα EW was measured for every bin by dividing the line flux of Hα by the level of the continuum. The continuum was determined by taking the median of 50 spectral pixels on either side of the trio of Hα and [NII] emission lines. Typically it is assumed that emission lines and continuum are equally affected by extinction. However, given the observed differences in the complex dust distribution comparing the Balmer decrement and continuum reddening (Fig. 5.7), it was deemed appropriate to apply a separate extinction correction for Hα line flux and the continuum. Hα line flux was corrected based on the dust extinction calculated through the Balmer decrement, which itself is based on Hα and thus clearly can be seen as the intrinsic dust reddening affecting the emission line. As discussed the continuum was de-reddened using the reddening parameter produced by fitting the continuum with pPXF. The resulting Hα EW map is shown in the left panel of Fig 5.9. This map can be interpreted as a tracer of the age of youngest stellar population (< 100 Myr) resulting from the most recent instantaneous starburst. Similarly to the star formation map, there is a clear sign of the Southern spiral arm. Additionally a spiral arm structure to the North of the nucleus is visible extending to the NW.

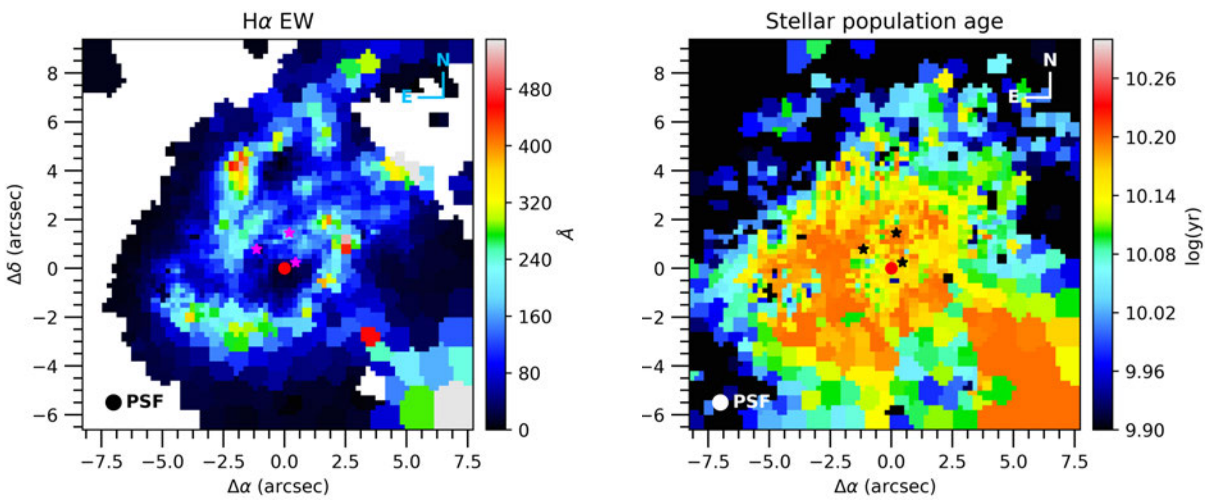

Figure 5.9: Hα EW corrected for dust extinction and continuum reddening on the left, see Section 5.3.6. Continuum fitted stellar population age on the right.

The right panel of Fig 5.9 shows the mass-weighted mean age of the stellar population(s) that contribute to the continuum, derived from fitting the continuum with pPXF. The continuum fit comes from a combination of stellar population models from Vazdekis et al. (2010), and the resulting mass-weighted mean age is derived from the combination of these models fitted by pPXF. As opposed to Hα EW, this traces the underlying older (»100Myr) population. Whereas the Hα EW map is very localized to the spiral arm structure, the continuum ages show a relatively old stellar population distributed fairly uniformly across the inner 4″ of the galaxy.

5.3.7 Metallicity and ionization source

Gas metallicity is an important tool to investigate the evolution of the star formation history of a galaxy. Measuring metallicity requires information on the gas temperature for a precise determination, the measurement of which is typically not possible in distant galaxies. Instead more commonly gas metallicity is determined using calibrated flux ratios of strong emission lines. One such ratio is O3N2, first introduced by Alloin et al. (1979):

$$\mathrm{O3N2} = \log \frac{[\mathrm{OIII}]\lambda 5007/\mathrm{H}\beta}{[\mathrm{NII}]\lambda 6583/\mathrm{H}\alpha} \tag{5.6}$$

This emission line diagnostic is widely used in the literature because of its insensitivity to dust reddening due to the small separation in wavelength of the emission lines used and the ease by which it can be measured. In this chapter metallicity is expressed as oxygen abundance, using the calibration introduced by Pettini and Pagel (2004):

$$12 + \log\,(\mathrm{O/H}) = 8.73 - 0.32 \times \mathrm{O3N2} \tag{5.7}$$

Fig. 5.10 shows the map of 12 + log(O/H) as obtained through the O3N2 method in the left panel. This map has not been corrected for reddening as the ratio of the flux of emission lines that spectrally lie close together is not sensitive to reddening. An AoN of > 5 was required for all four emission lines of the O3N2 diagnostic, which led to the masking of ~20% of the bins as seen in the figure, primarily a result of faint or non-existent Hβ or [OIII]. In the right panel the metallicity as derived from fitting the continuum with pPXF is shown. It is expressed as [Z/H], as the conversion to an oxygen scale to match the gas metallicity is not well defined (Nicholls et al., 2017). The emission line derived metallicity clearly peaks in the nuclear regions, whereas the continuum fitted metallicity associated with the stellar population peaks locally just South of the nucleus but is also high in the outer regions.

The line flux ratios used in the O3N2 method also form the axes of the most commonly used BPT diagram (Baldwin et al., 1981). This nebular emission line diagram is used to distinguish the ionization mechanism of nebular gas between HII regions and similar sources that are ionized by hot stars and related to star formation, and those that are ionized due to the presence of an active galactic nucleus or heated by shocks. Fig. 5.11 shows all bins that meet the aforementioned AoN requirement plotted on the BPT diagram, with a solid line indicating theoretical divisions (Kewley et al., 2001) and a dashed line empirical divisions (Kauffmann et al., 2003) between the different classes of objects. The plotted bins are colour coded based on the radial distance in arcseconds from the nucleus as seen in the near-IR. The line ratios at the SN positions are also shown, by

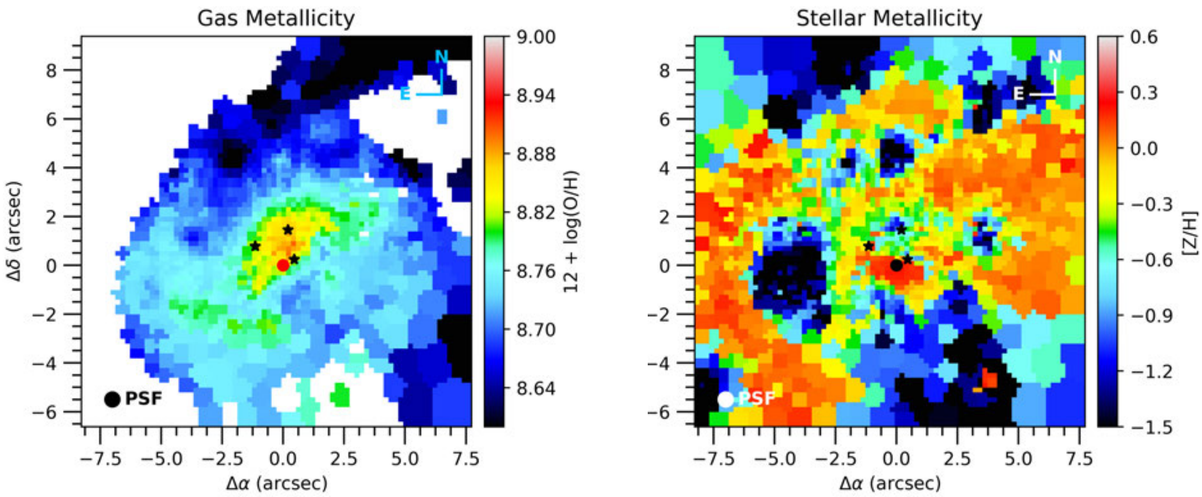

Figure 5.10: Oxygen abundance as calculated using the O3N2 method, expressed in 12 + log(O/H) on the left, see Section 5.3.7. Continuum fitted stellar metallicity on the right.

summing the line fluxes of all the spaxels within one 0.6″ seeing disk of a SN position. The bins that lie on the right of the solid line distinguishing the regions related to star formation (left) and AGN/shocks (right) have also been masked in the metallicity map, as the presence of shocks may affect the O3N2 diagnostic, independent of metallicity. As can be seen in the figure only a few bins have line ratios indicative of shocks and/or AGN. None of these bins lie near the nucleus so the presence of an AGN is unlikely. This agrees well with Risaliti et al. (2000), who found no evidence for any AGN contribution to the X-ray spectrum of IRAS 18293-3413. The SNe all lie in the region dominated by star formation.

5.3.8 Supernova sites

IRAS 18293-3413 has been host to two documented core-collapse supernovae: SN 2004ip and SN 2013if. SN 2004ip was discovered in the near-IR using AO-imager NACO on the VLT (Mattila et al., 2007), located 1.4″ (or 500 pc) projected distance from the nucleus, see Fig. 5.2. The discovery of SN 2013if was discussed in Chapter 2. In addition to these two published discoveries there has been a third CCSN discovery in IRAS 18293-3413, AT 2012xx, as was discussed in Chapter 4. Table 5.1 shows the subtypes and extinction determined through light curve fitting of these three SNe.

In order to accurately identify the SN sites in the MUSE data, the astrometry in the MUSE cube was matched with the near-IR AO image of IRAS 18293-3413 obtained with GeMS/GSAOI. Using centroiding in IRAF, the positions of four bright, compact sources in the IR image were determined with respect to the galaxy nucleus. The same four sources were identified in the MUSE cube, and

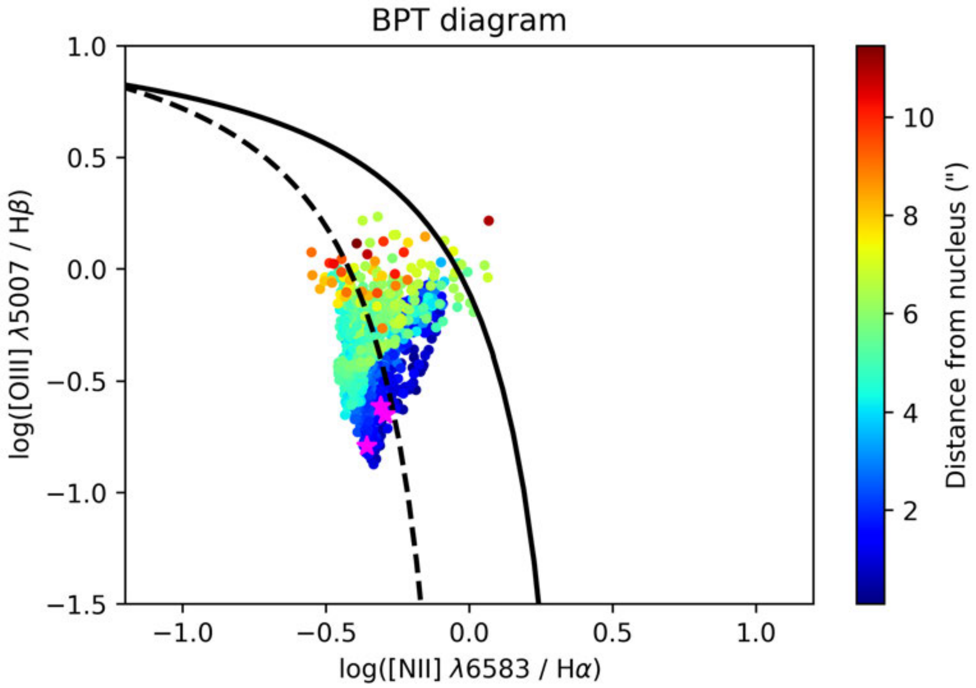

Figure 5.11: The BPT-NII diagram, distinguishing spaxels based on emission line ratios between primarily star forming (to the left of the solid line) and those affected by an AGN or heated by shocks (right of the solid line). The SN positions are indicated by the magenta stars.

the position of the nucleus identified as the average position from the offsets from the four field stars. With the nucleus at the (0,0) position, SN locations were then identified based on the offset in arcseconds determined in the near-IR AO discovery images or those reported in literature. The astrometric error was calculated by taking the square root of the quadratic sum of the centroiding uncertainties and the standard error of the mean of the four field star offsets. This resulted in an uncertainty of the alignment of the MUSE cube with the GSAOI image of 0.02″, which is within one MUSE spaxel.

The AO corrected FWHM of the MUSE data is 0.6″ and as a result the SN environments are defined here as the average across all spaxels within a 0.3″ radius (corresponding to 120 pc) of the SN positions. The astrometric uncertainties of the SN positions and the alignment are much smaller than 0.6″, so we do not include any additional margin to account for these. Table 5.1 shows the local conditions of the three supernovae, as well as the relevant light curve fitting results. Because the SN apertures consisted of 7-8 spaxels in a region with high signal-to-noise, the formal AoN ratios of the emission lines used to derive the properties in the table are very high (>100), so the formal statistical errors are therefore negligible. This means the errors will be driven by systematic uncertainties, and we assign a conservative error of 1% to the derived properties in the table to reflect this. The exception is the metallicity, where the uncertainty associated with the

Supernova	SN 2004ip	AT 2012xx	SN 2013if
Subtype	II	IIP	IIP
A_V (light curve fit)	5-40	$1.8^{+1.3}_{-0.9}$	$0.0^{+2.5}_{-0.0}$
A_V (Balmer decrement)	3.59	2.70	3.84
A_V (Continuum fit)	3.07	1.60	3.61
SFR density ($M_\odot$ yr^{-1} arcsec^{-2})	0.9	1.4	2.0
Hα EW (Å)	74	166	71
Metallicity (12 + log(O/H)	8.8±0.1	8.9±0.1	8.8±0.1

Table 5.1: The properties and environment conditions of the SNe in IRAS 18293-3413. Subtypes and light curve fitted extinctions are from Mattila et al. (2007) (SN 2004ip), Chapter 2 (SN 2013if), and Chapter 4 (AT 2012xx), and the local properties derived in this chapter. Errors to the derived properties are estimated to be 1% with the exception the metallicity, as discussed in the text.

O3N2 method is of order 0.1 dex (Pettini and Pagel, 2004). Note that the table does not show the summed SFR across the selected spaxels, but instead the SFR surface density so it can be compared to the values in Fig. 5.8.

5.4 Discussion

5.4.1 Do supernovae trace star formation in IRAS 18293-3413?

We expect CCSNe to trace ongoing star formation well, as CCSN progenitors are massive stars ($\gtrsim$ 8 $M_\odot$; Smartt, 2009) with relatively short lifetimes. Through project SUNBIRD we have obtained a large sample of exquisite AO observations of LIRGs having hosted CCSNe, but at the high spatial resolution provided by AO most CCSNe often did not coincide with structure as seen in K_s-band, see for example SN 2013cb in NGC 3110 (Chapter 2) and AT 2017jzy and the archival NICMOS transient in NGC 695 (Chapter 3). This is surprising, as in starburst galaxies the light from red supergiants is expected to dominate K_s-band (Engelbracht et al., 1998), which would make K_s-band a good tracer of recent SF. Kangas et al. (2013) investigated the association of CCSNe with several SFR tracers in starburst galaxies, and concluded that K_s-band traced SNe as well as Hα does. However, this was based on seeing limited observations, which will not have resolved near-IR structure as well as our AO observations have. It is worth noting our observed scarcity of SNe coinciding with near-IR bright structure does not appear to be a result of lack of detection

Bin ($M_\odot$ yr^{-1} arcsec^{-2})	Surface area (arcsec^2)	Total SF rate ($M_\odot$ yr^{-1})	Number of SNe
0.0 - 1.0	175.12	29.56	1
1.0 - 2.0	10.68	14.85	2
2.0 - 3.0	1.84	4.40	0
> 3.0	1.64	6.24	0

Table 5.2: The surface area and total SF rate in spaxels binned by SF rate density. Although the total size of the spaxels in the two bins with the highest SF rate density is small, the total SF rate in those spaxels is significant. However, no SNe have been detected in these bins. As described in the text, this could be related to dust extinction, although the sample size is too small to draw definitive conclusions.

efficiency. With the exception of the brightest innermost nuclei such as in IRAS 18293-3413 as shown in Section 2.8.6, we have shown we are capable of extracting a SN signal coincident with a bright background or compact object with the detections of SN 2013if (Chapter 2) and AT 2016jhy (Chapter 3). The discovery magnitudes of SN 2013if and AT 2016jhy of 18.53 and 18.10, respectively, were typical for the CCSNe discovered in project SUNBIRD. So, one of the main questions we aim to answer with this MUSE data set is whether, as opposed to AO K_s-band, ongoing star formation as traced by Hα *does* associate with our SNe, even at high spatial resolution.

Fig. 5.8 shows the SFR across IRAS 18293-3413, with the SN positions indicated. SFR in the galaxy peaks at ~4-5 $M_\odot$ yr^{-1} arcsec^{-2} and is concentrated along what appears to be a spiral arm south of the nucleus in a NW to SE direction. The SNe are positioned on the opposite side of the nucleus, with SFR within a 0.3″ error circle ranging from 0.9 $M_\odot$ yr^{-1} arcsec^{-2} for SN 2004ip to 2.0 $M_\odot$ yr^{-1} arcsec^{-2} for SN 2013if, see Table 5.1. It appears that, although the SN sites coincide with a region of relatively high SFR compared to the galaxy as a whole, they do not align with the spiral arm where star formation is focused, or align well with SFR as traced by Hα. We can quantify this by summing the dust corrected SF rate in the spaxels binned by SF rate density, see Table 5.2. No SNe have been discovered in the two bins with the highest SF rate density spaxels. While they are small in size, the two bins have a total SF rate of 10.64 $M_\odot$ yr^{-1}, comparable to the SF rate in the bin in which two SNe have been discovered.

This could be explained by the light curve derived subtypes of the CCSNe in this galaxy, as all three are believed to be Type II/IIP SNe. Anderson et al. (2012) found that Type IIP SNe do not closely follow star formation as compared with other CCSN subtypes, due to the relatively long-lived progenitors of Type IIP SNe. A different scenario is offered by Fig. 5.7, which shows the extinction in A_V affecting Balmer emission. The spiral arm along which star formation is peaking is also heavily affected by dust extinction. While this does not affect the intrinsic CCSN rate, it does reduce the efficiency at which they can be detected. The LIRGs in project SUNBIRD and preceding programs, from which the SN discoveries in IRAS 18293-3413 are a result, have been observed in near-IR so as to be less affected by the large amounts of dust present in LIRGs. However, even in the near-IR the effects of dust extinction will still reduce the duration for which a CCSN is bright enough to be detected, if at all.

The observed SNe in IRAS 18293-3413 were found in large part due to the relatively high local SFR. But their observability, meaning the duration for which they stood out from the host galaxy, was just as important. In Chapter 2 the SN recovery efficiency was modelled for IRAS 18293-3413 as a function of radius from the nucleus, and it was shown near the nucleus the efficiency at which simulated SNe were recovered was severely inhibited due to the effects of crowding and a bright background. This is one aspect of observability, but we also would expect SN recovery efficiency to be affected as a function of dust extinction. While it is beyond the scope of this chapter to create a model converting intrinsic SFR and dust extinction into a SN detection likelihood map, there is a natural way to approximate this. Observed Hα, not corrected for dust extinction, can be interpreted as a superposition of both SFR and dust extinction and as such is a tracer of SN detection likelihood: regions of high SFR (and thus high CCSN rate) and low extinction will be bright in Hα. Fig. 5.6 shows the observed Hα map of IRAS 18293-3413, and in fact all three SN sites are clumped around the local Hα peak, making clear observed Hα does associate with the SNe in this data set. This agrees well with the results of Anderson et al. (2012) and Kangas et al. (2013), both of which were based on observed Hα.

Compiling all the relevant parameters, we show in Fig. 5.12 the Balmer extinction versus SFR for all bins, coloured by observed Hα flux. The values derived at the SN positions have been indicated by magenta stars. As expected from Dopita et al. (2002), there is a clear positive trend of SFR with dust extinction. The plot also clearly shows how observed Hα relates to both SFR and extinction through the coloured layering: at a given SFR it is strongest in the bins with the lowest dust extinction. We would expect a similar trend for our CCSNe. To first order intrinsic CCSN rate will increase with SFR, while observability will decrease with dust extinction, which means in this plot we expect SNe to skirt the bottom envelope of the distribution. This is indeed the case for two SNe, while one SN falls in a region of moderate extinction at relatively low SFR. This is SN 2004ip, potentially the highest extincted SN discovery in the literature with 5-40 magnitudes extinction in

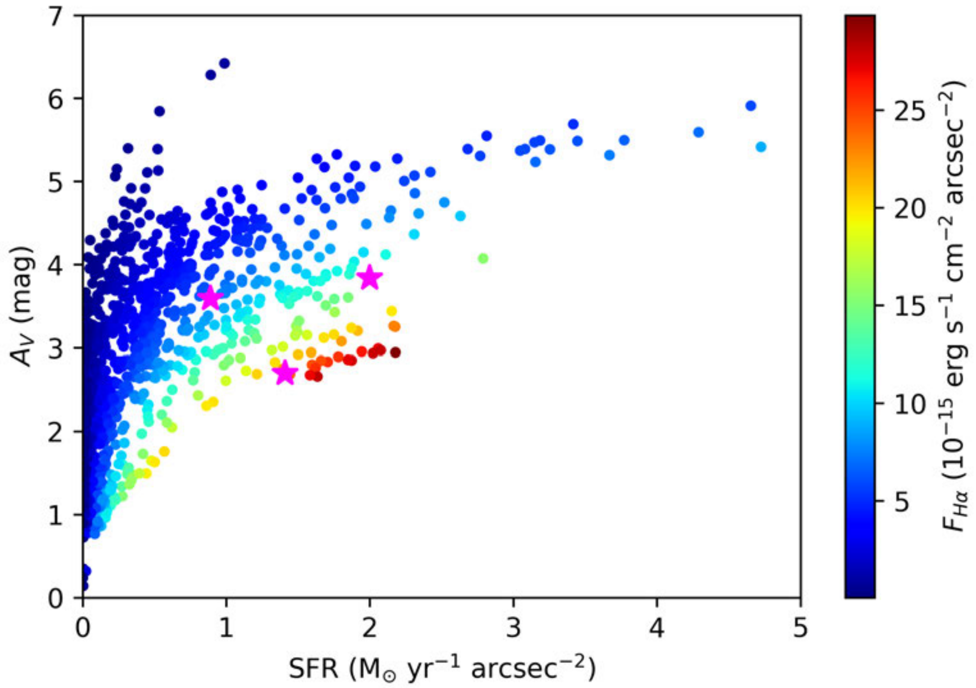

Figure 5.12: Extinction based on the Balmer decrement versus star formation rate for all bins shown in Fig. 5.8, see Section 5.4.1. The bins are colour coded by raw Hα, as plotted in Fig. 5.6. The local values at the positions of the SNe are indicated as magenta stars.

V (Mattila et al., 2007), which means it would have had a very short window of observability. This makes it an outlier in terms of observability, which explains its position in the plot.

Supernovae studies typically correct for missed nuclear SNe due to crowding, by using recovery efficiency experiments as described in Chapter 2. This case study clearly shows that in order to correct observed CCSN rates for the effects of dust extinction, it is vital in a dusty galaxy such as a LIRG to understand the relation between SN positions, dust extinction and star formation rate, at high spatial resolution. Simply stated, the fact that the SNe that we have observed all are located in a region of relatively high SFR and low extinction, implies we are not detecting a larger population of CCSNe that should occur in the regions with both the highest SFR and largest dust extinction. IFU data such as obtained with MUSE+GALACSI can now provide the spatial information necessary to resolve the detailed structure in LIRGs in Hα and Hβ, and through those Balmer extinction and SFR. This type of data proves to be essential to first properly convert the sample of SNe discoveries from project SUNBIRD to observed CCSN rates, and finally the determination of the missed SN fraction that affects current, and will affect future wide-field optical surveys.

5.4.2 A measure of dust morphology by comparing extinction tracers

By fitting the light curves of the SNe in IRAS 18293-3413 to templates, we have obtained measurements of the dust extinction affecting the SN light. The SNe have a fixed position, so they act as point tracers for dust extinction. The nebular emission is integrated along the line of sight of a region limited by spatial resolution, and the associated Balmer extinction can be interpreted as a weighted average. A comparison of these two independent tracers of dust extinction could provide information about the distribution of dust in the local SN environment, in particular if there is a trend across all three SNe in the comparison of the immediate SN extinction and the local average.

SN 2004ip was best fitted with a Type II light curve with an extinction in A_{V} of 5-40 magnitudes. While this is a poorly constrained range, even with 5 magnitudes it can be considered one of the more extincted SN discoveries in LIRGs, see Table 4.2. The extinction obtained through the Balmer decrement at the site of SN 2004ip is 3.59, see Table 5.1. With SN 2004ip more dust affected than the integrated local nebular emission, this is an indication that the progenitor could have been relatively dust enshrouded.

In the case of AT 2012xx the two different measurements agree within error, with $1.8^{+1.3}_{-0.9}$ magnitudes for the immediate SN extinction and 2.7 magnitudes for the local average extinction. However, in contrast with SN 2004ip the light curve of SN 2013if was fitted with little to no extinction, see Chapter 2. It was shown that although other CCSN subtypes could not be excluded, all template fits included an extinction of zero with a ~2.5 magnitude error. This is curious, because at the site of SN 2013if the dust extinction obtained through the Balmer decrement is the highest of all three SN sites, 3.53 magnitudes in A_{V}. Negligible extinction must mean the SN occurred in the foreground, or was located along a line of sight affected by unusually low extinction. In either case, there is no indication that its progenitor was dust enshrouded.

Based on these three events, there appears to be tension between the two different dust tracers. This indicates that the dust composition is not uniform at the spatial scale provided by MUSE, which in this case is ~120 pc. The local average measurement of extinction using the Balmer decrement is fairly robust with a high AoN, but due to limited epochs the light curve fitted SN extinctions will have larger uncertainties. In order to discern trends between these different dust tracers, a larger sample of high spatial resolution MUSE observations of the other CCSNe discovered in LIRGs would be required.

5.4.3 Constraining SN type through Hα EW

The SNe subtypes presented in Table 5.1 have been obtained through light curve fitting, but given the limited number of epochs available for these SNe this is not as reliable as spectroscopic typing. We explore whether the local environment can provide additional constraints to the subtypes, by constraining progenitor age and mass limits using Hα EW.

Hα EW can be converted to a stellar population age using simple stellar population (SSP) models from Starburst99 (Leitherer et al., 1999), assuming the local metallicity to be representative for the local stellar population. The age determined this way is the age of the most recent star formation event, as shown by Kuncarayakti et al. (2013). Kuncarayakti et al. (2016) have shown these models to be reliable for analysing young stellar populations with MUSE. If we assume the SN progenitor has been born in situ, the age of the youngest stellar population is a lower limit to the age of the SN progenitor, as the SN progenitor could have been born in a previous starburst. Using stellar evolution models the SN parent stellar population age can be converted into a SN progenitor initial mass, since stellar mass is the main driver of the lifetime of a star. As the age is a lower limit, the mass determined this way will be an upper limit. Such progenitor age and mass limits in turn could provide additional constraints to the SN subtype, as it is believed CCSN subtypes can have distinct ranges of progenitor masses (Smartt, 2009).

Table 5.1 shows the Hα EW for the three SN sites, ranging from 71 Å for SN 2013if to 166 Å for AT 2012xx. Fig. 5.13 shows the time evolution of Hα EW, adapted from Kuncarayakti et al. (2013), using Starburst99 models with a Salpeter IMF with α = 2.35 and M_{up} = 100 $M_\odot$. The Hα EW values of SN 2013if and AT 2012xx are overplotted as stars, with SN 2004ip not plotted as it would overlap with SN 2013if. As can be seen the SNe values represent a narrow range in age and mass, and is relatively insensitive to metallicity, indicated by black solid and striped lines, or the IMF used, with red and orange dotted lines the models for α = 3.30 and M_{up} = 100 $M_\odot$ and α = 2.35 and M_{up} = 30 $M_\odot$, respectively. The local SN Hα EW values correspond to an age for the youngest stellar population of ~6 Myr, which if we assume that to be the lower age limit of the progenitor, corresponds to an upper progenitor initial mass limit of ~30 $M_\odot$. Note that in the case of continuous SFR instead of a single starburst, there is no strong relation between Hα EW and age because stars are being formed continuously.

Based on light curve fitting SN 2004ip, AT 2012xx and SN 2013if have been typed Type II, IIP and IIP, respectively. Type IIP SNe are the most common Type II SNe and based on pre-explosion observations are thought to have the oldest and least massive CCSN progenitors with masses ranging to ~16.5 $M_\odot$ (Smartt, 2009). This falls well within our observed upper mass limit of ~30

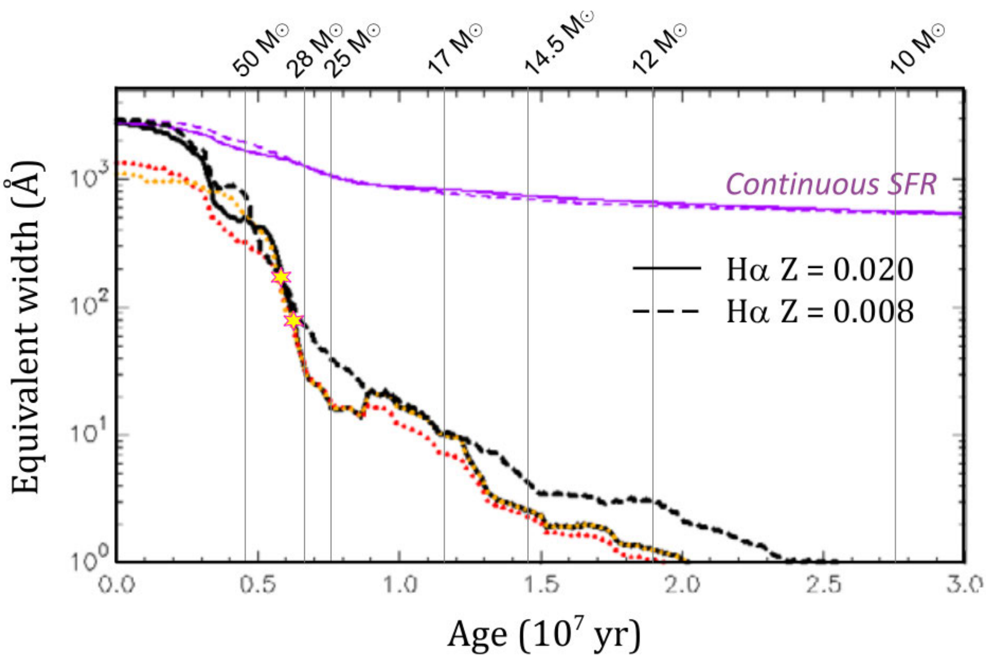

Figure 5.13: Shown by the solid black line is the evolution of Hα EW with time, assuming a single burst of star formation, using simple stellar population model Starburst99 with a Salpeter IMF with α = 2.35 and M_{up} = 100 $M_{\odot}$ and solar metallicity (Z = 0.02). The striped black line shows the model with subsolar metallicity, and the dotted lines different IMFs with α = 3.30 and M_{up} = 100 $M_{\odot}$ in red and α = 2.35 and M_{up} = 30 $M_{\odot}$ in orange. The Hα EW values of SN 2013if and AT 2012xx are indicated as yellow stars. The purple line shows the case of continuous star formation. The indicated masses associated with the ages are based on Padova stellar evolution models from Bressan et al. (1993) (Z = 0.02) and Fagotto et al. (1994) (Z = 0.008). Figure is adapted from Kuncarayakti et al. (2013).

$M_{\odot}$. Type Ib and Ic are thought to have more massive progenitors (Anderson et al., 2012). Through an environment study Kuncarayakti et al. (2017) obtained median initial masses of ∼30-33 $M_{\odot}$ for stripped envelope Type IIb/Ib/Ic SNe, assuming a single progenitor. This suggests that a stripped envelope SN scenario is unlikely for the three CCSNe discovered in IRAS 18293-3413, which is supported by the subtypes determined through light curve fits.

An important caveat to this method is the contribution to the continuum from an underlying older stellar population. Although a young stellar population will typically be much brighter at Hα, the contribution from an old population to the continuum could become significant at large mass fractions, such as found in the nuclear regions. This means that the continuum has increased, and Hα EW decreased, unrelated to the age of a single starburst. This would dilute Hα EW, in particular in regions of relatively weak Hα EW. We see in Fig. 5.9 from the continuum fit that an older population is present throughout the galaxy. A more sophisticated approach to obtain a more complete understanding of the local star formation history, and subsequently the age of the most recent starburst, would include both modelling of the recent (<100 Myr) star formation activity together with the underlying older (»100 Myr) population. Such methods are becoming available (e.g. Leja et al., 2017), but so far have not been extensively applied to IFU data.

This caveat has less impact on strong Hα EW, which in Fig. 5.9 is shown to trace the spiral arms. Where star formation as traced by Hα is primarily situated along the southern spiral arm, Hα EW peaks further along this spiral arm to the West, as well as along a spiral arm structure in the North. This means that the stellar continuum in those regions must be much weaker relative to Hα, so we expect a low stellar density. The near-IR image shown in Fig. 5.2 supports this view, with a lot of flux along the spiral arm nearest to the nucleus, but almost none further away from the nucleus. This could mean star formation has not been ongoing there, but triggered more recently than in the nuclear regions, potentially due to interaction with the companion NW from the galaxy (see Fig. 5.1). Large scale features such as these will be further investigated in an upcoming publication.

5.5 Summary

In this chapter we have presented optical IFU observations of SN factory IRAS 18293-3413 obtained with the MUSE facility, the combination of the state-of-the-art optical IFU spectrograph MUSE supported by its new AO system GALACSI. Based on this rich data set we have derived the properties of the stars, gas and dust in this LIRG, as well as the local conditions at the sites of three CCSNe. The unprecedented spatial resolution offered by MUSE in AO mode revealed a galaxy with complex structures in nebular emission, dust and SFR.

Based on the distribution of Hα, SFR and dust extinction as traced by the Balmer decrement, we find that the CCSNe hosted by IRAS 18293-3413, while located in regions with star formation, do not trace peak SFR well. Instead, they are clustered around the nuclear peak of observed, not dust-corrected, Hα. We conclude that the CCSNe positions are better traced by a combination of high SFR and low dust extinction, naturally traced by observed Hα. In addition to the effects of crowding and a bright background, this is an aspect of SN observability that will be crucial when determining the fraction of CCSNe that will be missed in SN surveys.

Additionally we use the relation between Hα equivalent width and stellar population age to place environmental limits on the ages and initial masses of the CCSN progenitors. The mass limits derived this way support the subtype of Type II derived for the SNe through light curve fitting. Although the method has certain caveats and uncertainties, the mass limit appears to exclude the more massive progenitors of Type IIb/Ib/Ic SNe. Finally, we compare the differences between the immediate SN extinction as derived from their light curves, and the local average extinction determined through the Balmer decrement. Between the three CCSNe we observe no trend but instead there appears to be tension between the two dust tracers, which is most likely related to structure in dust not resolved by MUSE.

6

Conclusions and future work

At the start of this thesis we showed that current observed CCSN rates are affected by statistical and systematic uncertainties, which severely hamper our ability to use CCSNe as an alternative tracer for the cosmic star formation history. Where upcoming next-generation survey telescopes such as ZTF and LSST will reduce statistical uncertainties by dramatically increasing the CCSN sample, any optical seeing-limited SN survey remains affected by systematic uncertainties, such as due to dust extinction and limits in spatial resolution. In 2015 we commenced with project SUNBIRD (Supernovae UNmasked By Infra-Red Detection), a targeted SN survey aimed to characterize the population of CCSNe that explode in the crowded and dust-obscured nuclear regions of luminous infrared galaxies (LIRGs), to improve the limits of the fraction of CCSNe that are and will be missed in this regime by wide-field optical SN surveys. In order to uncover CCSNe in LIRGs, we observed in the near-IR, which is less affected by dust extinction than the optical, with the use of state-of-the-art laser guide star adaptive optics (AO) imagers GeMS/GSAOI on the Gemini South telescope and NIRC2 on the Keck II telescope. The spatial resolution provided by AO is critical to discern the CCSN point sources against the bright and crowded background in the nuclear regions of LIRGs.

In this thesis we have shown the results and evaluated the efficiency of project SUNBIRD.

During the observing programs with GeMS/GSAOI and NIRC2 we obtained a total of ~90 epochs of AO imaging across a sample of 38 LIRGs. We discovered four photometrically confirmed CCSNe, and an additional five CCSN candidates. This included SN 2013if in IRAS 18293-3413, one of the most nuclear CCSN ever discovered in LIRGs with a projected distance to its host's nucleus of 0.5″ or 0.2 kpc. We also discovered AT 2017chi in NGC 5331 with, based on fitting its light curve, an extinction measure of 11.8 magnitudes in V-band, which makes it one of the most extincted SNe ever discovered. Finally we presented the discovery of AT 2017gbl in IRAS 23436+5257, an extremely near-IR bright transient superimposed on its host's nucleus. We conclude this is likely to be a tidal disruption event, making it the third TDE to have been discovered in a LIRG, strengthening the notion that LIRGs show an over-abundance of this rare type of transient.

To evaluate the impact of an AO-assisted SN survey in the near-IR we composed a sample of all CCSNe discovered in LIRGs in the optical and the IR. This included all CCSNe reported in the literature, the CCSNe and (archival) CCSN candidates discovered in project SUNBIRD, and three unpublished CCSNe (candidates) discovered with VLT/NACO. First, based on this sample we show that SN detection in LIRGs using near-IR observations is more efficient than in the optical, likely as a result of reduced effects of dust extinction. Second, we show that in the near-IR SN detection using AO is more efficient than in natural seeing conditions, likely as a result of spatial resolution. This is demonstrated by the distribution in radial offset from the nucleus of all CCSNe in our sample. Whereas the optical and near-IR non-AO discoveries drop off in the central kpc of LIRGs, the number of AO CCSN discoveries increases dramatically. This is confirmation that AO is critical to building a statistical sample of CCSNe in dust-obscured and crowded regions, required to accurately determine the fraction of CCSNe that are missed in this regime.

Finally, we show that a detailed understanding of the distribution of star formation and dust extinction in LIRGs will play a crucial role in determining the CCSN rate we expect to observe in a given galaxy. Our case study of SN factory IRAS 18293-3413, using optical IFU data from the cutting-edge AO-assisted MUSE facility, shows that the detection of SNe even at near-IR wavelengths is still highly dependent on the local dust conditions. The three CCSNe discoveries in IRAS 18293-3413 from near-IR AO surveys do not align well with the peak of (dust-corrected) star formation rate in the galaxy, as would have been expected given the relation between CCSNe and star formation. Instead they are better traced by observed (uncorrected) Hα, which scales linearly with star formation rate, but is affected by dust extinction. The fact that all three SN discoveries are located around regions of Hα emission with moderate SFR and extinction, combined with the empirical finding that high star formation rates are also associated with high extinction, implies the presence of a population of CCSNe tracing the highly-extincted SFR peak that are still not being observed.

Future work

During the course of project SUNBIRD and its preceding AO-assisted programs, we have discovered 11 photometrically confirmed CCSNe, as well as 7 CCSN candidates, based on a sample of ~250 observations using AO. This sample is expected to increase, as project SUNBIRD is an ongoing program with time currently scheduled on the Subaru telescope using its laser guide star AO imager IRCS. Based on the current discoveries and coverage, our collaboration is working on the determination of our observed CCSN rate. Although our method of detection has been demonstrably more efficient than the alternatives, in order to so, we also have to account for our limitations in detection efficiency. As was shown in Section 2.8.6, this is done by simulating artificial sources in a given epoch. The results of this experiment depends on image quality and galaxy morphology, and as such has to be done across all epochs. A comprehensive analysis covering all our facilities is due later this year (Reynolds et al., in prep).

As the case study with MUSE has shown, the distribution of dust and star formation in a galaxy as determined through high spatial resolution IFU data addresses a crucial aspect of SN observability. Spectroscopic information across galaxies at this level of spatial resolution has not been available before, so fully incorporating this kind of data into the determination of our SN recovery efficiency will require methods that are not yet developed. Our first objective is to perform this experiment using the data set of IRAS 18293-3413, and subsequently obtain MUSE+GALACSI observations of all LIRGs in our sample.

The expansion of the sample of LIRG observation with MUSE+GALACSI will also let us investigate the population of LIRG CCSNe in terms of local SN environment. Environmental SN study is an active field of research, but due to limitations in sample size this kind of work has not been performed in starburst galaxies. Through project SUNBIRD we not only have an increased CCSN sample in LIRGs, but also a large sample of high spatial resolution near-IR observations. Complementary AO-assisted MUSE observation would make this a powerful data set with which we can investigate not only the effects of extinction, but also large scale dynamics and local SN conditions in LIRGs, as explored in Chapter 5.

References

Adams, S. M., Kochanek, C. S., Beacom, J. F., Vagins, M. R., and Stanek, K. Z. (2013). Observing the Next Galactic Supernova. *ApJ*, 778:164.

Alard, C. (2000). Image subtraction using a space-varying kernel. *A&AS*, 144:363–370.

Alard, C. and Lupton, R. H. (1998). A Method for Optimal Image Subtraction. *ApJ*, 503:325–331.

Alloin, D., Collin-Souffrin, S., Joly, M., and Vigroux, L. (1979). Nitrogen and oxygen abundances in galaxies. *A&A*, 78:200–216.

Alonso-Herrero, A., García-Marín, M., Monreal-Ibero, A., Colina, L., Arribas, S., Alfonso-Garzón, J., and Labiano, A. (2009). PMAS optical integral field spectroscopy of luminous infrared galaxies. I. The atlas. *A&A*, 506:1541–1562.

Alonso-Herrero, A., Rieke, G. H., Rieke, M. J., Colina, L., Pérez-González, P. G., and Ryder, S. D. (2006). Near-Infrared and Star-forming Properties of Local Luminous Infrared Galaxies. *ApJ*, 650:835–849.

Anderson, J. P., Habergham, S. M., James, P. A., and Hamuy, M. (2012). Progenitor mass constraints for core-collapse supernovae from correlations with host galaxy star formation. *MNRAS*, 424:1372–1391.

Arcavi, I., Gal-Yam, A., Cenko, S. B., Fox, D. B., Leonard, D. C., Moon, D.-S., Sand, D. J., Soderberg, A. M., Kiewe, M., Yaron, O., Becker, A. B., Scheps, R., Birenbaum, G., Chamudot, D., and Zhou, J. (2012). Caltech Core-Collapse Project (CCCP) Observations of Type II Supernovae: Evidence for Three Distinct Photometric Subtypes. *ApJ*, 756:L30.

Arribas, S., Colina, L., Monreal-Ibero, A., Alfonso, J., García-Marín, M., and Alonso-Herrero, A. (2008). VLT-VIMOS integral field spectroscopy of luminous and ultraluminous infrared galaxies. I. The sample and first results. *A&A*, 479:687–702.

Bacon, R., Accardo, M., Adjali, L., Anwand, H., Bauer, S., Biswas, I., Blaizot, J., Boudon, D., Brau-Nogue, S., Brinchmann, J., Caillier, P., Capoani, L., Carollo, C. M., Contini, T., Couderc, P., Daguisé, E., Deiries, S., Delabre, B., Dreizler, S., Dubois, J., Dupieux, M., Dupuy, C., Emsellem, E., Fechner, T., Fleischmann, A., François, M., Gallou, G., Gharsa, T., Glindemann, A., Gojak, D., Guiderdoni, B., Hansali, G., Hahn, T., Jarno, A., Kelz, A., Koehler, C., Kosmalski, J., Laurent, F., Le Floch, M., Lilly, S. J., Lizon, J.-L., Loupias, M., Manescau, A., Monstein, C., Nicklas, H., Olaya, J.-C., Pares, L., Pasquini, L., Pécontal-Rousset, A., Pelló, R., Petit, C., Popow, E., Reiss, R., Remillieux, A., Renault, E., Roth, M., Rupprecht, G., Serre, D., Schaye, J., Soucail, G., Steinmetz, M., Streicher, O., Stuik, R., Valentin, H., Vernet, J., Weilbacher, P., Wisotzki, L., and Yerle, N. (2010). The MUSE second-generation VLT instrument. In *Ground-based and Airborne Instrumentation for Astronomy III*, volume 7735 of *Proc. SPIE*, page 773508.

Baldwin, J. A., Phillips, M. M., and Terlevich, R. (1981). Classification parameters for the emission-line spectra of extragalactic objects. *PASP*, 93:5–19.

Barbon, R., Buondí, V., Cappellaro, E., and Turatto, M. (1999). The Asiago Supernova Catalogue - 10 years after. *A&AS*, 139:531–536.

Bazin, G., Palanque-Delabrouille, N., Rich, J., Ruhlmann-Kleider, V., Aubourg, E., Le Guillou, L., Astier, P., Balland, C., Basa, S., Carlberg, R. G., Conley, A., Fouchez, D., Guy, J., Hardin, D., Hook, I. M., Howell, D. A., Pain, R., Perrett, K., Pritchet, C. J., Regnault, N., Sullivan, M., Antilogus, P., Arsenijevic, V., Baumont, S., Fabbro, S., Le Du, J., Lidman, C., Mouchet, M., Mourão, A., and Walker, E. S. (2009). The core-collapse rate from the Supernova Legacy Survey. *A&A*, 499:653–660.

Benn, C., Dee, K., and Agócs, T. (2008). ACAM: a new imager/spectrograph for the William Herschel Telescope. In *Ground-based and Airborne Instrumentation for Astronomy II*, volume 7014 of *Proc. SPIE*, page 70146X.

Bertin, E. (2006). Automatic Astrometric and Photometric Calibration with SCAMP. In Gabriel, C., Arviset, C., Ponz, D., and Enrique, S., editors, *Astronomical Data Analysis Software and Systems XV*, volume 351 of *Astronomical Society of the Pacific Conference Series*, page 112.

Bertin, E. and Arnouts, S. (1996). SExtractor: Software for source extraction. *A&AS*, 117:393–404.

Bertin, E., Mellier, Y., Radovich, M., Missonnier, G., Didelon, P., and Morin, B. (2002). The TERAPIX Pipeline. In Bohlender, D. A., Durand, D., and Handley, T. H., editors, *Astronomical*

Data Analysis Software and Systems XI, volume 281 of *Astronomical Society of the Pacific Conference Series*, page 228.

Botticella, M. T., Riello, M., Cappellaro, E., Benetti, S., Altavilla, G., Pastorello, A., Turatto, M., Greggio, L., Patat, F., Valenti, S., Zampieri, L., Harutyunyan, A., Pignata, G., and Taubenberger, S. (2008). Supernova rates from the Southern inTermediate Redshift ESO Supernova Search (STRESS). *A&A*, 479:49–66.

Botticella, M. T., Smartt, S. J., Kennicutt, R. C., Cappellaro, E., Sereno, M., and Lee, J. C. (2012). A comparison between star formation rate diagnostics and rate of core collapse supernovae within 11 Mpc. *A&A*, 537:A132.

Brandner, W., Grebel, E. K., Barbá, R. H., Walborn, N. R., and Moneti, A. (2001). Hubble Space Telescope NICMOS Detection of a Partially Embedded, Intermediate-Mass, Pre-Main-Sequence Population in the 30 Doradus Nebula. *AJ*, 122:858–865.

Bressan, A., Fagotto, F., Bertelli, G., and Chiosi, C. (1993). Evolutionary sequences of stellar models with new radiative opacities. II - Z = 0.02. *A&AS*, 100:647–664.

Bright, J., Fender, R., Anderson, G., and Cantwell, T. (2017). Radio Observations of the Nuclear Transient AT 2017gbl in IRAS 23436+5257. *The Astronomer's Telegram*, 10679.

Burston, A. J., Ward, M. J., and Davies, R. I. (2001). Investigating the central engine and excitation mechanisms of ultraluminous infrared galaxies: near-infrared spectroscopy. *MNRAS*, 326:403–415.

Buzzoni, B., Delabre, B., Dekker, H., Dodorico, S., Enard, D., Focardi, P., Gustafsson, B., Nees, W., Paureau, J., and Reiss, R. (1984). The ESO Faint Object Spectrograph and Camera (EFOSC). *The Messenger*, 38:9–13.

Cadonau, R., Sandage, A., and Tammann, G. A. (1985). Type I supernovae as standard candles. In Bartel, N., editor, *Supernovae as Distance Indicators*, volume 224 of *Lecture Notes in Physics, Berlin Springer Verlag*, pages 151–165.

Calzetti, D., Armus, L., Bohlin, R. C., Kinney, A. L., Koornneef, J., and Storchi-Bergmann, T. (2000). The Dust Content and Opacity of Actively Star-forming Galaxies. *ApJ*, 533:682–695.

Cappellari, M. (2017). Improving the full spectrum fitting method: accurate convolution with Gauss-Hermite functions. *MNRAS*, 466:798–811.

Cappellari, M. and Copin, Y. (2003). Adaptive spatial binning of integral-field spectroscopic data using Voronoi tessellations. *MNRAS*, 342:345–354.

Cappellari, M. and Emsellem, E. (2004). Parametric Recovery of Line-of-Sight Velocity Distributions from Absorption-Line Spectra of Galaxies via Penalized Likelihood. *PASP*, 116:138–147.

Cappellaro, E., Botticella, M. T., Pignata, G., Grado, A., Greggio, L., Limatola, L., Vaccari, M., Baruffolo, A., Benetti, S., Bufano, F., Capaccioli, M., Cascone, E., Covone, G., De Cicco, D., Falocco, S., Della Valle, M., Jarvis, M., Marchetti, L., Napolitano, N. R., Paolillo, M., Pastorello, A., Radovich, M., Schipani, P., Spiro, S., Tomasella, L., and Turatto, M. (2015). Supernova rates from the SUDARE VST-OmegaCAM search. I. Rates per unit volume. *A&A*, 584:A62.

Cappellaro, E., Evans, R., and Turatto, M. (1999). A new determination of supernova rates and a comparison with indicators for galactic star formation. *A&A*, 351:459–466.

Cardelli, J. A., Clayton, G. C., and Mathis, J. S. (1989). The relationship between infrared, optical, and ultraviolet extinction. *ApJ*, 345:245–256.

Carrasco, E. R., Edwards, M. L., McGregor, P. J., Winge, C., Young, P. J., Doolan, M. C., van Harmelen, J., Rigaut, F. J., Neichel, B., Trancho, G., Artigau, E., Pessev, P., Colazo, F., Tigner, J., Mauro, F., Lührs, J., and Rambold, W. N. (2012). Results from the commissioning of the Gemini South Adaptive Optics Imager (GSAOI) at Gemini South Observatory. In *Adaptive Optics Systems III*, volume 8447 of *Proc. SPIE*, page 84470N.

Catalán-Torrecilla, C., Gil de Paz, A., Castillo-Morales, A., Iglesias-Páramo, J., Sánchez, S. F., Kennicutt, R. C., Pérez-González, P. G., Marino, R. A., Walcher, C. J., Husemann, B., García-Benito, R., Mast, D., González Delgado, R. M., Muñoz-Mateos, J. C., Bland-Hawthorn, J., Bomans, D. J., Del Olmo, A., Galbany, L., Gomes, J. M., Kehrig, C., López-Sánchez, Á. R., Mendoza, M. A., Monreal-Ibero, A., Pérez-Torres, M., Sánchez-Blázquez, P., Vilchez, J. M., and Califa Collaboration (2015). Star formation in the local Universe from the CALIFA sample. I. Calibrating the SFR using integral field spectroscopy data. *A&A*, 584:A87.

Chambers, K. C., Magnier, E. A., Metcalfe, N., Flewelling, H. A., Huber, M. E., Waters, C. Z., Denneau, L., Draper, P. W., Farrow, D., Finkbeiner, D. P., Holmberg, C., Koppenhoefer, J., Price, P. A., Saglia, R. P., Schlafly, E. F., Smartt, S. J., Sweeney, W., Wainscoat, R. J., Burgett,

W. S., Grav, T., Heasley, J. N., Hodapp, K. W., Jedicke, R., Kaiser, N., Kudritzki, R.-P., Luppino, G. A., Lupton, R. H., Monet, D. G., Morgan, J. S., Onaka, P. M., Stubbs, C. W., Tonry, J. L., Banados, E., Bell, E. F., Bender, R., Bernard, E. J., Botticella, M. T., Casertano, S., Chastel, S., Chen, W.-P., Chen, X., Cole, S., Deacon, N., Frenk, C., Fitzsimmons, A., Gezari, S., Goessl, C., Goggia, T., Goldman, B., Grebel, E. K., Hambly, N. C., Hasinger, G., Heavens, A. F., Heckman, T. M., Henderson, R., Henning, T., Holman, M., Hopp, U., Ip, W.-H., Isani, S., Keyes, C. D., Koekemoer, A., Kotak, R., Long, K. S., Lucey, J. R., Liu, M., Martin, N. F., McLean, B., Morganson, E., Murphy, D. N. A., Nieto-Santisteban, M. A., Norberg, P., Peacock, J. A., Pier, E. A., Postman, M., Primak, N., Rae, C., Rest, A., Riess, A., Riffeser, A., Rix, H. W., Roser, S., Schilbach, E., Schultz, A. S. B., Scolnic, D., Szalay, A., Seitz, S., Shiao, B., Small, E., Smith, K. W., Soderblom, D., Taylor, A. N., Thakar, A. R., Thiel, J., Thilker, D., Urata, Y., Valenti, J., Walter, F., Watters, S. P., Werner, S., White, R., Wood-Vasey, W. M., and Wyse, R. (2016). The Pan-STARRS1 Surveys. *ArXiv e-prints*.

Choi, P. I., Yan, L., Im, M., Helou, G., Soifer, B. T., Storrie-Lombardi, L. J., Chary, R., Teplitz, H. I., Fadda, D., Marleau, F. R., Lacy, M., Wilson, G., Appleton, P. N., Frayer, D. T., and Surace, J. A. (2006). Star Formation Rates and Extinction Properties of IR-luminous Galaxies in the Spitzer First Look Survey. *ApJ*, 637:227–241.

Chomiuk, L., Soderberg, A. M., Chevalier, R. A., Bruzewski, S., Foley, R. J., Parrent, J., Strader, J., Badenes, C., Fransson, C., Kamble, A., Margutti, R., Rupen, M. P., and Simon, J. D. (2016). A Deep Search for Prompt Radio Emission from Thermonuclear Supernovae with the Very Large Array. *ApJ*, 821:119.

Cresci, G., Mannucci, F., Della Valle, M., and Maiolino, R. (2007). A NICMOS search for obscured supernovae in starburst galaxies. *A&A*, 462:927–931.

Dahlen, T., Strolger, L.-G., and Riess, A. G. (2008). The Extended HST Supernova Survey: The Rate of SNe Ia at z > 1.4 Remains Low. *ApJ*, 681:462–469.

Dahlen, T., Strolger, L.-G., Riess, A. G., Mattila, S., Kankare, E., and Mobasher, B. (2012). The Extended Hubble Space Telescope Supernova Survey: The Rate of Core Collapse Supernovae to z ˜ 1. *ApJ*, 757:70.

Dahlen, T., Strolger, L.-G., Riess, A. G., Mobasher, B., Chary, R.-R., Conselice, C. J., Ferguson, H. C., Fruchter, A. S., Giavalisco, M., Livio, M., Madau, P., Panagia, N., and Tonry, J. L. (2004). High-Redshift Supernova Rates. *ApJ*, 613:189–199.

Davies, L. J. M., Driver, S. P., Robotham, A. S. G., Grootes, M. W., Popescu, C. C., Tuffs, R. J., Hopkins, A., Alpaslan, M., Andrews, S. K., Bland-Hawthorn, J., Bremer, M. N., Brough, S., Brown, M. J. I., Cluver, M. E., Croom, S., da Cunha, E., Dunne, L., Lara-López, M. A., Liske, J., Loveday, J., Moffett, A. J., Owers, M., Phillipps, S., Sansom, A. E., Taylor, E. N., Michalowski, M. J., Ibar, E., Smith, M., and Bourne, N. (2016). GAMA/H-ATLAS: a meta-analysis of SFR indicators - comprehensive measures of the SFR-M_* relation and cosmic star formation history at $z < 0.4$. *MNRAS*, 461:458–485.

Dessart, L., Waldman, R., Livne, E., Hillier, D. J., and Blondin, S. (2013). Radiative properties of pair-instability supernova explosions. *MNRAS*, 428:3227–3251.

Djupvik, A. A. and Andersen, J. (2010). The Nordic Optical Telescope. *Astrophysics and Space Science Proceedings*, 14:211.

Dopita, M. A., Armus, L., Kewley, L. J., Rich, J. A., Sanders, D., Appleton, P. N., Chan, B. H. P., Charmandaris, V., Evans, A. S., Frayer, D. T., Howell, J. H., Inami, H., Mazzarella, J. A., Petric, A., Stierwalt, S., and Surace, J. (2011). Modeling IR spectral energy distributions: a pilot study of starburst parameters and silicate absorption curves for some GOALS galaxies. *Ap&SS*, 333:225–239.

Dopita, M. A., Pereira, M., Kewley, L. J., and Capaccioli, M. (2002). Star Formation Rates in Interacting Starburst Galaxies. *ApJS*, 143:47–72.

d'Orgeville, C., Diggs, S., Fesquet, V., Neichel, B., Rambold, W., Rigaut, F., Serio, A., Araya, C., Arriagada, G., Balladares, R., Bec, M., Boccas, M., Duran, C., Ebbers, A., Lopez, A., Marchant, C., Marin, E., Montes, V., Moreno, C., Petit Vega, E., Segura, C., Trancho, G., Trujillo, C., Urrutia, C., Veliz, P., and Vucina, T. (2012). Gemini South multi-conjugate adaptive optics (GeMS) laser guide star facility on-sky performance results. In *Adaptive Optics Systems III*, volume 8447 of *Proc. SPIE*, page 84471Q.

Drake, A. J., Djorgovski, S. G., Mahabal, A., Beshore, E., Larson, S., Graham, M. J., Williams, R., Christensen, E., Catelan, M., Boattini, A., Gibbs, A., Hill, R., and Kowalski, R. (2009). First Results from the Catalina Real-Time Transient Survey. *ApJ*, 696:870–884.

Drake, A. J., Djorgovski, S. G., Prieto, J. L., Mahabal, A., Balam, D., Williams, R., Graham, M. J., Catelan, M., Beshore, E., and Larson, S. (2010). Discovery of the Extremely Energetic Supernova 2008fz. *ApJ*, 718:L127–L131.

Eastman, R. G., Schmidt, B. P., and Kirshner, R. (1996). The Atmospheres of Type II Supernovae and the Expanding Photosphere Method. *ApJ*, 466:911.

Eikenberry, S., Bandyopadhyay, R., Bennett, J. G., Bessoff, A., Branch, M., Charcos, M., Corley, R., Dewitt, C., Eriksen, J.-D., Elston, R., Frommeyer, S., Gonzalez, A., Hanna, K., Herlevich, M., Hon, D., Julian, J., Julian, R., Lasso, N., Marin-Franch, A., Marti, J., Murphey, C., Raines, S. N., Rambold, W., Rashkind, D., Warner, C., Leckie, B., Gardhouse, W. R., Fletcher, M., Hardy, T., Dunn, J., Wooff, R., and Pazder, J. (2012). FLAMINGOS-2: the facility near-infrared wide-field imager and multi-object spectrograph for Gemini. In *Ground-based and Airborne Instrumentation for Astronomy IV*, volume 8446 of *Proc. SPIE*, page 84460I.

Elbaz, D., Dickinson, M., Hwang, H. S., Díaz-Santos, T., Magdis, G., Magnelli, B., Le Borgne, D., Galliano, F., Pannella, M., Chanial, P., Armus, L., Charmandaris, V., Daddi, E., Aussel, H., Popesso, P., Kartaltepe, J., Altieri, B., Valtchanov, I., Coia, D., Dannerbauer, H., Dasyra, K., Leiton, R., Mazzarella, J., Alexander, D. M., Buat, V., Burgarella, D., Chary, R.-R., Gilli, R., Ivison, R. J., Juneau, S., Le Floc'h, E., Lutz, D., Morrison, G. E., Mullaney, J. R., Murphy, E., Pope, A., Scott, D., Brodwin, M., Calzetti, D., Cesarsky, C., Charlot, S., Dole, H., Eisenhardt, P., Ferguson, H. C., Förster Schreiber, N., Frayer, D., Giavalisco, M., Huynh, M., Koekemoer, A. M., Papovich, C., Reddy, N., Surace, C., Teplitz, H., Yun, M. S., and Wilson, G. (2011). GOODS-Herschel: an infrared main sequence for star-forming galaxies. *A&A*, 533:A119.

Elias, J. H., Joyce, R. R., Liang, M., Muller, G. P., Hileman, E. A., and George, J. R. (2006a). Design of the Gemini near-infrared spectrograph. In *Society of Photo-Optical Instrumentation Engineers (SPIE) Conference Series*, volume 6269 of *Proc. SPIE*, page 62694C.

Elias, J. H., Rodgers, B., Joyce, R. R., Lazo, M., Doppmann, G., Winge, C., and Rodríguez-Ardila, A. (2006b). Performance of the Gemini near-infrared spectrograph. In *Society of Photo-Optical Instrumentation Engineers (SPIE) Conference Series*, volume 6269 of *Proc. SPIE*, page 626914.

Engelbracht, C. W., Rieke, M. J., Rieke, G. H., Kelly, D. M., and Achtermann, J. M. (1998). The Nuclear Starburst in NGC 253. *ApJ*, 505:639–658.

Erben, T., Schirmer, M., Dietrich, J. P., Cordes, O., Haberzettl, L., Hetterscheidt, M., Hildebrandt, H., Schmithuesen, O., Schneider, P., Simon, P., Deul, E., Hook, R. N., Kaiser, N., Radovich, M., Benoist, C., Nonino, M., Olsen, L. F., Prandoni, I., Wichmann, R., Zaggia, S., Bomans, D., Dettmar, R. J., and Miralles, J. M. (2005). GaBoDS: The Garching-Bonn Deep Survey.

IV. Methods for the image reduction of multi-chip cameras demonstrated on data from the ESO Wide-Field Imager. *Astronomische Nachrichten*, 326:432–464.

Ergon, M., Jerkstrand, A., Sollerman, J., Elias-Rosa, N., Fransson, C., Fraser, M., Pastorello, A., Kotak, R., Taubenberger, S., Tomasella, L., Valenti, S., Benetti, S., Helou, G., Kasliwal, M. M., Maund, J., Smartt, S. J., and Spyromilio, J. (2015). The Type IIb SN 2011dh: Two years of observations and modelling of the lightcurves. *A&A*, 580:A142.

Ergon, M., Sollerman, J., Fraser, M., Pastorello, A., Taubenberger, S., Elias-Rosa, N., Bersten, M., Jerkstrand, A., Benetti, S., Botticella, M. T., Fransson, C., Harutyunyan, A., Kotak, R., Smartt, S., Valenti, S., Bufano, F., Cappellaro, E., Fiaschi, M., Howell, A., Kankare, E., Magill, L., Mattila, S., Maund, J., Naves, R., Ochner, P., Ruiz, J., Smith, K., Tomasella, L., and Turatto, M. (2014). Optical and near-infrared observations of SN 2011dh - The first 100 days. *A&A*, 562:A17.

Evans, R. (1997). Visual supernova searching with the 40 inch telescope at Siding Spring Observatory. *Publ. Astron. Soc. Australia*, 14:204–7.

Fagotto, F., Bressan, A., Bertelli, G., and Chiosi, C. (1994). Evolutionary sequences of stellar models with new radiative opacities. IV. Z=0.004 and Z=0.008. *A&AS*, 105:29–38.

Farrah, D., Surace, J. A., Veilleux, S., Sanders, D. B., and Vacca, W. D. (2005). Space Telescope Imaging Spectrograph Ultraviolet/Optical Spectroscopy of “Warm” Ultraluminous Infrared Galaxies. *ApJ*, 626:70–88.

Fassia, A., Meikle, W. P. S., Vacca, W. D., Kemp, S. N., Walton, N. A., Pollacco, D. L., Smartt, S., Oscoz, A., Aragón-Salamanca, A., Bennett, S., Hawarden, T. G., Alonso, A., Alcalde, D., Pedrosa, A., Telting, J., Arevalo, M. J., Deeg, H. J., Garzón, F., Gómez-Roldán, A., Gómez, G., Gutiérrez, C., López, S., Rozas, M., Serra-Ricart, M., and Zapatero-Osorio, M. R. (2000). Optical and infrared photometry of the Type IIn SN 1998S: days 11-146. *MNRAS*, 318:1093–1104.

Fazio, G. G., Hora, J. L., Allen, L. E., Ashby, M. L. N., Barmby, P., Deutsch, L. K., Huang, J.-S., Kleiner, S., Marengo, M., Megeath, S. T., Melnick, G. J., Pahre, M. A., Patten, B. M., Polizotti, J., Smith, H. A., Taylor, R. S., Wang, Z., Willner, S. P., Hoffmann, W. F., Pipher, J. L., Forrest, W. J., McMurty, C. W., McCreight, C. R., McKelvey, M. E., McMurray, R. E., Koch, D. G., Moseley, S. H., Arendt, R. G., Mentzell, J. E., Marx, C. T., Losch, P., Mayman, P., Eichhorn, W., Krebs, D., Jhabvala, M., Gezari, D. Y., Fixsen, D. J., Flores, J., Shakoorzadeh, K., Jungo, R., Hakun, C., Workman, L., Karpati, G., Kichak, R., Whitley, R., Mann, S., Tollestrup, E. V., Eisenhardt, P., Stern, D., Gorjian, V., Bhattacharya, B., Carey, S., Nelson, B. O., Glaccum, W. J., Lacy, M., Lowrance, P. J., Laine, S., Reach, W. T., Stauffer, J. A., Surace, J. A., Wilson, G., Wright, E. L., Hoffman, A., Domingo, G., and Cohen, M. (2004). The Infrared Array Camera (IRAC) for the Spitzer Space Telescope. *ApJS*, 154:10–17.

Filippenko, A. V., Li, W. D., Treffers, R. R., and Modjaz, M. (2001). The Lick Observatory Supernova Search with the Katzman Automatic Imaging Telescope. In Paczynski, B., Chen, W.-P., and Lemme, C., editors, *IAU Colloq. 183: Small Telescope Astronomy on Global Scales*, volume 246 of *Astronomical Society of the Pacific Conference Series*, page 121.

Foreman-Mackey, D., Hogg, D. W., Lang, D., and Goodman, J. (2013). emcee: The MCMC Hammer. *PASP*, 125:306.

Gal-Yam, A. (2012). Luminous Supernovae. *Science*, 337:927.

Gal-Yam, A. (2017). *Observational and Physical Classification of Supernovae*, page 195.

Gall, E. E. E., Kotak, R., Leibundgut, B., Taubenberger, S., Hillebrandt, W., Kromer, M., Burgett, W. S., Chambers, K., Flewelling, H., Huber, M. E., Kaiser, N., Kudritzki, R. P., Magnier, E. A., Metcalfe, N., Smith, K., Tonry, J. L., Wainscoat, R. J., and Waters, C. (2018). An updated Type II supernova Hubble diagram. *A&A*, 611:A25.

Giavalisco, M., Ferguson, H. C., Koekemoer, A. M., Dickinson, M., Alexander, D. M., Bauer, F. E., Bergeron, J., Biagetti, C., Brandt, W. N., Casertano, S., Cesarsky, C., Chatzichristou, E., Conselice, C., Cristiani, S., Da Costa, L., Dahlen, T., de Mello, D., Eisenhardt, P., Erben, T., Fall, S. M., Fassnacht, C., Fosbury, R., Fruchter, A., Gardner, J. P., Grogin, N., Hook, R. N., Hornschemeier, A. E., Idzi, R., Jogee, S., Kretchmer, C., Laidler, V., Lee, K. S., Livio, M., Lucas, R., Madau, P., Mobasher, B., Moustakas, L. A., Nonino, M., Padovani, P., Papovich, C., Park, Y., Ravindranath, S., Renzini, A., Richardson, M., Riess, A., Rosati, P., Schirmer, M., Schreier, E., Somerville, R. S., Spinrad, H., Stern, D., Stiavelli, M., Strolger, L., Urry, C. M., Vandame, B., Williams, R., and Wolf, C. (2004). The Great Observatories Origins Deep Survey: Initial Results from Optical and Near-Infrared Imaging. *ApJ*, 600:L93–L98.

Graham, M. J., Djorgovski, S. G., Drake, A. J., Stern, D., Mahabal, A. A., Glikman, E., Larson, S., and Christensen, E. (2017). Understanding extreme quasar optical variability with CRTS - I. Major AGN flares. *MNRAS*, 470:4112–4132.

Graur, O., Bianco, F. B., and Modjaz, M. (2015). A unified explanation for the supernova rate-galaxy mass dependence based on supernovae detected in Sloan galaxy spectra. *MNRAS*, 450:905–925.

Graur, O., Poznanski, D., Maoz, D., Yasuda, N., Totani, T., Fukugita, M., Filippenko, A. V., Foley, R. J., Silverman, J. M., Gal-Yam, A., Horesh, A., and Jannuzi, B. T. (2011). Supernovae in the Subaru Deep Field: the rate and delay-time distribution of Type Ia supernovae out to redshift 2. *MNRAS*, 417:916–940.

Grossan, B., Spillar, E., Tripp, R., Pirzkal, N., Sutin, B. M., Johnson, P., and Barnaby, D. (1999). An Infrared Search for Extinguished Supernovae in Starburst Galaxies. *AJ*, 118:705–718.

Guillochon, J., Parrent, J., Kelley, L. Z., and Margutti, R. (2017). An Open Catalog for Supernova Data. *ApJ*, 835:64.

Haan, S., Surace, J. A., Armus, L., Evans, A. S., Howell, J. H., Mazzarella, J. M., Kim, D. C., Vavilkin, T., Inami, H., Sanders, D. B., Petric, A., Bridge, C. R., Melbourne, J. L., Charmandaris, V., Diaz-Santos, T., Murphy, E. J., U, V., Stierwalt, S., and Marshall, J. A. (2011). The Nuclear Structure in Nearby Luminous Infrared Galaxies: Hubble Space Telescope NICMOS Imaging of the GOALS Sample. *AJ*, 141:100.

Hakobyan, A. A., Mamon, G. A., Petrosian, A. R., Kunth, D., and Turatto, M. (2009). The radial distribution of core-collapse supernovae in spiral host galaxies. *A&A*, 508:1259–1268.

Hamuy, M., Folatelli, G., Morrell, N. I., Phillips, M. M., Suntzeff, N. B., Persson, S. E., Roth, M., Gonzalez, S., Krzeminski, W., Contreras, C., Freedman, W. L., Murphy, D. C., Madore, B. F., Wyatt, P., Maza, J., Filippenko, A. V., Li, W., and Pinto, P. A. (2006). The Carnegie Supernova Project: The Low-Redshift Survey. *PASP*, 118:2–20.

Hamuy, M. and Pinto, P. A. (2002). Type II Supernovae as Standardized Candles. *ApJ*, 566:L63–L65.

Hancock, P. J., Gaensler, B. M., and Murphy, T. (2011). Visibility Stacking in the Quest for Type Ia Supernova Radio Emission. *ApJ*, 735:L35.

Hartwig, T., Bromm, V., and Loeb, A. (2017). Detection strategies for the first supernovae with JWST. *ArXiv e-prints*.

Hatano, K., Branch, D., and Deaton, J. (1998). Extinction and Radial Distribution of Supernova Properties in Their Parent Galaxies. *ApJ*, 502:177–181.

Hayward, C. C., Lanz, L., Ashby, M. L. N., Fazio, G., Hernquist, L., Martínez-Galarza, J. R., Noeske, K., Smith, H. A., Wuyts, S., and Zezas, A. (2014). The total infrared luminosity may significantly overestimate the star formation rate of quenching and recently quenched galaxies. *MNRAS*, 445:1598–1604.

Herrero-Illana, R., Pérez-Torres, M. Á., and Alberdi, A. (2012). Evidence of nuclear disks in starburst galaxies from their radial distribution of supernovae. *A&A*, 540:L5.

Herrero-Illana, R., Pérez-Torres, M. Á., Randriamanakoto, Z., Alberdi, A., Efstathiou, A., Väisänen, P., Kankare, E., Kool, E., Mattila, S., Ramphul, R., Romero-Cañizales, C., and Ryder, S. (2017). Star formation and AGN activity in a sample of local Luminous Infrared Galaxies through multi-wavelength characterization. *ArXiv e-prints*.

Hodapp, K. W., Jensen, J. B., Irwin, E. M., Yamada, H., Chung, R., Fletcher, K., Robertson, L., Hora, J. L., Simons, D. A., Mays, W., Nolan, R., Bec, M., Merrill, M., and Fowler, A. M. (2003). The Gemini Near-Infrared Imager (NIRI). *PASP*, 115:1388–1406.

Holoien, T. W.-S., Brown, J. S., Stanek, K. Z., Kochanek, C. S., Shappee, B. J., Prieto, J. L., Dong, S., Brimacombe, J., Bishop, D. W., Basu, U., Beacom, J. F., Bersier, D., Chen, P., Danilet, A. B., Falco, E., Godoy-Rivera, D., Goss, N., Pojmanski, G., Simonian, G. V., Skowron, D. M., Thompson, T. A., Woźniak, P. R., Ávila, C. G., Bock, G., Carballo, J.-L. G., Conseil, E., Contreras, C., Cruz, I., Andújar, J. M. F., Guo, Z., Hsiao, E. Y., Kiyota, S., Koff, R. A., Krannich, G., Madore, B. F., Marples, P., Masi, G., Morrell, N., Monard, L. A. G., Munoz-Mateos, J. C., Nicholls, B., Nicolas, J., Wagner, R. M., and Wiethoff, W. S. (2017a). The ASAS-SN bright supernova catalogue - II. 2015. *MNRAS*, 467:1098–1111.

Holoien, T. W.-S., Brown, J. S., Stanek, K. Z., Kochanek, C. S., Shappee, B. J., Prieto, J. L., Dong, S., Brimacombe, J., Bishop, D. W., Bose, S., Beacom, J. F., Bersier, D., Chen, P., Chomiuk, L., Falco, E., Godoy-Rivera, D., Morrell, N., Pojmanski, G., Shields, J. V., Strader, J., Stritzinger, M. D., Thompson, T. A., Woźniak, P. R., Bock, G., Cacella, P., Conseil, E., Cruz, I., Fernandez, J. M., Kiyota, S., Koff, R. A., Krannich, G., Marples, P., Masi, G., Monard, L. A. G., Nicholls, B., Nicolas, J., Post, R. S., Stone, G., and Wiethoff, W. S. (2017b). The ASAS-SN Bright Supernova Catalog – III. 2016. *ArXiv e-prints*.

Holoien, T. W.-S., Stanek, K. Z., Kochanek, C. S., Shappee, B. J., Prieto, J. L., Brimacombe, J., Bersier, D., Bishop, D. W., Dong, S., Brown, J. S., Danilet, A. B., Simonian, G. V., Basu, U., Beacom, J. F., Falco, E., Pojmanski, G., Skowron, D. M., Woźniak, P. R., Ávila, C. G., Conseil, E., Contreras, C., Cruz, I., Fernández, J. M., Koff, R. A., Guo, Z., Herczeg, G. J., Hissong, J., Hsiao, E. Y., Jose, J., Kiyota, S., Long, F., Monard, L. A. G., Nicholls, B., Nicolas, J., and Wiethoff, W. S. (2017c). The ASAS-SN bright supernova catalogue - I. 2013-2014. *MNRAS*, 464:2672–2686.

Hopkins, A. M. and Beacom, J. F. (2006). On the Normalization of the Cosmic Star Formation History. *ApJ*, 651:142–154.

Horiuchi, S., Beacom, J. F., Kochanek, C. S., Prieto, J. L., Stanek, K. Z., and Thompson, T. A. (2011). The Cosmic Core-collapse Supernova Rate Does Not Match the Massive-star Formation Rate. *ApJ*, 738:154.

Howell, D. A. (2011). Type Ia supernovae as stellar endpoints and cosmological tools. *Nature Communications*, 2:350.

Jencson, J. E., Kasliwal, M. M., Adams, S. M., Bond, H. E., De, K., Johansson, J., Karambelkar, V., Lau, R. M., Tinyanont, S., Ryder, S. D., Cody, A. M., Masci, F. J., Bally, J., Blagorodnova, N., Castellón, S., Fremling, C., Gehrz, R. D., Helou, G., Kilpatrick, C. D., Milne, P. A., Morrell, N., Perley, D. A., Phillips, M., Smith, N., van Dyk, S. D., and Williams, R. E. (2019). The SPIRITS sample of Luminous Infrared Transients: Uncovering Hidden Supernovae and Dusty Stellar Outbursts in Nearby Galaxies. *arXiv e-prints*.

Jencson, J. E., Kasliwal, M. M., Adams, S. M., Bond, H. E., Lau, R. M., Johansson, J., Horesh, A., Mooley, K. P., Fender, R., De, K., O'Sullivan, D., Masci, F. J., Cody, A. M., Blagorodnova, N., Fox, O. D., Gehrz, R. D., Milne, P. A., Perley, D. A., Smith, N., and Van Dyk, S. D. (2018). SPIRITS 16tn in NGC 3556: A heavily obscured and low-luminosity supernova at 8.8 Mpc. *ArXiv e-prints*.

Jencson, J. E., Kasliwal, M. M., Johansson, J., Contreras, C., Castellón, S., Bond, H. E., Monson, A. J., Masci, F. J., Cody, A. M., Andrews, J. E., Bally, J., Cao, Y., Fox, O. D., Gburek, T., Gehrz, R. D., Green, W., Helou, G., Hsiao, E., Morrell, N., Phillips, M., Prince, T. A., Simcoe, R. A., Smith, N., Tinyanont, S., and Williams, R. (2017). SPIRITS 15c and SPIRITS 14buu: Two Obscured Supernovae in the Nearby Star-forming Galaxy IC 2163. *ApJ*, 837:167.

Jester, S., Schneider, D. P., Richards, G. T., Green, R. F., Schmidt, M., Hall, P. B., Strauss, M. A., Vanden Berk, D. E., Stoughton, C., Gunn, J. E., Brinkmann, J., Kent, S. M., Smith, J. A., Tucker, D. L., and Yanny, B. (2005). The Sloan Digital Sky Survey View of the Palomar-Green Bright Quasar Survey. *AJ*, 130:873–895.

Kangas, T., Mattila, S., Kankare, E., Kotilainen, J. K., Väisänen, P., Greimel, R., and Takalo, A. (2013). Spatial distributions of core-collapse supernovae in infrared-bright galaxies. *MNRAS*, 436:3464–3479.

Kankare, E., Kool, E., Mattila, S., and Ryder, S. (2017a). SUNBIRD Transient Discovery Report for 2017-01-02. *Transient Name Server Discovery Report*, 10.

Kankare, E., Kotak, R., Mattila, S., Lundqvist, P., Ward, M. J., Fraser, M., Lawrence, A., Smartt, S. J., Meikle, W. P. S., Bruce, A., Harmanen, J., Hutton, S. J., Inserra, C., Kangas, T., Pastorello, A., Reynolds, T., Romero-Cañizales, C., Smith, K. W., Valenti, S., Chambers, K. C., Hodapp, K. W., Huber, M. E., Kaiser, N., Kudritzki, R.-P., Magnier, E. A., Tonry, J. L., Wainscoat, R. J., and Waters, C. (2017b). A population of highly energetic transient events in the centres of active galaxies. *Nature Astronomy*, 1:865–871.

Kankare, E., Mattila, S., Ryder, S., Fraser, M., Pastorello, A., Elias-Rosa, N., Romero-Cañizales, C., Alberdi, A., Hentunen, V.-P., Herrero-Illana, R., Kotilainen, J., Pérez-Torres, M.-A., and Väisänen, P. (2014). The nature of supernovae 2010O and 2010P in Arp 299 - I. Near-infrared and optical evolution. *MNRAS*, 440:1052–1066.

Kankare, E., Mattila, S., Ryder, S., Kool, E., Kotak, R., Kotilainen, J., Kuncarayakti, H., Perez-Torres, M., Randriamanakoto, Z., Reynolds, T., Romero-Canizales, C., Smartt, S., and Vaisanen, P. (2018). Discovery of supernova candidate AT 2018ec in NGC 3256 with HAWK-I/GRAAL. *The Astronomer's Telegram*, 11156.

Kankare, E., Mattila, S., Ryder, S., Pérez-Torres, M.-A., Alberdi, A., Romero-Canizales, C., Díaz-Santos, T., Väisänen, P., Efstathiou, A., Alonso-Herrero, A., Colina, L., and Kotilainen, J. (2008). Discovery of a Very Highly Extinguished Supernova in a Luminous Infrared Galaxy. *ApJ*, 689:L97.

Kankare, E., Mattila, S., Ryder, S., Väisänen, P., Alberdi, A., Alonso-Herrero, A., Colina, L., Efstathiou, A., Kotilainen, J., Melinder, J., Pérez-Torres, M.-A., Romero-Cañizales, C., and Takalo, A. (2012). Discovery of Two Supernovae in the Nuclear Regions of the Luminous Infrared Galaxy IC 883. *ApJ*, 744:L19.

Kasen, D. and Woosley, S. E. (2009). Type II Supernovae: Model Light Curves and Standard Candle Relationships. *ApJ*, 703:2205–2216.

Kasliwal, M. M., Bally, J., Masci, F., Cody, A. M., Bond, H. E., Jencson, J. E., Tinyanont, S., Cao, Y., Contreras, C., Dykhoff, D. A., Amodeo, S., Armus, L., Boyer, M., Cantiello, M., Carlon, R. L., Cass, A. C., Cook, D., Corgan, D. T., Faella, J., Fox, O. D., Green, W., Gehrz, R. D., Helou, G., Hsiao, E., Johansson, J., Khan, R. M., Lau, R. M., Langer, N., Levesque, E., Milne, P., Mohamed, S., Morrell, N., Monson, A., Moore, A., Ofek, E. O., O' Sullivan, D., Parthasarathy, M., Perez, A., Perley, D. A., Phillips, M., Prince, T. A., Shenoy, D., Smith, N., Surace, J., Van Dyk, S. D., Whitelock, P. A., and Williams, R. (2017). SPIRITS: Uncovering Unusual Infrared Transients with Spitzer. *ApJ*, 839(2):88.

Kauffmann, G., Heckman, T. M., Tremonti, C., Brinchmann, J., Charlot, S., White, S. D. M., Ridgway, S. E., Brinkmann, J., Fukugita, M., Hall, P. B., Ivezić, Ž., Richards, G. T., and Schneider, D. P. (2003). The host galaxies of active galactic nuclei. *MNRAS*, 346:1055–1077.

Kennicutt, Jr., R. C. (1998). Star Formation in Galaxies Along the Hubble Sequence. *ARA&A*, 36:189–232.

Kewley, L. J., Dopita, M. A., Sutherland, R. S., Heisler, C. A., and Trevena, J. (2001). Theoretical Modeling of Starburst Galaxies. *ApJ*, 556:121–140.

Kool, E. (2017). SUNBIRD Transient Discovery Report for 2017-03-20. *Transient Name Server Discovery Report*, 330.

Kool, E. (2018a). SUNBIRD Transient Discovery Report for 2018-01-23. *Transient Name Server Discovery Report*, 109.

Kool, E. (2018b). SUNBIRD Transient Discovery Report for 2018-05-03. *Transient Name Server Discovery Report*, 574.

Kool, E., Ryder, S., Mattila, S., and Kankare, E. (2016). SUNBIRD Transient Discovery Report for 2016-12-22. *Transient Name Server Discovery Report*, 1073.

Kool, E., Ryder, S., Mattila, S., and Kankare, E. (2017a). SUNBIRD Transient Discovery Report for 2017-01-02. *Transient Name Server Discovery Report*, 9.

Kool, E., Ryder, S., Mattila, S., and Kankare, E. (2017b). SUNBIRD Transient Discovery Report for 2017-05-15. *Transient Name Server Discovery Report*, 555.

Kool, E. C., Ryder, S., Kankare, E., Mattila, S., Reynolds, T., McDermid, R. M., Pérez-Torres, M. A., Herrero-Illana, R., Schirmer, M., Efstathiou, A., Bauer, F. E., Kotilainen, J., Väisänen, P., Baldwin, C., Romero-Cañizales, C., and Alberdi, A. (2018). First results from

GeMS/GSAOI for project SUNBIRD: Supernovae UNmasked By Infra-Red Detection. *MNRAS*, 473:5641–5657.

Kool, E. C., Ryder, S., Mattila, S., Reynolds, T., Cannizzaro, G., Kankare, E., McDermid, R., Fraser, M., Perez-Torres, M., Wevers, T., Jonker, P., Vaisanen, P., Sweet, S., and Tucker, B. E. (2017c). Discovery of luminous near-infrared transient AT 2017gbl in IRAS 23436+5257. *The Astronomer's Telegram*, 10651.

Koss, M., Mushotzky, R., Baumgartner, W., Veilleux, S., Tueller, J., Markwardt, C., and Casey, C. M. (2013). Studying Faint Ultra-hard X-Ray Emission from AGN in GOALS LIRGs with Swift/BAT. *ApJ*, 765:L26.

Krisciunas, K., Hamuy, M., Suntzeff, N. B., Espinoza, J., Gonzalez, D., Gonzalez, L., Gonzalez, S., Koviak, K., Krzeminski, W., Morrell, N., Phillips, M. M., Roth, M., and Thomas-Osip, J. (2009). Do the Photometric Colors of Type II-P Supernovae Allow Accurate Determination of Host Galaxy Extinction? *AJ*, 137:34–41.

Kuncarayakti, H., Anderson, J. P., Galbany, L., Maeda, K., Hamuy, M., Aldering, G., Arimoto, N., Doi, M., Morokuma, T., and Usuda, T. (2017). Constraints on core-collapse supernova progenitors from explosion site integral field spectroscopy. *ArXiv e-prints*.

Kuncarayakti, H., Doi, M., Aldering, G., Arimoto, N., Maeda, K., Morokuma, T., Pereira, R., Usuda, T., and Hashiba, Y. (2013). Integral Field Spectroscopy of Supernova Explosion Sites: Constraining the Mass and Metallicity of the Progenitors. I. Type Ib and Ic Supernovae. *AJ*, 146:30.

Kuncarayakti, H., Galbany, L., Anderson, J. P., Krühler, T., and Hamuy, M. (2016). Unresolved versus resolved: testing the validity of young simple stellar population models with VLT/MUSE observations of NGC 3603. *A&A*, 593:A78.

Le Floc'h, E., Papovich, C., Dole, H., Bell, E. F., Lagache, G., Rieke, G. H., Egami, E., Pérez-González, P. G., Alonso-Herrero, A., Rieke, M. J., Blaylock, M., Engelbracht, C. W., Gordon, K. D., Hines, D. C., Misselt, K. A., Morrison, J. E., and Mould, J. (2005). Infrared Luminosity Functions from the Chandra Deep Field-South: The Spitzer View on the History of Dusty Star Formation at 0 < z < 1. *ApJ*, 632:169–190.

Leaman, J., Li, W., Chornock, R., and Filippenko, A. V. (2011a). Nearby supernova rates from the Lick Observatory Supernova Search - I. The methods and data base. *MNRAS*, 412:1419–1440.

Leaman, J., Li, W., Chornock, R., and Filippenko, A. V. (2011b). Nearby supernova rates from the Lick Observatory Supernova Search - I. The methods and data base. *MNRAS*, 412:1419–1440.

Leitherer, C., Schaerer, D., Goldader, J. D., Delgado, R. M. G., Robert, C., Kune, D. F., de Mello, D. F., Devost, D., and Heckman, T. M. (1999). Starburst99: Synthesis Models for Galaxies with Active Star Formation. *ApJS*, 123:3–40.

Leja, J., Johnson, B. D., Conroy, C., van Dokkum, P. G., and Byler, N. (2017). Deriving Physical Properties from Broadband Photometry with Prospector: Description of the Model and a Demonstration of its Accuracy Using 129 Galaxies in the Local Universe. *ApJ*, 837:170.

Leloudas, G., Fraser, M., Stone, N. C., van Velzen, S., Jonker, P. G., Arcavi, I., Fremling, C., Maund, J. R., Smartt, S. J., Krìhler, T., Miller-Jones, J. C. A., Vreeswijk, P. M., Gal-Yam, A., Mazzali, P. A., De Cia, A., Howell, D. A., Inserra, C., Patat, F., de Ugarte Postigo, A., Yaron, O., Ashall, C., Bar, I., Campbell, H., Chen, T.-W., Childress, M., Elias-Rosa, N., Harmanen, J., Hosseinzadeh, G., Johansson, J., Kangas, T., Kankare, E., Kim, S., Kuncarayakti, H., Lyman, J., Magee, M. R., Maguire, K., Malesani, D., Mattila, S., McCully, C. V., Nicholl, M., Prentice, S., Romero-Cañizales, C., Schulze, S., Smith, K. W., Sollerman, J., Sullivan, M., Tucker, B. E., Valenti, S., Wheeler, J. C., and Young, D. R. (2016). The superluminous transient ASASSN-15lh as a tidal disruption event from a Kerr black hole. *Nature Astronomy*, 1:0002.

Lenzen, R., Hartung, M., Brandner, W., Finger, G., Hubin, N. N., Lacombe, F., Lagrange, A.-M., Lehnert, M. D., Moorwood, A. F. M., and Mouillet, D. (2003). NAOS-CONICA first on sky results in a variety of observing modes. In Iye, M. and Moorwood, A. F. M., editors, *Instrument Design and Performance for Optical/Infrared Ground-based Telescopes*, volume 4841 of *Proc. SPIE*, pages 944–952.

Leonard, D. C., Filippenko, A. V., Gates, E. L., Li, W., Eastman, R. G., Barth, A. J., Bus, S. J., Chornock, R., Coil, A. L., Frink, S., Grady, C. A., Harris, A. W., Malkan, M. A., Matheson, T., Quirrenbach, A., and Treffers, R. R. (2002). The Distance to SN 1999em in NGC 1637 from the Expanding Photosphere Method. *PASP*, 114:35–64.

Levesque, E. M. and Leitherer, C. (2013). Modeling Tracers of Young Stellar Population Age in Star-forming Galaxies. *ApJ*, 779:170.

Li, W., Chornock, R., Leaman, J., Filippenko, A. V., Poznanski, D., Wang, X., Ganeshalingam, M., and Mannucci, F. (2011a). Nearby supernova rates from the Lick Observatory Supernova

Search - III. The rate-size relation, and the rates as a function of galaxy Hubble type and colour. *MNRAS*, 412:1473–1507.

Li, W., Leaman, J., Chornock, R., Filippenko, A. V., Poznanski, D., Ganeshalingam, M., Wang, X., Modjaz, M., Jha, S., Foley, R. J., and Smith, N. (2011b). Nearby supernova rates from the Lick Observatory Supernova Search - II. The observed luminosity functions and fractions of supernovae in a complete sample. *MNRAS*, 412:1441–1472.

Liu, Q.-Z., Hu, J.-Y., Hang, H.-R., Qiu, Y.-L., Zhu, Z.-X., and Qiao, Q.-Y. (2000). The supernova 1998S in NGC 3877: Another supernova with Wolf-Rayet star features in pre-maximum spectrum. *A&AS*, 144:219–225.

Long, K. S. (2017). *Galactic and Extragalactic Samples of Supernova Remnants: How They Are Identified and What They Tell Us*, page 2005.

MacLeod, C. L., Ivezić, Ž., Sesar, B., de Vries, W., Kochanek, C. S., Kelly, B. C., Becker, A. C., Lupton, R. H., Hall, P. B., Richards, G. T., Anderson, S. F., and Schneider, D. P. (2012). A Description of Quasar Variability Measured Using Repeated SDSS and POSS Imaging. *ApJ*, 753:106.

Madau, P. and Dickinson, M. (2014). Cosmic Star-Formation History. *ARA&A*, 52:415–486.

Magnelli, B., Elbaz, D., Chary, R. R., Dickinson, M., Le Borgne, D., Frayer, D. T., and Willmer, C. N. A. (2009). The $0.4 < z < 1.3$ star formation history of the Universe as viewed in the far-infrared. *A&A*, 496:57–75.

Magnelli, B., Elbaz, D., Chary, R. R., Dickinson, M., Le Borgne, D., Frayer, D. T., and Willmer, C. N. A. (2011). Evolution of the dusty infrared luminosity function from $z = 0$ to $z = 2.3$ using observations from Spitzer. *A&A*, 528:A35.

Maiolino, R., Vanzi, L., Mannucci, F., Cresci, G., Ghinassi, F., and Della Valle, M. (2002). Discovery of two infrared supernovae: A new window on the SN search. *A&A*, 389:84–92.

Mannucci, F., Della Valle, M., and Panagia, N. (2007). How many supernovae are we missing at high redshift? *MNRAS*, 377:1229–1235.

Mannucci, F., Maiolino, R., Cresci, G., Della Valle, M., Vanzi, L., Ghinassi, F., Ivanov, V. D., Nagar, N. M., and Alonso-Herrero, A. (2003). The infrared supernova rate in starburst galaxies. *A&A*, 401:519–530.

Matheson, T., Joyce, R. R., Allen, L. E., Saha, A., Silva, D. R., Wood-Vasey, W. M., Adams, J. J., Anderson, R. E., Beck, T. L., Bentz, M. C., Bershady, M. A., Binkert, W. S., Butler, K., Camarata, M. A., Eigenbrot, A., Everett, M., Gallagher, J. S., Garnavich, P. M., Glikman, E., Harbeck, D., Hargis, J. R., Herbst, H., Horch, E. P., Howell, S. B., Jha, S., Kaczmarek, J. F., Knezek, P., Manne-Nicholas, E., Mathieu, R. D., Meixner, M., Milliman, K., Power, J., Rajagopal, J., Reetz, K., Rhode, K. L., Schechtman-Rook, A., Schwamb, M. E., Schweiker, H., Simmons, B., Simon, J. D., Summers, D., Young, M. D., Weyant, A., Wilcots, E. M., Will, G., and Williams, D. (2012). The Infrared Light Curve of SN 2011fe in M101 and the Distance to M101. *ApJ*, 754:19.

Mattila, S., Dahlen, T., Efstathiou, A., Kankare, E., Melinder, J., Alonso-Herrero, A., Pérez-Torres, M. Á., Ryder, S., Väisänen, P., and Östlin, G. (2012). Core-collapse Supernovae Missed by Optical Surveys. *ApJ*, 756:111.

Mattila, S., Greimel, R., Gerardy, C., Meikle, W. P. S., Monard, L. A. G., Boles, T., Pugh, H., Graham, J., and Li, W. (2005a). Supernova 2005V in NGC 2146. *IAU Circ.*, 8474.

Mattila, S., Greimel, R., Gerardy, C., Meikle, W. P. S., Monard, L. A. G., Boles, T., Pugh, H., Graham, J., and Li, W. (2005b). Supernovae 2005Q, 2005R, 2005S, 2005T, 2005U. *IAU Circ.*, 8473.

Mattila, S. and Meikle, W. P. S. (2001). Supernovae in the nuclear regions of starburst galaxies. *MNRAS*, 324:325–342.

Mattila, S., Meikle, W. P. S., and Greimel, R. (2004). Highly extinguished supernovae in the nuclear regions of starburst galaxies. *New Astron. Rev.*, 48:595–600.

Mattila, S., Pérez-Torres, M., Efstathiou, A., Mimica, P., Fraser, M., Kankare, E., Alberdi, A., Aloy, M. Á., Heikkilä, T., Jonker, P. G., Lundqvist, P., Martí-Vidal, I., Meikle, W. P. S., Romero-Cañizales, C., Smartt, S. J., Tsygankov, S., Varenius, E., Alonso-Herrero, A., Bondi, M., Fransson, C., Herrero-Illana, R., Kangas, T., Kotak, R., Ramírez-Olivencia, N., Väisänen, P., Beswick, R. J., Clements, D. L., Greimel, R., Harmanen, J., Kotilainen, J., Nandra, K., Reynolds, T., Ryder, S., Walton, N. A., Wiik, K., and Östlin, G. (2018). A dust-enshrouded tidal disruption event with a resolved radio jet in a galaxy merger. *Science*, 361:482–485.

Mattila, S., Väisänen, P., Farrah, D., Efstathiou, A., Meikle, W. P. S., Dahlen, T., Fransson, C., Lira, P., Lundqvist, P., Östlin, G., Ryder, S., and Sollerman, J. (2007). Adaptive Optics Discovery of

Supernova 2004ip in the Nuclear Regions of the Luminous Infrared Galaxy IRAS 18293-3413. *ApJ*, 659:L9–L12.

McGregor, P., Hart, J., Stevanovic, D., Bloxham, G., Jones, D., Van Harmelen, J., Griesbach, J., Dawson, M., Young, P., and Jarnyk, M. A. (2004). Gemini South Adaptive Optics Imager (GSAOI). In Moorwood, A. F. M. and Iye, M., editors, *Ground-based Instrumentation for Astronomy*, volume 5492 of *Proc. SPIE*, pages 1033–1044.

McMullin, J. P., Waters, B., Schiebel, D., Young, W., and Golap, K. (2007). CASA Architecture and Applications. In Shaw, R. A., Hill, F., and Bell, D. J., editors, *Astronomical Data Analysis Software and Systems XVI*, volume 376 of *Astronomical Society of the Pacific Conference Series*, page 127.

Melinder, J., Dahlen, T., Mencía Trinchant, L., Östlin, G., Mattila, S., Sollerman, J., Fransson, C., Hayes, M., Kankare, E., and Nasoudi-Shoar, S. (2012). The rate of supernovae at redshift 0.1-1.0. The Stockholm VIMOS Supernova Survey III. *A&A*, 545:A96.

Miluzio, M., Cappellaro, E., Botticella, M. T., Cresci, G., Greggio, L., Mannucci, F., Benetti, S., Bufano, F., Elias-Rosa, N., Pastorello, A., Turatto, M., and Zampieri, L. (2013). HAWK-I infrared supernova search in starburst galaxies. *A&A*, 554:A127.

Modjaz, M. (2011). Stellar forensics with the supernova-GRB connection. *Astronomische Nachrichten*, 332:434–447.

Müller, B. (2017). The Core-Collapse Supernova Explosion Mechanism. In Eldridge, J. J., Bray, J. C., McClelland, L. A. S., and Xiao, L., editors, *The Lives and Death-Throes of Massive Stars*, volume 329 of *IAU Symposium*, pages 17–24.

Neichel, B., Lu, J. R., Rigaut, F., Ammons, S. M., Carrasco, E. R., and Lassalle, E. (2014a). Astrometric performance of the Gemini multiconjugate adaptive optics system in crowded fields. *MNRAS*, 445:500–514.

Neichel, B., Rigaut, F., Vidal, F., van Dam, M. A., Garrel, V., Carrasco, E. R., Pessev, P., Winge, C., Boccas, M., d'Orgeville, C., Arriagada, G., Serio, A., Fesquet, V., Rambold, W. N., Lührs, J., Moreno, C., Gausachs, G., Galvez, R. L., Montes, V., Vucina, T. B., Marin, E., Urrutia, C., Lopez, A., Diggs, S. J., Marchant, C., Ebbers, A. W., Trujillo, C., Bec, M., Trancho, G., McGregor, P., Young, P. J., Colazo, F., and Edwards, M. L. (2014b). Gemini multiconjugate adaptive optics system review - II. Commissioning, operation and overall performance. *MNRAS*, 440:1002–1019.

Nicholls, D. C., Sutherland, R. S., Dopita, M. A., Kewley, L. J., and Groves, B. A. (2017). Abundance scaling in stars, nebulae and galaxies. *MNRAS*, 466:4403–4422.

Osterbrock, D. E. (1989). *Astrophysics of gaseous nebulae and active galactic nuclei*.

Patat, F. (1996). *Supernovae: alcune recenti problematiche*.

Perez-Torres, M., Alberdi, A., Beswick, R. J., Lundqvist, P., Herrero-Illana, R., Romero-Cañizales, C., Ryder, S., della Valle, M., Conway, J., Marcaide, J. M., Mattila, S., Murphy, T., and Ros, E. (2015). Core-collapse and Type Ia supernovae with the SKA. *Advancing Astrophysics with the Square Kilometre Array (AASKA14)*, page 60.

Perez-Torres, M., Kool, E., Ryder, S., Mattila, S., Fraser, M., and Kankare, E. (2017). VLBA observations of the nuclear transient AT 2017gbl in IRAS 23436+5257. *The Astronomer's Telegram*, 10712.

Perlmutter, S., Aldering, G., Goldhaber, G., Knop, R. A., Nugent, P., Castro, P. G., Deustua, S., Fabbro, S., Goobar, A., Groom, D. E., Hook, I. M., Kim, A. G., Kim, M. Y., Lee, J. C., Nunes, N. J., Pain, R., Pennypacker, C. R., Quimby, R., Lidman, C., Ellis, R. S., Irwin, M., McMahon, R. G., Ruiz-Lapuente, P., Walton, N., Schaefer, B., Boyle, B. J., Filippenko, A. V., Matheson, T., Fruchter, A. S., Panagia, N., Newberg, H. J. M., Couch, W. J., and Project, T. S. C. (1999). Measurements of Ω and Λ from 42 High-Redshift Supernovae. *ApJ*, 517:565–586.

Pettini, M. and Pagel, B. E. J. (2004). [OIII]/[NII] as an abundance indicator at high redshift. *MNRAS*, 348:L59–L63.

Randriamanakoto, Z., Escala, A., Väisänen, P., Kankare, E., Kotilainen, J., Mattila, S., and Ryder, S. (2013). Near-infrared Adaptive Optics Imaging of Infrared Luminous Galaxies: The Brightest Cluster Magnitude-Star Formation Rate Relation. *ApJ*, 775:L38.

Rau, A., Kulkarni, S. R., Law, N. M., Bloom, J. S., Ciardi, D., Djorgovski, G. S., Fox, D. B., Gal-Yam, A., Grillmair, C. C., Kasliwal, M. M., Nugent, P. E., Ofek, E. O., Quimby, R. M., Reach, W. T., Shara, M., Bildsten, L., Cenko, S. B., Drake, A. J., Filippenko, A. V., Helfand, D. J., Helou, G., Howell, D. A., Poznanski, D., and Sullivan, M. (2009). Exploring the Optical Transient Sky with the Palomar Transient Factory. *PASP*, 121:1334.

Rayner, J. T., Toomey, D. W., Onaka, P. M., Denault, A. J., Stahlberger, W. E., Vacca, W. D., Cushing, M. C., and Wang, S. (2003). SpeX: A Medium-Resolution 0.8-5.5 Micron Spectrograph and Imager for the NASA Infrared Telescope Facility. *PASP*, 115:362–382.

Rees, M. J. (1988). Tidal disruption of stars by black holes of 10 to the 6th-10 to the 8th solar masses in nearby galaxies. *Nature*, 333:523–528.

Richmond, M. W., Filippenko, A. V., and Galisky, J. (1998). The Supernova Rate in Starburst Galaxies. *PASP*, 110:553–571.

Riess, A. G., Filippenko, A. V., Challis, P., Clocchiatti, A., Diercks, A., Garnavich, P. M., Gilliland, R. L., Hogan, C. J., Jha, S., Kirshner, R. P., Leibundgut, B., Phillips, M. M., Reiss, D., Schmidt, B. P., Schommer, R. A., Smith, R. C., Spyromilio, J., Stubbs, C., Suntzeff, N. B., and Tonry, J. (1998). Observational Evidence from Supernovae for an Accelerating Universe and a Cosmological Constant. *AJ*, 116:1009–1038.

Rigaut, F., Neichel, B., Boccas, M., d'Orgeville, C., Vidal, F., van Dam, M. A., Arriagada, G., Fesquet, V., Galvez, R. L., Gausachs, G., Cavedoni, C., Ebbers, A. W., Karewicz, S., James, E., Lührs, J., Montes, V., Perez, G., Rambold, W. N., Rojas, R., Walker, S., Bec, M., Trancho, G., Sheehan, M., Irarrazaval, B., Boyer, C., Ellerbroek, B. L., Flicker, R., Gratadour, D., Garcia-Rissmann, A., and Daruich, F. (2014). Gemini multiconjugate adaptive optics system review - I. Design, trade-offs and integration. *MNRAS*, 437:2361–2375.

Risaliti, G., Gilli, R., Maiolino, R., and Salvati, M. (2000). The hard X-ray emission of luminous infrared galaxies. *A&A*, 357:13–23.

Rodríguez-Zaurín, J., Arribas, S., Monreal-Ibero, A., Colina, L., Alonso-Herrero, A., and Alfonso-Garzón, J. (2011). VLT-VIMOS integral field spectroscopy of luminous and ultraluminous infrared galaxies. III. The atlas of the stellar and ionized gas distribution. *A&A*, 527:A60.

Romero-Cañizales, C., Herrero-Illana, R., Pérez-Torres, M. A., Alberdi, A., Kankare, E., Bauer, F. E., Ryder, S. D., Mattila, S., Conway, J. E., Beswick, R. J., and Muxlow, T. W. B. (2014). The nature of supernovae 2010O and 2010P in Arp 299 - II. Radio emission. *MNRAS*, 440:1067–1079.

Rousset, G., Lacombe, F., Puget, P., Hubin, N. N., Gendron, E., Fusco, T., Arsenault, R., Charton, J., Feautrier, P., Gigan, P., Kern, P. Y., Lagrange, A.-M., Madec, P.-Y., Mouillet, D., Rabaud, D., Rabou, P., Stadler, E., and Zins, G. (2003). NAOS, the first AO system of the VLT: on-sky performance. In Wizinowich, P. L. and Bonaccini, D., editors, *Adaptive Optical System Technologies II*, volume 4839 of *Proc. SPIE*, pages 140–149.

Sanders, D. B., Mazzarella, J. M., Kim, D.-C., Surace, J. A., and Soifer, B. T. (2003). The IRAS Revised Bright Galaxy Sample. *AJ*, 126:1607–1664.

Sarzi, M., Falcón-Barroso, J., Davies, R. L., Bacon, R., Bureau, M., Cappellari, M., de Zeeuw, P. T., Emsellem, E., Fathi, K., Krajnović, D., Kuntschner, H., McDermid, R. M., and Peletier, R. F. (2006). The SAURON project - V. Integral-field emission-line kinematics of 48 elliptical and lenticular galaxies. *MNRAS*, 366:1151–1200.

Sarzi, M., Iodice, E., Coccato, L., Corsini, E. M., de Zeeuw, P. T., Falcón-Barroso, J., Gadotti, D. A., Lyubenova, M., McDermid, R. M., van de Ven, G., Fahrion, K., Pizzella, A., and Zhu, L. (2018). The Fornax3D project: overall goals, galaxy sample, MUSE data analysis and initial results. *ArXiv e-prints*.

Scalzo, R., Yuan, F., Childress, M. J., Moller, A., Schmidt, B., Tucker, B. E., Zhang, B., Astier, P., Betoule, M., and Regnault, N. (2017). The SkyMapper Transient Survey. *ArXiv e-prints*.

Schirmer, M. (2013). THELI: Convenient Reduction of Optical, Near-infrared, and Mid-infrared Imaging Data. *ApJS*, 209:21.

Schirmer, M., Carrasco, E. R., Pessev, P., Garrel, V., Winge, C., Neichel, B., and Vidal, F. (2015). Gemini Frontier Fields: Wide-field Adaptive Optics K_s-band Imaging of the Galaxy Clusters MACS J0416.1-2403 and Abell 2744. *ApJS*, 217:33.

Schlafly, E. F. and Finkbeiner, D. P. (2011). Measuring Reddening with Sloan Digital Sky Survey Stellar Spectra and Recalibrating SFD. *ApJ*, 737:103.

Shappee, B. J., Prieto, J. L., Grupe, D., Kochanek, C. S., Stanek, K. Z., De Rosa, G., Mathur, S., Zu, Y., Peterson, B. M., Pogge, R. W., Komossa, S., Im, M., Jencson, J., Holoien, T. W.-S., Basu, U., Beacom, J. F., Szczygieł, D. M., Brimacombe, J., Adams, S., Campillay, A., Choi, C., Contreras, C., Dietrich, M., Dubberley, M., Elphick, M., Foale, S., Giustini, M., Gonzalez, C., Hawkins, E., Howell, D. A., Hsiao, E. Y., Koss, M., Leighly, K. M., Morrell, N., Mudd, D., Mullins, D., Nugent, J. M., Parrent, J., Phillips, M. M., Pojmanski, G., Rosing, W., Ross, R., Sand, D., Terndrup, D. M., Valenti, S., Walker, Z., and Yoon, Y. (2014). The Man behind the

Curtain: X-Rays Drive the UV through NIR Variability in the 2013 Active Galactic Nucleus Outburst in NGC 2617. *ApJ*, 788:48.

Smartt, S. J. (2009). Progenitors of Core-Collapse Supernovae. *ARA&A*, 47:63–106.

Smith, N., Li, W., Foley, R. J., Wheeler, J. C., Pooley, D., Chornock, R., Filippenko, A. V., Silverman, J. M., Quimby, R., Bloom, J. S., and Hansen, C. (2007). SN 2006gy: Discovery of the Most Luminous Supernova Ever Recorded, Powered by the Death of an Extremely Massive Star like η Carinae. *ApJ*, 666:1116–1128.

Smith, R. M., Dekany, R. G., Bebek, C., Bellm, E., Bui, K., Cromer, J., Gardner, P., Hoff, M., Kaye, S., Kulkarni, S., Lambert, A., Levi, M., and Reiley, D. (2014). The Zwicky transient facility observing system. In *Ground-based and Airborne Instrumentation for Astronomy V*, volume 9147 of *Proc. SPIE*, page 914779.

Stritzinger, M. and Moriya, T. (2018). Workshop 8: Supernovae. *ArXiv e-prints*.

Strolger, L.-G., Dahlen, T., Rodney, S. A., Graur, O., Riess, A. G., McCully, C., Ravindranath, S., Mobasher, B., and Shahady, A. K. (2015). The Rate of Core Collapse Supernovae to Redshift 2.5 from the CANDELS and CLASH Supernova Surveys. *ApJ*, 813:93.

Tadhunter, C., Spence, R., Rose, M., Mullaney, J., and Crowther, P. (2017). A tidal disruption event in the nearby ultra-luminous infrared galaxy F01004-2237. *Nature Astronomy*, 1:0061.

Taylor, M., Cinabro, D., Dilday, B., Galbany, L., Gupta, R. R., Kessler, R., Marriner, J., Nichol, R. C., Richmond, M., Schneider, D. P., and Sollerman, J. (2014). The Core Collapse Supernova Rate from the SDSS-II Supernova Survey. *ApJ*, 792:135.

Tody, D. (1993). IRAF in the Nineties. In Hanisch, R. J., Brissenden, R. J. V., and Barnes, J., editors, *Astronomical Data Analysis Software and Systems II*, volume 52 of *Astronomical Society of the Pacific Conference Series*, page 173.

U, V., Sanders, D. B., Mazzarella, J. M., Evans, A. S., Howell, J. H., Surace, J. A., Armus, L., Iwasawa, K., Kim, D.-C., Casey, C. M., Vavilkin, T., Dufault, M., Larson, K. L., Barnes, J. E., Chan, B. H. P., Frayer, D. T., Haan, S., Inami, H., Ishida, C. M., Kartaltepe, J. S., Melbourne, J. L., and Petric, A. O. (2012). Spectral Energy Distributions of Local Luminous and Ultraluminous Infrared Galaxies. *ApJS*, 203:9.

Umeda, H. and Yoshida, T. (2017). *Nucleosynthesis in Spherical Explosion Models of Core-Collapse Supernovae*, page 1753.

Utrobin, V. P. (2007). An optimal hydrodynamic model for the normal type IIP supernova 1999em. *A&A*, 461:233–251.

Väisänen, P., Escala, A., Kankare, E., Kotilainen, J., Mattila, S., Rajpaul, V., Randriamanakoto, Z., Reunanen, J., Ryder, S., and Zijlstra, A. (2012). Central regions of LIRGs: rings, hidden starbursts, Supernovae and star clusters. In *Journal of Physics Conference Series*, volume 372 of *Journal of Physics Conference Series*, page 012045.

Väisänen, P., Ryder, S., Mattila, S., and Kotilainen, J. (2008). A Pair of Leading Spiral Arms in a Luminous Infrared Galaxy? *ApJ*, 689:L37.

Valdés, J. R., Berta, S., Bressan, A., Franceschini, A., Rigopoulou, D., and Rodighiero, G. (2005). NIR spectroscopy of luminous infrared galaxies and the hydrogen recombination photon deficit. *A&A*, 434:149–161.

Valenti, S., Fraser, M., Benetti, S., Pignata, G., Sollerman, J., Inserra, C., Cappellaro, E., Pastorello, A., Smartt, S. J., Ergon, M., Botticella, M. T., Brimacombe, J., Bufano, F., Crockett, M., Eder, I., Fugazza, D., Haislip, J. B., Hamuy, M., Harutyunyan, A., Ivarsen, K. M., Kankare, E., Kotak, R., Lacluyze, A. P., Magill, L., Mattila, S., Maza, J., Mazzali, P. A., Reichart, D. E., Taubenberger, S., Turatto, M., and Zampieri, L. (2011). SN 2009jf: a slow-evolving stripped-envelope core-collapse supernova. *MNRAS*, 416:3138–3159.

van Buren, D., Jarrett, T., Terebey, S., Beichman, C., Shure, M., and Kaminski, C. (1994). Supernova 1992bu in NGC 3690. *IAU Circ.*, 5960.

Vazdekis, A., Sánchez-Blázquez, P., Falcón-Barroso, J., Cenarro, A. J., Beasley, M. A., Cardiel, N., Gorgas, J., and Peletier, R. F. (2010). Evolutionary stellar population synthesis with MILES - I. The base models and a new line index system. *MNRAS*, 404:1639–1671.

Vink, J. (2017). *Supernova 1604, Kepler's Supernova, and its Remnant*, page 139.

Wang, L., Baade, D., Baron, E., Bernard, S., Bromm, V., Brown, P., Clayton, G., Cooke, J., Croton, D., Curtin, C., Drout, M., Doi, M., Dominguez, I., Finkelstein, S., Gal-Yam, A., Geil, P., Heger, A., Hoeflich, P., Jian, J., Krisciunas, K., Koekemoer, A., Lunnan, R., Maeda, K., Maund, J., Modjaz, M., Mould, J., Nomoto, K., Nugent, P., Patat, F., Pacucci, F., Phillips, M., Rest, A., Regos, E., Sand, D., Sparks, B., Spyromilio, J., Staveley-Smith, L., Suntzeff, N., Uddin, S., Villarroel, B., Vinko, J., Whalen, D., Wheeler, J., Wood-Vasey, M., Yang, Y., and Yue, B. (2017). A First Transients Survey with JWST: the FLARE project. *ArXiv e-prints*.

Weilbacher, P. M., Streicher, O., Urrutia, T., Pécontal-Rousset, A., Jarno, A., and Bacon, R. (2014). The MUSE Data Reduction Pipeline: Status after Preliminary Acceptance Europe. In Manset, N. and Forshay, P., editors, *Astronomical Data Analysis Software and Systems XXIII*, volume 485 of *Astronomical Society of the Pacific Conference Series*, page 451.

Whelan, J. and Iben, Jr., I. (1973). Binaries and Supernovae of Type I. *ApJ*, 186:1007–1014.

Wilkins, S. M., Trentham, N., and Hopkins, A. M. (2008). The evolution of stellar mass and the implied star formation history. *MNRAS*, 385(2):687–694.

Williams, B. J. and Temim, T. (2017). *Infrared Emission from Supernova Remnants: Formation and Destruction of Dust*, page 2105.

Wizinowich, P. L., Le Mignant, D., Bouchez, A. H., Campbell, R. D., Chin, J. C. Y., Contos, A. R., van Dam, M. A., Hartman, S. K., Johansson, E. M., Lafon, R. E., Lewis, H., Stomski, P. J., Summers, D. M., Brown, C. G., Danforth, P. M., Max, C. E., and Pennington, D. M. (2006). The W. M. Keck Observatory Laser Guide Star Adaptive Optics System: Overview. *PASP*, 118:297–309.

Xiao, L., Galbany, L., Eldridge, J. J., and Stanway, E. R. (2018). Core-collapse supernovae ages and metallicities from emission-line diagnostics of nearby stellar populations. *ArXiv e-prints*.

Yamada, R., Oyabu, S., Kaneda, H., Yamagishi, M., Ishihara, D., Kim, J. H., and Im, M. (2013). A Relation of the PAH 3.3 μm Feature with Star-forming Activity for Galaxies with a Wide Range of Infrared Luminosity. *PASJ*, 65:103.

Zhang, K., Wang, X., Zhang, J., Zhang, T., Ganeshalingam, M., Li, W., Filippenko, A. V., Zhao, X., Zheng, W., Bai, J., Chen, J., Chen, J., Huang, F., Mo, J., Rui, L., Song, H., Sai, H., Li, W., Wang, L., and Wu, C. (2016). Optical Observations of the Type Ia Supernova SN 2011fe in M101 for Nearly 500 Days. *ApJ*, 820:67.

Zwart, J. T. L., Barker, R. W., Biddulph, P., Bly, D., Boysen, R. C., Brown, A. R., Clementson, C., Crofts, M., Culverhouse, T. L., Czeres, J., Dace, R. J., Davies, M. L., D'Alessandro, R., Doherty, P., Duggan, K., Ely, J. A., Felvus, M., Feroz, F., Flynn, W., Franzen, T. M. O., Geisbüsch, J., Génova-Santos, R., Grainge, K. J. B., Grainger, W. F., Hammett, D., Hills, R. E., Hobson, M. P., Holler, C. M., Hurley-Walker, N., Jilley, R., Jones, M. E., Kaneko, T., Kneissl, R., Lancaster, K., Lasenby, A. N., Marshall, P. J., Newton, F., Norris, O., Northrop, I., Odell, D. M., Petencin, G., Pober, J. C., Pooley, G. G., Pospieszalski, M. W., Quy, V., Rodríguez-Gonzálvez, C., Saunders, R. D. E., Scaife, A. M. M., Schofield, J., Scott, P. F., Shaw, C., Shimwell, T. W., Smith, H., Taylor, A. C., Titterington, D. J., Velić, M., Waldram, E. M., West, S., Wood, B. A., Yassin, G., and AMI Consortium (2008). The Arcminute Microkelvin Imager. *MNRAS*, 391:1545–1558.